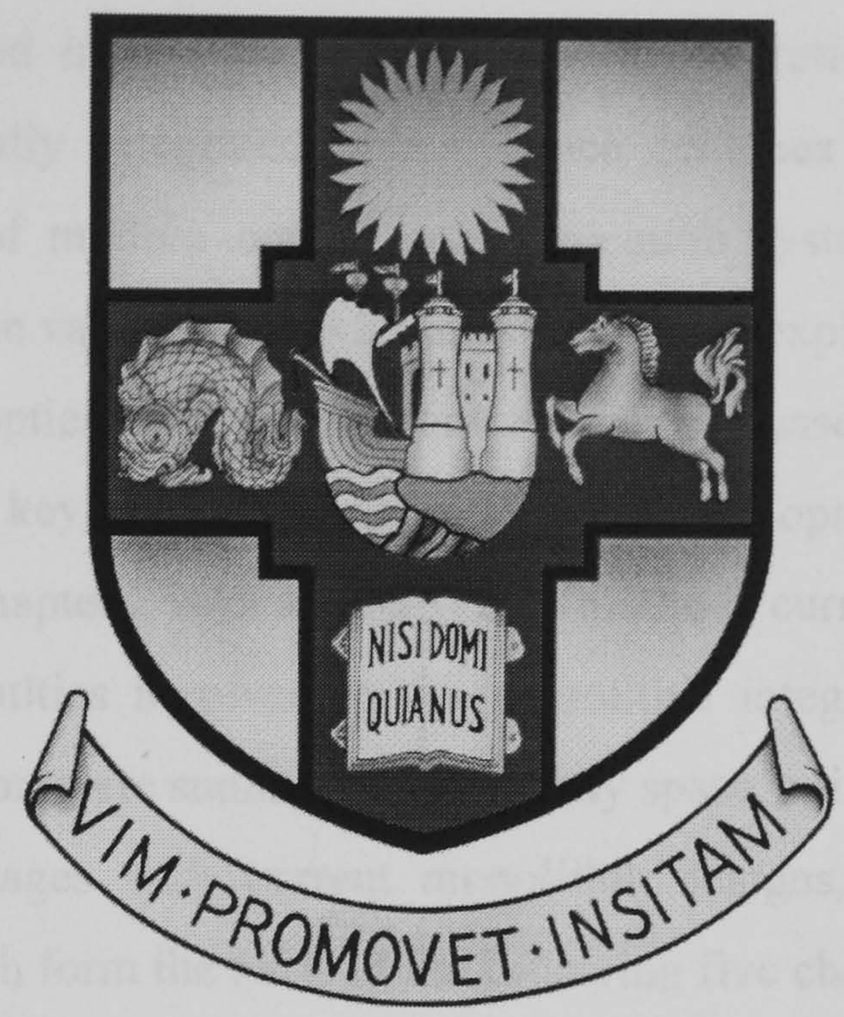

Monolithic Integration of Optical Space Switches

A dissertation submitted to the University of Bristol in accordance with the requirements of the degree of Ph.D. in the Faculty of Electrical and Electronic Engineering

Mark Owen September 1998

Word Count 44366

Abstract

The work presented in this thesis concerns the theoretical design, fabrication and assessment of monolithically integrated optical space switches for future optical routing networks. The evolution of modern optical communication systems is first summarised in chapter 1, which outlines the various methods currently used to exploit the bandwidth of optical fibre. The future role of optical communications is then discussed, where the optical space switch is shown to be the key component required for future optical routing networks. This introduction continues in chapter 2 with an analysis of methods currently used to design optical space switches. The difficulties involved in the monolithic integration of these devices are discussed together with a complete summary of the many space switches reported to date. After highlighting the disadvantages with current monolithic designs, three entirely new space switches are proposed which form the basis of the following five chapters of work.

Chapter 3 begins by discussing the role of Two Dimensional Integrated Optics (2DIO) in space switch development. A novel *NxN* 2DIO space switch architecture is proposed for the InP/InGaAs/InGaAsP material system, and is theoretically designed in order to achieve acceptable device performance. Calculations show that the final 4x4 switch would operate with a net fibre to fibre gain, crosstalk of less than -40dB and occupy only $2x2mm^2$ of an InP wafer.

Chapters 4, 5 and 6 describe the second space switch presented in this thesis, which operates in the 1.5μm communication window and is grown in the InP/InGaAs/InGaAsP material system. Chapter 4 starts with the theoretical optimisation of the device size in order to achieve the most compact switch possible, while still maintaining an acceptable loss and crosstalk performance. The fabrication of several InP devices is then described in chapter 5, which have been made to justify the theoretical calculations made in chapter 4. This discussion also provides an insight into the many fabrication issues posed by InP crosspoint fabrication. Finally chapter 6 describes the experimental measurement and assessment of these devices. This analysis allows an estimate of the performance of the final 4x4 space switch. Results show that the device would operate with net fibre to fibre gains of the order of 10dB, crosstalk figures of less than -50dB, and occupy approximately $1x2mm^2$ of an InP wafer. The device presented is the smallest broadcast 4x4 space switch proposed in the literature to date, which is an order of magnitude improvement on existing InP space switch designs.

Finally chapter 7 describes a third method for achieving space switching by using wavelength conversion and passive wavelength routing. A novel multi-wavelength laser is used to demonstrate 1x4 space switching at 2.488Gbits/s. This is currently the highest modulation rate achieved by a monolithic integrated multi-wavelength laser.

Chapter 8 concludes with a summary of the main points of this thesis and suggestions for future work.

I'm rhieni

Acknowledgements

I would first like to thank my supervisor Prof. Ian White for the many opportunities he has given me over the last three years. I have greatly benefited from his guidance and constant source of novel ideas. Many thanks must also go to Dr. Michael Robertson at BT Research Laboratories, my industrial supervisor, for encouragement and financial support along with EPSRC under the CASE award scheme.

Much of this work would have taken far longer without the constant source of inspiration provided by Dr. Mehdi Asghari. He has taught me all I know about two dimensional integrated optics, and any theoretical misgivings contained herein I graciously devote to him. I would also like to thank Dr. Kai Poguntke at BT who had the patience to sift through the numerous calculations made in Chapter 4, and taught me much of what I know about mask design and InP device fabrication. The work presented in Chapter 7 could not have been achieved without the fabrication of the MGC laser and I am indebted to Dr. Kai Poguntke and Dr. Michael Robertson together with their colleagues at BT for this gracious donation.

I would like to thank all the people at Glasgow University who helped in fabricating the test structures which formed the basis of Chapters 5 and 6. Firstly Prof. John Marsh and Prof. Chris Wilkinson for allowing my 3 month placement and secondly Dr. Catrina Bryce, Miss. Joan Carson and Mrs. Louis Hobbs for their clean room expertise and discussions on fabrication. Most importantly I would like to thank Dr. Yahong Qian for completing the fabrication of the test structures and all the technical support staff at Glasgow who made the fabrication of the devices possible.

No acknowledgements page could be complete without individual thanks to many of my colleagues at Bristol University. My time would not have been as enjoyable if it was not for the office banter provided by (in no particular order) Dr. Philip 'Leslie' Mason, Dr. Roger Griffiths, Dr. Marc Stephens, Mr. Adrian Wonfor, Mr. Mike Cowin, Dr. Kevin Williams, Dr. Philip Dowd, Mr. John Bainbridge, Mr. Lutz Raddatz, along with the numerous other people who form the optics group.

Special thanks must also go to Dr. Siyuan Yu for his tuition on clean room fabrication and all the support (both technical and comical) provided by Mr. Bob Bowden, Mr. Bob Butler, Mr. Rob Davies, Mr. Mike Penny and Mr. John Smith down in the workshop.

Most of all I would like to thank my parents, brother and girlfiend for their support and encouragement.

Monolithic Integration of Optical Space Switches

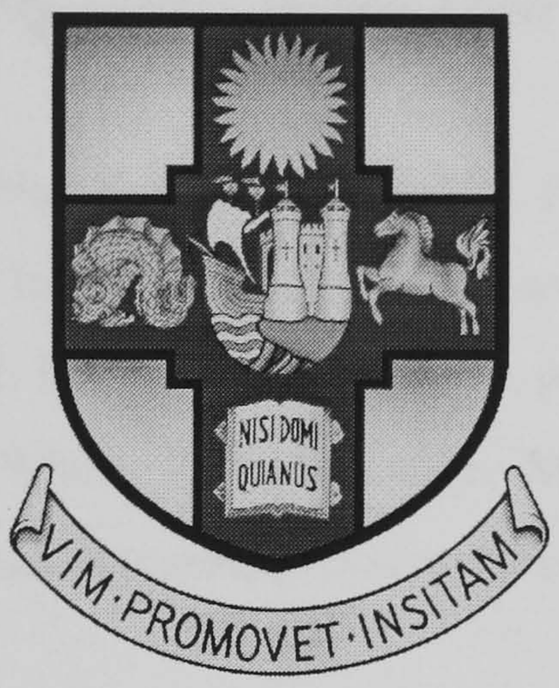

Submitted by Mark Owen for the degree of Ph.D.
Department of Electrical and Electronic Engineering
University of Bristol
September 1998

Copyright and Author's Declaration

I declare that the work in this dissertation was carried out in accordance with the regulations of the university of Bristol. The work is original except where indicated by special reference in the text and no part of the dissertation has been submitted for any other degree.
Any views expressed in the dissertation are those of the author and in no way represent those of the University of Bristol. The dissertation has not been presented to any other University for examination either in the United Kingdom or overseas.

Signed M A Owen *Date* 20/10/98.

Publications

A list of publications resulting from this work is presented below.

1) M. Owen, R.V. Penty, I.H. White, K.R. Poguntke, M.J. Robertson "Demonstration of Multi Wavelength Picosecond Pulse Generation with resonant RF Drive using a monolithically Integrated Multi-Grating Cavity Laser", Invited Paper CLEO Europe 1998, Paper No. CWG1.
2) M. Owen, M. Asghari, I.H. White, K.R. Poguntke, M.J. Robertson "Theoretical Design of a Novel NxN Two Dimensional Integrated Optical Crosspoint Switch Architecture", Journal of Lightwave Technology, Vol. 16, No. 3, March 1998, pp.380-387.
3) M. Owen, M. Asghari, I.H. White, K.R. Poguntke, M.J. Robertson "Design of Mirror Structures for Two Dimensional Integrated Optical Crosspoint Switches", CLEO Europe 1996, paper CuTuK61.
4) M. Owen, M. Asghari, I.H. White, K.R. Poguntke, M.J. Robertson "Theoretical Analysis of a Novel NxN Two Dimensional Integrated Optical Cross-connect", SIOE 1997 Paper No. 20.
5) M. Owen, J.D. Bainbridge, M.F.C. Stephens, "All Optical Wavelength Conversion at 2.488Gbits/s using a Multi-Wavelength Laser", SIOE 1998, Paper No. 37.
6) M. Owen, J.D. Bainbridge, M.F.C. Stephens, "Highly Flexible all-Optical Wavelength Conversion at 2.488Gbits/s using a multi-output wavelength Laser", CLEO 1998, Paper No. CThZ6.
7) M. Owen, M.F.C. Stephens, J.D. Bainbridge, R.V. Penty, I.H. White, K.R. Poguntke, M.J. Robertson, "All-Optical 1x4 Network Switching and Simultaneous Wavelength Conversion using an Integrated Multi-Wavelength Laser", Accepted ECOC 98.
8) M. Owen, J.D. Bainbridge, M.F.C. Stephens, I.H. White, R.V. Penty, "All optical Wavelength Conversion At 2.488Gbits/s using the Integrated Multi-Grating Cavity (MGC) Laser", IEE colloquia on WDM networking June 98.
9) M.F.C. Stephens, J.D. Bainbridge, M. Owen, I.H. White, R.V. Penty, "Demonstration of Simultaneous all-optical Wavelength Conversion and tone reading/replacing in an integrated SOA/DFB laser", submitted to Electronics Letters July 1998.
10) M.F.C. Stephens, J.D. Bainbridge, M. Owen, I.H. White, R.V. Penty, "Demonstration of Simultaneous all-optical Wavelength Conversion and tone reading/replacing in an integrated SOA/DFB laser", CLEO Europe 1998, Paper No. CThH101.
11) M.F.C. Stephens, M. Owen, J.D. Bainbridge, R.V. Penty, I.H. White, "All-Optical Wavelength Conversion of a 2.488Gbit/s Signal with Simultaneous 2R Regeneration and Pilot tone reading/replacing", accepted ECOC 98.
12) M.F.C. Stephens, J.D. Bainbridge, M. Owen, R.V. Penty, I.H. White, M.J. Fice "A Technique For Wavelength Converting A 2.488Gb/s Signal Whilst Simultaneously

Monitoring And Replacing A Wavelength Identifying Pilot Tone" IEE colloquia on WDM networking June 98.

13) Y. Qian, A.C. Bryce, J.H. Marsh, C.D.W. Wilkinson, M.Owen, R.V. Penty, I.H. White, M.J. Robertson, "Fabrication of test structures for a 4x4 InP/InGaAsP Integrated Optical Switching Matrix", CLEO Europe 1998, Paper No. CTuC5.

14) M. Owen, R.V. Penty, I.H. White, K.R. Poguntke, M.J. Robertson "Multi-Wavelength Picoscond Pulse Generation using a monolithically Integrated Multi-Grating Cavity Laser", ISLC 98 Japan, Paper No. ThB4.

15) M. Owen, M.F.C. Stephens, J.D. Bainbridge, R.V. Penty, I.H. White, K.R. Poguntke, M.J. Robertson, "All-Optical 1x4 Network Switching and Simultaneous Wavelength Conversion using an Integrated Multi-Wavelength Laser", Vol. 34, No. 20, October 1998.

16) J.D. Bainbridge, A.R. Sharafi, I.H. White, M.A. Cowin, M.F.C. Stephens, M.Owen, R.V. Penty, K.M. Guild, A. Tzanakaki, M.J. O'Mahony, G.H.B. Thompson, S.J. Clements, C.B. Rogers, "All-optical routing using a 12x12 passive InP wavelength selective router and tuneable wavelength conversion", IEE colloquia on WDM networking June 98.

17) Y.H. Qian, M.Owen, M.L. Kc, B.C. Qiu, S.D. McDougall, O.P Kowalski, C.J. Hamilton, A.C. Bryce, C.D.W. Wilkinson, R.V. Penty, I.H. White, S. Perrin, D. Rogers, M.J. Robertson, "Three band-gap QW intermixing in the InP/InGaAs/InGaAsP System for a Monolithically Integrated Optical Switch", submitted SPIE 98.

Contents

Tables and Figures

Monolithic Integration of Optical Space Switches

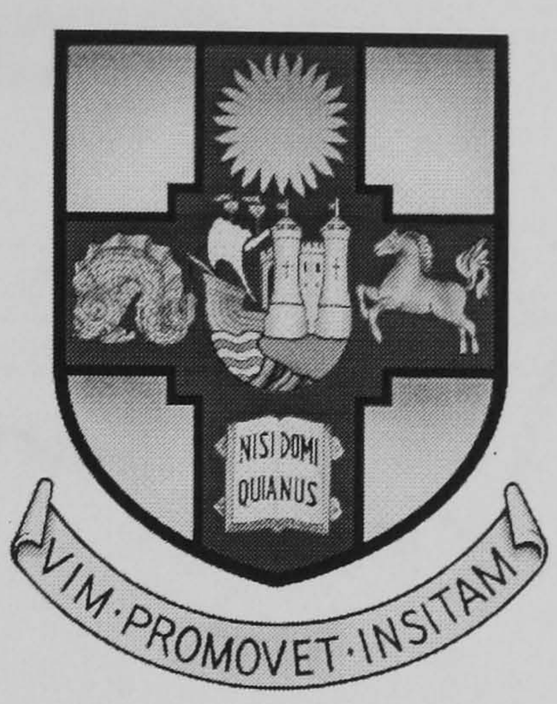

Chapter 1

1.1 Introduction

The work presented in this thesis investigates the monolithic integration of optical space switches in the InP/InGaAsP/InGaAs material system. This chapter will give a brief introduction to the reasons why optical space switches are required for future telecommunication systems. It will be shown that the space switch is a core component required for future optical network schemes. However, in order for these devices to become viable, more effective methods must be found to monolithically integrate them onto semiconductor substrates. Wavelength conversion and passive wavelength routing could also play an important role in space switch development, especially in Wavelength Division Multiplexing (WDM) schemes. Thus methods of achieving wavelength routing will also be discussed.

1.2 Development of Optical Communications

1.2.1 A Brief Introduction

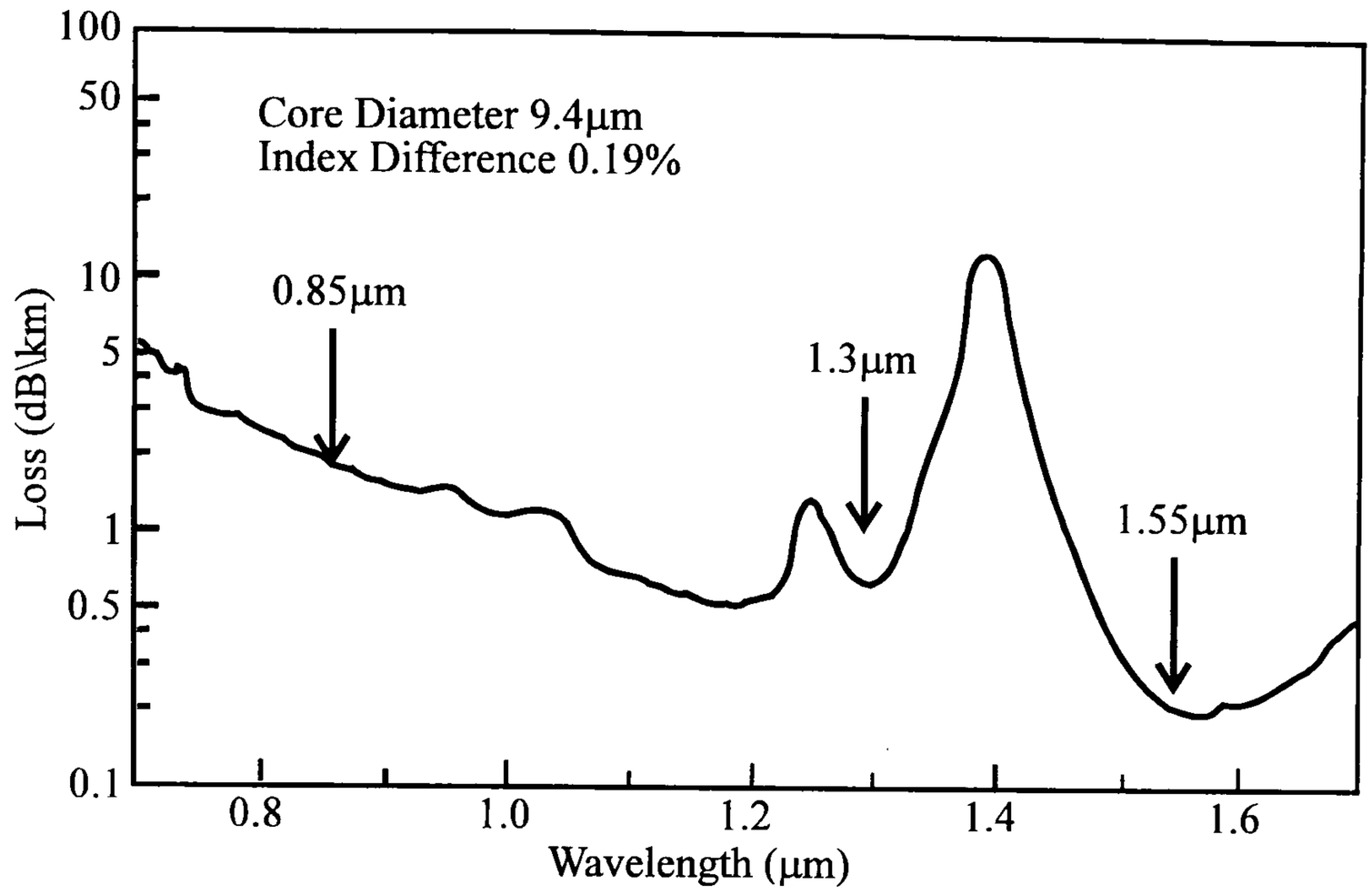

Figure 1.1 Measured loss in a single mode fibre as a function of wavelength (after[1])

The advent of the single-mode fibre in the early 1970's presented engineers with a low loss transmission medium which marked the dawn of the modern optical communications revolution. Optical fibre offers terahertz of bandwidth compared with conventional coaxial cable, which is limited to around a gigahertz. However, unlocking this enormous potential has not been easy. It is only lately, almost thirty years after its conception, that commercial systems are beginning to fully utilise the enormous communications capacity offered by optical fibre.

The first optical communication systems used multimode fibre and AlGaAs Fabry Perot (FP) laser sources which operated at wavelengths around 0.85μm. However, these systems were limited owing to significant optical loss with transmission distance. Figure 1.1, plots the material loss of optical fibre as a function of wavelength, which indicates a value of around 2dB/km at 0.85μm. This constrained the practical link length to around 10km, before which the optical signal had to be 'regenerated'. At the time, with no adequate method of 'all-optically' amplifying the signal, this involved an electronic technique of detecting the transmitted signal and remodulating a secondary laser source. The so called 'repeaters' were expensive and the modal dispersion of the multi-mode fibre limited the communication data rate to around 100Mbits/s [2].

Meanwhile, work in the InGaAsP material system had resulted with lasers operating at 1.3μm, which had the advantage of a lower fibre loss of ≈0.5dB/km (figure 1.1). The distance between repeaters could be increased five fold, resulting in spans of more than 50km and drastically reduced repeater numbers and therefore cost. With the use of single mode fibre, modal dispersion was eliminated and the data rate could be vastly improved up to 2Gbits/s.

1.3μm lasers also offered advantages in zero material dispersion (figure 1.2), which meant Fabry Perot lasers could still be used at the higher data rates. However, the number of optical regenerators required for a link still imposed cost limitations on the total length of the network. Economic considerations thus prompted a third generation of optical communications. These systems operated at 1.5μm, the absorption minimum of single mode fibre (figure 1.1).

1.2.2 The 1.5μm Window and the DFB Laser

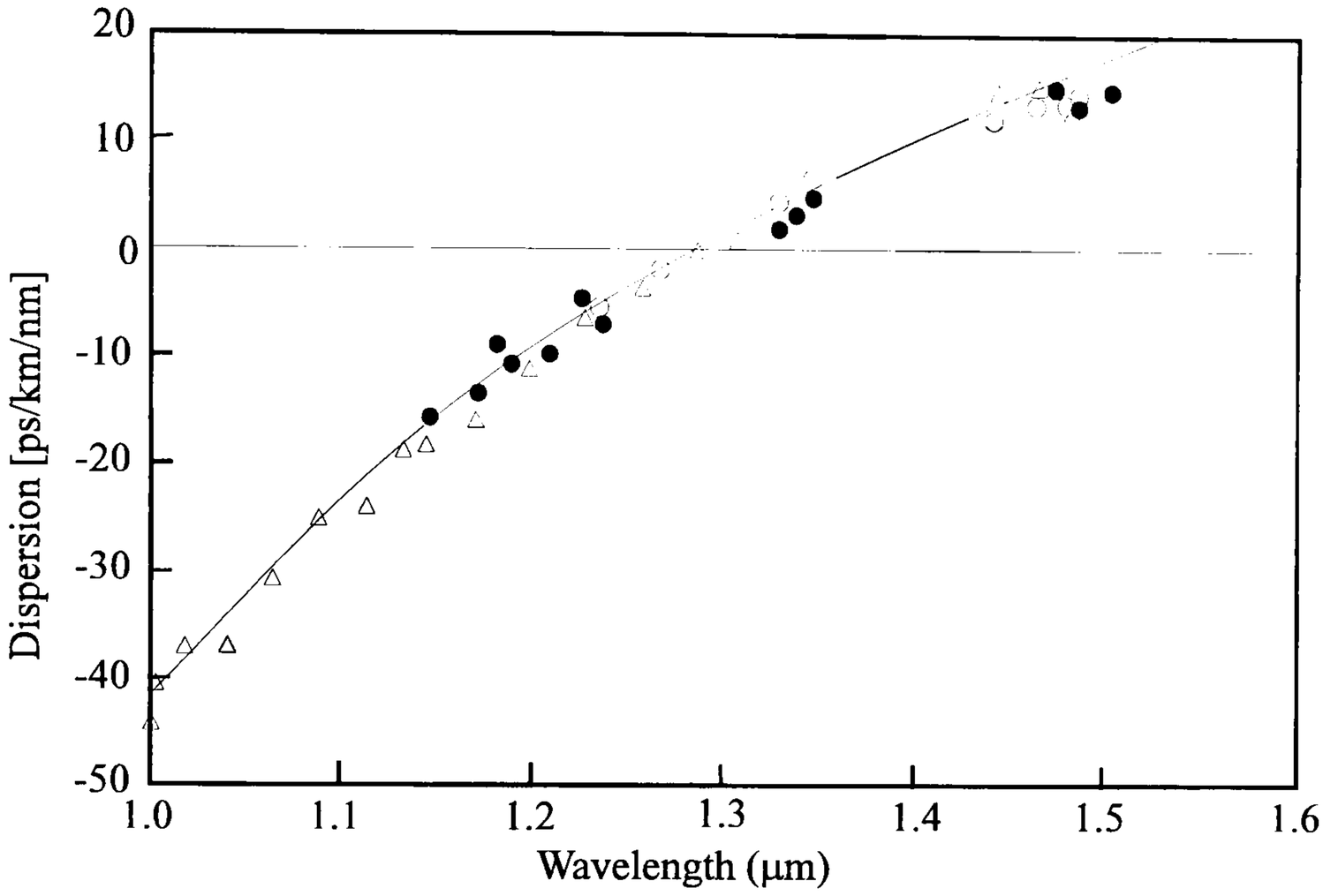

Figure 1.2 Measured Material dispersion for a typical single-mode fibre (after[3])

At 1.5μm the repeater spacing can easily exceed 100km for moderate bit rates [4]. However, at high bit rates (>1Gbit/s), the repeater spacing is not limited by fibre loss but by chromatic dispersion (the refractive index dependence of silica as a function wavelength as plotted in figure 1.2) [5]. Typical sources contain a range of wavelengths (or spectral width) which, over large fibre links, reach the detector at different times. This causes individual bits to merge together as the signal travels down the fibre. In an FP laser the spectral width may be several nanometers, which limits the maximum transmission distance for a given modulation speed (4km for a 2.5Gbit/s bit stream at 1.55μm [6]). Two methods have been used in order to overcome this problem. The first led to the development of Dispersion Shifted Fibre (DSF). By controlling the geometry of the fibre, the zero dispersion point plotted in figure 1.2 may be shifted to 1.55μm [7]. This solution seems ideal, however to date, the vast majority of installed optical fibre is standard, with a dispersion minimum at 1.3μm. It is currently too expensive to upgrade all existing systems to DSF, thus other methods had to be found in order to overcome dispersion.

The second method involved reducing the linewidth of the lasing mode, which led to the development of the Distributed FeedBack (DFB) laser and Distributed Bragg Reflector (DBR) laser. Both designs restrict the optical frequencies which are able to resonate inside the laser cavity by the use of a Bragg reflection grating [8]. This forces the device to lase in a single longitudinal mode with a linewidth of approximately 0.1nm. This can increase the transmission distance for a given bit rate by 100 fold compared with a standard 1.5μm FP laser. However, even a DFBs transmission distance is still limited by fibre dispersion. Several methods have been implemented to increase this transmission distance still further, but are far beyond the scope of this thesis.

1.2.3 The Erbium Doped Fibre Amplifier (EDFA)

With the advent of narrow linewidth sources, research into coherent detection systems began in order to increase the receiver sensitivity and increase the repeater-repeater distance still further [9]. However, a method of all-optically amplifying the signal was required so that electronic regeneration could be eliminated. Repeaters not only limited the maximum possible bit rate, by introducing an 'electronic bottleneck' into the network, they also made upgrading to higher rates extremely expensive. The breakthrough came with the development of the Erbium Doped Fibre Amplifier (EDFA). The amplifier consists of optical fibre doped with erbium, which is optically pumped by a semiconductor laser at 980nm or 1480nm. The process is extremely efficient and the EDFA may be spliced directly into the network, where it can provide optical gains of up to 54dB with very low noise figures in the 1530-1565nm window (figure 1.3).

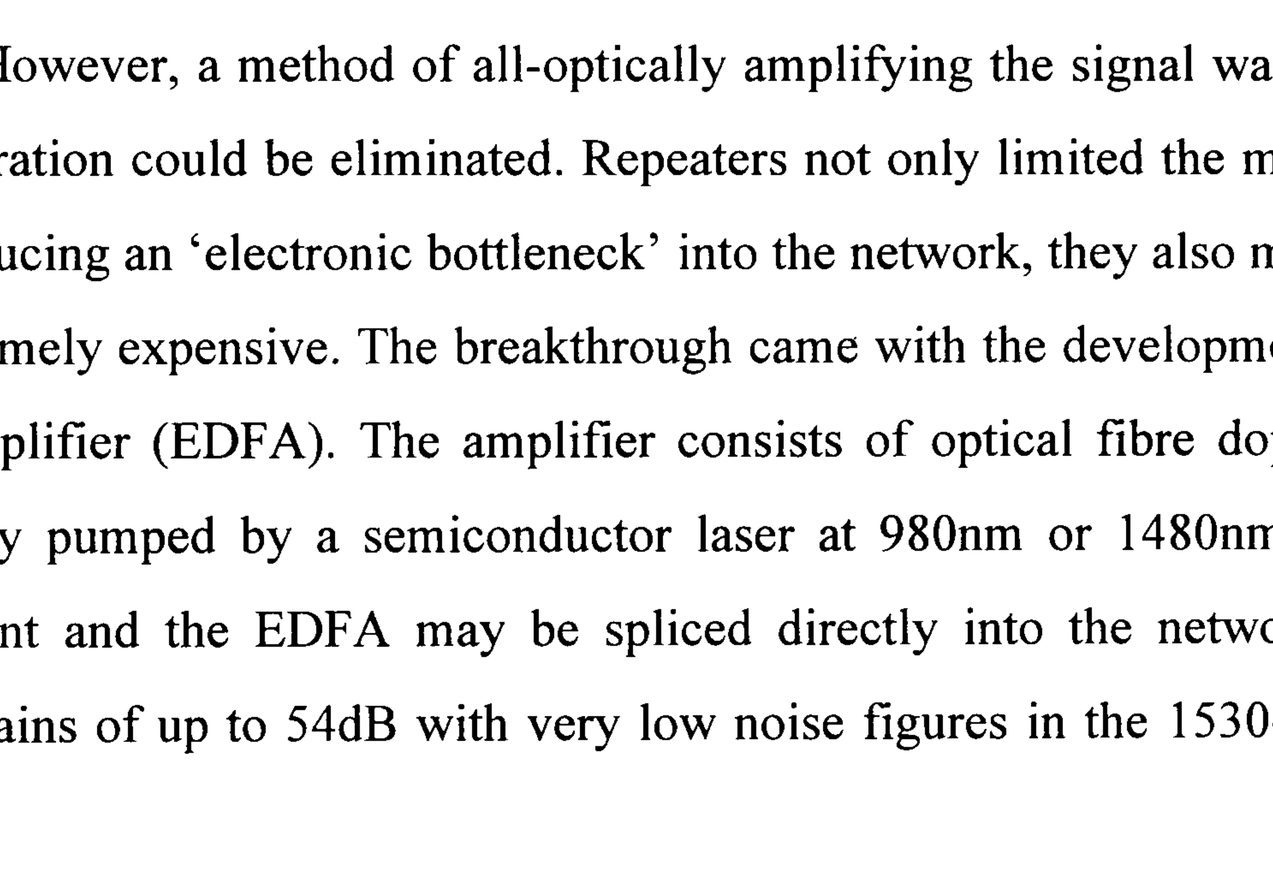

Figure 1.3 Experimentally measured gain flattened EDFA as a function of input wavelength

Thus current communications systems operate at 1.5μm, with narrow linewidth sources to increase transmission distance and use EDFAs to remove the need for regeneration. Although 1.3μm systems are extremely attractive for minimising dispersion, without a low cost all-optical amplifier the associated cost of electronic repeaters limits their implementation. There is increasing interest in Praseodymium doped Fluoride amplifiers for 1300nm amplification [10], however these amplifiers are costly and currently very inefficient. There have been two main advantages in designing optical networks at 1.5μm. Firstly the loss is almost half that at 1300nm, and secondly an effective amplifier overcomes any loss limitation imposed by optical fibre. EDFAs are not only vastly cheaper than regenerators, but are also future proof, allowing upgrades to higher bit-rates and implementation of multiplexing schemes such as WDM and OTDM. These multiplexing schemes are discussed in the next section and are used to improve the communication capacity of optical fibre.

1.3 Future Communications Systems

Currently there is a communications revolution. The advent of the internet and video conferencing coupled with the next generation of services such as interactive computer communication, home shopping and video on demand will all require large amounts of communications capacity. Indeed current forecasts expect the demand on communication systems to double every year [11]. Only optical communications can deliver the bandwidth required for the future expectations of the global communications network. Two networking schemes have so far been adopted for these future systems, dense Wavelength Division Multiplexing (WDM) and Optical Time Division Multiplexing (OTDM).

1.3.1 Optical Time Division Multiplexing (OTDM)

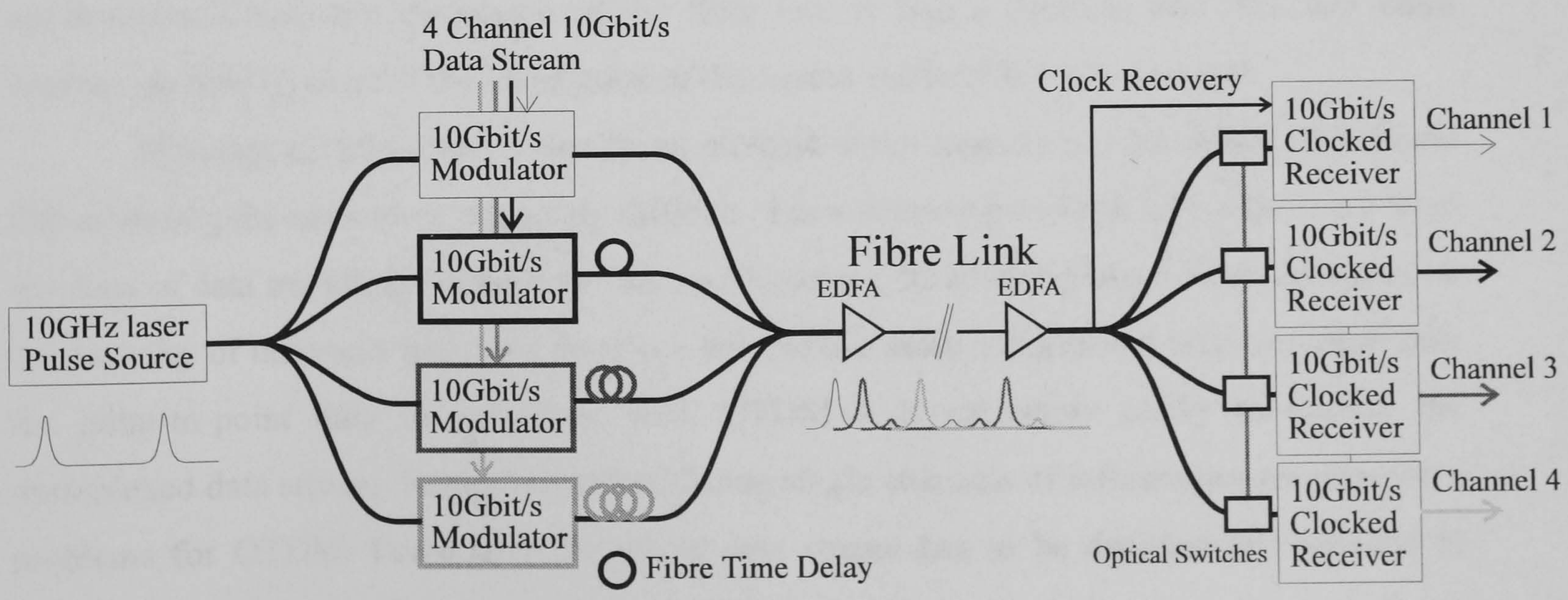

Figure 1.4 Schematic diagram of a 4 Channel OTDM System

10Gbit/s optical and electronic technologies are becoming well established. Over the past few years it has become almost commonplace to demonstrate networking functions at 10Gbit/s. However, an increase to 40Gbits/s is currently difficult because the direct modulation of the optical signal is limited by any driver or receiver electronics. Thus the maximum data rate of a conventional point to point fibre link is currently restricted. However, coding schemes can be used in order to increase the capacity of the link whilst still retaining 10Gbits/s technology. Optical Time Division Multiplexing (OTDM) is one such coding scheme which is discussed as follows.

Semiconductor lasers are well suited to generate streams of optical pulses, with very short pulse widths (~10ps) at tens of gigahertz (100ps) repetition rates. This has been demonstrated by both mode-locking [12] and gain switching [13] of the semiconductor laser. By optically splitting a pulse stream, each portion may be modulated at its repetition rate as shown schematically in figure 1.4. This may be accomplished by using devices such as the Electroabsorption modulator [14] or Mach Zehnder Interferometer [15] (these devices are discussed in more detail in Chapter 2). Each modulated channel may then be interleaved in time, by delaying each channel with the appropriate amount of fibre (~2cms per channel at 10Gbits/s), before being transmitted down the same optical fibre. Thus by using 10Gbit technology the capacity of the fibre has been increased 4 fold to 40Gbits/s. The channels may be decoded by incorporating clock recovery and a synchronised receiver [16].

The potential communications increase offered by OTDM is significant. The maximum number of channels that maybe multiplexed is for obvious reasons related to the pulse width and repetition rate of the source. More importantly, the number of channels is also extremely dependent on the pulse to pulse jitter. This is the timing error between each successive pulse as it leaves the laser. Variations in the firing rate of the source has severe implications for OTDM and there is currently much interest in producing low pulse width, low jitter sources for OTDM applications. Chromatic dispersion of the fibre link is also a problem and thus low chirp sources are also required if the installation of dispersion shifted fibre is to avoided.

Although OTDM offers a significant increase in the capacity of optical fibre, it is found that accessing the network is extremely difficult . For a point-to-point link where there are large amounts of data travelling between two distinct locations, its advantages are clear. However, as the capacity of networks increases there is a need to use more complicated schemes other than for point-to-point data transmission. With OTDM it is extremely costly to decode the multiplexed data stream. Removing and replacing single channels of information are expensive problems for OTDM. Potentially the whole data stream has to be decoded and recoded to provide access to the network. This requires expensive active components such as electroabsorption modulators. Thus a second, potentially more flexible scheme has been

proposed which multiplexes data in the wavelength rather than time domain. Wavelength Division Multiplexing (WDM) has the advantage that decoding can be performed by purely passive components, which reduces network costs and increases flexibility.

1.3.2 Wavelength Division Multiplexing

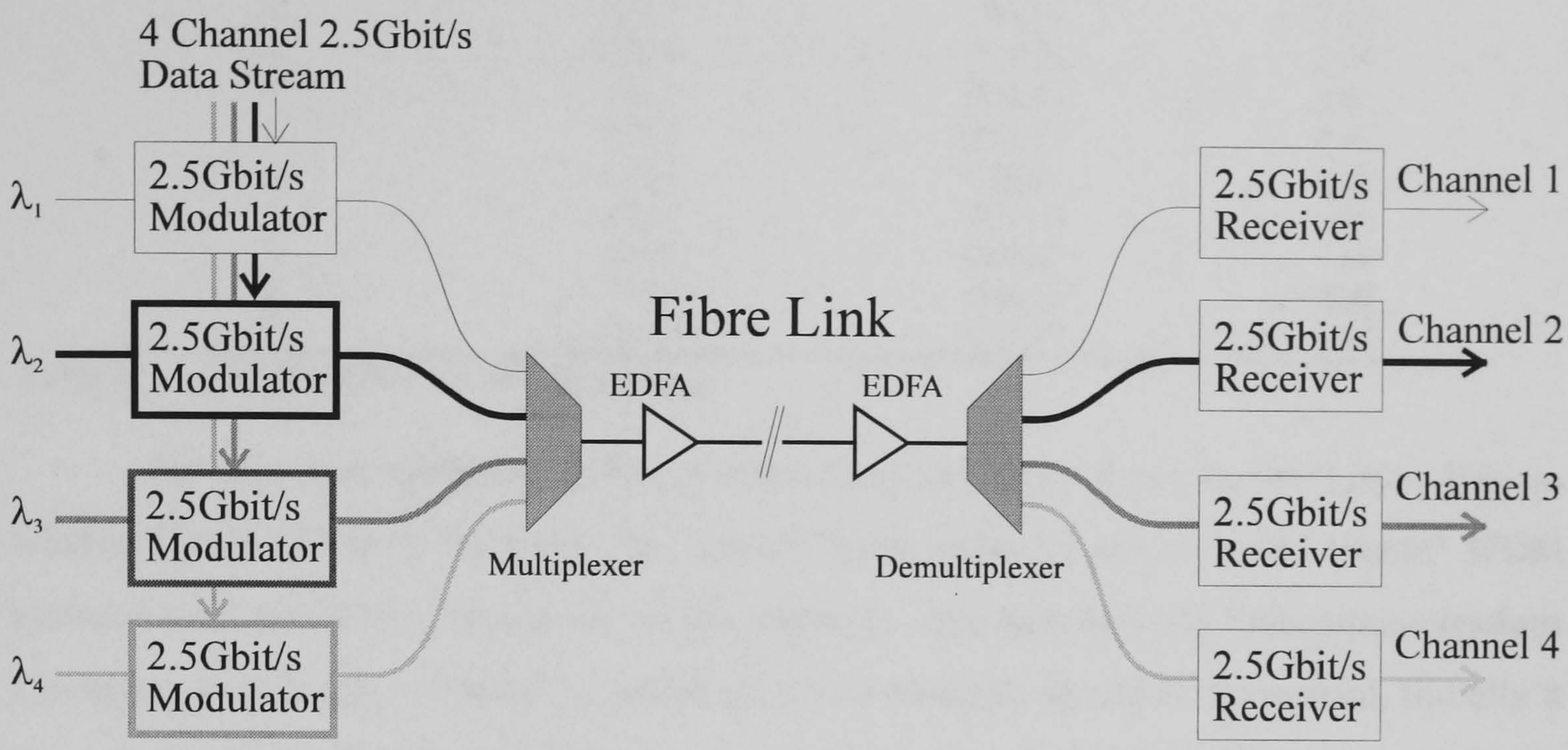

Figure 1.5 A Four Channel Point to Point WDM Network giving 4x2.5Gbits/s

With the advent of the DFB and Erbium Doped Fibre amplifier in the late 1980's, Wavelength Division Multiplexing (WDM) became a realistic possibility. WDM involves the simultaneous encoding of data on a number of different wavelengths as shown schematically in figure 1.5. A number of narrow linewidth sources, such as DFBs, are first amplitude modulated (generally NRZ) independently. Each wavelength may then be multiplexed together onto a single fibre for transmission across the link. An optical coupler can be used to achieve multiplexing however this technique incurs a $10log_{10}(Channel\ Number)$ dB loss penalty and as such limits the number of channels [17]. More efficient multiplexing may be achieved from a diffraction grating, whose loss is independent of the channel number. Many types of monolithically integrated grating (de)multiplexer have been proposed in the literature. A description of each type is given in Chapter 7. However they may be briefly summarised by the Rowland reflection grating [18,19], the 2DIO transmission grating [20] and the waveguide phased array [21-24]. Providing each wavelength channel is within the EDFA gain window (1530-1570nm), then any number of WDM channels may be amplified simultaneously by the EDFA, thus dramatically increasing the data capacity of the fibre link [25]. Channel extraction is easily achieved by the use of a purely passive demultiplexer.

Channel Number	Channel Frequency (THz)	Channel Wavelength (nm)	Channel Spacing (nm)
-6	192.5	1557.35	0.81
-5	192.6	1556.54	0.81
-4	192.7	1555.73	0.81
-3	192.8	1554.93	0.81
-2	192.9	1554.12	0.81
-1	193.0	1553.32	0.80
0	193.1	1552.51	0.80
1	193.2	1551.71	0.80
2	193.3	1550.91	0.80
3	193.4	1550.10	0.80
4	193.5	1549.30	0.80
5	193.6	1548.50	0.80
6	193.7	1547.70	0.80

Table 1.1 The ITU Grid for WDM systems

There is approximately 5THz of optical bandwidth available in the 1.5μm Erbium window (1530-1570nm). By using very closely space channels, the so called 'dense' WDM system could potentially access all of this capacity. The International Telecommunications Union has introduced a standard by which all WDM channels should be referenced. Initially it was recommended that the use of the $1s_2$ - $2p_8$ Krypton line at 193.686221THz should be used as the absolute centre frequency reference for the 1.55μm WDM network [26]. This corresponds to a wavelength of 1547.82543nm, with channels then equally spaced by 100GHz around this value. However, more recently a standard has been proposed which is based on exact multiples of 100GHz centred about 193.100THz. This standard has now been adopted and is termed the ITU grid which is outlined in table 1.1 [27].

Although dense WDM offers a tremendous bandwidth increase over single mode fibre, it is not without its problems. Originally the channel spacing was standardised to 200GHz (~1.6nm), which over the past few years has moved to the ITU 100GHz grid (~0.8nm). Currently, there is increasing demand for a further move to a 50GHz channel spacing (~0.4nm). This imposes extremely tight tolerances on WDM demultiplexers and DFB lasers, to avoid drifting into adjacent channels. The major problem is the variation of material refractive index with temperature. In a DFB (InGaAsP/InGaAs/InP) this results in a lasing wavelength dependence of approximately 0.1nm/°C [28]. This can be actively controlled by monitoring the lasing wavelength of the device and employing feedback to adjust the mount temperature. However, this results in very expensive laser packages. A similar temperature dependence with channel wavelength is exhibited by monolithically integrated demultiplexers. However, gradually these issues are being addressed. Very recently a phased waveguide array has been demonstrated with an 8GHz (0.05nm) channel stability over an operating temperature of 85°C without the need for temperature control [29].

1.3.3 Wavelength Routing Optical Networks

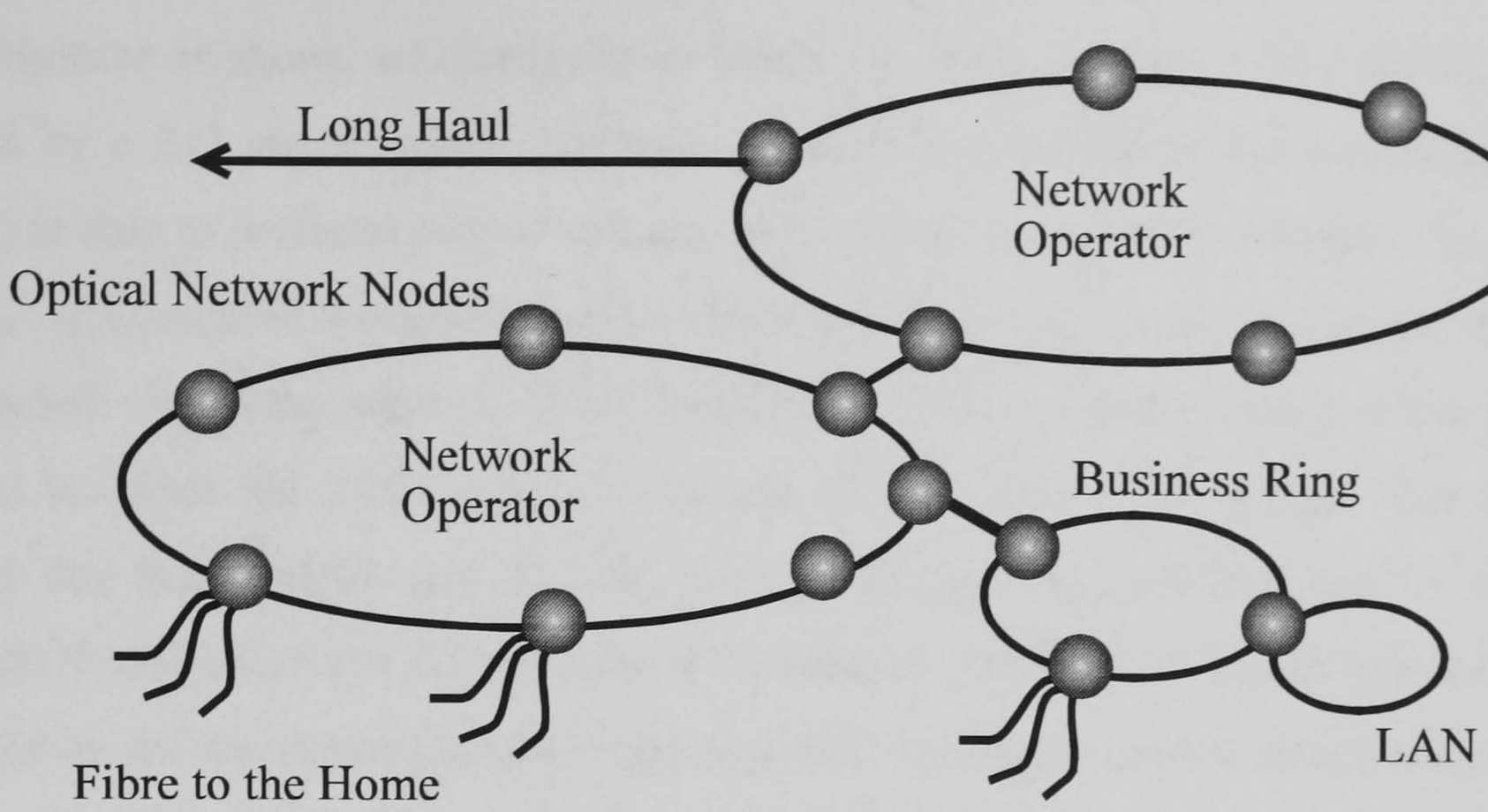

Figure 1.6 Future All-optical Routing Network (after [30])

So far WDM and OTDM has been discussed in terms of point-to-point links, whereby several signals have been multiplexed together onto a single fibre in order to increase the capacity of the link between two distinct points. More recently there have been proposals to implement in the optical domain some of the functions previously done in the electronic domain: namely broadcast the data directly to the end user. This requires components which are able to route data between different regions of the optical network (figure 1.6). For these so called 'routing' networks WDM has many advantages over OTDM, since individual channels can be more easily demultiplexed. This section discusses some of the many devices which will be required for the future optical routing network. It will be shown that the crosspoint switch is one of the most crucial.

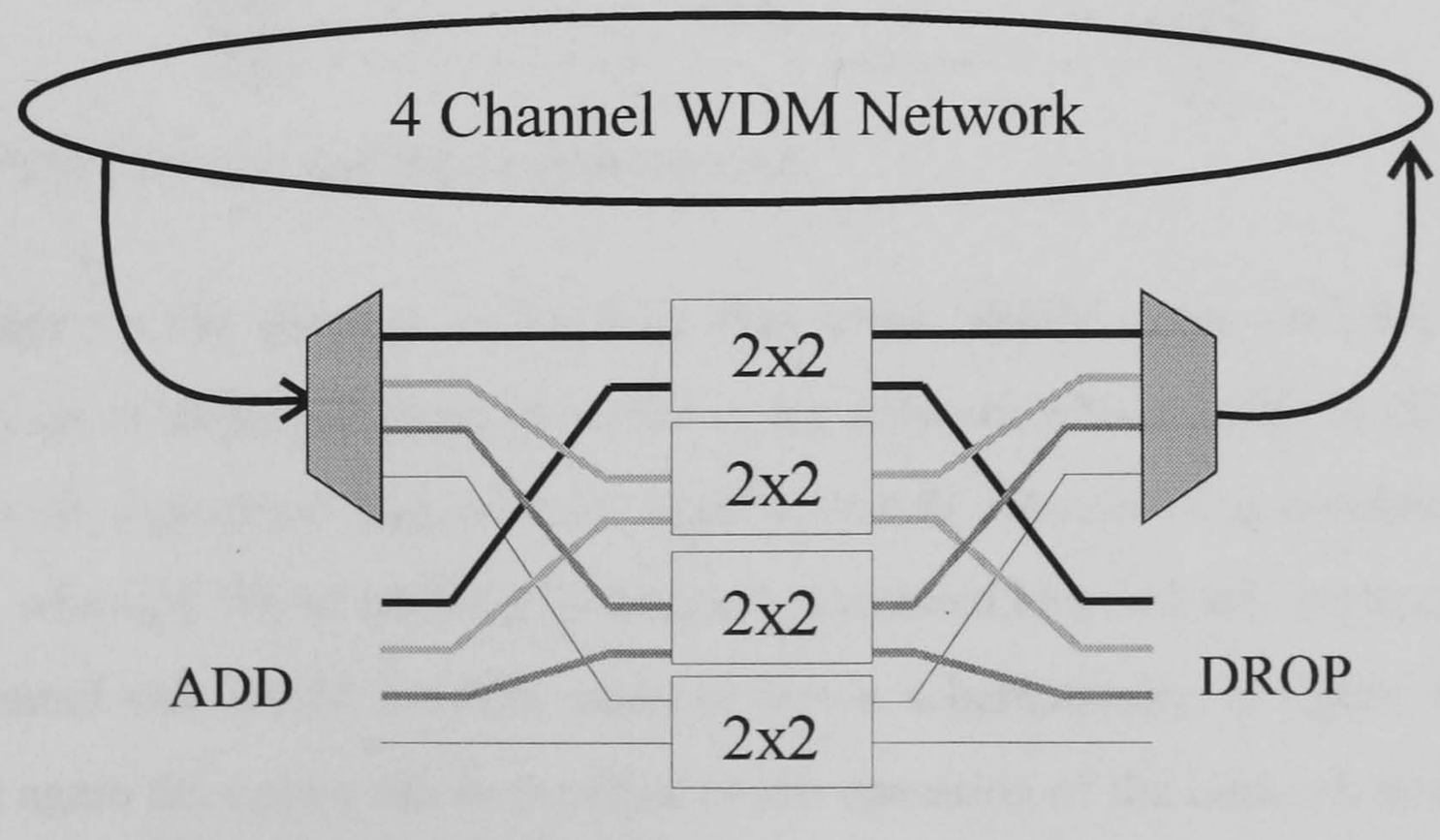

Figure 1.7 Four Channel ADD/DROP WDM network node.

Compared with OTDM it is relatively straightforward to get on and off a WDM network since decoding can be achieved passively by a monolithically integrated (de)multiplexer as shown schematically in figure 1.7. Each channel is first decoded and then switched by a 2x2 space switch. The space switch (also known as the crosspoint or cross-connect) is able to preferentially switch any of its inputs to any of its outputs. The prefix 2x2 indicates the number of inputs and outputs (input x output). Thus each wavelength channel may be 'switched' out of the network (to the DROP port) and a corresponding wavelength may be switched in (from the ADD port), by the use of each crosspoint switch. This function is essential for both WDM and OTDM routing network applications, and is termed the ADD/DROP demultiplexer [31]. Indeed, a 16 channel ADD/DROP switch has recently been fabricated on InP by monolithically integrating two waveguide phased arrays and sixteen 2x2 crosspoint switches [32]. The crosspoint lies at the device core and provides the 'switching' capacity that is required. However, this is not its only possible application. It is also required in more elaborate network switches such as the WDM node which is discussed as follows.

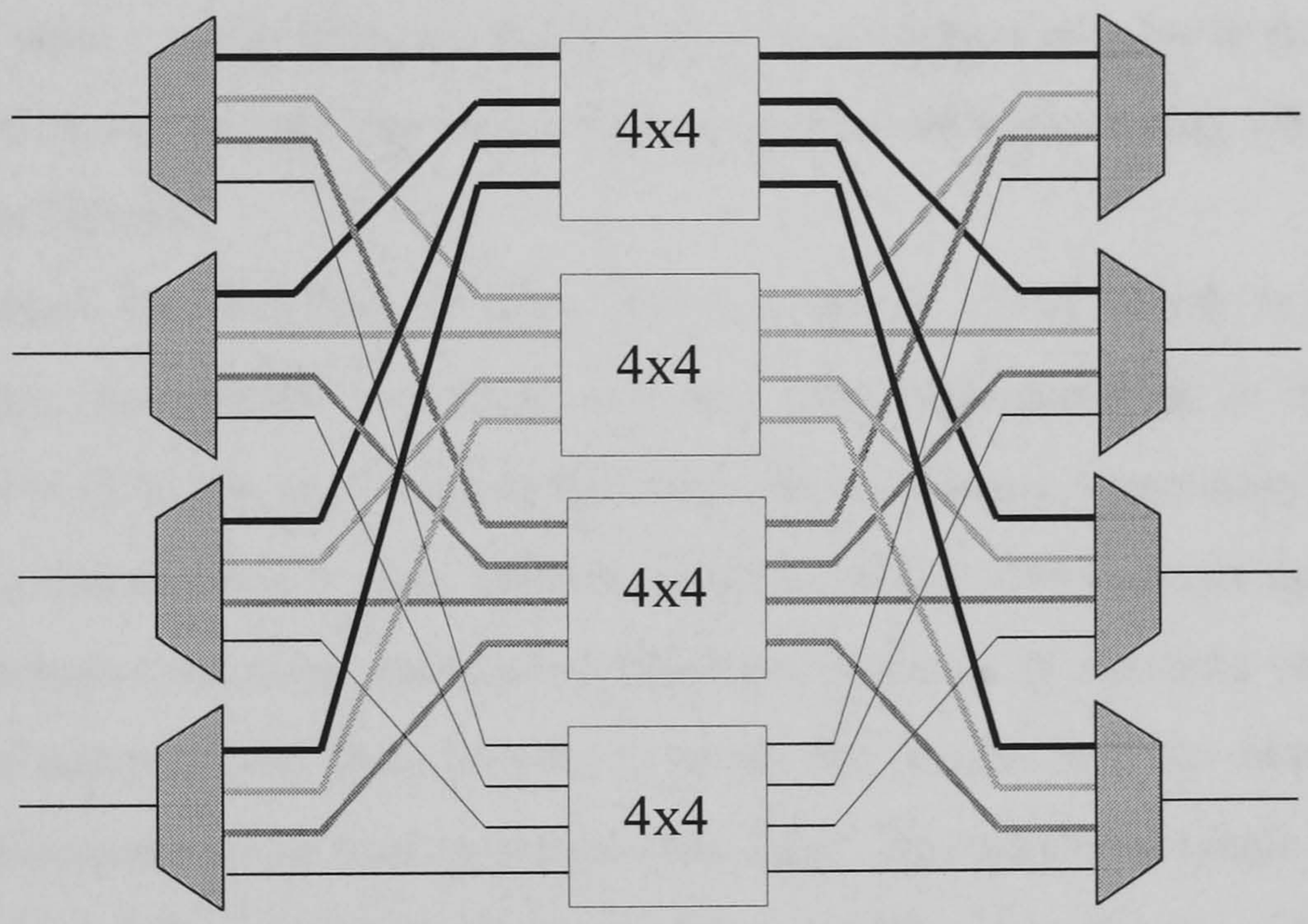

Figure 1.8 Four Channel 4x4 WDM network node.

In order for the network to be fully functional, WDM space switches are required. These devices lie at major junctions or nodes in the network where traffic is directed between different network operators, (figure 1.6). Such a switch consists of a number of input and output fibres, whereby WDM traffic may be freely switched between any input and any output. Such a 4 channel 4x4 WDM network node is drawn schematically in figure 1.8. It may be observed that again the crosspoint is essential to the operation of the network node. In this case a higher order 4x4 crosspoint is required, one for each of the 4 WDM channels. A 4x4 node has been given as an example here, but in general even higher order cross-connects (8x8, 16x16, 32x32) are required for future routing networks [31]. Thus in order to make these network

nodes reliable and cost effective, methods must be found in order to monolithically integrate high order crosspoint devices with high levels of performance. The monolithic design of these devices forms the basis of this thesis.

1.4 Wavelength Conversion in a WDM Network Node.

1.4.1 Passive Wavelength Routing (PWR)

It has been shown that an *NxN* crosspoint is an essential component for the next generation of optical routing networks. The crosspoint allows data travelling on an many optical fibres to be exchanged, thus providing optical connectivity across the network. However until now, no description of the crosspoint design has been given here. Indeed, it will be left to Chapter 2 to discuss in detail the conventional methods behind crosspoint switch design. Very briefly, traditional methods physically connect each input fibre to each output, via an arrangement of optical waveguides and digital optical switches. However, in the case of a WDM network node a subtly different method may be employed in order to route traffic. This involves the use of wavelength conversion and passive wavelength routing which is discussed in more detail as follows.

Apart from the shuffling of data between optical fibres which is achieved by a crosspoint switch, wavelength conversion has also been highlighted as an essential part of network control [33]. In the case of the WDM network node drawn schematically in figure 1.8, it may be shown that at times it is not sufficient only to shuffle data between optical fibres. For example, wavelength contention arises when two input channels of the same wavelength are to be routed to the same output. Thus in order to avoid this limitation it has been proposed that wavelength conversion may be used to convert one signal from one wavelength to another [34]. This avoids the need for optical buffering which presently is extremely difficult, and thus providing there is redundancy in the number of wavelength channels, contention can always be averted.

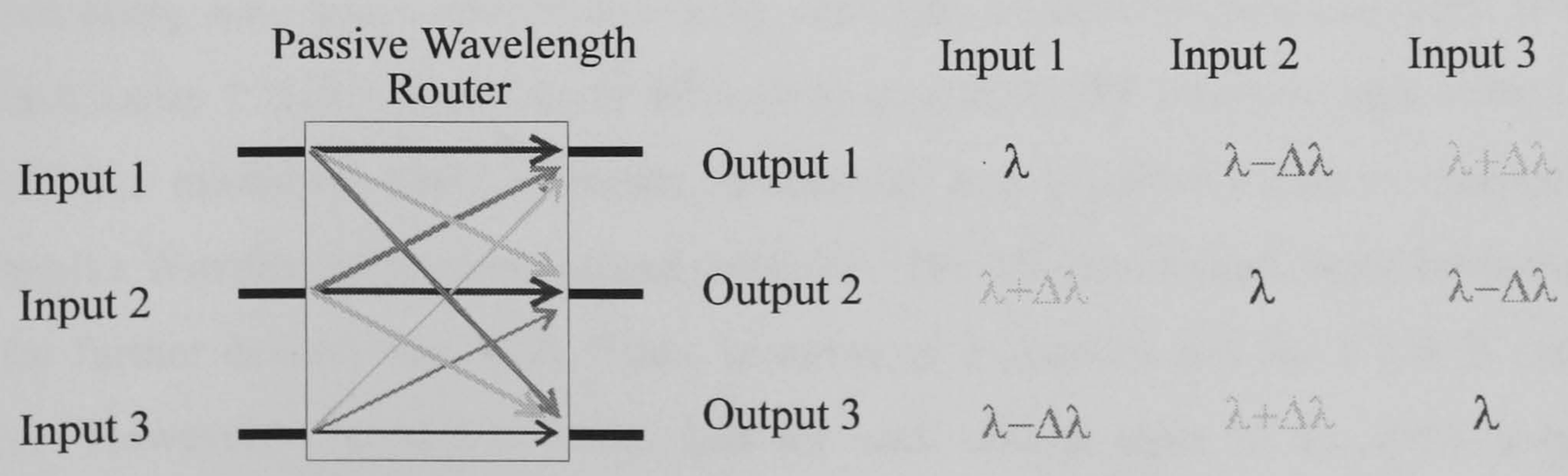

Figure 1.9 Wavelength routing using a passive multi input (de)multiplexer.

Given that wavelength conversion is essential, it has been recently proposed that wavelength conversion may also be used as the actual method of routing data from each input to each output [35]. This can be achieved by using a wavelength converter together with a Passive Wavelength Router (PWR) shown schematically in figure 1.9. The PWR is essentially a multi input demultiplexer. Each input demultiplexes a set of wavelengths with centre λ and spacing $\Delta\lambda$ to each respective output waveguide. By designing the demultiplexer correctly (such that the Free spectral Range (FSR) of the grating is equal to the number of outputs, N, times the channel spacing $\Delta\lambda$), only N wavelengths are ever required to uniquely route every input to every output without ever having contention [36]. Thus in order to be able to switch an input to an output, the signal must first be wavelength converted to the required wavelength which selects the required output. An example of such a 4 channel 4x4 WDM passive wavelength routing network node is drawn schematically in figure 1.10. Indeed a 1x4 space switching using passive wavelength routing has recently been achieved at 2.488Gbits/s using a tuneable DBR laser and a 4x4 waveguide phased array demultiplexer [37].

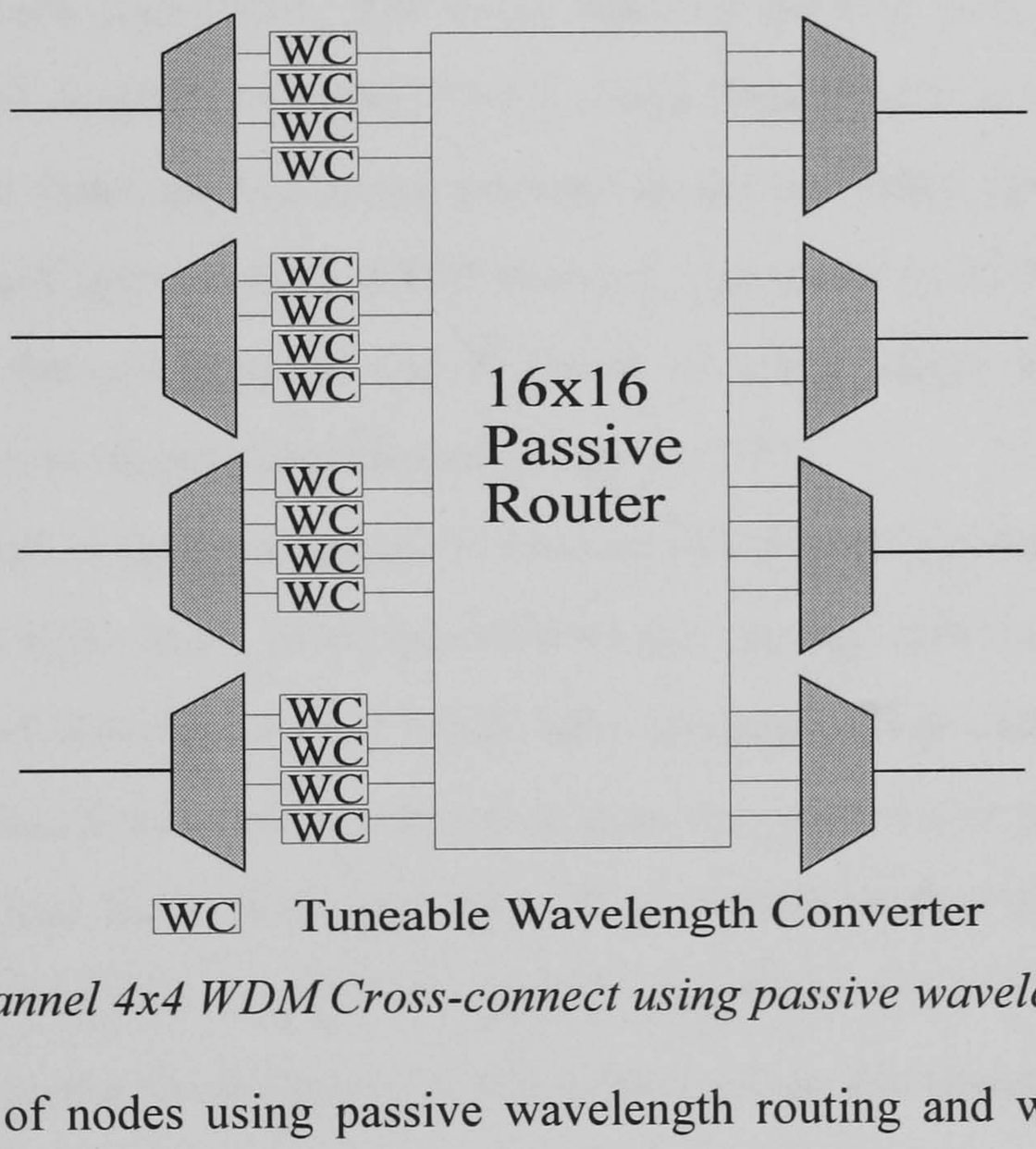

Figure 1.10 Four Channel 4x4 WDM Cross-connect using passive wavelength routing

Construction of nodes using passive wavelength routing and wavelength conversion may have many advantages over nodes using conventional optical cross-connects. It will be shown in Chapter 2 that it is extremely difficult to monolithically integrate high order (greater than 8x8) into microchip form. However, in contrast, it is essentially easy to construct high order Passive Wavelength Routers, indeed orders of 128x128 have already been fabricated with scope for further development [38]. Thus, in terms of scalability and the PWR is extremely attractive. However, it should be noted that for each optical input to the PWR a tuneable wavelength converter is required. Thus for the practical implementation, cheap and efficient methods must be found to achieve wavelength conversion. Methods for achieving tuneable wavelength conversion are therefore discussed in the next section.

1.4.2 Tuneable Wavelength Conversion

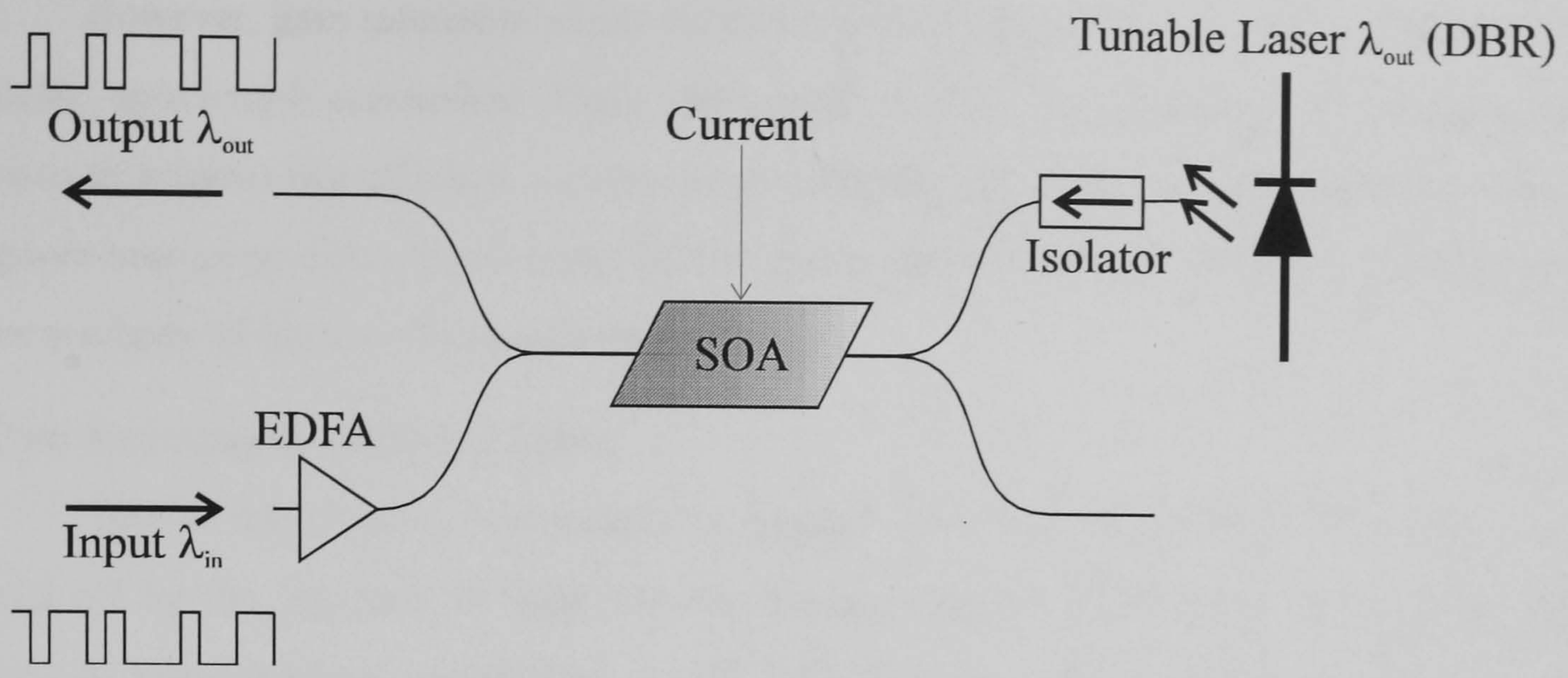

Figure 1.11 Tuneable Wavelength Conversion using counter propagation and an angle facet Semiconductor Optical Amplifier (SOA).

Many methods have been employed over the last decade in order to achieve efficient and tuneable wavelength conversion. The most reported method uses gain saturation in an Semiconductor Optical Amplifier (SOA) [39-42]. Gain Saturation is a nonlinearity in a SOA which is caused when there are too many photons in the amplifier cavity. This reduces the overall gain of the amplifier which in WDM systems, can cause patterning and inter-channel crosstalk. However, the nonlinearity can be used to good effect to induce wavelength conversion. This has been shown schematically in figure 1.11.

The input signal is first pre-amplified with an EDFA and injected into the SOA cavity. This perturbs the gain of the SOA, thus a tuneable source injected into the cavity sees an optical gain proportional (and inverted) to the input light intensity. This causes patterning on the tuneable wavelength and hence data is converted from one wavelength to the other. A counter propagating regime has been discussed here [43], where both the tuneable and input wavelengths enter the amplifier cavity from opposite ends of the SOA. This avoids the need for post filtering to remove the input signal for the output, which for tuneable conversion is very difficult. However, counter propagating schemes tend to suffer from crosstalk generated by the finite reflection of the SOA facet. This causes the input to leak onto the output introducing a Bit Error Rate (BER) penalty to the converter. This problem may be reduced by having very good Anti Reflection (AR) coatings and/or using an angled facet SOA [44].

Wavelength conversion using gain saturation in an SOA has been achieved at 40Gbits/s with input powers of 10dBm and extinction ratios of 9dB [45]. However, disadvantages with the technique are the high component count to achieve conversion. The implementation of such a converter in a high order WDM network node would be wholly impractical. This is because

for an *NxN* switch N^2 converters would be required, which make the node size and cost unfeasible.

However, gain saturation is not the only method that has been used in order to achieve tuneable wavelength conversion. Many other methods have been employed in semiconductor devices to achieve fast efficient conversion. A complete discussion of each technique will not be given here as an entire thesis could be devoted to the subject [46]. However, as a summary, other methods which have been used are given as

1. Gain Saturation in DFBs and DBRs.

This is the simplest wavelength conversion technique whereby a DFB laser can be turned off by the injection of light into the lasing cavity. A modulation of the input signal causes a corresponding modulation on the lasing output of the DFB. By monolithically integrating an SOA with the DFB, the input wavelength does not require pre amplification with an EDFA. Thus 10Gbit/s conversion has been demonstrated with very low input powers (~0.8dBm) over 375km of dispersion shifted fibre [47]. However, owing to the nature of the DFB, tuneable conversion is only possible over ~1nm (for 10°C temperature tuning) and ~5nm (using a split contact and current tuning). However tuneable wavelength conversion has been achieved over the entire erbium window (1530nm-1560nm) using a DBR laser, with 3dBm input powers [48].

2. Cross Phase modulation using an Interferometer [49,50]

This technique uses two SOAs in the arms of a Mach Zehnder Interferometer. By injecting the input signal into one side of the device, the phase difference between both arms can be changed by π radians between the on and off states of the input. A tuneable wavelength signal injected into the other side therefore sees constructive and destructive interference in the interferometer, proportional to the input signal power. Wavelength conversion with penalty free transmission over 60km of standard fibre has been demonstrated at 10Gbits/s [51]. Cross phase modulation has the advantage that the converted signal can be either inverted or non-inverted. The scheme also has the advantage of being very power efficient (~4dBm input power compared with ~10dBm for gain saturation).

3. Four Wave Mixing in a Semiconductor Amplifier

Four wave mixing is a third order non-linear effect which arises when more than one optical frequency is present in a medium. For two input frequencies the result is a product of the interacting fields which generates beat frequencies at the sum and difference of the input frequencies. If data is superimposed on one of the input wavelengths then it is automatically 'converted' onto both beat wavelengths. Four Wave Mixing has the advantage that both phase and amplitude information is converted and thus is the only method of wavelength conversion

that is strictly independent of data coding format. An 18Gbit/s signal has been converted with a 15nm tuning range using this technique [52]. However, the process is very inefficient and thus large input powers are required.

Although there are many methods reported for achieving wavelength conversion, the component count required for each converter can be considerable. Thus given the number of wavelength converters required in a Passive Wavelength Routed space switch, it is still unclear whether or not wavelength routing will be used in WDM network nodes. In Chapter 7 a single monolithically integrated device will be presented that incorporates many of the aspects required for wavelength routing. A 1x4 wavelength routing function will be demonstrated at 2.488Gbits/s, together with other functions required for PWR such as multiple wavelength conversion and WDM multiplexing.

1.5 Scope of this Thesis

In conclusion, a brief introduction to the next generation of optical routing networks has been discussed. It has been shown that there is a clear role for the optical crosspoint switch operating at 1.55μm. In order for these switches to operate efficiently it is desirable to monolithically integrate the crosspoint into microchip form. This not only decreases the cost of the component but also increases reliability. Chapter 2 will discuss the methods used to monolithically integrate high order crosspoint switches. A review of current crosspoint design will be given, highlighting the problems associated with monolithic engineering. Building on the disadvantages of current designs two new architectures will be proposed which are discussed in Chapters 3, 4, 5 and 6. Passive Wavelength Routing has also been highlighted as a possible method for achieving the crosspoint logic. This is demonstrated with a multi-wavelength laser in Chapter 7.

1.6 References

[1] T. Miya, Y. Terunuma, T. Hosaka, T. Miyoshita, "Ultimate Low Loss Single-Mode Fibre at 1.55μm", Electronics Letters, Vol. 15, No. 4, Febuary 1979, pp106-108.

[2] G.P. Agrawal, N.P. Dutta, "Semiconductor Lasers - Second Edition", Van Nostrand Reinhold, Chapter 1.

[3] A. Sugimura, K. Daikoku, N. Imoto, T. Miya, "Wavelenth Dispersion Characteristics of Single Mode Fibres in the Low Loss Region", IEEE JQE QE-16, No. 2, Febuary 1980, pp215-225.

[4] P.S. Henry, "Lightwave Primer", IEEE JQE, vol. QE-21, No. 12, 1985, pp1862-1865.

[5] L.G. Cohen, L. Chinlon, W.G. French, "Tailoring zero chromatic dispersion into the 1.5-1.6um low-loss spectral region of single-mode fibres", Electronics Letters, Vol. 15, No. 12, 1979, p334-335.

[6] G.P. Agrawal, N.P. Dutta, "Semiconductor Lasers - Second Edition", Van Nostrand Reinhold, Chapter 1.

[7] B.J. Ainslie, K.J. Beales, D.M. Cooper, C.R. Day, J.D. Rush, "Monomode Fiber With Ultralow Loss And Minimum Dispersion At 1.55μm", Electronics Letters, 1982, Vol.18, No.19, pp.842-844.

[8] H. Kogelnik, C.V. Shank, "Coupled-Wave Theory of Distributed Feedback Lasers", J. Applied. Phys, Vol. 43, No. 5, May 1972, pp 2327-2335.

[9] T. Okoshi, "Recent Advances in Coherent Optical Fibre Communication Systems", IEEE JLT, Vol 5, No.1, 1987, pp314-320.

[10] M. Shimizu, T. Kanamori, J. Temmyo, M. Wada, M. Yamada, Y. Terunuma, Y. Ohishi, S. Sudo, "28.3dB Gain 1.3um Band Pr-Doped Flouride Amplifier Module Pumped by 1.017um InGaAs-LD's", IEEE PTL, Vo. 5, No. 6, pp654-657, 1993.

[11] M. Asghari, "Two Dimensional Integrated Optics", Ph.D. Thesis, Universityof Bath 1995.

[12] E. Lach, D. Baums, C. Haisch, *et al* "Monolithically Integrated active/passive cavity mode locked MQW laser realised by Selective Area Growth", Proceedings of ECIO '95, Deflt Netherlands, April 1995.

[13] C. Lin, C.A. Burrus, G. Einstein, R.S. Tucker, P. Besomi, R.J. Nelson, "11.2Ghz picosecond Optical Pulse Generation in Gain Switched short Cavity InGaAsP injection Lasers by High Frequency direct Modulation", Electronics Letters, Vol. 20, No. 6, 1984, pp239-240.

[14] N. Souli, F. Devaux, A. Ramadane *et al* "InGaAsP/InGaAsP Multiple Quantum well Modulator With Improved Saturation Intensity and Bandwidth Over 20GHz", IEEE PTL, Vol.4, No. 7, 1992, pp720-722.

[15] D.L. Lee, "Electromagnetic Principles of Integrated Optics", John, Wiley & Sons 1986, pp 5.

[16] A.D. Ellis, T. Widdowson, X. Shan, D.G. Moodie, "3-Node, 40-Gbit/s OTDM Network Experiment Using Electrooptic Switches", Electronics Letters, 1994, Vol.30, No.16, pp.1333-1334.

[17] Mehdi Asgari, "Two Dimensional Integrated Optics", Ph.D. Thesis, University of Bath 1995.

[18] J.B.D Soole, A. Scherer, H.P. LeBlanc,N.C. Andereadakis, R. Bhat, M.A. Koza, "Monolithic InP-Based grating Spectrometer for WDM Sytems at 1.5μm", Electronics Letters, Vol. 27, No. 2, 1991. pp32-33.

[19] M. Fallahi, K.A. McGreer, A. Delage, R. Normandin, I.M. Templeton *et al*, "Demonstration of Grating Demultiplexer in GaAs/AlGaAs Suitable for Integration", Electronics Letters, Vol. 28, No. 24, 1992, pp2217-2218.

[20] S.M. Ohja, G.H.B. Thompson, C.G. Cureton, C.B. Rogers, S.J. Clements, M. Asghari, I.H. White, "Demonstration of a Low Loss Integrated InGaAsP/InP Demultiplexer device with Low Polarisation Sensitivity", Electronics Letters, Vol. 29, No. 9, 1993, pp805-807.

[21] M. Zarngibl, C. Dragone, C.H. Joyner, "Demonstration of a 15x15 arrayed waveguide multiplexer on InP", IEEE PTL, Vol. 4, No. 11, 1992, pp1250-1253.

[22] M.R. Amersfoort, C.R. de Boer, M.K. Smit *et al* "Phased Array Wavelength Demultiplexer with Flattened Wavelength response", Electronics Letters, Vol. 30, No. 4, pp300-302.

[23] C. Dragone, C.A. Edwards, R.C. Kistler, "Integrated Optics NxN Multiplexer on Silicon", IEEE PTL, Vol. 3, 1991, pp896-899.

[24] H. Takahashi, Y. Hibino, I. Nishi, "Polarisation Insensitive Arrayed Waveguide Grating Wavelength Multiplexer on Silicon", Optics Letters, Vol. 17, 1992, pp499-501.

[25] C.A. Brackett, "Foreward - Is there an Emerging Consensus on WDM Networking ?", JLT, Vol. 14, no. 6, June 1996, pp936-941.

[26] C. Gamache, M. Tetu, C. Latrasse, N Cyr, M.A. Duguay, B. Villeneuve, "An Optical Frequency Scale in Exact Multiples of 100GHz for Standardization of Multifrequency Communications", IEEE PTL, Vol. 8 No.2, Febuary 1996, pp290-292.

[27] R.C. Bray, D.M. Baney, "Optical Networks:Backbones for Universal Connectivity", HP Journal, December 1997, pp 19-31.

[28] G.P. Agrawal, N.P. Dutta, "Semiconductor Lasers - Second Edition", Van Nostrand Reinhold, Chapter 1.

[29] Y. Inoue, A. Kaneko, F. Hanawa, H. Takahashi, K. Hattori, "Athermal Silica-Based Arrayed Waveguide Grating Multiplexer", Electronics Letters Volo. 33, No. 23, pp 1945-1946.

[30] "Components of Choice for the Optical Network Revolution", Nortel Promotional Advertisment.

[31] C.A. Brackett, "Foreward - Is there an Emerging Consensus on WDM Networking ?", JLT, Vol. 14, no. 6, June 1996, pp936-941.

[32] K. Okamoto, M. Okuno, A. Himeno, Y. Ohmori, "16 Channel optical add/drop multiplexer consisting of arrayed-waveguide gratings and double-gate switches", Electronics Letters, Vol. 32, No. 16, August 1996, pp 1471-1472.

[33] C.A. Brackett, "Dense Wavelength Division Multiplexing Networks: Principles and Applications", IEEE Journal on Selected Areas in Communications, Vol. 8, No. 6, August 1990, pp 948-964.

[34] C.A. Bracket, A.S. Acompora, J. Sweitizer, G. Tangonan *et al* "A Scalable Multiwavelength Multihop Optical Network", JLT, Vol. 11, No. 4, April 1993, pp736-745.

[35] F. Masetti, J. Benoit, F. Brillouet, J.M. Gabriagues, *et al* "High-Speed, High-Capacity ATM Optical Switches For Future Telecommunication Transport Networks", IEEE Journal On Selected Areas In Communications, 1996, Vol.14, No.5, pp.979-998

[36] J.D. Bainbridge, I.H. White, R.V. Penty, M. Asghari, *et al* "Demonstration of Integrated 12x12 InGaAsP/InP grating wavelength router at 2.5Gbit/s channel bit rates", Electronics Letters, Vol. 33, No. 17, August 1997, pp1458-1460.

[37] A.A.M. Staring, L.H. Spiekman, C. van Dam., E.J. Jansen, *et al* "Space-Switching 2.5Gbit/s Signals Using Wavelength Conversion and Phased Array Routing", Electronics Letters, Vol. 32, No. 4, Febuary 1996, pp 377-378.

[38] K. Omaoto, K. Moriwaki, S. Suzuki, "Fabrication of 64x64 Arrayed Waveguide Grating Multiplexer on Silicon", Electronics Letters, Vol. 31, No. 3, Febuary 1995, pp184-186.

[39] C. Joergensen, T. Durhuus, C. Braagaard, B. Mikkelsen, K.E. Stubkjaer "4 Gbits/s Optical Wavelength Conversion Using Semiconductor Optical Amplifiers" IEEE Photonics Technology Letters, 1993, Vol.5, No.6, pp.657-660

[40] J.M. Wiesenfeld, B. Glance, J.S. Perino, A.H. Gnauck "Wavelength Conversion At 10 Gbits/s Using A Semiconductor Optical Amplifier" IEEE Photonics Technology Letters, 1993, Vol.5, No.11, pp.1300-1303.

[41] J.M. Wiesenfeld, J.S. Perino, A.H. Gnauck, B. Glance "Bit Error Rate Performance For Wavelength Conversion At 20 Gbit/s", Electronics Letters, 1994, Vol.30, No.9, pp.720-721

[42] J.S. Perino, J.M. Wiesenfield, B. Glance "Fiber Transmission Of 10Gbit/s Signals Following Wavelength Conversion Using A Traveling-Wave Semiconductor Optical Amplifier" Electronics Letters, 1994, Vol.30, No.3, pp.256-258

[43] T. Durhuus, B. Mikkelson, C. Oergensen, S.L. Danielsen, K.E. Stubkjaer, "All-Optical wavelength Conversion by Semiconductor Optical Amplifiers", JLT, Vol. 14, No. 6, pp942-954.

[44] W. Rideout, R. Holmstrom, J. Lacourse, E. Medland, W. Powazinik, "Ultra low reflectivity semiconductor amplifiers with angled facets", Electronics Letters 1990, Vol. 23 pp990-991.

[45] C. Joergensen, S.L. Danielsen, M. Vaa, B. Mikkelsen, K.E. Stubkjear, P. Doussiere, F. Pommerau, L. Goldstein, M. Goix, "40Gbits/s All-Optical Wavelength Conversion by Semiconductor Optical Amplifiers", Electronics Letters, Vol. 32, No. 4, 1996, pp367-368.

[46] M.F.C. Stephens "High Speed All Optical Wavelength Conversion" Ph.D. Thesis University of Bristol, January 1998.

[47] M.F.C Stephens, R.V. Penty, I.H. White *et al,* "Low Input Power Wavelength Conversion at 10Gbits/s using a Integrated Amplifier/DFB Laser and Subsequent Transmission Over 375km of Fibre", Accepted for publication in IEE Photonics Technology Letters December 1997.

[48] H. Yasaka, H. Ishii, K. Takahata, K. Oe, Y. Yoshikuni, H. Tsuchiya, "Broad Range Tunable Wavelength Conversion of Hgh bit rate Signals Using a SuperStructure Grating DBR Laser", JQE, QE-32, No.3, March 1996, pp463-469.

[49] C. Joergensen, S.L. Danielsen, T. Durhuus, B. Mikkelsen, K.E. Stubkjaer, *et al* "Wavelength Conversion By Optimized Monolithic Integrated Mach-Zehnder Interferometer" IEEE Photonics Technology Letters, 1996, Vol.8, No.4, pp.521-523

[50] T. Durhuus, C. Joergensen, B. Mikkelsen, R.J.S. Pedersen, K.E. Stubkjaer "All-Optical Wavelength Conversion By SOAs In A Mach-Zehnder Configuration" IEEE Photonics Technology Letters, 1994, Vol.6, No.1, pp.53-55.

[51] T. Durhuus, B. Mikkelson, C. Oergensen, S.L. Danielsen, K.E. Stubkjaer, "All-Optical wavelength Conversion by Semiconductor Optical Amplifiers", JLT, Vol. 14, No. 6, pp942-954.

[52] R. Schnabel, W. Pieper, M. Ehrhardt, M. Eiselt, H.G. Weber "Wavelength Conversion And Switching Of High-Speed Data Signals Using Semiconductor Laser Amplifiers" Electronics Letters, 1993, Vol.29, No.23, pp.2047-2048

Monolithic Integration of Optical Space Switches

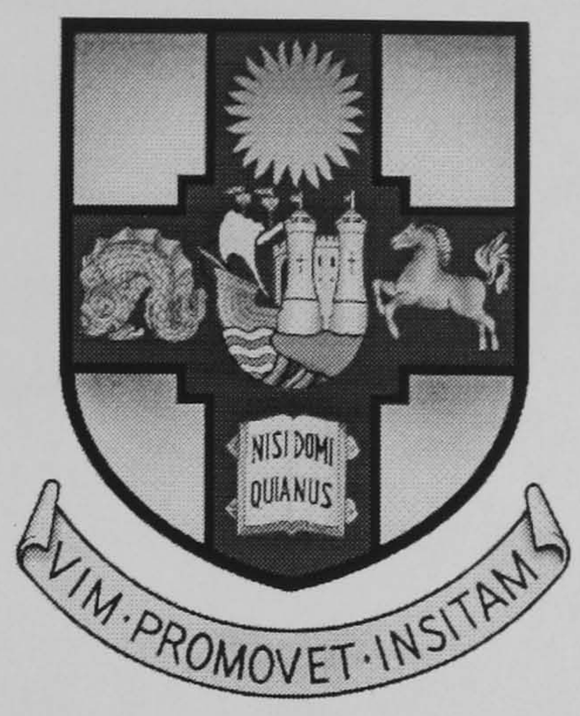

Chapter 2

2.1 Optical Crosspoint Switches

Chapter one has discussed the reasons why optical cross-connects, or crosspoints are required in the next generation of telecommunication networks. This chapter will show that the InGaAsP/InGaAs/InP material system currently posses many of the attributes required for high performance optical crosspoint switch development. To date very few high order monolithically integrated InP crosspoints have been fabricated, and never before above 4x4. This chapter discusses how 8x8 cross-connects or larger can be realised and integrated onto InP semiconductor substrates. The existing methods used to design optical crosspoints and the disadvantages of currently developed devices will be discussed. This will allow an understanding of the drawbacks of these devices, hence three new architectures will be proposed, which will form the focus of the proceeding five chapters of work.

2.2 Crosspoint Switch Design

2.2.1 The ideal Crosspoint Switch

An NxN crosspoint switch is used to shuffle optical data between *N* optical fibres. It usually consists of *N* optical fibre inputs followed by a complex serious of switches that allow optical connections to be made to the *N* outputs. The 'ideal' crosspoint would sit completely transparent in a communications network and would not be affected by input polarisation or incur loss or crosstalk. Simple driving electronics would also be preferred and it also must be capable of routing gigabits of optical data per second.

2.2.2 Material System

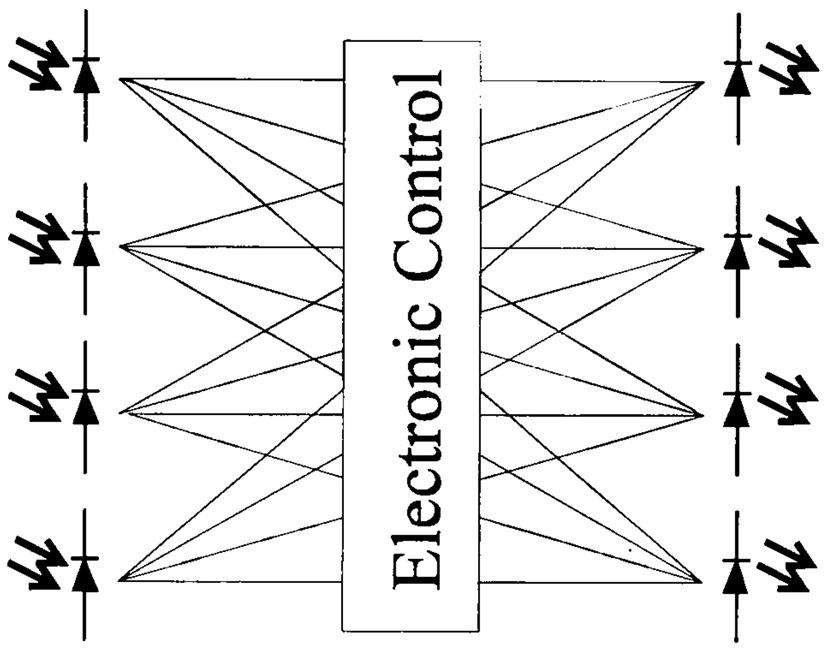

Figure 2.1 Schematic diagram of an Opto-Electronic Crosspoint Switch

The material system used to fabricated the crosspoint switch is the first step to achieving the 'ideal' cross-connect. At first sight the simplest method of achieving the crosspoint logic could be achieved electronically as shown schematically in figure 2.1. The inputs consist of photodiodes which trigger logic circuits to remodulate laser sources on each output. Indeed, this method is currently adopted in many systems such as Local Area Networks (LAN). However, in future telecommunication systems where very high optical data rates are used, opto-electronic crosspoints have severe disadvantages since they introduce an 'electronic bottle neck' to the network. The optical output is also fixed with wavelength and coding format, limiting the possible upgrading to more elaborate coding schemes.

Over the last decade this limitation has lead to the development of many optical cross-connects. This allows the optical data to be routed to each output via a series of optical waveguides and digital optical switches. In these devices the output is a direct copy of the optical input and is not limited by the optical wavelength, bit rate nor polarisation. In order to reduce the component count, increase reliability and hence reduce the device cost it is essential that the devices are integrated monolithically. This has been achieved in four distinct material systems, namely Lithium Niobate; Polymer; Gallium Arsenide and Indium Phosphide. A

summary of the performance of these devices will be given later, in section 2.3.4. However, for now, it should be noted that InGaAsP/InGaAs/InP is the only material system capable of introducing optical gain to a crosspoint switch operating at 1.55μm. Lithium Niobate, Polymer and Gallium Arsenide all introduce a significant optical loss (~10dB) at this wavelength, especially as the device order, *N*, is increased. For this reason alone Indium Phosphide is currently considered to be the material most suited to crosspoint switch development at 1.55μm.

2.2.3 Broadcast and Point to Point Architectures

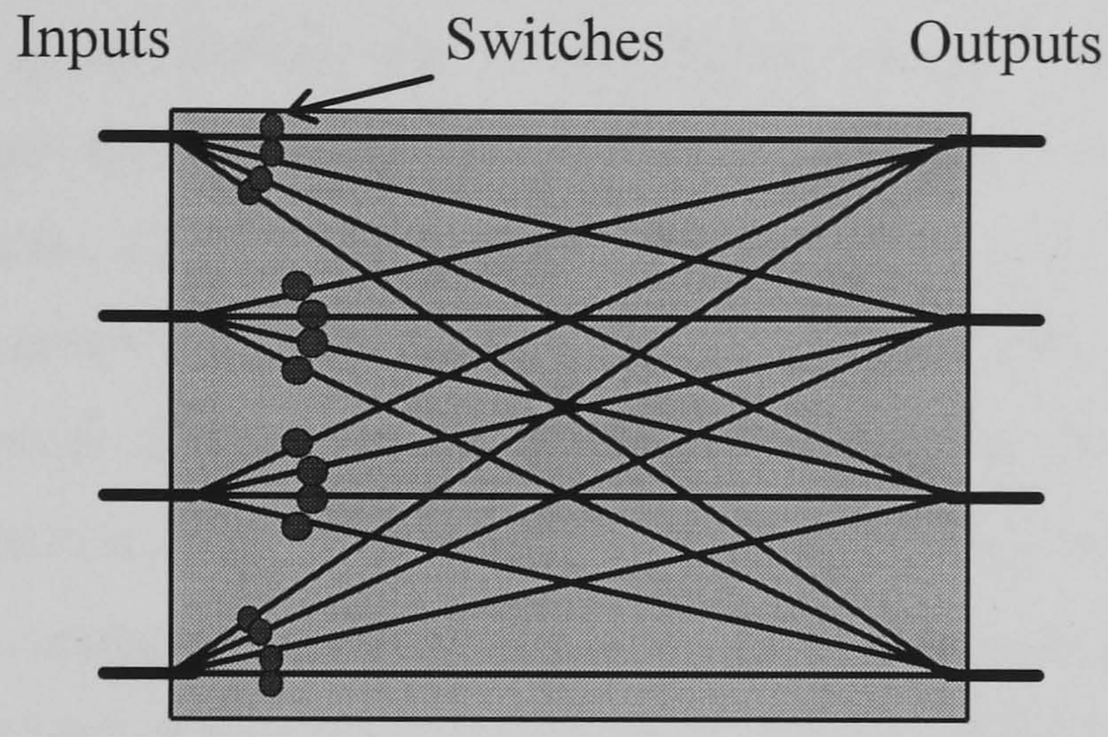

Figure 2.2 Schematic diagram of a Broadcast 4x4 Crosspoint Switch (Clos)

The method of routing and switching each input to each output, or architecture used, is the second step to achieving the 'ideal' cross-connect. The architecture can be crucial to final device performance, of which there are two main categories, termed *Broadcast Network,* and *Point to Point Network.* Each type performs the crosspoint logic in a slightly different way with a marked difference in performance. For example, one such 4x4 *broadcast* architecture is drawn schematically in figure 2.2. The inputs are first split four ways, turned on or off by digital optical switches, and then routed to each consecutive output. Thus every input can be *broadcast* to every output. Broadcast networks tend to have high losses since there is an inherent $10log_{10}N$ dB loss when splitting the inputs N ways. Also if the device is to perform single moded there is a further $10log_{10}N$ dB loss by combining N incoherent beams to the single moded output waveguide. By reducing the switch functionality and allowing an input to be routed to a single output *only*, the loss can be reduced to $10log_{10}N$ dB and a so called *point to point* architecture is realised, an example of which is shown in figure 2.3.

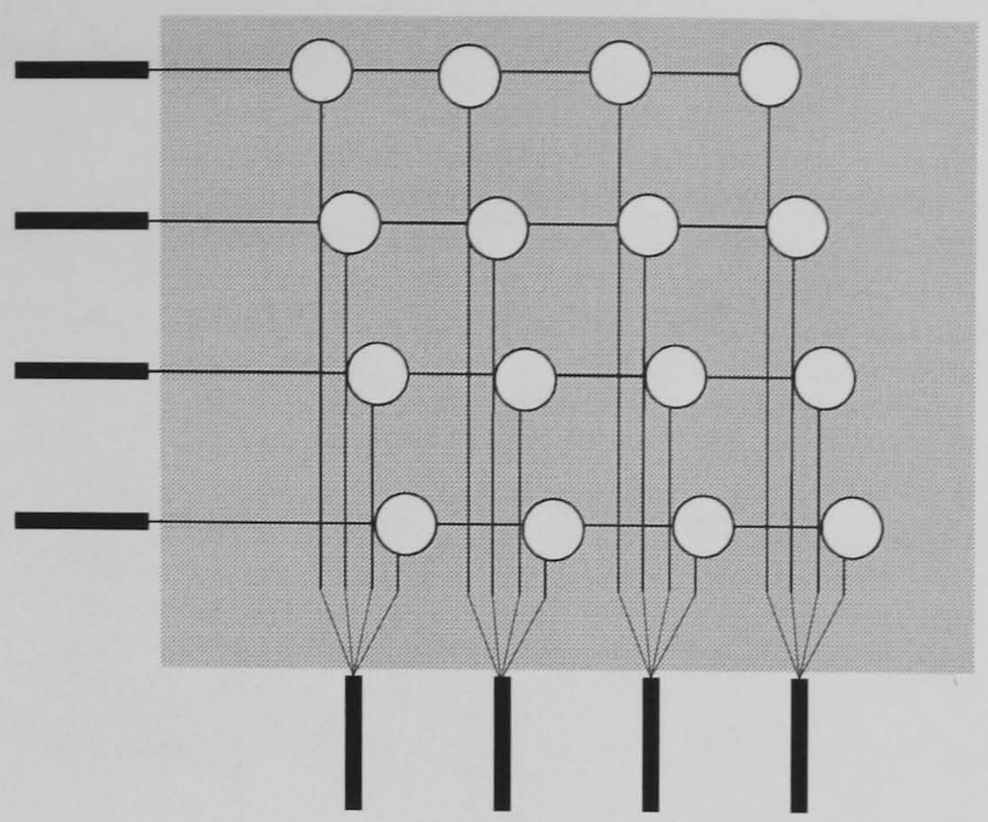

Figure 2.3 Schematic diagram of a Point to Point 4x4 Crosspoint Switch (Classic Crossbar)

It may first appear that this may be the only two ways to perform the crosspoint logic. However, surprisingly, there are a multitude of other Broadcast and Point to Point architectures that can accomplish the same functions. All these architectures have been developed over the last few decades, primarily for the electrical domain. They could all be fabricated optically, however most encounter difficulties when extended to large switch dimensions *N*. For example, the broadcast architecture drawn schematically in figure 2.2 tends to suffer from a large number of optical crossings, especially when applied to a large device orders (N^2-N dependence). This is not much of a problem if the switch is constructed from modular optical components and a network of fibre optic cable [1, 2]. However when attempting to monolithically integrate the device onto a semiconductor substrate optical waveguide crossings can increase the device loss and crosstalk so generally they should be avoided. Thus, this particular architecture is unsuitable for high order cross-connects unless the crossing loss can be reduced to an expectable level. However, before concentrating on the problems involved with monolithic integration, an introduction to various other types of crosspoint architecture will be given in the next section.

2.2.4 Multilevel Crosspoint Architectures

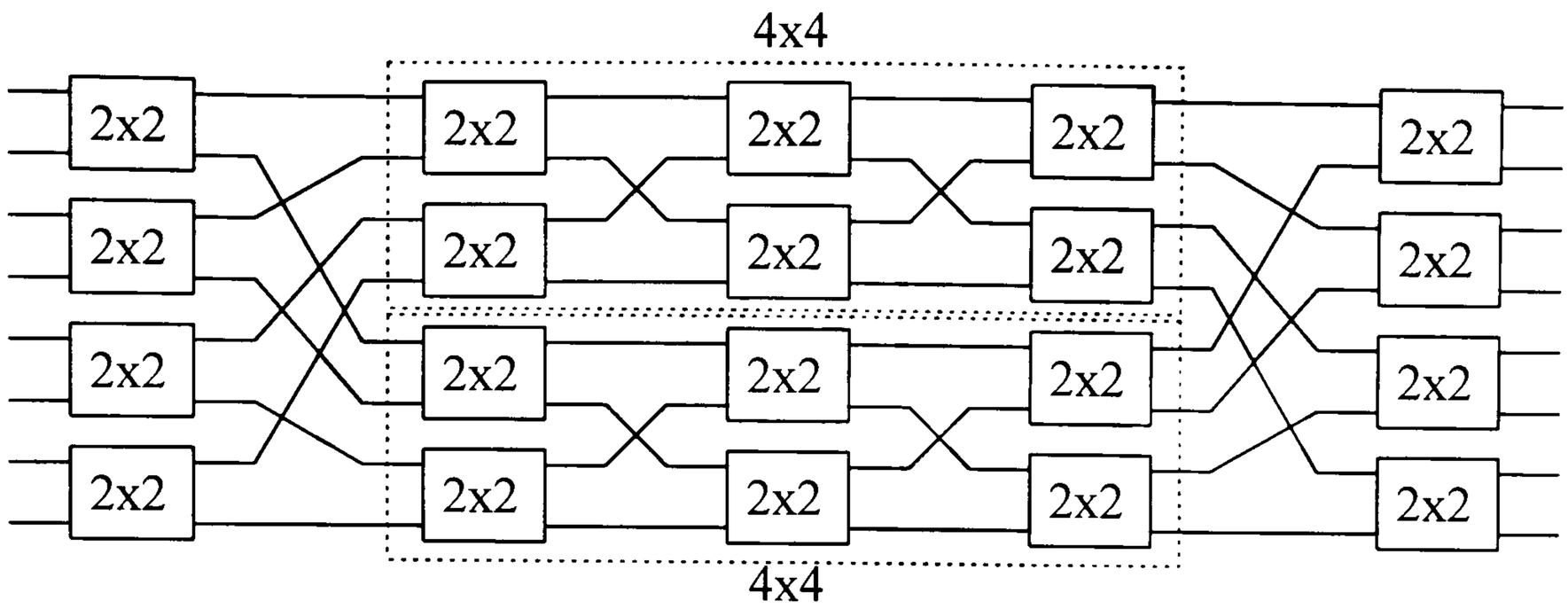

Figure 2.4 Schematic diagram of the Benes Multi-level Architecture.

Both the classic crossbar and single stage Clos structures introduced in figures 2.2 and 2.3 fall into the category of a single level architectures. That is the crosspoint only ever switches the optical input once. It may first appear that this is the only conceivable way to realise a cross-connect and therefore the minimum number of digital optical switches required is N^2. However, the number of digital switches can be reduced by using architectures that have several levels of switching. The Benes architecture drawn schematically in figure 2.4 is one such example of the so called multi-level architecture. An 8x8 version is shown here but may be extended to any number of inputs or outputs. The switch consists of $2log_2N-1$ levels of lower order 2x2 crosspoints and requires a total number of $2Nlog_2N-2N$ digital switches [3]. Indeed, the dashed boxes represent a 4x4 Benes network, and it may be shown that an NxN crosspoint may be constructed from any number of smaller order cross-connects. However, although the number of switches has been reduced, this has been done at the expense of increased control complexity. That is multiple switches have to be set simultaneously to achieve a single input/output path. However, not only has the device control increased but its functionality has also been reduced. The Benes architecture falls into the category of a *rearrangeably non blocking* switch, one of four further categories that fall under the broadcast and point to point cross-connects which have been discussed earlier (figure 2.5). These categories are discussed as follows

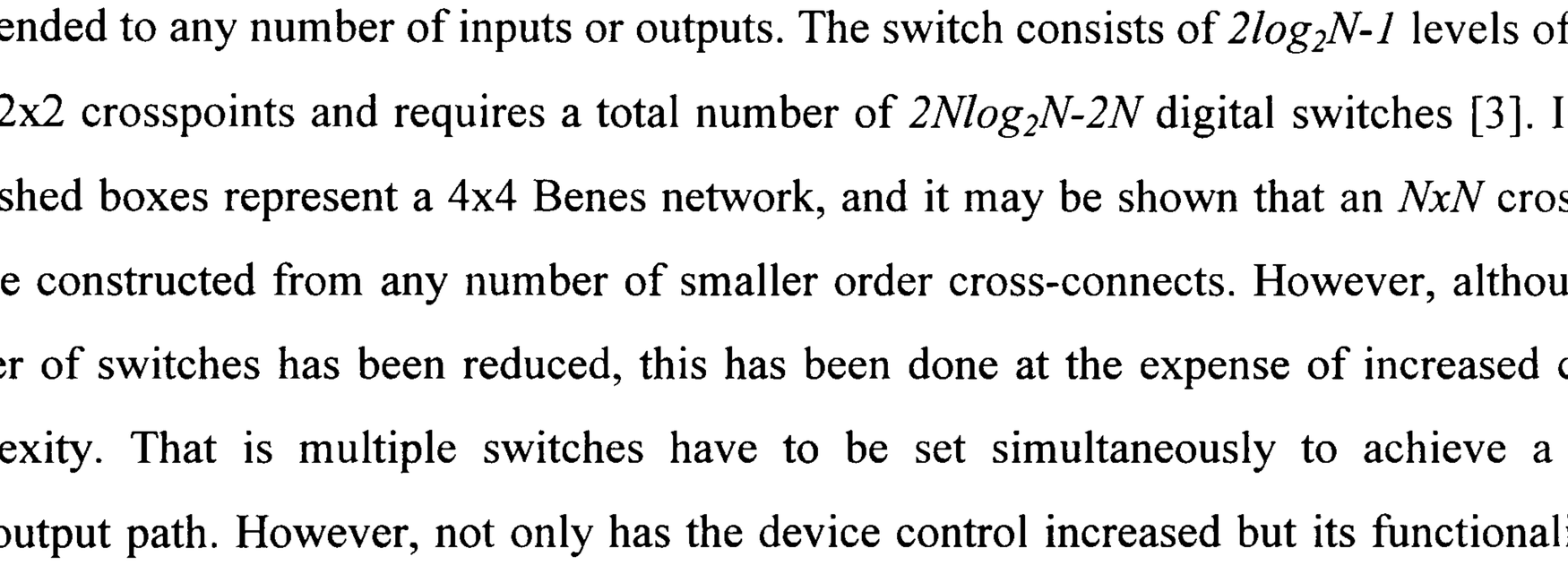

Figure 2.5 Hierarchical Structure of Crosspoint Architectures.

Blocking - An architecture is blocking if some input/output permutations cannot be realised.

Rearrangeable nonblocking - All input to output permutations are possible, but if at some point a new connection is required there may be conflict with existing connections. In this case all the connections will have to be torn down and rearranged in order for the new connection to be made.

Non-Blocking in the wide Sense - Here an algorithm exists which guarantees that there will be no conflict with any future connection without having to rearrange existing connections.

A network is *Strictly Non-Blocking* if an input can always be made to an output without the use of an algorithm.

Thus by reducing the number of switching elements and hence possibly switch size, the Benes architecture requires considerable computational control in order to maintain its full operating potential. It should also be noted that the more computational time require to set up an architecture the slower the overall switching speed.

Generally speaking the above categories have been labelled in order of complexity and number of optical switches required. Blocking architectures are the simplest type of cross-connect, they have relatively little complexity since they are not capable of routing every input to every output. However, a strictly non-blocking architecture (as drawn schematically in figures 2.2 and 2.3) requires substantially more routing and switching potential (and therefore larger device size) in order to achieve the greater operation flexibility.

There are many types of multilevel architectures that may be found in the literature; Banyan, Omega, Shuffle, Double Crossbar, N-stage Planar to name but a few. A complete description of each is not given here as each architecture is well documented and may be found in the literature [4-8]. From the viewpoint of monolithic integration, the advantages of using multi-level architectures in InP crosspoint design are a matter for discussion. It may be observed from the Benes architecture (figure 2.4), that the interconnections between each crosspoint are as complicated as a single level architecture (figure 2.2), which does not require the same computational control. The same may be said of the many other types of multi-level architecture. Thus, in this thesis the discussion will be focused on fabricating the largest single stage strictly non-blocking InP crosspoint currently possible (of the order of 8x8), which may then be packaged and used in a multi-level architecture (such as the Benes) to create very much larger cross-connects.

2.3 Monolithic Integration of Crosspoint Switches

Many different cross-connect architectures have been introduced in the previous section. However all these architectures must achieve three basic functions in order to achieve the crosspoint logic. They must all provide

1. a split (and combine),
2. a switch, and finally
3. a shuffle of each input to each output.

The methods used to monolithically achieve these three basic functions are discussed in the proceeding sections, after which a summary of the many cross-connect devices fabricated to date will be given.

2.3.1 The Optical Coupler

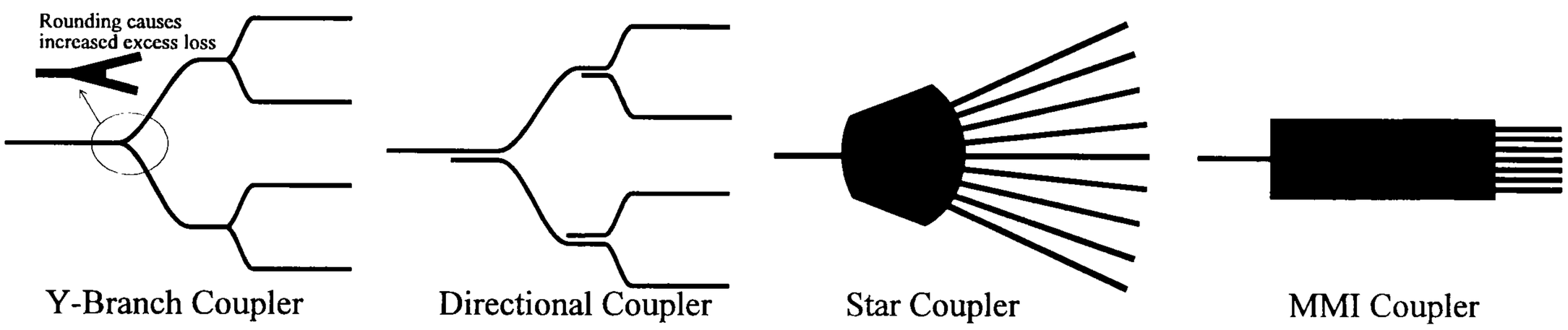

Figure 2.6 Methods of achieving optical splitting in Integrated Optics.

There are several methods for achieving optical splitting in integrated optics. This can be accomplished by several integrated optical components namely the directional coupler [9], Y-branch coupler [10-13], star coupler [14-17] and the Multi-Mode Interference (MMI) coupler [18-21] as shown in figure 2.6. The principle of optical splitting of each design are discussed as follows

1. Y-Branch Coupler. The branching of a single waveguide into two with a waveguide S-bend can achieve 50/50 power splitting between the output waveguides. However, the component is not suitable for large numbers of outputs (since the multiple stages required make the coupler very long). Also there are fabrication problems at the branch, since the resolution of the photolithographic process causes rounding at the junction. This increases the excess loss.
2. Directional Coupler. This method of splitting relies on the evanescent tails of optical modes which cause power to be coupled into a neighbouring waveguide (as discussed in chapter 4). The splitting ratio maybe controlled by adjusting the length of the coupling region and/or

the separation of the waveguides. The wavelength bandwidth of the coupler tends to be small since 50/50 coupling is only optimised at one wavelength. As with the Y-Branch, the directional coupler is not suitable to large number of outputs, since multiple couplers are required

3. Star Coupler. Light diverging from an input waveguide may be coupled into a number of output waveguides. The coupler is very well suited to large number of output waveguides and has a large wavelength bandwidth. However, owing to the gaussian power distribution across the output guides there is a compromise required between excess loss and power splitting uniformity.
4. Multimode Interference Coupler (MMI). Light injected into a multimode waveguide, excites multiple modes, which propagate down the guide with different effective indices. Owing to the approximately quadratic relationship between mode number and effective index, this causes multiple 'images' of the input to be formed at discrete positions down the guide. By calculating the exact waveguide length required to obtained multiple images a MMI coupler can be fabricated (this procedure is discussed in more detail in chapter 4).

2.3.2 The Optical Switch

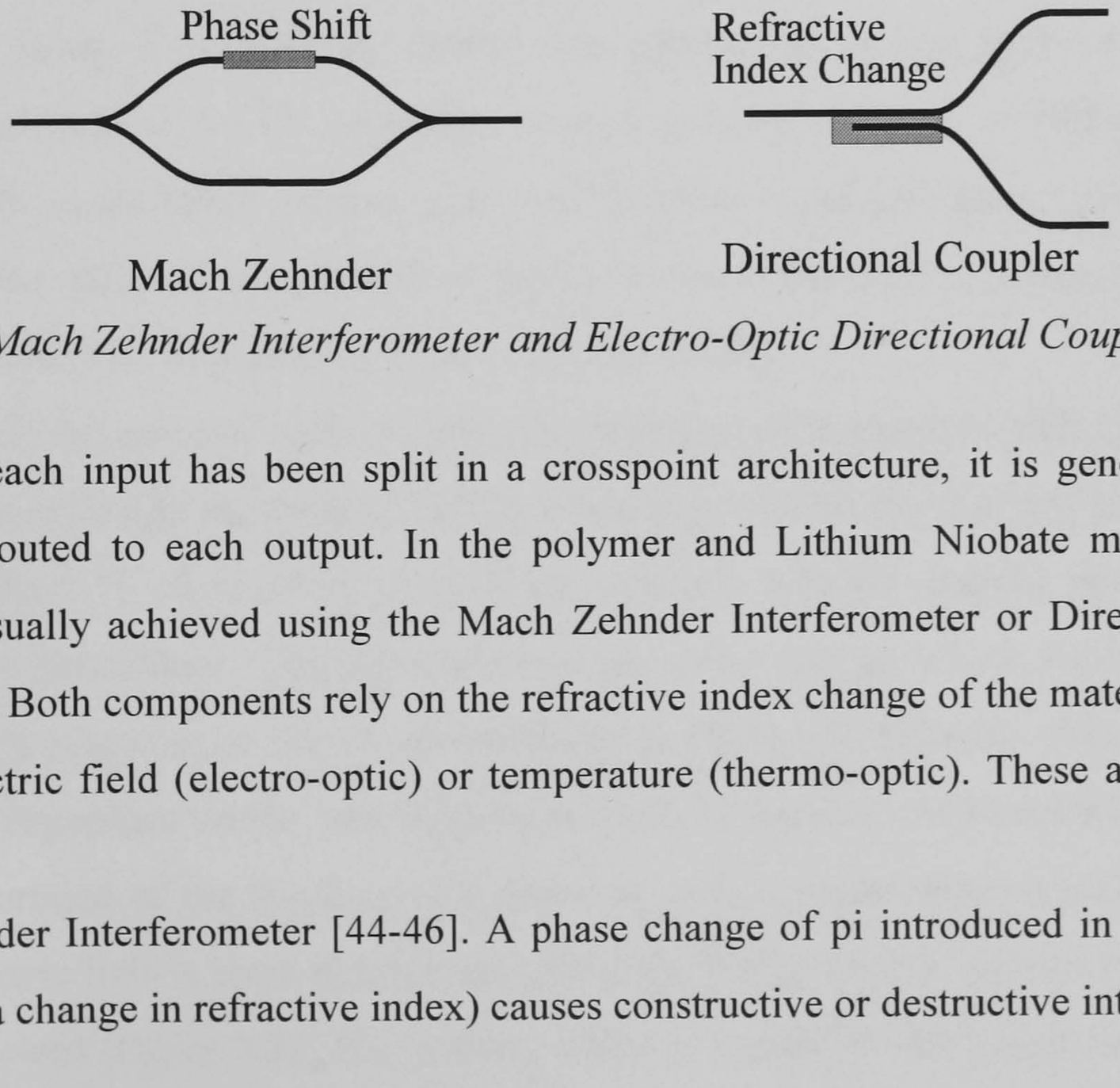

Figure 2.7 Mach Zehnder Interferometer and Electro-Optic Directional Coupler

After each input has been split in a crosspoint architecture, it is generally switched before being routed to each output. In the polymer and Lithium Niobate material systems switching is usually achieved using the Mach Zehnder Interferometer or Directional coupler switch [22,23]. Both components rely on the refractive index change of the material with either an applied electric field (electro-optic) or temperature (thermo-optic). These are discussed as follows

1. Mach Zehnder Interferometer [44-46]. A phase change of pi introduced in one arm of the switch (by a change in refractive index) causes constructive or destructive interference at the output.
2. Directional Coupler [62-68]. A refractive index change in the coupling region between the two parallel running waveguides can cause power to be coupled between the two output waveguides.

Both these methods of switching can also be achieved in the Gallium Arsenide and Indium Phosphide material systems. However, it is found that more compact switching may be achieved by two other types of switch which are discussed as follows.

Firstly, many Indium Phosphide based cross-connects use the Semiconductor Optical Amplifier (SOA) as the primary switching mechanism in the architecture [48,51-54,56,59]. Unbiased, an input signal injected into the SOA is absorbed ('off' state), while providing around 25dB of gain when electrically pumped ('on' state). Thus the SOA not only provides a switching mechanism, it also compensates for any component losses in the architecture.

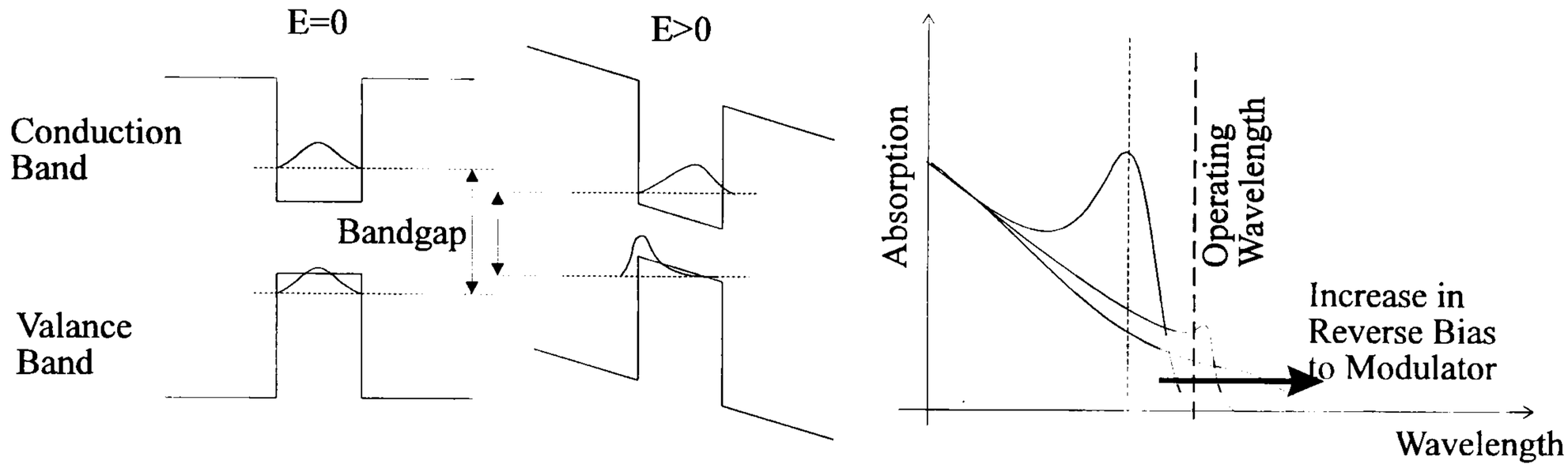

Figure 2.8 The Quantum Confined Stark Effect (after [30]).

Secondly, the change of material absorption with applied electric field may be used in a semiconductor using a component termed the Electro-Absorption (EA) Modulator. The principle of operation of the EA modulator is well documented [24], of which there are two kinds which rely on the Franz Keldish, [25], and Quantum Confined Stark Effect (QCSE) [26-28]. However the effect is far superior in the latter (up to 50 times in magnitude, but not in bandwidth), as such this discussion will be limited to QCSE.

It is well documented that the effective bandgap of a quantum well may be deduced from the laws of quantum mechanics [29]. In a quantum well an electron and hole's position is confined, therefore the Heisenburg Uncertainty principle requires that the particle has a non zero momentum uncertainty. This translates to a zero point energy, which displaces the ground state energy of the particle, as shown schematically in figure 2.8. Thus the effective bandgap of the material is dependent on the well width and depth of the well. At zero bias, the absorption in the neighbourhood of the bandgap of a quantum well is shown schematically in figure 2.8 [30]. As an electric field is applied perpendicular to the well, the potential that the electrons and holes see is skewed (figure 2.8). The primary effect is to modify the zero-point energy of the particles, and hence the bandgap energy. Thus the absorption edge of the well is shifted towards higher wavelength. The effect can be strengthened by increasing the numbers of wells by forming Multi-Quantum Well (MQW) layers.

2.3.3 The Shuffling of inputs to outputs

Finally, one of the key issues for monolithic integration is the shuffling size of the final device. The shuffling size of a monolithically integrated crosspoint is determined by the two factors so far discussed in this chapter, material system and architecture used. A review of current crosspoint technology later in this chapter will show that the material system and architecture are inextricably linked. It is found that multilevel architectures are suited for the polymer/Lithium Niobate material systems, where as single stage architectures are preferred for Indium Phosphide. This may be explained as follows.

In general polymer devices require most importantly ultra low loss. There is no satisfactory mechanism to date for pumping plastics to achieve optical gain (the so called 'plastic laser') and as such all the components in the switch have to optimised carefully to reduce loss to a minimum. In order to switch, the refractive index of the polymer is generally modulated using the electro-optic or thermo-optic effect in Mach-Zehnder switches, as discussed previously. So far only polymers which exhibit a very low refractive index change have been found of around $1x10^{-4}K^{-1}$, and this leads to long digital switch sizes often of a few centimetres [43]. However with polymers this is not a problem since the substrate is cheap and available in large quantities. The same statement may be said of Lithium Niobate.

With Indium Phosphide, however, the situation is somewhat different. The most important issue is that of device size. The cost of InP substrates is currently many orders of magnitude above that of silicon. Thus the number of devices per wafer must be maximised in order to reduce device cost. The problem is exacerbated in terms of device yield. Large areas are more prone to dust contamination between photolithography processing steps, resulting in an even lower number of devices per wafer. On the other hand passive InP waveguides can be monolithically integrated with optical amplifiers, this has been done using a variety of different techniques such as disordering [31], bandgap selective growth [32], and selective area regrowth [33]. Indeed, many crosspoint switches have already been fabricated this way, this will be discussed in more detail a little later. Thus ultra low loss components are not as essential, since 'on the chip' amplifiers can compensate for any lossy components. For example, waveguide mirrors [34-36] which exhibit moderate losses of approximately 1dB can be considered, since these components drastically reduce the device size and hence increase device yield and reduce costs.

Thus, by considering the material system two major device issues during shuffling have been highlighted, that of *size* and *loss*. However, there is one other very important factor which ties in very closely to both device size and loss, only mentioned very briefly so far, that is the number of waveguide crossings in an architecture.

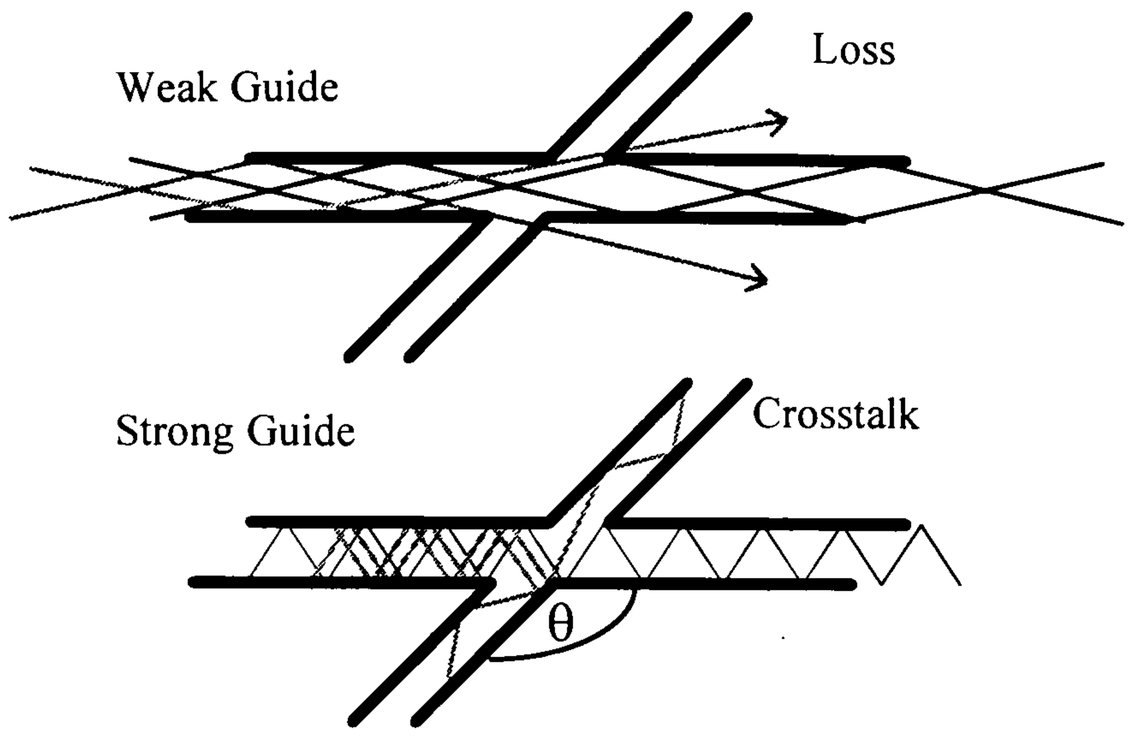

Figure 2.9 Loss and Crosstalk introduced by a waveguide crossing

The key element to any crosspoint architecture is the shuffling of waveguides to each output. In general, as the device order increases the number of waveguide crossings increases dramatically. Large numbers of waveguide crossings can introduce both loss and crosstalk to a device, this will be examined rigorously in chapter 4. However, for now, a brief understanding of this phenomenon can obtained by considering the classical ray picture of light propagating down an optical waveguide, as shown schematically in figure 2.3. Two single moded waveguide crossings are shown with different refractive index steps, Δn. One is weakly guided (Δn small of the order of 0.001-0.01), and the other strongly guided (Δn large approximately 1-2). The rays propagate down each guide by Total Internal Reflection, at a characteristic angle (ignoring the Goos-Haenchen shift) which is proportional to Δn and is given by [37]

$$\theta = \sin^{-1}\left(\frac{2\pi m}{\lambda}\Delta n\right) \tag{2.1}$$

For the weak guide, as some rays traverse the crossing they are no longer guided and are radiated contributing to a crossing loss. A strong guide loses an even greater number of rays due to the higher reflection angle (hence more loss). However, more importantly, depending on the crossing angle some rays can fall within the numerical aperture of the crossing guide, thus contributing to a crosstalk penalty.

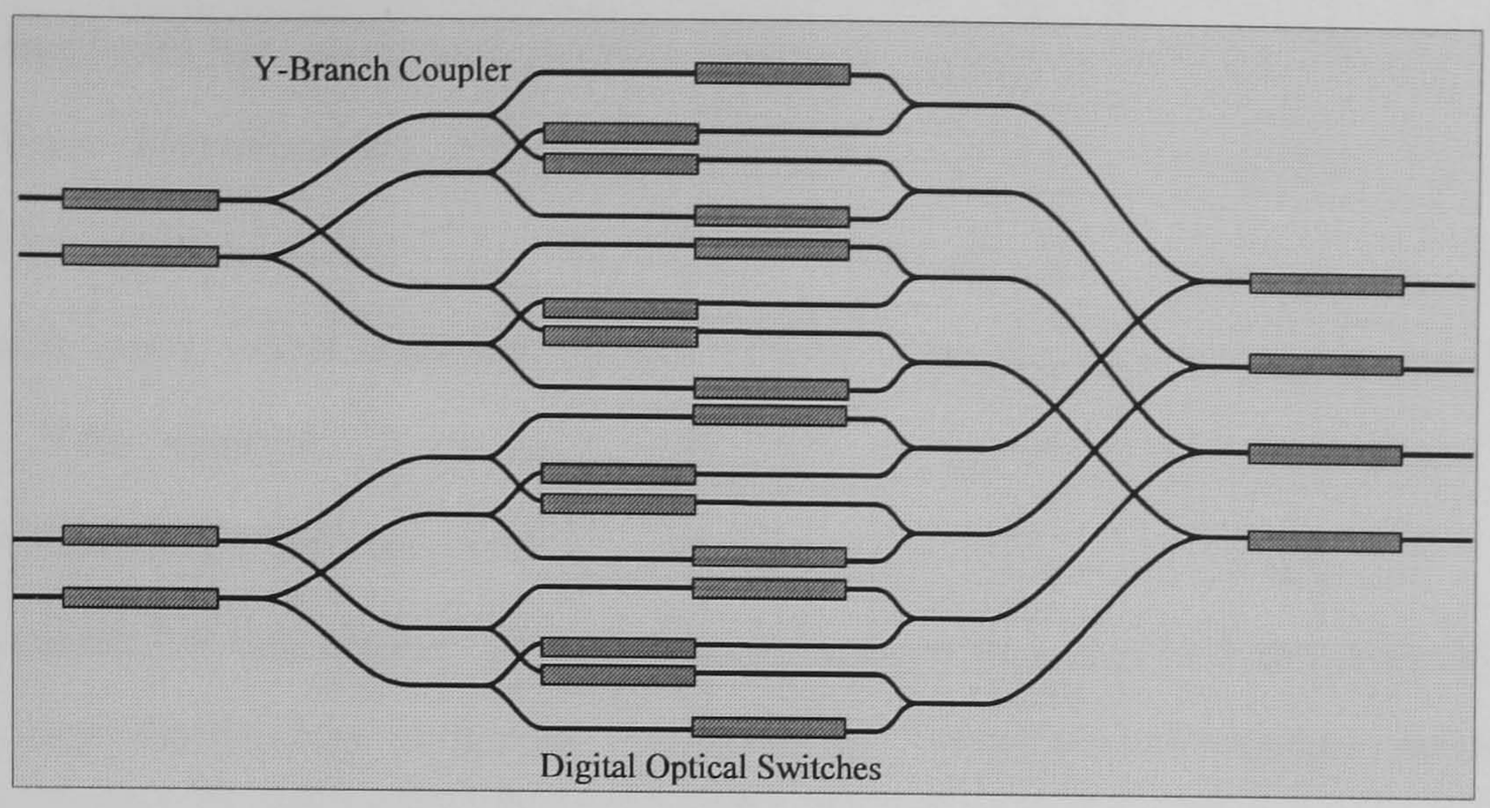

Figure 2.10 A Typical 4x4 Monolithically Integrated Crosspoint (after[74])

Lower crossing angles leading to higher crosstalk values for both strong and weakly guided waveguides. Thus it is desirable not only to choose architectures which minimise waveguide crossings - to reduce loss, but architectures which maximise crossing angle as well as using weakly guided waveguides. However it should also be noted that weak guides immediately imply large devices. In general it will be shown that, to date crosspoint design has used the S-Bend waveguide in order to shuffle each input to each output. An example of such a device is shown schematically in figure *2.10*. However, low index guides cannot 'reflect' light around abrupt changes in direction, since the critical angle is too low. Thus large radii of curvature waveguides are required in the bends (often up to tens of millimetres) to provide low loss shuffling of the mode to each output. This increases device size, which is acceptable in material systems such as Lithium Niobate, but unacceptable on InP since the substrate is so expensive. This contradiction between device size and waveguide crossings is illustrated schematically in figure 2.11. Thus a method must be found for InP to make low crosstalk/loss crossings (or avoid them all together) while maintaining compact device sizes.

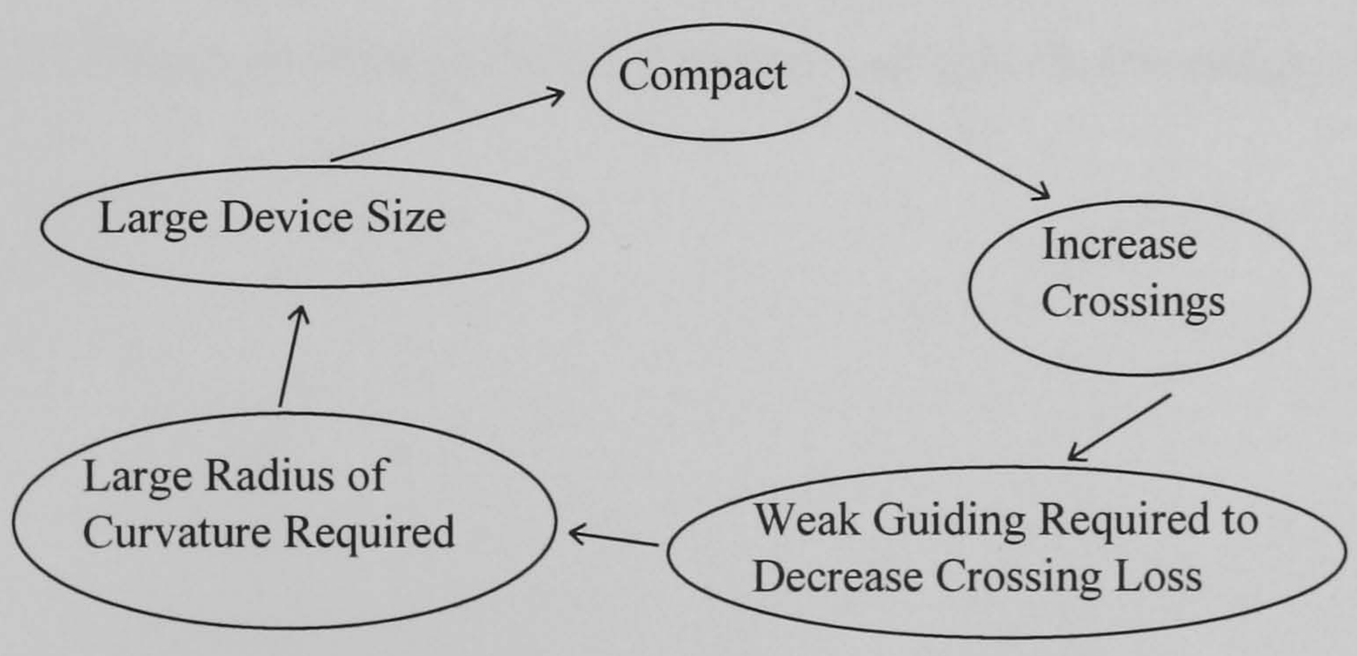

Figure 2.11 Contradiction between Device Size and Loss

Two methods are proposed in this thesis to achieve this. The first method uses the concept of Two Dimensional Integrated Optics, whereby waveguide crossings can be eliminated all together (Section 2.4). Secondly, a conventional waveguide crosspoint switch is proposed which uses Total Internal (TIR) Mirrors in order to achieve compact shuffling (Section 2.5). This method is by no means new, however it will be shown that compact shuffling is not the only requirement for compact crosspoint switch design.

A summary of the optical crosspoints which have already been realised will now be given in the next section in order to complete an overview of current optical crosspoint technology.

2.3.4 Crosspoints Fabricated to date

There are numerous papers on optical crosspoint switches reported in the literature ranging from simple 2x2 designs up to very large matrices of even 32x32 [89]. Firstly a brief introduction of the simplest crosspoint, a 2x2, will be given, as these devices form the platform off which any order crosspoint may be realised.

The design of the basic 2x2 switch stems back to the mid eighties with over twenty different designs published in a variety of material systems. Table 2.1 summarises the 2x2 crosspoint switches published in the literature to date. The essential attributes of each device has been noted in the 13 categories, from date of publication to more technical specifications such as operating wavelength, device loss (or gain), device crosstalk and device size. It may be noted that there are four distinct material systems which have been so far reported, Gallium Arsenide (GaAs), Lithium Niobate ($LiNO_3$), Polymer and Indium Phosphide (InP).

Ref	Year	Authors	Material System	Size (mm)	Switch	λ (nm)	Optical Gain	Drive	Speed	Shuffle	Coupler	Architecture	Crosstalk
[38]	1987	NEC	GaAs/AlGaAs	3x1.2	QCSE	860	-24dB	10V	3.6Ghz	TIR M	TIR M	Broadcast	20dB
[39]	1988	Wuthrich	GaAs/AlGaAs	-	MZ	1150	-	7.5V	-	-	D	Blocking	20dB
[40]	1994	OKI	$LiNbO_3$	18	e-DC	1300	-	40V	-	SB	YB	Blocking	25dB
[41]	1996	NTT	$LiNbO_3$	75x60	e-MZI	1550	-4dB	1700V	<100ns	SB	D	Blocking	-
[42]	1991	BT	$LiNbO_3$	-	e-DC	1300	-5.7dB	30V	-	SB	D	Point to Point	17dB
[43]	1993	NTT	Polymer	30	t-MZI	1300	-0.6dB	4.8mW	9ms	SB	D	Blocking	-
44,45	1996	N.Keil	Polymer	25	t-MZI	1500	-4.5dB	50mW	ms	SB	YB	Point to Point	25dB
46,47	1996	S.G. Han	Polymer	-	t-MZI	1300	-	30V	-	SB	YB	Blocking	10dB
[48]	1990	I.H. White	InP/InGaAsP	0.4x0.2	SOA	1550	0dB	300mA	-	TIR Y	YB	Broadacst	20dB
[49]	1992	AT&T	InP	0.25x1.2	SOA	1550	N/A	50mA	-	SB	YB	Point to Point	12dB
[50]	1992	Erricson	InGaAsP/InP	3x3	SOA	1550	-20dB	100mA	-	SB	YB	Broadcast	40-50dB
[51]	1993	G. Glastre	InP/InGasAsP	-	DC	1550	0dB	1-6mA	-	SB	D	Blocking	17dB
[52]	1993	Hitachi	InP	0.8x5.8	YB_OS	1550	+4dB	100mA	-	SB	YB	Broadcast	40dB
53,54	1993	BT	InGaAsP-InP	1.2x1.8	SOA	1550	-3dB	200mA	-	TIR M	TIR	Broadcast	>45dB
[55]	1994	Nippon	InGaAlAs/	-	-	1550	-16dB	-	2GHz	SB	-	-	15dB
[56]	1995	NEC	InGaAsP/InP	5x1	SOA	1550	+5dB	100mA	-	SB	YB	Broadcast	-
[57]	1995	Agrawal	InGaAsP/InP	-	QCSE	1575	-22dB	6V	10GHz	SB	MMI	Blocking	15dB
58,59	1996	CNET	InGaAsP/InP	0.5x3	SOA	1550	+10dB	160mA	-	SB	YB	Broadcast	-
[60]	1996	J.Lethold	InP/InGaAsP	9x1.3	MZI	1550	-8dB FF	190mA	few ps	SB	MMI's	Blocking	20dB
[61]	1996	K.R. Oh	InGaAsP/InP	-	SOA	1550	-1dB FF	80mA	-	SB	YB	Broadcast	42dB

QCSE - Quantum Confined Stark Effect
t-MZI - Temperature Controlled Mach Zehnder
e-MZI - Electro-Optic Mach Zehnder Interferometer
e-DC - Electro-Optic Directional Coupler
YP_OS - Electro-Optic Y-Branch Optical Switch
D - Directional Coupler
SB - S Bend Waveguide
TIR - Total Internal Reflecting Mirror
M - Mirror
FF - Fibre to Fibre Loss
YB - Y Branch Coupler
MMI- Multi Mode Interference Coupler

Table 2.1 2x2 Monolithically Integrated Crosspoint Switches Fabricated to date (1/1/98)

Many conclusions may be deduced from table 2.1. Firstly there has been considerable interest in InP 2x2 devices over the last decade. This is because InP has the potential of introducing optical gain to the switched signal by using the Semiconductor Amplifier (SOA) gate switch. This method of switching has already been discussed earlier on in this chapter, however it may be observed that many lossless broadcast crosspoints have been fabricated. The SOA gate is also responsible for the lowest crosstalk figures, owing to its extremely high extinction ratio on switching.

Secondly, most devices use S-Bend waveguides and Y-Branches in order to shuffle each input to each output. This is because both the S-Bend and Y-branch can be patterned in one photolithographic processing step, which makes device fabrication very simple. However, even in a low order 2x2 switch the use of Y-Branches and S-Bends produce the largest device sizes. It may be noted that devices which use Total Internal Reflection (TIR) mirrors in order to split and shuffle each input to each output exhibit much smaller dimensions. However, TIR devices require substantially more processing as will become apparent in section 2.5 of this chapter.

Ref	Year	Authors	Material System	Size (mm)	Switch	λ (nm)	Optical Gain	Drive	Shuffle	Coupler	Architecture	Pol.	Xtalk
[62]	1986	NEC	$Ti:LiNbO_3$	-	e-DC	1300	-5.2dB FF	13V	SBend(SB)	D	Crossbar(M)	-	>35dB
[63]	1988	Erricsson	$Ti:LiNbO_3$	49x12	e-DC	1300	-8.4dB	50V	SBend (SB)	D	Tree(M)	Ind.	>35dB
[64]	1988	NEC	$Ti:LiNbO_3$	65	e-DC	1300	-6dB	30V	SB (10mm)	D	Simp. Tree(M)	<0.1dB	15dB
[65]	1990	Erricsson	$Ti:LiNbO_3$	-	ME	1300	-9.2dB	60V	SB (53mm)	YB	Tree(M)	Dep.	10dB
[66]	1992	NTT	SiO_2/InP	5x40	SOA	1550	-32dB	80mA	S-Bend(SB)	YB	Broadcast (S)	-	15dB
[67]	1994	N. Keil	Polymer	20x0.2	t-MZI	1550	-10dB FF	70mW	S Bend (SB)	D	Blocking(M)	<0.5dB	-
[68]	1995	N. Keil	Polymer	45x2	t-MZI	1550	-9dB FF	31mW	S-Bend(SB)	D	Benes (M)	<0.5dB	17.5dB
69,70	1991	NEC	GaAs/AlGaAs	15x1	e-DC	1300	-10.8dB	22V	SB(4mm)	D	Simp. Tree(M)	-	30dB
[71]	1992	Mc.Don.Doug.	GaAs	2x3	SOA	850	-4dB FF	-	TIR Mirror	TIR	Broadcast (S)	-	30dB
[72]	1997	NTT	GaAs/InGaAs	1x1.2	SOA	980	0dB	16mA	TIR YB	YB	Benes(M)	-	>20dB
73,74	**1992**	**Erricsson**	**InGaAs/InP**	**7x3**	**SOA**	**1550**	**-2dB FF**	**50mA**	**SB(1mm)**	**YB**	**Broadcast (S)**	**Ind.**	**40dB**
[75]	1993	NTT	InGaAlAs	9x0.4	QCSE	1550	-18dB	6V	SB(4mm)	D	Benes (M)	-	17dB
[76]	1994	Hitachi	InGaAsP/InP	12x2	YB-SOA	1550	+4dB	50mA	S Bend	Y	Crossbar (M)	-	54dB
[77]	1995	Nippon	InGaAsAs	-	e-DC	1550	-21dB FF	10V	-	-	-	-	13dB

QCSE - Quantum Confined Stark Effect
T-MZI - Temperature Controlled Mach Zehnder
E-MZI - Electro-Optic Mach Zehnder Interferometer
E-DC - Electro-Optic Directional Coupler
ME. Mode Evolution Digital optical Switch.

SB - S Bend Waveguide (Radius of Curvature in Brackets)
TIR - Total Internal Reflecting Mirror
D - Directional Coupler
YB - Y Branch Coupler
M- multi-level Architecture S- Single Stage Architecture

Table 2.2 4x4 Monolithically Integrated Crosspoint Switches Fabricated to date (1/1/98)

Moving on to N=4, table 2.2 summarises the monolithically integrated 4x4 crosspoints so far reported. Again, the majority of devices use Y-Branches and S-bends in order to realise the crosspoint logic. Total Internal reflection has been used extremely effectively in GaAs in order to fabricate extremely small 4x4 crosspoints, especially [71,72], however TIR has not yet been used in InP. Semiconductor optical amplifiers have been used again to good effect in order to fabricate lossless devices with extremely low crosstalk. The smallest lossless 4x4 InP crosspoint (broadcast) so far fabricated to date is highlighted for comparison with the architectures proposed later in this chapter. The device has already been briefly introduced in figure 2.10.

Finally, in order to complete the introduction to crosspoint switch design, table 2.3 summarises the monolithically integrated crosspoints switches of order greater than 8. It may be observed that no device has yet been fabricated in InP. All the designs use multilevel architectures in order to achieve switching. Essentially, these devices are natural extensions of 2x2 switches demonstrated in table 2.1, which have been used in multi-level architectures in order to increase the device order. So far this has only been monolithically demonstrated on Lithium Niobate since out of all the material systems it is the most mature, and the low cost of the substrate allows such integration. It may be observed that this method of integration yields extremely large monolithic devices of the order of centimetres, which is wholly unsuitable for InP. All the devices use the refractive index change of the material in order to generate optical switching. To date, no device has been fabricated which introduces optical gain to the signal, thus all the devices perform with point to point operation, and incur a significant loss compared with the input signal.

Ref	Year	Authors	Material System	Size (mm)	Switch	λ (nm)	Loss	Drive	Shuffle	Coupler	Architecture	Crosstalk
8x8												
[78]	1992	NEC	GaAs/AlGaAs	27x3	e-DC	1300	8.7dB	25V	SB(4mm)	DC	Simplified Tree	23dB
[79,80]	1994	NTT	SiO_2 - TiO_2	52x53	T-MZI	1300	3.8dB	26mW	SB(5mm)	DC	Crossbar	25dB
[81]	1986	Ericsson	Ti:$LiNbO_3$	2x64	e-DC	1300	7dB	24.6V	SB(30mm)	DC	Crossbar	18.6dB
[82]	1988	Plessey	Ti:$LiNbO_3$	0.5x66	e-DC	1300	5.5dB	26V	SB(40mm)	DC	Rearrangable	20dB
[83]	1989	OKI	Ti:$LiNbO_3$	7x61	e-DC	1300	20dB	11V	SB(40mm)	DC	Simplified Tree	13dB
[84]	1990	NEC	Ti:$LiNbO_3$	6x65	e-DC	1300	12dB	85V	SB(40mm)	DC	Simplified Tree	18.7dB
[85]	1990	AT&T	Ti:$LiNbO_3$	8x66	e-DC	1300	-	9.2V	S-Bend(SB)	DC	Dilated Benes	30dB
[86]	1992	Karroy	Ti:$LiNbO_3$	10x37	SAW	633	17dB	125mW	Free Space	N/A	Sym. Nonblock	12dB
[87]	1994	Ericsson	Ti:$LiNbO_3$	15x80	ME	1550	15dB	105V	S Bend (SB)	YB	Tree	10dB
16x16												
[88]	1991	GEC	Ti:$LiNbO_3$	7x66	e-DC	1300	-	60V	SB(37mm)	DC	Benes	20dB
32x32												
[89]	1994	OKI	Ti:$LiNbO_3$	-	e-DC	1300	11dB	24V	SB(40mm)	DC	Banyan	18dB

e-DC - Electro-optic Directional Coupler switch
ME. Mode Evolution Digital optical Switch.
T-MZI - Temperature Mach Zehnder Interferometer.
SAW- Acousto Optic Switch
SB - S-Bend Waveguide
DC - Directional Coupler
TIR - Total Internal Reflection
YB - Y Branch

Table 2.3 8x8, 16x16, 32x32 Monolithically Integrated Crosspoint Switches Fabricated to date (1/1/98)

2.3.5 Summary

Thus it has been shown that, to date, very few high order monolithically integrated InP crosspoints have been fabricated, and never before above 4x4. An introduction to the various methods of crosspoint switch design has been given, and the problems associated with the monolithic integration has also been discussed. The proceeding sections will now introduce three new crosspoint designs which are proposed in this thesis, which will potentially allow 8x8 lossless cross-connects to fabricated on InP substrates. Namely, the two dimensional integrated optical crosspoint switch, the conventional waveguide crosspoint and the demonstration of a 1x4 passive wavelength router using a multi-wavelength laser.

2.4 Two Dimensional Integrated Optical Crosspoint Switches

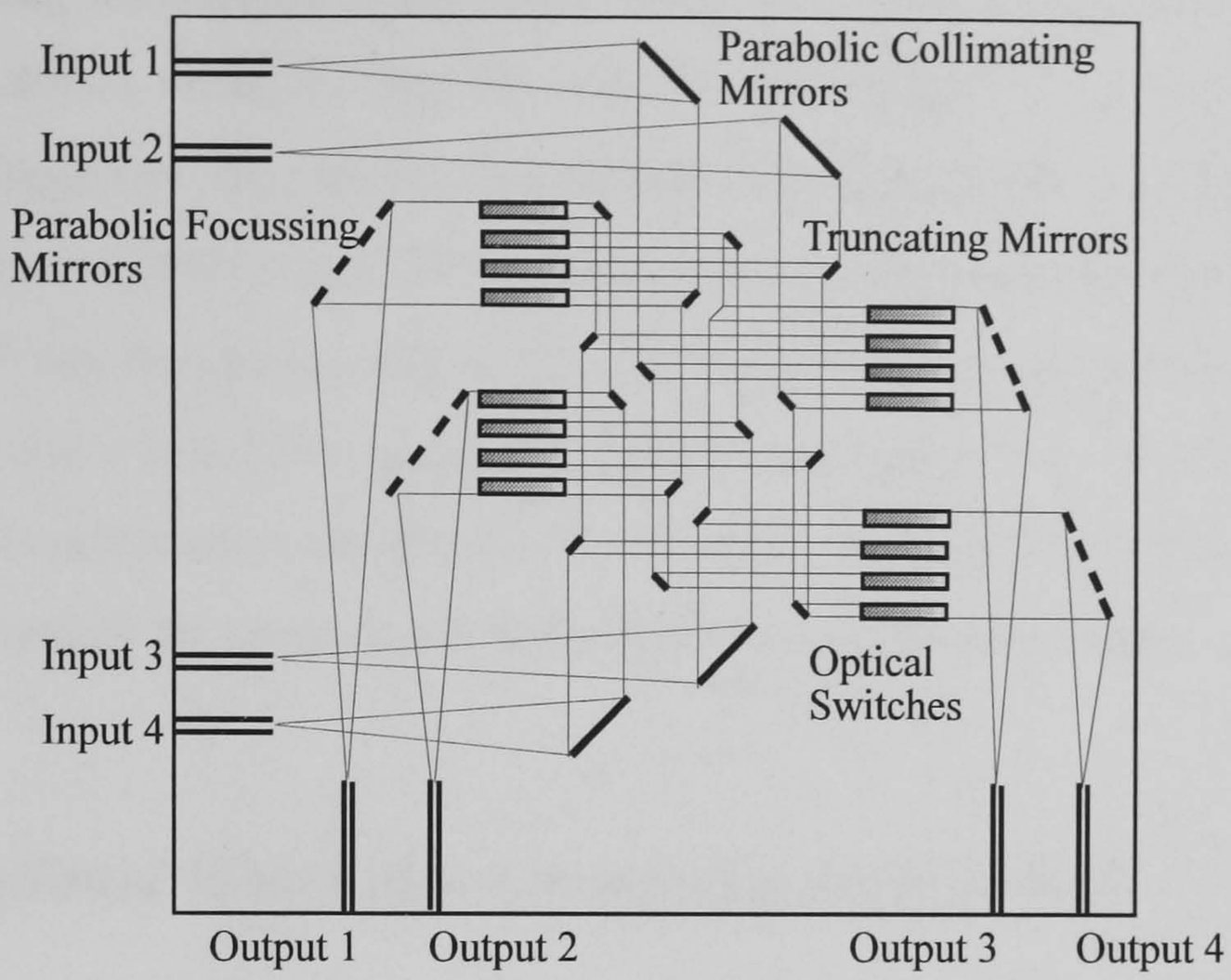

Figure 2.12 4x4 2DIO Crosspoint Architecture (Plan View)

It has been shown that the main problem associated with InP crosspoint design is the compromise required between device size and number of waveguide crossings and therefore crosstalk and loss (illustrated in figure 2.11). The last section has shown to date that (apart from one novel acousto-optic switch [86]) all integrated crosspoint development has concentrated on an integrated waveguide approach. Therefore waveguide crossings cannot be avoided in order to shuffle each input to each output. Thus it has been advantageous to use networking architectures which minimise the number of waveguide crossings. However, in Chapter 3 a entirely new concept in crosspoint switch design will be discussed. By designing a monolithically integrated space switch which does not use waveguides during the shuffling of inputs to outputs, the need for waveguide crossings is eliminated. This has been proposed by using Two Dimensional integrated Optics (2DIO), whereby light propagates in a slab waveguide with no lateral waveguiding [90], as shown schematically in figure 2.12.

Light enters the device through input waveguides where it is injected into the 2DIO slab waveguide, and is free diverge laterally until it is collimated by parabolic mirrors. The collimated light then enters a matrix of N^2 truncating mirrors, which simultaneously split and shuffle each input to every output. The architecture used is an extension of the single stage Clos drawn schematically in figure 2.2 and the device therefore operates as a broadcast network. The light then passes through banks of amplifier switches, which allow the inputs to be switched to each output while providing gain to compensate for the intrinsic device loss. Each switched input is then focused down to the output waveguides via N parabolic output mirrors, which may be thought of as a novel type of 2DIO mirrored star coupler.

The 2DIO crosspoint has many advantages over current crosspoint devices. Since the crossing of optical paths is acceptable, an architecture can be used which can reduce the switch size by **maximising** the number of crossings. Also, only three mirrors per path are required regardless of the device order, *N*. Thus the 2DIO crosspoint has the potential for low loss and scalability. In comparison, the conventional optical waveguide device may have a multitude of couplers, Total Internal Reflecting (TIR) mirrors or waveguide bends through one optical path.

Chapter 3 will discuss the role of 2DIO in monolithically integrated crosspoint design. It will be shown that a 4x4 2DIO crosspoint switch operating in the 1.55μm communications window on InP, is predicted to exhibit less than -40dB crosstalk and is less than 2x2mm^2. If fabricated this would be the smallest InP 4x4 crosspoint switch built to date.

2.5 A Conventional Waveguide Crosspoint Architecture

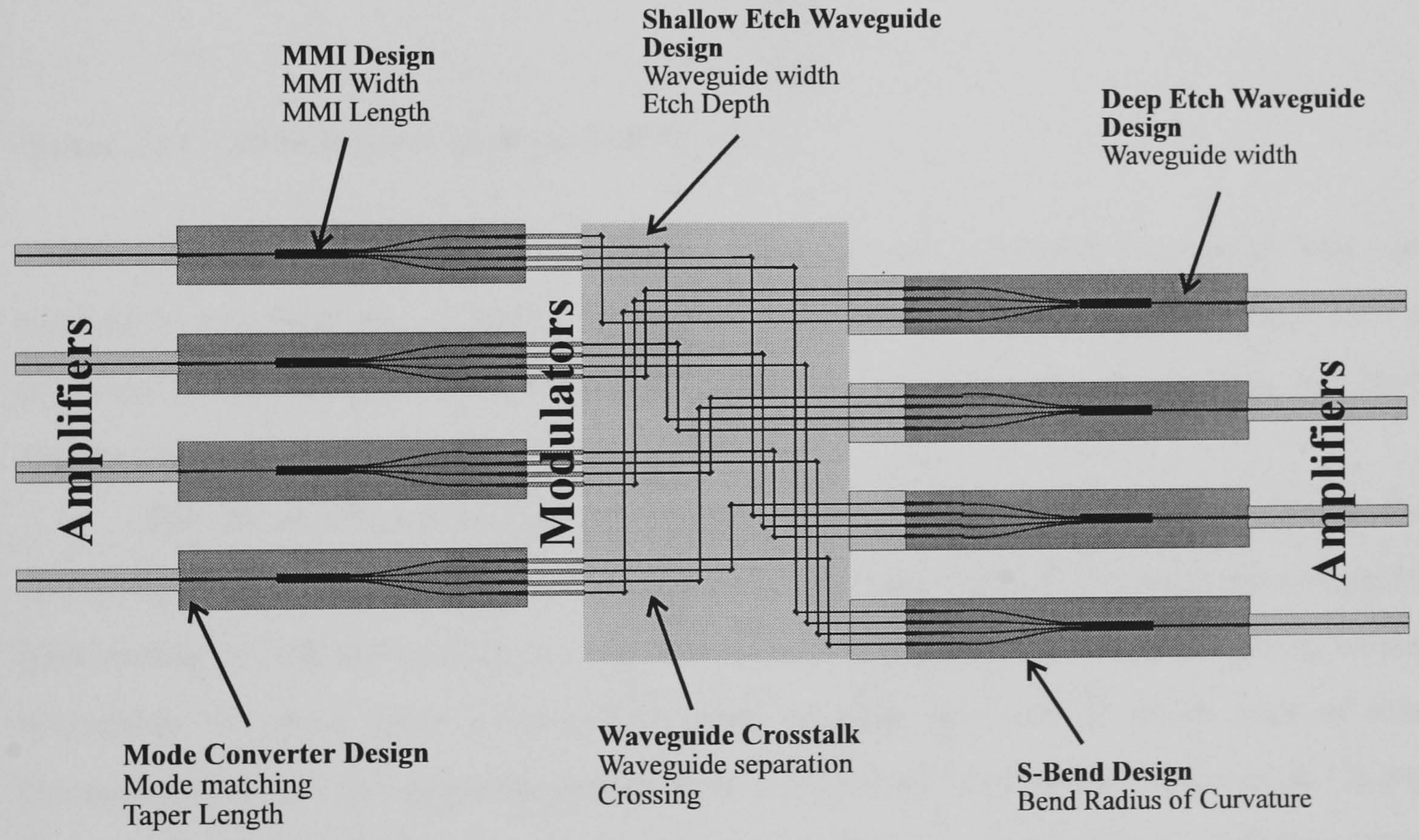

Figure 2.13 Schematic diagram of the proposed 4x4 InP Crosspoint switch Architecture

In this section a conventional waveguide crosspoint switch which is drawn schematically in figure 2.13 is presented. This section will discuss the motivation behind the architecture, by comparing it with the current methods of crosspoint design. It will be shown that the device makes many advances in crosspoint switch technology on InP.

As with the previous 2DIO design, the waveguide crosspoint architecture drawn in figure 2.13 is an extension of the single stage Clos drawn schematically in figure 2.2. The crosspoint therefore forms a broadcast architecture which is capable of routing every input to

every output. Traditionally broadcast architectures are very large. However, here this device maintains the high level broadcast functionality, while being extremely compact. Indeed the design drawn above measures only 1x2mm on a mask plate, which is an order of magnitude smaller in area, than a smallest InP 4x4 constructed to date [74] (3x7mm). This has been achieved by the use of TIR mirrors, Electro-Absorption Modulators and a combination of strong and weak waveguiding, which are discussed as follows.

2.5.1 Total Internal Reflecting Mirrors

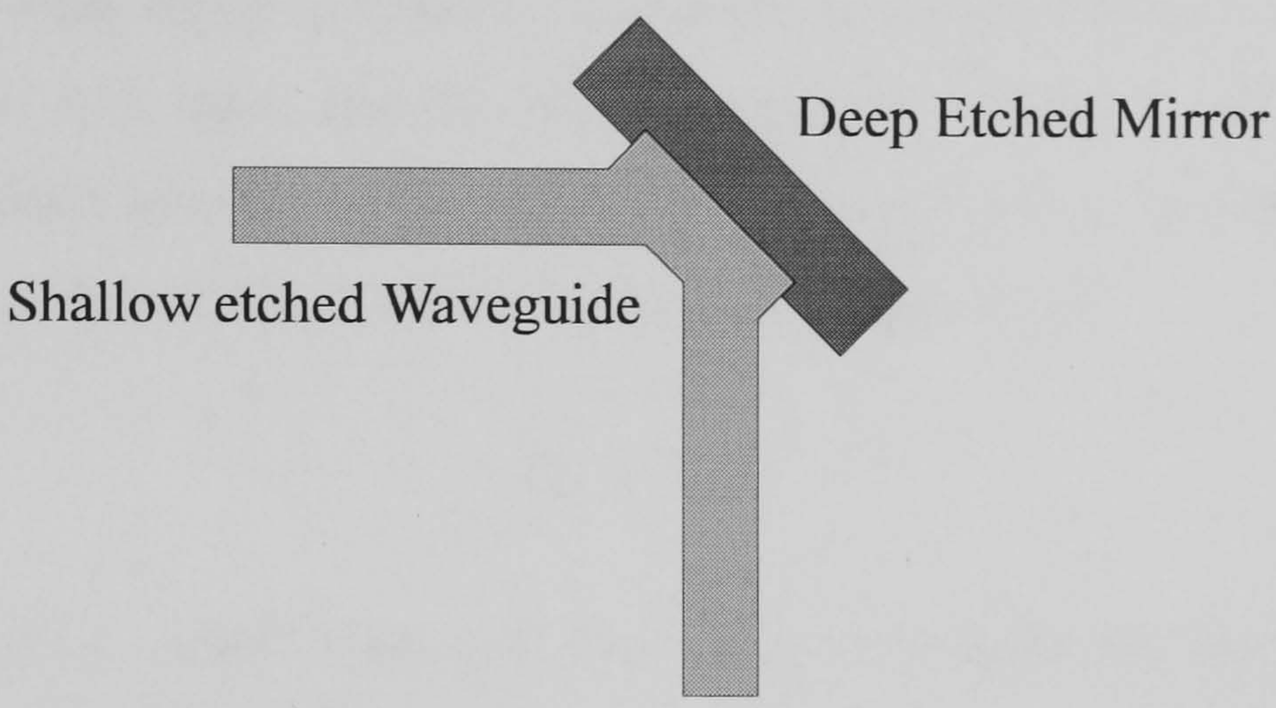

Figure 2.14 Total Internal Reflecting (TIR) Mirror

In order to shuffle each input to each output, traditionally both waveguide bends and waveguide crossings are normally required. Unfortunately, bends and large numbers of crossings are incompatible since crossings require very weak guiding for low loss and bends require strong guiding for compact size.

TIR (Total Internal Reflecting) mirrors (figure 2.14) have been used in several 2x2 crosspoint designs [48,54,71,72] in order overcome this contention. TIR mirrors are compatible with weakly guided waveguides and can take up substantially less wafer area than an S-Bend waveguide. However, from a fabrication point of view they add a whole host of extra processing steps and thus make the device more complicated (this will be discussed in Chapter 5). Also, they can be quite lossy components (approximately 1dB per mirror), which currently limits their widespread implementation. However, it should be noted from figure 2.13, that in this architecture there are only ever 2 mirrors per path **irrespective of *N***. Therefore, since the primary advantage of InP is the monolithic integration of Semiconductor Optical Amplifiers (SOAs) with the final device, the drastic reduction in size of the *shuffle* stage (whilst maintaining low loss crossings) in this case totally justifies their use. However, the use of TIR mirrors is not the only reason the device has been made so compact. Surprisingly the choice of optical switch used in the cross-connect has a very big influence on its size. This will be discussed in the next section.

2.5.2 Semiconductor Amplifiers and Electro-Absorption Modulators

To date integrated waveguide space switches fabricated on InP have generally used Semiconductor Optical Amplifiers (SOA) in order to switch light to each output [48,51-54,56,59]. The SOA not only provides a switching mechanism (as discussed earlier), it also compensates for any component losses in the architecture. From this standpoint it is a very attractive optical switch. Indeed, several 'Lossless' crosspoints have been fabricated on InP. and use this mechanism extremely effectively.

However, when trying to construct high order crosspoints where device size is of the utmost importance, it is found that the switch separation becomes a very important factor. Since in this broadcast architecture N^2 switches are required, it may be observed from figure 2.13 that the approximate width, D_y, of the cross-connect is given by

$$D_y \approx \Delta N^2 \tag{2.2}$$

where Δ is the optical switch separation. Thus in order to make the device as compact as possible it is essential to have Δ as small as possible.

In the case of the Optical Amplifier, Δ is limited to the thermal effects between each SOA on the chip. Since each amplifier will draw approximately 200mA of current CW in order to deliver approximately 25dB of gain [53], the thermal demands are great. It has been experimentally determined that the centre to centre separation of each amplifier should be no less than 200μm [91,92], in order to have a low thermal interaction. Such a high value generates very large device sizes. For example, it may be observed from figure 2.15, that equation 2.2 predicts a device width of well over 10mm for an 8x8 cross-connect. This figure is currently far too large for monolithic integration in the InP material system. Thus an optical switch which is able to operate far closer to its neighbour 'on chip' must be used to decrease the device size further than currently demonstrated.

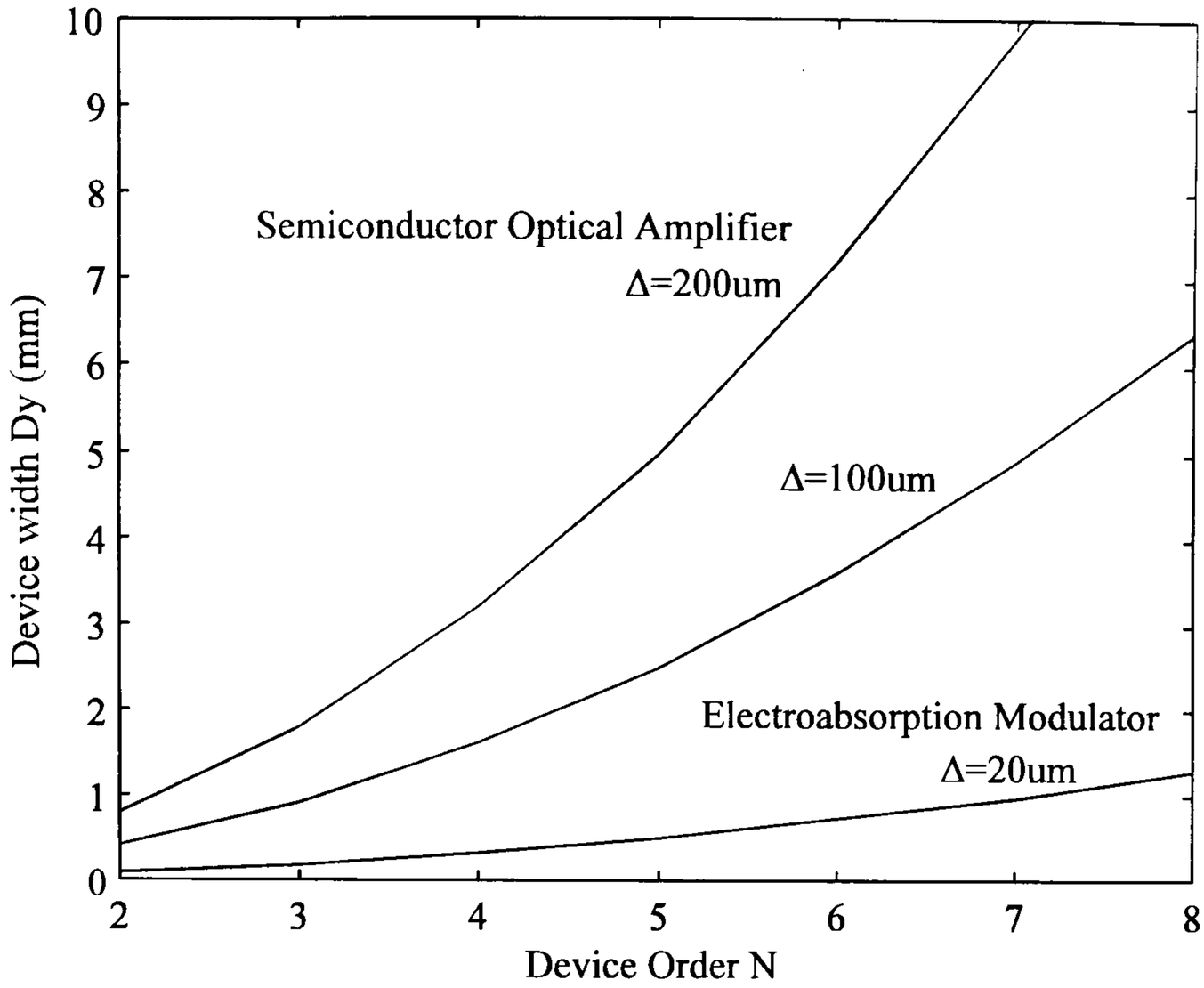

Figure 2.15 Variation of Device Width, D_y, with Switch Separation, Δ, predicted by equation 2.2.

The electroabsorption (EA) modulator is an optical switch which does not suffer from the thermal problems associated with the SOA. It is a reverse bias component, as such it does not draw current and is not prone to ohmic heating. Modulators may therefore be integrated far closer to each another on a wafer, which is ultimately limited by the optical rather than electrical interactions between them [57]. It will be shown in chapter 4, that for the device considered here, optical coupling between two adjacent modulators is found to be negligible when Δ=20μm. Thus it may be observed from figure 2.15 by implementing the EA modulator as the primary switching mechanism there is a saving in the device width of 10 fold.

Device speed is also vastly improved by the use of EA modulators compared with the SOA. In an SOA, the switching speed is limited to the carrier lifetime (the timescale with which the carrier density may be modified within the semiconductor) which is of the order of a nanosecond for InGaAs/InGaAsP [93]. Thus the switching speed is limited to around a gigahertz. In the EA modulator, the response speed is limited by the parasitics of the electrical connections, not by any other physical effect, such as heat dissipation or carrier lifetime [30]. Indeed, theoretical calculations have predicted EA modulators operating with a 3dB electrical bandwidth of 3THz [24].

The size and speed advantages of the electroabsorption modulator has lead to the development of many crosspoint switches [38,57,75]. However, it should be noted that since the EA modulator works on a principle of absorption, it has a finite insertion loss. This is typically of the order of 3-10dB depending on the modulator design and operating wavelength. Thus in order to increase device performance SOAs must also be integrated with the final cross-connect in order to compensate for the component losses in final device. In the device

considered here (figure 2.13) it has been proposed that these amplifiers are positioned at the input and outputs of the device. However, the device requires the integration of passive waveguides, optical amplifiers together with Electro-absorption modulators, this poses some interesting fabrication difficulties. All three components require materials with different bandgap energies. This problem may be highlighted in the next section by discussing the physical mechanism behind each.

2.5.3 Monolithic Integration of EA Modulators, SOAs and Passive waveguides

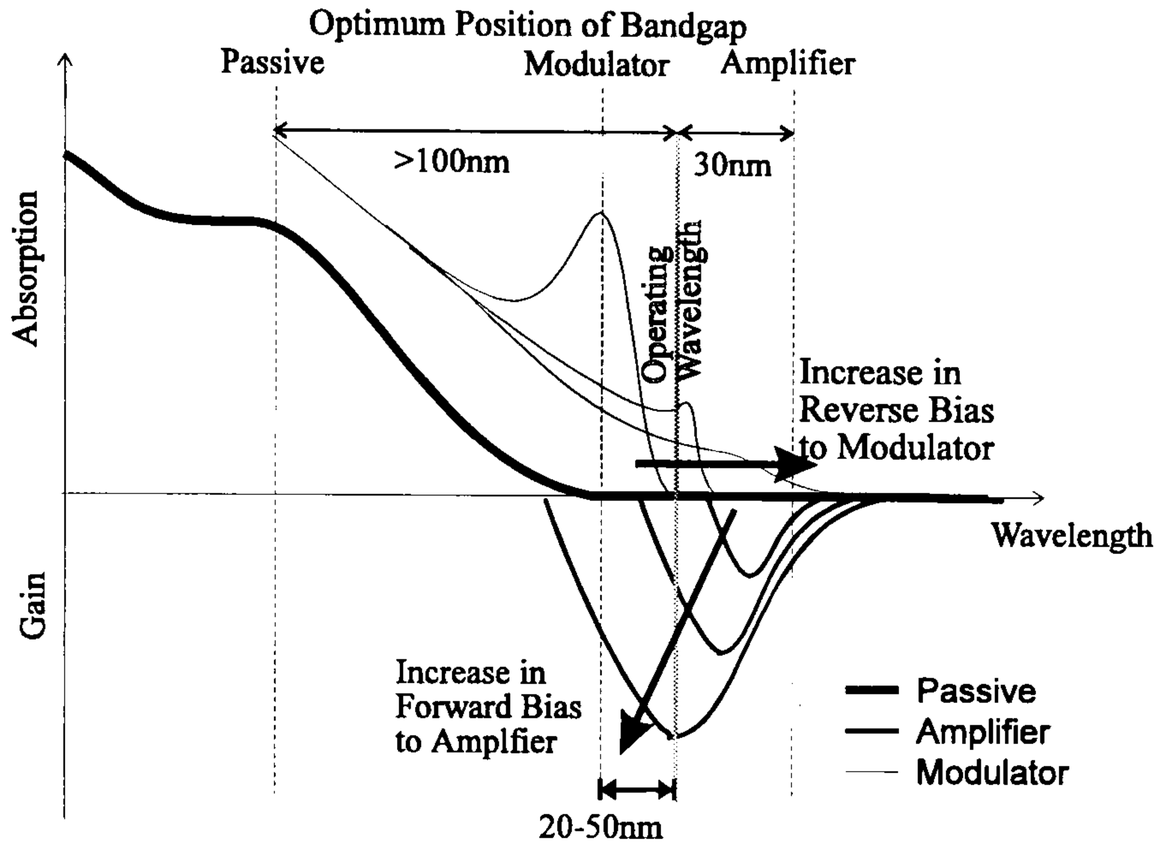

Figure 2.16 Integration of Amplifiers, EA Modulators and Passive waveguides.

In order for the EA modulator to work effectively with high extinction ratio and low insertion loss, the operating wavelength should be typically 20-50nm above the band-edge at zero bias (figure 2.16). However in an SOA, on forward biasing, peak optical gain is achieved below the bandgap (in wavelength), which decreases with increasing carrier injection (owing to band filling [94]). Passive waveguides are formed when operating far above the bandgap (approximately 100-150nm), so there is no absorption (since the photons do not have enough energy to create electron-hole pairs). Thus a method must be used in order to engineer the material bandgap across the wafer, with three distinct values for the amplifier, modulator and passive waveguides. This has already been achieved by Selective Area Regrowth [95,96], whereby different materials are selectively grown by MOVPE on different areas of the wafer which correspond to the passive/amplifier/modulator regions. It is initially proposed in this thesis that the crosspoint is fabricated by this process, which will be discussed in more detail in chapters 4 and 5.

2.5.4 Strong and Weak Waveguiding .

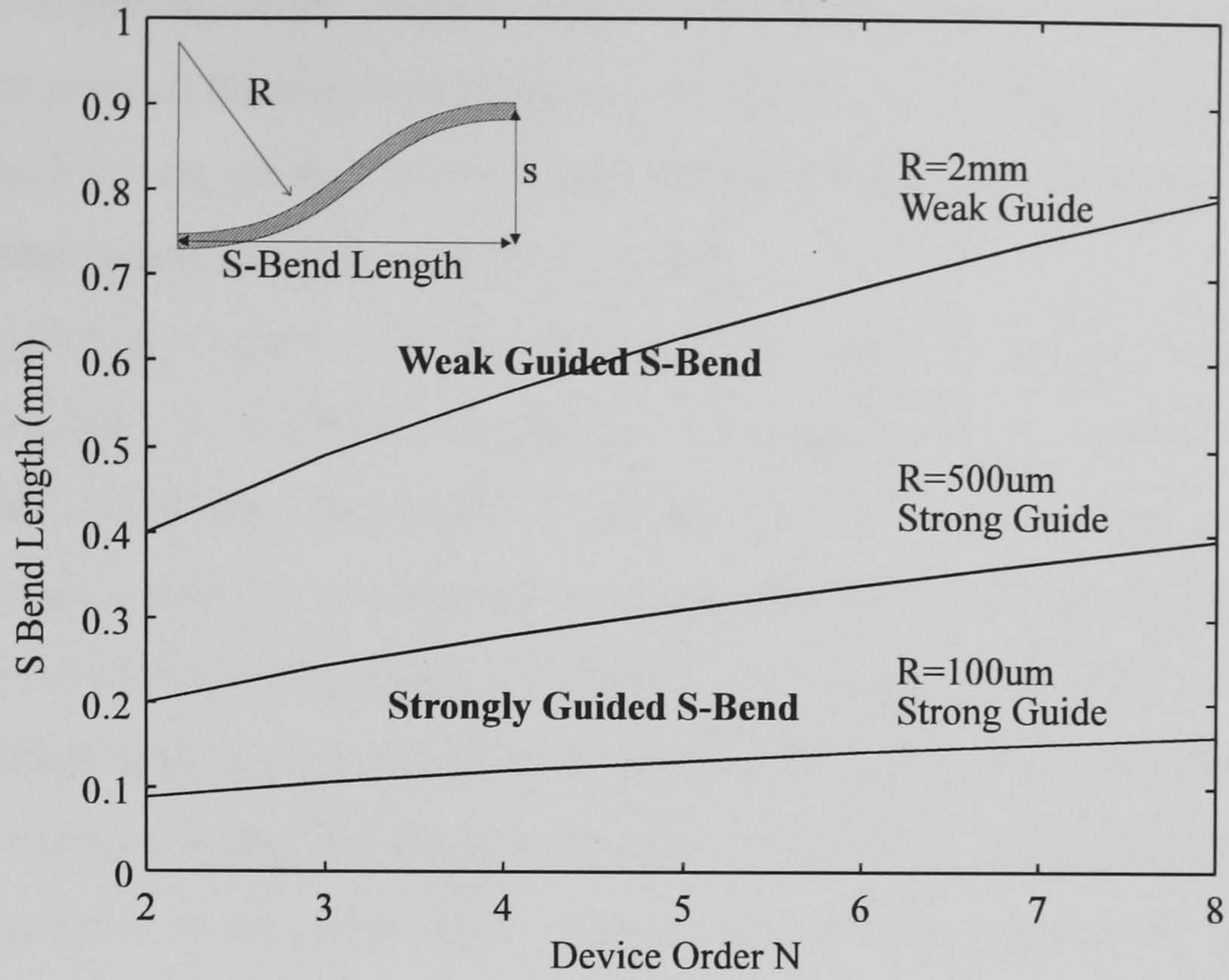

Figure 2.17 Variation of S-Bend Length as a function of Radius of Curvature

Finally, a further reduction in size of the space switch can achieved by examining the choice of optical coupler used in device design. Optical splitting can be accomplished by several integrated optical components discussed earlier, namely the directional coupler, Y-branch coupler, star coupler and the Multi-Mode Interference (MMI) coupler. However, all require waveguide S-Bends in order to separate the outputs before they are fed into the bank of electroabsorption modulators. It is found during the design of all the couplers that it is the S-Bend waveguide which generally makes the largest contribution the coupler size. Thus in order to make each coupler as small as possible it is necessary to minimise the S-bend length. This is highlighted in figure 2.17, where the S-Bend length has been calculated as a function of device order, *N*, assuming an output waveguide separation of Δ=20μm. It may be observed that there is an expected proportional relationship between radius of curvature of the S-bend and its length. It may be noted that a reduction in the radius of curvature of the S-Bend from 2mm to 100μm results in a component length saving by a factor of 5. Thus in order to attain the smallest coupler possible it is essential to use an S-Bend with the smallest radius of curvature.

However, since low loss waveguide crossings were required in the shuffle stage of the device it has been necessary to design a very weak waveguide for the crosspoint. If the same type of guide were used in the coupler, this would result in S-Bend radii of curvature of the order of 2mm, in order to reduce the loss of the bend to an acceptable level (see Chapter 4). This would therefore result in extremely large coupler sizes. Indeed they would contribute to half of the total device length. Thus in order to reduce the coupler length it is necessary to

increase the guiding strength so that the radius of curvature of the S-bend may be reduced. Fortunately, in this device, a second fabrication level already exists which can be used to increase the waveguiding in the coupler. This is required to form the TIR mirror, and is the deep etch which goes all the way through to the waveguide core. S-bend waveguides fabricated on InP, with such strong guiding have already been fabricated and have resulted with 30μm radius of curvature bends yielding negligible losses [97].

Thus compact S-bends can be integrated into the cross-connect with a negligible increase of processing, by using the deep etching required for the TIR mirror. It is found that this immediately determines the choice of coupler for use in the device, since directional couplers, Y-Branches and star couplers are not very efficient when implemented in a strongly guided waveguide. This is because they all require the evanescent tails of weakly guided modes in order to perform with low excess losses. However, the MMI coupler is perfectly suited to operating with strong guiding and many have been fabricated on InP to date [98, 99]. Indeed the coupler becomes more fabrication tolerant, polarisation insensitive and its optical bandwidth increases if deep etching is employed [100].

Deep etching of the coupler stages of the device adds other complexities to the design since efficient optical coupling must be achieved between the strong and weak guided waveguides. This is accomplished with the use of tapered mode converters, which is discussed in chapter 4.

2.5.5. Summary

Thus the motivation behind the crosspoint design drawn schematically in figure 2.13 has been discussed. From the use of TIR mirrors to make the shuffle section as compact as possible, through to the choice of the electro-absorption modulator as the key optical switch to reduce the device width, and finally the choice of deep etched MMI coupler.

The complete theoretical design of the device outlined above will be discussed in Chapter 4 which will be the main focus of this thesis. From the design of the weak waveguide to ensure low loss crossings, TIR mirror design, deep etch waveguides which are required for the MMIs and S-bend waveguides, through to mode converters which are required in order to achieve a low loss transition between the regions of strong and weak waveguiding. Following on from this analysis, chapter 5 will discuss the fabrication difficulties of constructing the crosspoint switch. Several test structures will be proposed which have been designed and fabricated in order to validate the theoretical predictions made in Chapter 4. Finally loss analysis of these test structures in chapter 6 which will enable predictions to be made on the final 4x4 crosspoint performance.

2.6 Wavelength Routing and the WDM Cross-Connect

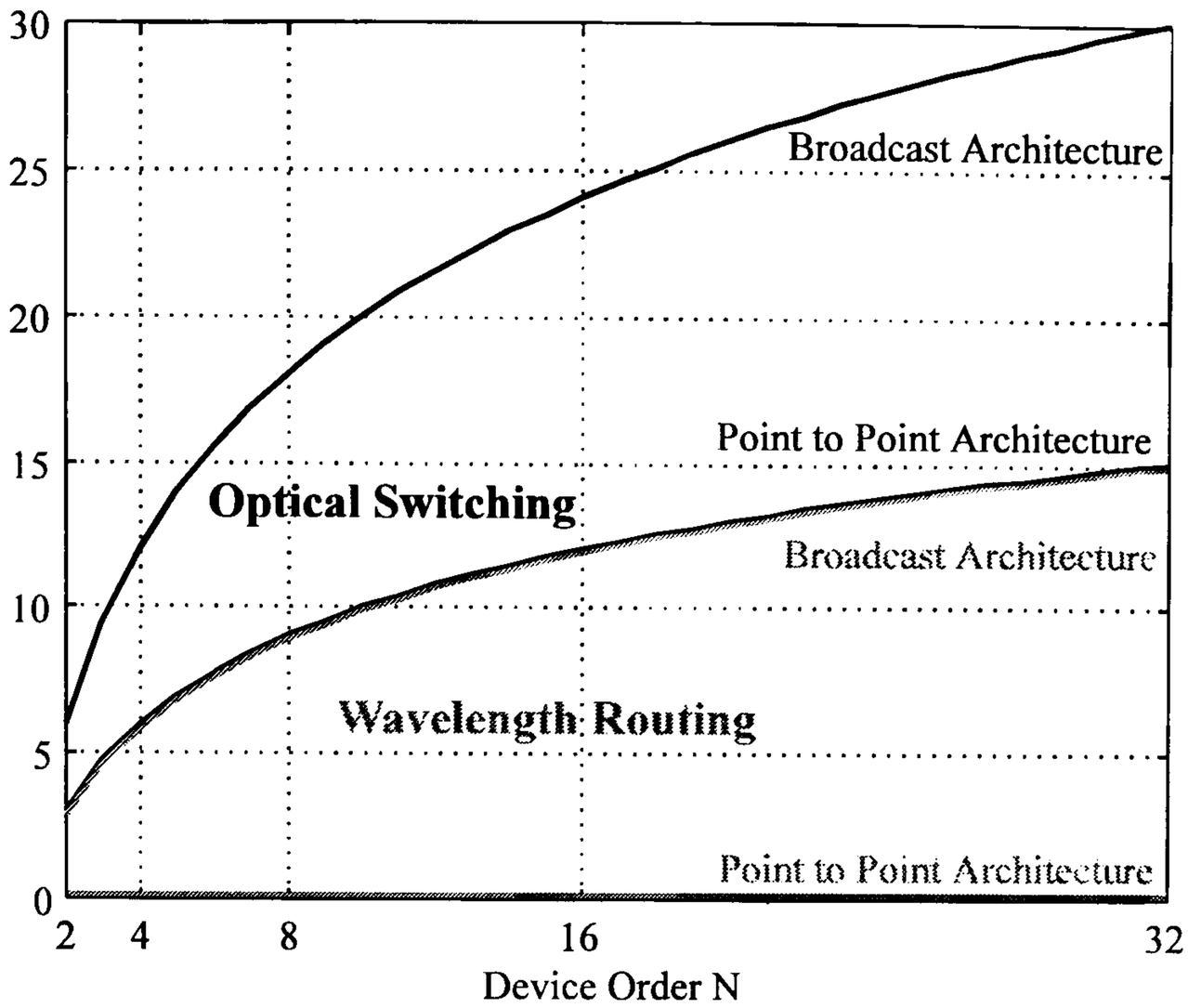

Figure 2.18 Relative Loss Merits of Physical Switching and Wavelength Routing

Up until now this discussion has been limited to achieving optical cross-connects based on the electronic analogue, whereby optical splitters, digital optical switches and a network of routing waveguides are used to form the space switch architecture. However, this has severe implications if the architecture is extended to very high device orders (>16x16), since there is an inherent loss associated with this method of switching. For a single mode cross-connect the theoretical minimum loss is plotted in figure 2.18. It may be observed, that even for a moderate optically switched broadcast architecture of $N=8$, the *theoretical* minimum loss is 18dB. This loss can be compensated for by using monolithically integrated SOAs as discussed previously (typical gain approximately 25dB [101]). However, the cascadability of these devices with many amplifier stages could be a matter of some concern. Chapter 1 has briefly discussed another method for achieving space switching, using wavelength conversion and Passive Wavelength Routing (PWR). It may be observed from figure 2.18, that a point to point PWR crosspoint offers no excess losses as a function of device order, N. As such their impact on very high order cross-connects N>32 could be great.

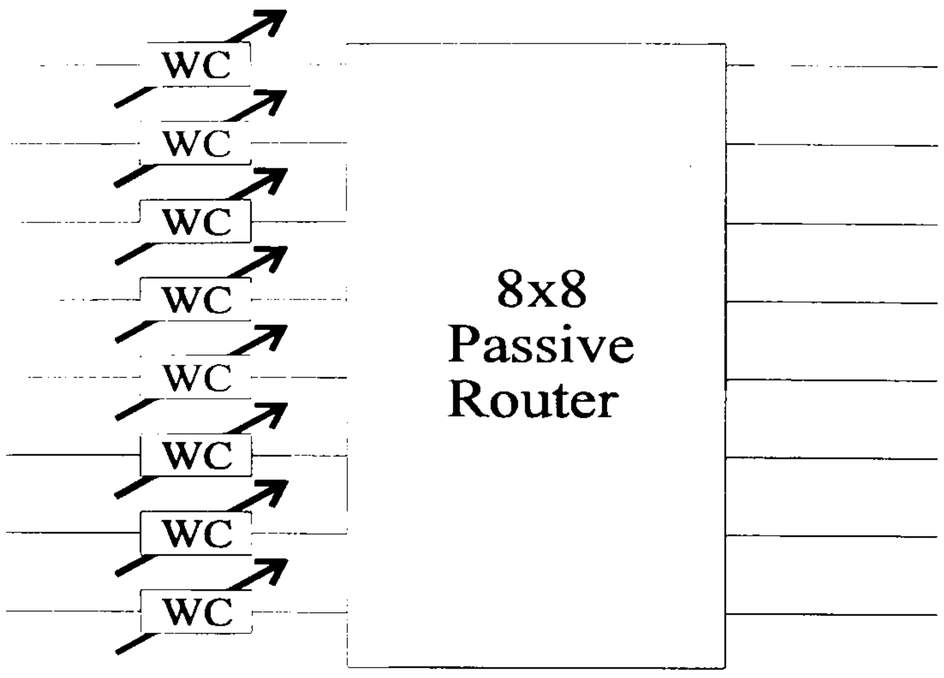

Figure 2.19 An 8x8(WC) Point to Point Wavelength Converting architecture using an 8x8 Passive Wavelength Router (PWR).

A possible 8x8(WC) version is shown schematically in figure 2.19, using this technique. One of the many attractions of this space switch is not only its scalability in terms of loss, but also in terms of fabrication. It relatively easy to fabricate high order wavelength routers, indeed up to 128 channels have so far been reported [102], with potential for even higher orders. The size of such devices is also very compact, of the order of millimetres. In order to route any input to any output, it is necessary to convert the input signal onto a wavelength that corresponds to each output of the demultiplexer. This can be achieved by the variety of different mechanisms already discussed in chapter 1. Thus, no complex interconnections are required between input and output. Instead shuffling is achieved in a transparent manner, according to the wavelength of the signal at each optical input to the router.

Owing to the many potential advantages of this technique, chapter 7 investigates a method for demonstrating wavelength routing in a monolithically integrated laser. The Multi-Channel Grating (MGC) laser developed by BT research laboratories Martlesham Heath, is used in order to demonstrate a 1x4 point to point crosspoint switch. By using gain saturation effects, wavelength conversion and routing is achieved at 2.5Gbit/s. This is currently the fastest modulation rate achieved in a monolithic integrated multi-wavelength laser.

2.7 References

[1] G. Wenger, M. Schienle, J. Berllermann, *et al* "A Completely Packaged Strictly Nonblocking 8x8 Optical Matrix Switch on InP/InGaAsP", JLT, Vol. 14, No. 10, October 1996, pp 2333-2337.

[2] E.J. Murphy, T.O. Murphy, A.F. Ambrose, R.W. Irvin, B.H.Lee, P.Peng, G.W. Richards, A. Yorinks, "16x16 strictly Nonblocking Guided-Wave Optical Switching System", JLT, Vol.14, No. 3, March 1996, pp353-358.

[3] R.A. Spankle, "Architectures for Guided-Wave Optical Space Switching Systems", IEE Com. Mag, Vol.25 No. 5, May 1987, pp42-48.

[4] R.A. Spankle, "An N-Stage planar Optical Permutation Network", Applied Optics, Vol. 26, April 1987.

[5] V.E. Benes, "Mathematical Theory of Connecting Networks and Telephone Traffic", New York Academic Press, 1965.

[6] C. Clos, "A Study of Non-Blocking Switching Networks", Bell sys. Tech, March 1953, pp407-424.

[7] R.A. Spankle, "Architectures for large Non-Blocking Optical Space Switches", IEE JQE, Vol. QE-22, June 1986, pp 964-968.

[8] R.A. Spankle, "Architectures for Guided-Wave Optical Space Switching Systems", IEE Com. Mag, Vol.25 No. 5, May 1987, pp42-48.

[9] Dietricht Marcuse "Light Transmission Optics Second Edition" Van Nostrand Reinhold Company.

[10] H.P. Chan, S.Y. Cheng, P.S. Chung, "Low Loss Wide-Angle Symmetric Y-Branch Waveguide", Electronics Letters, March 1996, Vol. 32, No. 7, pp 652-654.

[11] H. Hatami-Hanza, M.J. Leader, P.L. Chu, I.M. Skinner, "A Novel Wide-Angle Low-Loss Dielectric Slab Waveguide Y-Branch", JLT, 1994, No. 2, pp208-213.

[12] H.B. Lin, R.S. Cheng, W.S. Wang, "Wide Angle Low Loss Single mode symetric Y-Junctions", IEEE PTL, 1994, Vol. 6, No. 7, pp825-827.

[13] M. Rangaraji, M. Minkata, S. Kawakami, "Low Loss Integrated optical Y-Branch", JLT, 1989, Vol. 7, pp 753-758.

[14] K. Suziki, F. Koyama, A. Matsutani, J. Kato, T. Mukaihara, K. Iga, " Miniature Semiconductor Optical Power Splitters With Submicrometer Wide Aperature", Electronics Letters, March 1996, Vol. 32. No. 7, pp 654-655.

[15] M. Zirngibl, C. Dragone, C.H. Joyner, M. Kuznetsov, U. Koren, " Efficient 1x16 Optical Power Splitter Based on InP", Electronics Letters, June 1992, Vol. 28, No. 13, pp 1212-1213.

[16] C. Dragone "Efficient NxN Star Couplers using Fourier Optics", JLT March 1989, Vol. 7, No. 3, pp 479-489.

[17] C. Dragone, C.H. Henry, I.P. Kaminow,R.C. Kistler, "Efficient Multichannel Integrated Optics Star Coupler on Silicon", IEEE PTL, 1989, Vol. 1, pp241-243.

[18] L.B. Soldano, E.C.M. Pennings, "Optical Multi-Mode Interference Devices Based on Self-Imaging: Principles and Applications" JLT Vol. 13, No. 4 April 1995, pp615-627.

[19] M. Bachmann, P.A. Besse and H. Melchior, "Overlapping-image multimode interference couplers

with a reduced number of self-images for uniform and nonuniform power splitting" Applied Optics Vol.34 No. 30 1995, pp6898-6910.

[20] P.A. Besse, M. Bachmann, H. Melchior, L.B. Soldano, M.K. Smit "Optical Bandwidth and Fabrication Tolerances of Multimode Interference Couplers" JLT Vol. 12 No. 6 1994, pp1004-1007.

[21] L.H. Spiekmann, Y.S. Oei, E.G. Metaal, F.H. Groen, I. Moerman, M.K. Smit, "Extremely small Multimode Interference couplers and Ultrashort Bends on InP by Deep Etching", IEEE PTL Vol. 6, No. 8 August 1994 pp1008-1010.

[22] N. Keil, H.H. Yao, C. Zawadzki, "Polymer Waveguide Optical Switch With Less Than -40dB Polarization-Independent Crosstalk", Electronics Letters, 1996, Vol.32, No.7, pp.655-657

[23] N. Keil, H.H. Yao, C. Zawadzki, "(2x2) Digital Optical Switch Realized By Low-Cost Polymer Waveguide Technology", Electronics Letters, 1996, Vol.32, No.16, pp.1470-1471

[24] T.H. Wood, "Multiple Quantum Well (MQW) Waveguide Modulators", JLT, Vol. 6, No. 6, June 1988, pp 743-757.

[25] G.P Agrawal, N.P Dutta, "Semiconductor Lasers Second Edition", Van Nostrnad Reinhold pp 536..

[26] T.H. Wood et al "High-Speed Modulation with GaAs/AlGaAs quantum wells in a p-i-n Diode Structue", Appl. Phys. Lett. Vol. 44, 1984, pp 16-20.

[27] D.A.B Miller et al "Band-Edge Electroabsorption in Quantum Well Structures : The Quantum Confined Stark Effect", Phys. Rev. Lett, Vol. 53, 1984, pp2173-2175.

[28] D.A.B Miller et al "Electric Field Dependance of Optical Absorption Near the Bandgap of Quantum-Well Structures", Phys. Rev. B, Vol.32, 1985, pp1043-1051.

[29] R. Dingle, "Confined Carrier States in Ultra-thin Semiconductor Heterostructures", Advances in Solid State Physics 15, Vol. 21, 1975.

[30] T.H. Wood, "Multiple Quantum Well (MQW) Waveguide Modulators", JLT, Vol. 6, No. 6, June 1988, pp 743-757.

[31] A. McKee, C.J. McLean, G. Lullo, A.C. Bryce, R.M. De La Rue, J.H. Marsh, C.C. Button, "Monolithic Integration in InGaAs-InGaAsP multiple-Quantum-Well Structures Using Laser Intermiximg" IEEE JQE, Vol. 33, No. 1, January 1997, pp45-55.

[32] K. Hamamoto, K. Komatsu, "Insertion-loss free 2x2 InGaAsP/InP optical Switch Fabricated using Bandgap Energy Controlled Selective MOVPE", Elec. Lett Vol. 31 No. 20, Spetember 1995, pp 1779-1781.

[33] A. W. Nelson *et al* "The role of MOVPE in the Manufacture of High Performnace InP Based Optoelectronic Devices", J. Crystal Growth, Vol. 93, 1988, pp792-802.

[34] P. Bachmann, H. Kaufman, "GaAs Single-mode rib Waveguides with Reactive Ion-Etched Totally Reflecting Corner Mirrors", JLT, 1985, No. 3, pp785-788.

[35] L. Faustini, C. Coriasso, A. Stano, C. Cacciatore, D. Campi, "Loss Analysis and Interference Effect in Semiconductor Integrated Waveguide Turning Mirrors", IEEE PTL, Vol. 8, No. 10, October 1996 pp1355-1357.

[36] E. Gini, G. Guekos, H. Melchior, "Low Loss Corner Mirrors with 45° Deflection Angle for Integrated Optics", Elec. Lett. Vol. 28, No. 5, Febuary 1992, pp 499-500.

[37] D.L. Lee, "Electromagnetic Principles of Optics", John Wiley& Sons, pp67.

[38] A. Ajisawa, M. Fujiwara, J. Shimizu, M. Sugimoto, M. Uchida,Y Ohta, "Monolithically Integrated Optical Gate 2x2 Matrix Switch Using GaAs/AlGaAs Multiple Quantum Well Structure", Electronics Letters, 1987, Vol.23, No.21, pp.1121-1122.

[39] C. Wuthrich, F.K. Reinhart, W. Baer, J. Faist, "Low-Drive-Voltage, "Low-Loss AlGaAs/GaAs 2x2 Switch" Electronics Letters, 1988, Vol.24, No.16, pp.1047-1048

[40] H. Okayama, M. Kawahara, "Low-Crosstalk 2x2 Digital Optical Switch", Electronics Letters, 1994, Vol.30, No.5, pp.403-405

[41] M. Abe, T. Kitagawa, K. Hattori, A. Himeno, Y. Ohmori "Electrooptic Switch Constructed With A Poled Silica-Based Waveguide On A Si Substrate", Electronics Letters, 1996, Vol.32, No.10, Pp.893-894.

[42] A. Mcguire, M. Scott, A.P. Thomas, R.C. Booth, "Practical Low-Voltage 2x2 Polarization Independent $LiNbO_3$ Digital Optical Switch", Electronics Letters, 1991, Vol.27, No.12, pp.1025-1026.

[43] Y. HIda, H. Onose, S. Imamura, "Polymer Waveguide Thermooptic Switch with Low Electric Power Consumption at 1.3μm", IEEE PTL, Vol.5 No. 7, July 1993, pp 873-784.

[44] N. Keil, H.H. Yao, C. Zawadzki, "Polymer Wave-Guide Optical Switch With Less-Than-40dB Polarization-Independent Crosstalk", Electronics Letters, 1996, Vol.32, No.7, pp.655-657

[45] N. Keil, H.H. Yao, C. Zawadzki, "(2x2) Digital Optical Switch Realized By Low-Cost Polymer Waveguide Technology", Electronics Letters, 1996, Vol.32, No.16, pp.1470-1471.

[46] S.G. Han, H.I. Lee, M.H. Lee, H.J. Lee, H.Y. Kim, Y.H. Won, "High-Performance 2x2 Polymeric Electrooptic Switch With Modified Bifurcation Optically-Active Wave-Guide Structure", Electronics Letters, 1996, Vol.32, No.21, pp.1994-1995

[47] W.Y. Hwang, M.C. Oh, H.M. Lee, H. Park, J.J. Kim, "Polymeric 2x2 Electrooptic Switch Consisting Of Asymmetric Y Junctions And Mach-Zehnder Interferometer", IEEE Photonics Technology Letters, 1997, Vol.9, No.6, pp.761-763

[48] I.H. White, J.J.S. Watts, J.E. Carroll, C.J. Armistead, D.J. Moule, J.A. Champelovier, "InGaAsP 400x200um Active Crosspoint Switch Operating at 1.5um using novel Reflective Y-Branch Coupler Components", Electronics Letters, May 1990, Vol. 26, No. 10, pp 617-618.

[49] M.G. Young, U. Koren, B.I. Miller, M. Chien, M.A. Newkirk, J.M. Verdiell, "A compact 2x2 Amplifier Switch with Integrated DBR LAsers Operating at 1.55μm", IEEE PTL, Vol. 4, No. 9, September 1992, pp 1047-1049.

[50] M. Janson, L. Lundgren, A.C. Morner, M. Rask, B. Stoltz, M. Gustavsson, L. Thylen, "Monolithically Integrated 2x2 InGaAsP/InP Laser-Amplifier Gate Switch Arrays", Electronics Letters, 1992, Vol.28, No.8, pp.776-778.

[51] G. Glastre, D. Rondi, A. Enard, E. Lallier, R. Blondeau, M. Papuchon, "Monolithic Integration Of 2x2 Switch And Optical Amplifier With 0dB Fiber To Fiber Insertion Loss Grown By LP-MOVCD", Electronics Letters, 1993, Vol.29, No.1, pp.124-126.

[52] T. Kirihara, M. Ogawa, H. Inoue, K. Ishida, "Lossless And Low-Crosstalk Characteristics In An InP-Based 2x2 Optical Switch", IEEE Photonics Technology Letters, 1993, Vol.5, No.9, pp.10591061.

[53] J.D. Burton, P.J. Fiddyment, M.J. Robertson, P. Sully, "Monolithic InGaAs-InP Amplifier Gate Switch Matrix", IEEE JQE, No. 6, Vo. 29, June 1993, pp 2023-2027.

[54] G. Sherlock, J.D. Burton, P.J. Fiddyment, P.C. Sully, A.E. Kelly, M.J. Robertson, "Integrated 2x2 Optical Switch with Gain", Electronics Letters , January 1994, Vol. 30, No. 2, pp 137-138.

[55] K. Kawano, M. Kohtoku, N. Yoshimoto, S. Sekine, Y. Noguchi, "2x2 InGaAlAs/InAlAs Multiquantum-Well (MQW) Directional Coupler Wave-Guide Switch Modules Integrated With Spotsize Converters", Electronics Letters, 1994, Vol.30, No.4, pp.353-355.

[56] K. Hamamoto, K. Kamatsu, "Insertion Loss Free 2x2 InGaAsP/InP Optical Switch Fabricated Using Bandgap Energy Controlled Selective MOVPE", Electronics Letters, Vol. 31, No. 20, September 1995, pp 1779-1780.

[57] N. Agrawal, C.M. Weinert, H.I. Ehrke, G.G. Mekonnen, D. Franke, "Fast 2x2 Mach-Zehnder Optical Space Switches Using InGaAsP-InP Multi-Quantum-Well Structures", IEEE Photonics Technology Letters, 1995, Vol.7, No.6, pp.644645

[58] F. Dorgeuille, B. Mersali, T. Feuillade, S. Sainson, J. Brandon, S. Slempkes, M. Carre, "Monolithic InGaAsP-InP Tapered Laser-Amplifier Gate 2x2 Switch Matrix With Gain", Electronics Letters, 1996, Vol.32, No.7, pp.686-688.

[59] F. Dorgeuille, B. Mersali, T. Feuillade, S. Sainson, S. Slempkes, M. Foucher, "Novel Approach for Simple Fabrication of High-Performance InP switch Matrix Based on Laser Amplifier Gates", IEEE PTL , Vol. 8, No. 9, September 1996, pp 1178-1180.

[60] J. Leuthold, J. Eckner, C. Holtmann, R. Hess, H. Melchior, "All-Optical 2x2 Switches With 20dB Extinction Ratios", Electronics Letters, 1996, Vol.32, No.24, pp.2235-2236

[61] K.R. Oh, J.H. Ahn, J.S. Kim, S.W. Lee, H.M. Kim, K.E. Pyun, H.M. Park, "2x2 InGaAsP/InP Laser-Amplifier Gate Switch Arrays Using Reactive Ion Etching", Electronics Letters, 1996, Vol.32, No.1, pp.39-40.

[62] G.A. Bogert, E.J. Murphy, R.T. Ku, "Low Crosstalk 4x4 Ti:$LiNbO_3$ Optical Switch With Permanently", Journal Of Lightwave Technology, 1986, Vol.4, No.10, pp.1542-1545

[63] P. Granestrand, B. Lagerstrom, P. Svensson, L. Thylen, B. Stolz, K. Bergvall, H. Olofsson, "Tree Structures Poaraisation Independent 4x4 Switch Matrix In $LiNbO_3$", Electronics Letters, September 1988, Vol. 24, No. 19, pp1199-1200.

[64] H. Nishimoto, S.Suzuki, M. Kondo, "Polarisation Independent $LiNbO_3$ 4x4 Matrix Switch", Electronics Letters, September 1988, Vol. 24, No. 188, pp1122-1123.

[65] P. Granestrand, B. Lagerstrom, P. Svensson, L. Thylen, B. Stoltz, "Integrated-Optics 4x4 Switch Matrix With Digital Optical Switches" Electronics Letters, 1990, Vol.26, No.1, pp.4-5

[66] Y. Yamada, H. Terui, Y. Ohmori, M. Yamada, A. Himerno, M. Kobayashi, "Hybrid Integrated 4x4 Optical Gate Matrix Switch Using Silica Based Optical Waveguide and LD Array Chips", JLT, Vol. 10, No. 3, March 1992, pp 383-389.

[67] N. Keil, H.H. Yao, C. Zawadzki, B. Strebel "4x4 Polymer Thermooptic Directional Coupler Switch At 1.55μm", Electronics Letters, 1994, Vol.30, No.8, pp.639-640.

[68] N. Keil, H.H. Yao, C. Zawadzki, B. Strebel, "Rearrangeable Nonblocking Polymer Wave-Guide

Thermooptic 4x4 Switching Matrix With Low-Power Consumption At 1.55μm" Electronics Letters, 1995, Vol.31, No.5, pp.403-404

[69] K. Komatsu, K. Hamamoto, M. Sugimoto, A. Ajisawa, Y. Kohga, A. Suzuki, "4x4 GaAs/AlGaAs Optical Matrix Switches with uniform Device Characteristics Using Alternating Electrooptic Guided Wave Directional Couplers", JLT, July 1991, Vol. 9, No. 7, pp 871-878.

[70] K. Hamaoto, S. Sugou, K. Komatsu, M. Kitamura, "Extremely Low Loss 4x4 GaAs/AlGaAs Optical switch Matrix", Electronics Letters, August 1993, Vol. 29, No. 17, pp 1581-1582.

[71] D.K. Probst, L.G. Perrymore, B.C. Johnson, R.J. Blackwell, J.A. Priest, "Demonstration Of An Integrated, Active 4x4 Photonic Crossbar", IEEE Photonics Technology Letters, 1992, Vol.4, No.10, pp.1139-1141

[72] S. Oku, Y. Shibata, T. Takeshita, M. Ikeda, "Lossless operation of 4x4 laser diode optical gate switches using Y reflection type branching/combining circuits for large-scale integration" IEE Proceedings-Optoelectronics, 1997, Vol.144, No.2, pp.61-68

[73] M. Gustavsson, B. Lagerstrom, L. Thylen, M. Janson *et al*, " Monolithically Integrated 4x4 InGaAsP/InP Laser Amplifier Gate Switch Arrays", Electronics Letters, November 1992, Vol. 28, No. 24, pp 2223-2224.

[74] W. van Berlo, M. Janson, L. Lundgren *et al* "Polarisation Insesitive Monolithic 4x4 InGaAsP-InP Laser Amplifier Gate Switch Matrix", IEEE PTL, Vo. 9, No. 11, November 1995, pp1291-1293.

[75] H. Takeuchi, Y. Hasumi, S. Kondo, Y. Noguchi "4x4 Directional Coupler Switch Matrix With An InGaAlAs/InAlAs Multiquantum-Well Structure", Electronics Letters, 1993, Vol.29, No.6, pp.523-524

[76] T. Kirihara, M. Ogawa, H. Inoue, H. Kodera, K. Ishida, "Lossless and Low Crosstalk Characteristics in an InP-Based 4x4 Optical switch With Integrated single Stage Optical amplifiers", IEEE PTL, Febuary 1994, Vol. 6, No. 2, pp 218-221.

[77] K. Kawano, S. Sekine, H. Takeuchi, M. Wada, M. Kohtoku, N. Yoshimoto, "4x4 InGaAlAs/InAlAs MQW Directional Coupler Wave-Guide Switch Modules Integrated With Spot-Size Converters And Their 10Gbit/S Operation", Electronics Letters, 1995, Vol.31, No.2, p.96-97.

[78] K. Hamamoto, T. Anan, K. Komatsu, M. Sugimoto, H. Mito, "First 8x8 Semiconductor Optical Matrix Switches Using GaAs/AlGaAs Electrooptic Guided wave Directional Couplers", Electronics Letters, Febuary 1992, Vol. 28, No. 5, pp 441-442.

[79] R. Nagase, A. Himeno, M. Okuno, K. Kato, K. Yukimatsu, M. Kawachi, "Silica-Based 8x8 Optical Matrix Switch Module With Hybrid Integrated Driving Circuits And Its System Application", Journal Of Lightwave Technology, 1994, Vol.12, No.9, pp.1631-1639.

[80] M. Okuno, K. Kato, Y. Ohmori, M. Kawachi, T. Matsunaga, "Improved 8x8 Integrated Optical Matrix Switch Using Silica-Based Planar Lightwave Circuits" Journal Of Lightwave Technology, 1994, Vol.12, No.9, pp.1597-1606

[81] P. Granestrand, B. Stoltz, L. Thylen, K. Bergvall, W. Doldissen, H. Heinrich, D. Hoffmann, "Strictly Nonblocking 8x8 Integrated Optical siwtch Matrix", Electronics Letters, July 1986, Vol.22 No. 25. pp 816-818.

[82] P.J. Duthie, M.J. Wale, "Rearrangeably Nonblocking 8x8 Guided Wave Optical Switch", Electronics

Letters, Vol. 24, No. 10, pp 594-596.

[83] A. Matoba, H. Okayama, R. Shibuya, T. Ishida, "Low Drive Voltage 8x8 Ti:$LiNbO_3$ Switch with simplified tree structre", Electronics Letters, January 1989, Vol. 25, No. 2, pp 165-166.

[84] H. Nishinoto, M. Iwasaki, S. suzuki, M. Kondo, "Polarisation Independent $LiNbO_3$ 8x8 Matrix Switch2, IEEE PTL Vol. 2, No. 9, September 1990, pp 634-636.

[85] J.E. Watson, M.A. Milbrodt, K. Bahadori, M.F. Dautartas *et al* "A Low-Voltage 8x8 Ti-$LiNbO_3$ Switch With A Dilated-Benes Architecture", Journal Of Lightwave Technology, 1990, Vol.8, No.5, pp.794-801

[86] A. Karroy, C.S. Tsai, "8x8 Symmetrical Nonblocking Integrated Acousto-optic Space Switch Module On $LiNbO_3$", IEEE Photonics Technology Letters, 1992, Vol.4, No.7, pp.731-734

[87] P.Granestrand, B. Lagerstrom, P. Svensson, H. Olofsson, J.E. Falk, B. Stolz, "Pigtailed Tree-Structures 8x8 $LiNbO_3$ Switch Matrix with 112 Digital Optical Switches", IEEE PTL, Vol. 6, No. 1, January 1994, pp 71-73.

[88] P.J. Duthie, M.J. Wale, "16x16 Single Chip Switch array in Lithium Niobate", Electronics Letters, July 1991, No. 14, Vol. 27, pp 1265-1267.

[89] H. Okayama, M. Kawahara, "Prototype 32x32 Optical Switch Matrix", Electronics Letters, 1994, Vol.30, No.14, pp.1128-1129

[90] M.Gibbon, G.H.B Thompson, S.J. Clements, D.J. Moule, C.B. Rogers, C.G. Cureton 'Optical Performance of Integrated 1.5μm Grating Wavelength-Demultiplexer on InP-Based Waveguide' Electronic Letters, Vol. 25, No. 21 pp 1441-1442, 1989.

[91] Private Communication with Dr. M.J. Robertson, Head of Optoelectronics Research, BT Research Laboratories Martlesham Heath, Ipswich.

[92] J.D. Burton, P.J. Fiddyment, M.J. robertson, P.Sully, "Monolithic InGaAsP-InP Laser Amplifier Gate Switch Matrix", IEEE JQE, Vol. 29, No. 6, June 1993, pp 2023-2030.

[93] T.P. Pearsall (editor), "GaInAsP Alloy Semiconductors", John Wiley & Sons, 1982 pp395.

[94] G.P Agrawal, N.P Dutta, "Semiconductor Lasers Second Edition", Van Nostrand Reinhold pp 92.

[95] U. Koren, B.I. Miller *et al* "Polarisation Insensitive Semiconductor Optical amplifier with Integrated Electroabsorption Modulators", Electronics Letters, January 1996, Vol. 32, No. 2, pp111-113.

[96] A Ramdane, F. Devaux, N. Souli, D. Delprat, A. Ougazzaden, "Monolithic integration of Multiple-Quantum-Well Lasers and Modulator for High-Speed Transmission", IEEE Journal of Selected Topics in Quantum Electrnoics, June 1996, Vol. 2, No. 2, pp326-335.

[97] L.H. Spiekman, Y.S. Oei, E.G. Metaal, F.H. Groen, P. Demeester, M.K. Smit, "Ultrasmall waveguide bends : the corner mirrors of the future ?" IEE Proc Opt. Vol. 142, No. 1, Febuary 1995 pp61-65.

[98] P.A. Besse, M. Bachmann, H. Melchior, L.B. Soldano, M.K. Smit "Optical Bandwidth and Fabrication Tolerances of Multimode Interference Couplers" JLT Vol. 12 No. 6 1994, pp1004-1007.

[99] L.H. Spiekmann, Y.S. Oei, E.G. Metaal, F.H. Groen, I. Moerman, M.K. Smit, "Extremely small Multimode Interference couplers and Ultrashort Bends on InP by Deep Etching", IEEE PTL Vol. 6, No. 8 August 1994 pp1008-1010.

[100] L.B. Soldano, E.C.M. Pennings, "Optical Multi-Mode Interference Devices Based on Self-Imaging: Principles and Applications" JLT Vol. 13, No. 4 April 1995, pp615-627.

[101] J.D. Burton, P.J. Fiddyment, M.J. Robertson, P.C. Sully, "Monolithic InGaAsP-InP Laser Amplifier Gate switch Matrix", IEE JQE, Vol. 29, No. 6, June 1993, pp2023-2027.

[102] "Fabrication of a 128 channel AWG Multiplexer with 25GHz Channel spacing", Electronics Letters 1996, No. 32, Vol. 16, pp474-475

Monolithic Integration of Optical Space Switches

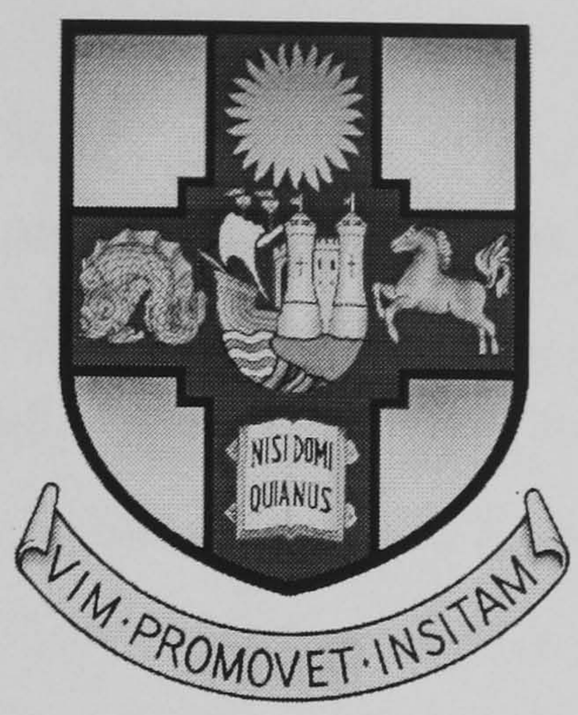

Chapter 3

3.1 Theoretical Design of a Novel NxN Two Dimensional Integrated Optical Crosspoint Switch Architecture

---

A novel Two Dimensional Integrated Optical (2DIO) crosspoint switch architecture is proposed for the InGaAsP/InGaAs/InP material system, which is achieved by the use of novel 2DIO beam splitters. A Modal Propagation Model (MPM) is used to optimise device size, loss and crosstalk and study beam propagation in a 2DIO slab waveguide. Theoretical results show that a lossless 4x4 2DIO crosspoint device less than 2x2mm^2 in size is predicted to exhibit less than -40dB crosstalk.

3.2 Introduction and Motivation

The ability to switch optical data between a number of optical fibres, *N*, is required in many WDM and ATM networking schemes. This can be performed by the strictly non-blocking *N*x*N* crosspoint switch [1] which will be an essential part of many future photonic communication systems. It is desirable to perform the switching in the optical rather than electrical domain in order to overcome electronic bottlenecks at high data rates. This has led to the development of many optical crosspoint devices [2-6]. Each use a variety of switch architectures (crossbar [2],tree [3,4], simplified tree [5,6]) to perform the crosspoint logic. However, all the architectures are similar in that they must provide at ***least once*** a *split*, *shuffle & switch* and *combine* of inputs. Thus at some point in the switching architecture there is a need for optical paths to cross. The number of crossings dramatically increasing with switch order *N* and architecture complexity [1].

To date all integrated optical crosspoint development has concentrated on an integrated waveguide approach. In these devices large numbers of waveguide crossings are undesirable since they increase the path loss and crosstalk [7]. This is not a serious problem at very low switch orders i.e. *N*=2. However as *N* is increased it is advantageous to use networking schemes that minimise crossings [1]. However, in Two Dimensional Integrated Optics (2DIO) light propagates in a slab waveguide with no lateral guiding [8], deep etched mirror structures [9] are then used to manipulate the beam in the slab. Owing to the unguided nature of the propagating modes, crossing optical paths suffer a negligible crosstalk and loss penalty [10]. Thus the realisation of a high order 2DIO crosspoint switch could offer many advantages over the conventional integrated waveguide approach.

3.3 2DIO Crosspoint Architectures

A schematic drawing of a 2x2 2DIO crosspoint is shown in figure 3.1a and extended to *N*x*N* in figure 3.1b. The material system considered is InGaAsP/InGaAs/InP operating at a wavelength of 1.55μm. Light enters the device through input waveguides where it is injected into the 2DIO slab waveguide, and is free to diverge until it is collimated by parabolic mirrors. The mirror equations being traced by the dotted lines (figure 3.1a). The collimated light then enters the **mirror matrix**. This consists of N^2 *planar* truncating mirrors which simultaneously *split* and *shuffle* the inputs to every output. The architecture used is an extension of a tree structure and the device therefore operates as a broadcast network i.e. every input can be switched to any output [1]. The light then passes through an array of spatial filters (deep etches) which are angled in order to stop reflections back into the mirror matrix. This reduces the

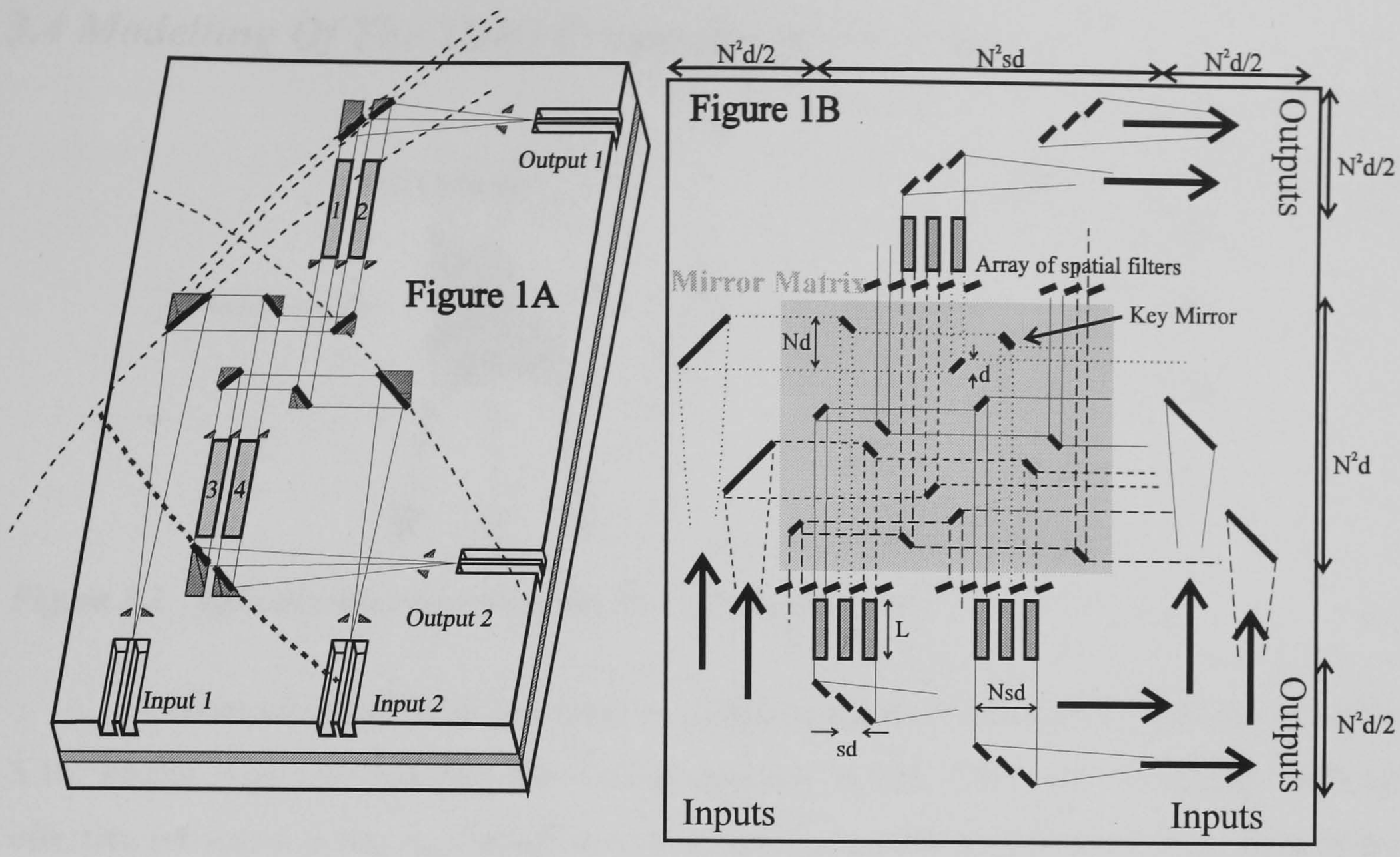

Figure 3.1 *a : 2x2 2DIO crosspoint switch -perspective view.*
b : A generalised NxN crosspoint architecture - plan view.

device crosstalk before the signal passes through a bank of broad area amplifier gate switches (shaded regions). The amplifiers allow the inputs to be routed to each output while providing gain to compensate for the intrinsic device loss. Each switched input is then focused down to the output waveguides via *N* parabolic output mirrors, which may be thought of as a novel type of 2DIO mirrored star coupler.

The 2DIO crosspoint has many advantages over current crosspoint devices. Since the crossing of optical paths is acceptable, an architecture can be used which can reduce the switch size by maximising the number of crossings. Also, only three mirrors per path are required regardless of the device order, *N*. Thus the 2DIO crosspoint has the potential for low loss and scalability. In comparison, a current optical waveguide device may have a multitude of couplers, Total Internal Reflecting (TIR) mirrors or waveguide bends through one optical path.

However, owing to the unguided nature of the propagating optical modes in the 2DIO approach, the mirror matrix must be designed carefully in order to avoid crosstalk between different input channels. The novel method of splitting and shuffling input beams through the matrix also requires a detailed analysis of beam truncation which has been investigated using a 2DIO beam propagation model.

3.4 Modelling Of The 2DIO Crosspoint Architecture

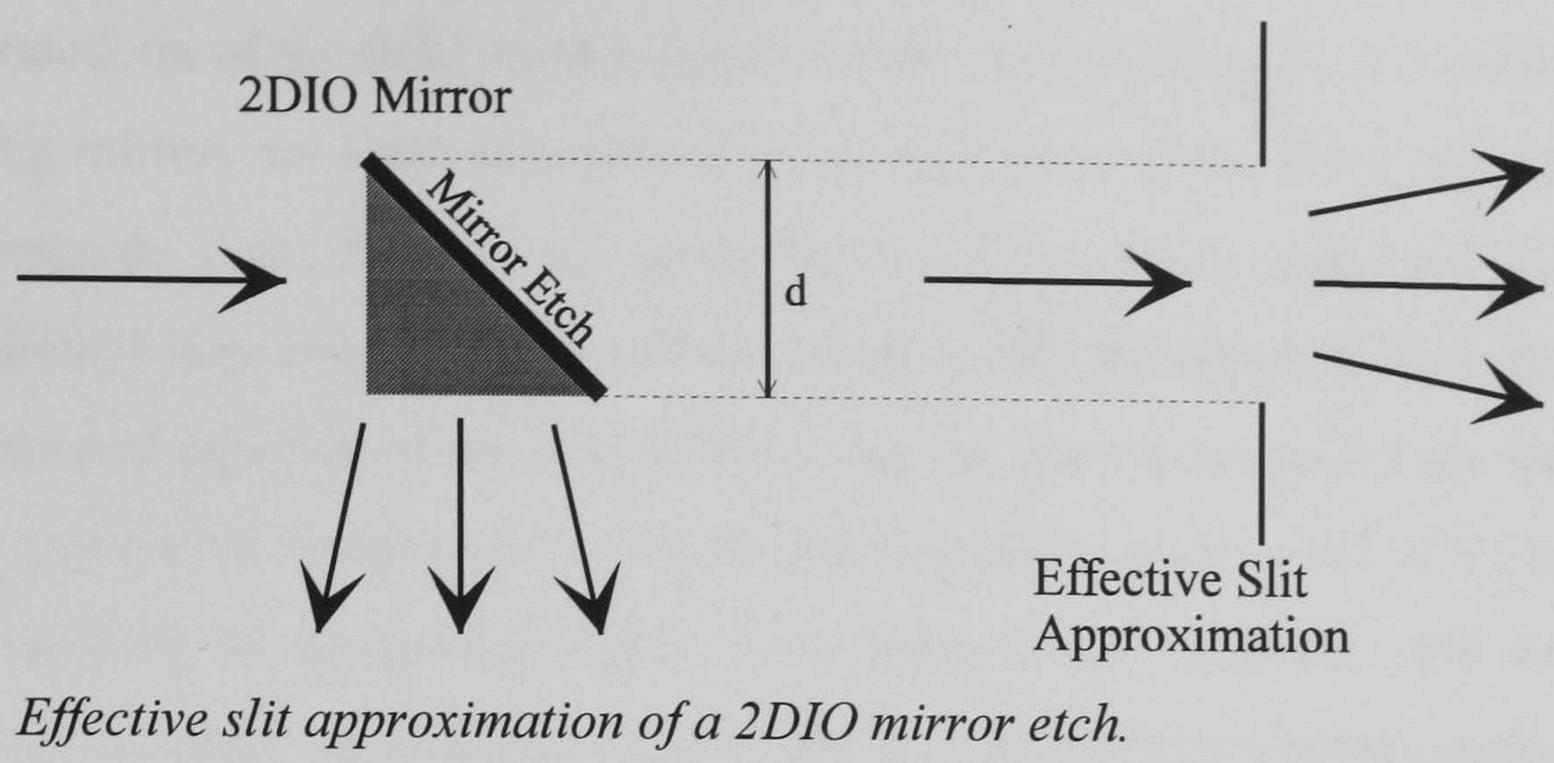

Figure 3.2 Effective slit approximation of a 2DIO mirror etch.

A series of assumptions are made in analysing the *N*x*N* crosspoint illustrated in figure 3.1b. Firstly it is assumed that the light propagates in the 2DIO slab waveguide with an effective refractive index, n_{eff}, which is used to account for the confinement of the light in the vertical plane. Secondly, the mirrors can be approximated to effective slits as shown in figure 3.2. This assumption is valid provided that the mirrors have no surface roughness, and there is negligible diffraction over the area of the mirror i.e. shaded region of figure 3.2.

The analysis may then be greatly simplified by only considering the longest path through the device, labelled the '*key mirror*'. It is this input/output path which will ultimately determine the performance, since all other paths with suffer considerably less divergence in the mirror matrix. The architecture may then be redrawn in block form (figure 3.3), this separates the device optimisation into 4 main categories. These are discussed independently as follows.

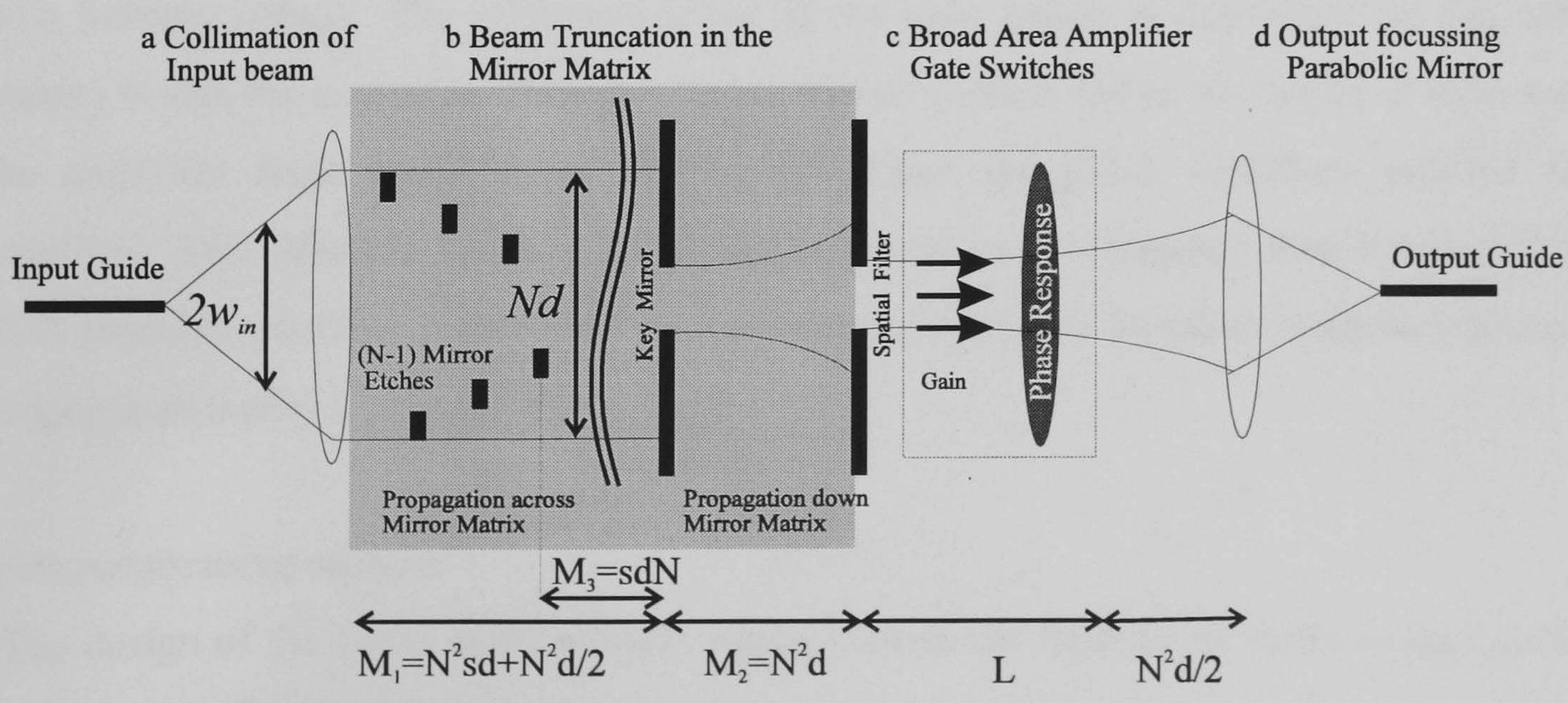

Figure 3.3 Block Diagram for the key mirror path of the 2DIO Crosspoint device

(a) Collimation of the input beam

The electromagnetic field collimated by the input parabolic mirror can be calculated by the Fourier transform of the field propagating from the input waveguide. It is assumed that the collimating mirrors are large enough to prevent truncation of the diverging beam from the input waveguide. Also, that they can be designed so that a beam of any FWHM (full width half maximum) may be collimated onto the mirror matrix by adjusting the position of input waveguides and equation of the mirror. Providing the input waveguides are weakly guided and only support the fundamental mode, the field incident on one input of the mirror matrix can be assumed to be gaussian [11]. This immediately simplifies the mirror matrix optimisation to solely analysing truncation effects of an input zero order gaussian field with arbitrary FWHM.

(b) Beam Truncation in the mirror matrix

The truncation effects of the mirror matrix are given by the solution of the wave-equation subject to the boundary conditions imposed by the mirrors. A modal propagation model (MPM) has been written in order to determine the propagating electromagnetic field after each truncation. These results are discussed in *Section 3.5*.

(c) Broad Area Amplifier Gate Switches

It is proposed that the intrinsic device loss can be compensated by the use of broad area amplifier gate switches. However, owing to the finite aperture of each amplifier, diffraction ripples will occur in the field distribution within it. These ripples would in turn lead to complex transverse carrier density profiles across the amplifier width (bat ears [12]), due to hole burning effects. The refractive index of the gain region is dependent on the carrier density inside the amplifier. Thus this lateral spatial dependence on the speed of light across the amplifier facet would result in complex transverse phase variations emitted from amplifier. The effective focusing of the output signal to a waveguide then becomes lossy. This potential problem is analysed by a combination of rate equation analysis and modal propagation theory in *Section 3.6.*

(d) Output focusing mirrors.

The design of the novel 2DIO coupler which focuses the light down to the output guide is discussed in *Section 3.7.*

3.5 Theoretical Analysis Of The Mirror Matrix

3.5.1 The truncation of a plane wave

In order to optimise the splitting and shuffling action of the mirror matrix, the concept of beam truncation in a slab waveguide must first be examined. Initially the truncation of a *plane* wave by an effective slit is studied. This permits validation of the MPM and reveals some initial insight into the problem of beam truncation.

Consider a plane wave with an effective slab wavelength of $\lambda_{eff,} = \lambda_0/n_{eff}$ incident on a slit of width *d*. Initially a first order approximation can be used in order to determine roughly the propagation after truncation [13]. This involves mode matching a zero order Hermite Gaussian beam (Appendix B) to the field at the slit by maximising the overlap integral $\Sigma(w_0)$, described by the function

$$\Sigma(w_0) = \int_{-\infty}^{\infty} \phi(x)\Psi^*(x, w_o, z=0)dx \tag{3.1}$$

where $\phi(x)$ *is* the *normalised* field at the slit, and $\Psi(x,w_{0,z=0})$ is a *normalised* zero order Hermite Gaussian with beam waist w_0. [13] For an incident plane wave, as discussed here, the calculation yields a Gaussian beam waist of

$$w_{0\approx} d/2. \tag{3.2}$$

Thus the truncation can be represented, to a first approximation, by a zero order Gaussian, emanating from the slit, with a waist $w_{0\approx} d/2$.

By including higher order Hermite Gaussian terms a more accurate propagation can be determined, which results in the MPM calculation plotted in figure 3.4. By scaling the x-axis to *d*, and the y-axis by a factor

$$z_s = \frac{\pi}{\lambda_{eff}}\left(\frac{d}{2}\right)^2 \tag{3.3}$$

the solution is generalised for any wavelength or slit width*. It can be observed that the MPM solution predicts a sinc function at $z_s>1$ (Raleigh range) which is in total agreement to the field

* It should be noted that the eigenfunction solution is not valid unless $d>>\lambda_{eff}$

predicted by the Fraunhofer diffraction of a single slit [14]. Indeed, the comparison of the predicted MPM farfield with the expected Fourier transform is used as a test for the validity of the results quoted in this thesis.

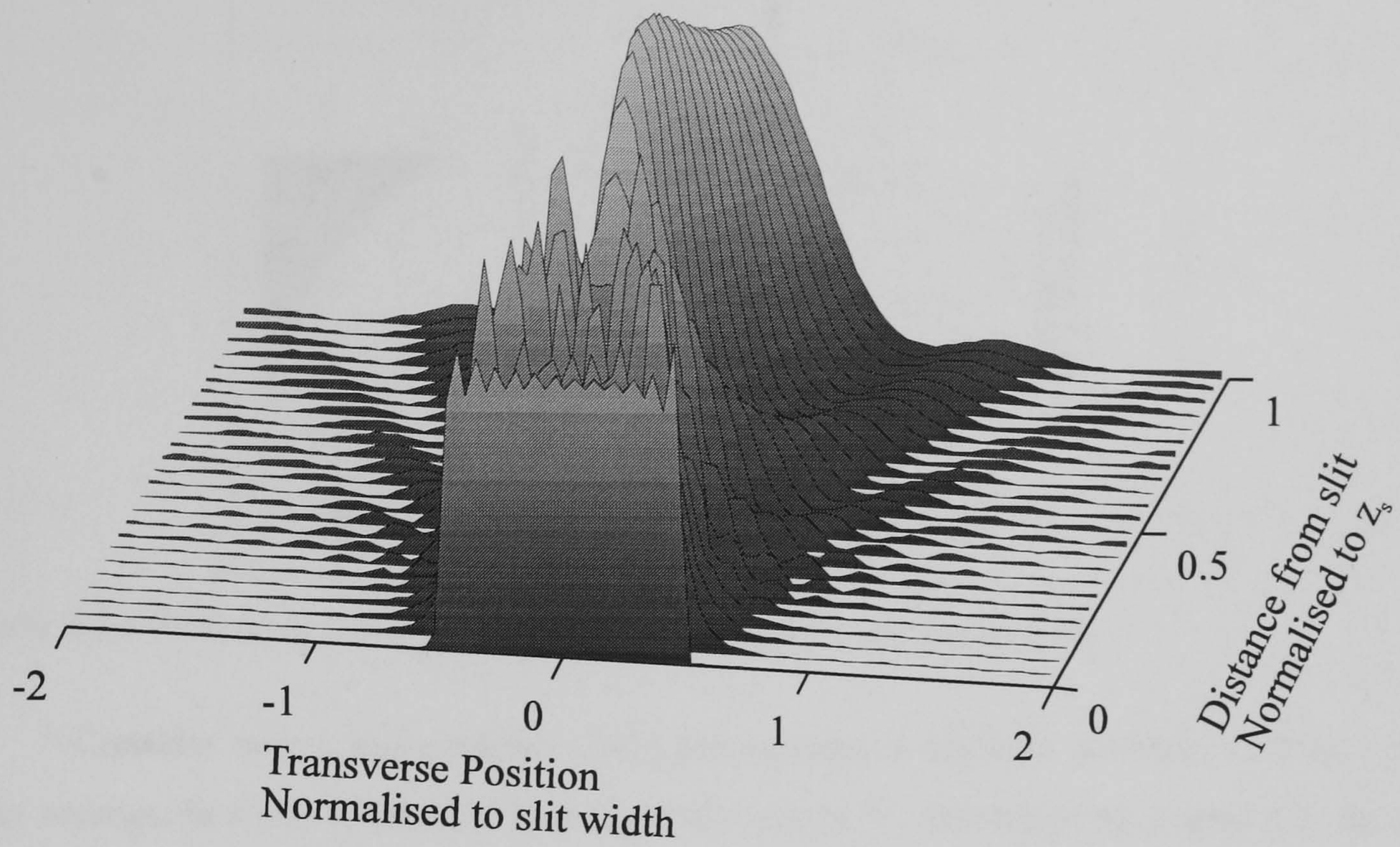

Figure 3.4 Truncation of a plane wave by a slit, d

It may be observed that the intensity in figure 3.4 increases to maximum before adopting the traditional sinc function in the farfield. This implies that the diffraction profile has narrowed since energy must be conserved over the direction of propagation. The narrowing effect is seen to occur at a distance approximately $0.5z_s$ from the truncation or

$$z_p \approx \frac{\pi}{8\lambda_{eff}} d^2 \tag{3.4}$$

and will be observed later when calculating the propagation in the mirror matrix. It will therefore be used for optimum positioning of the amplifier gate switches within the crosspoint architecture.

3.5.2 The truncation of a collimated waveguide field

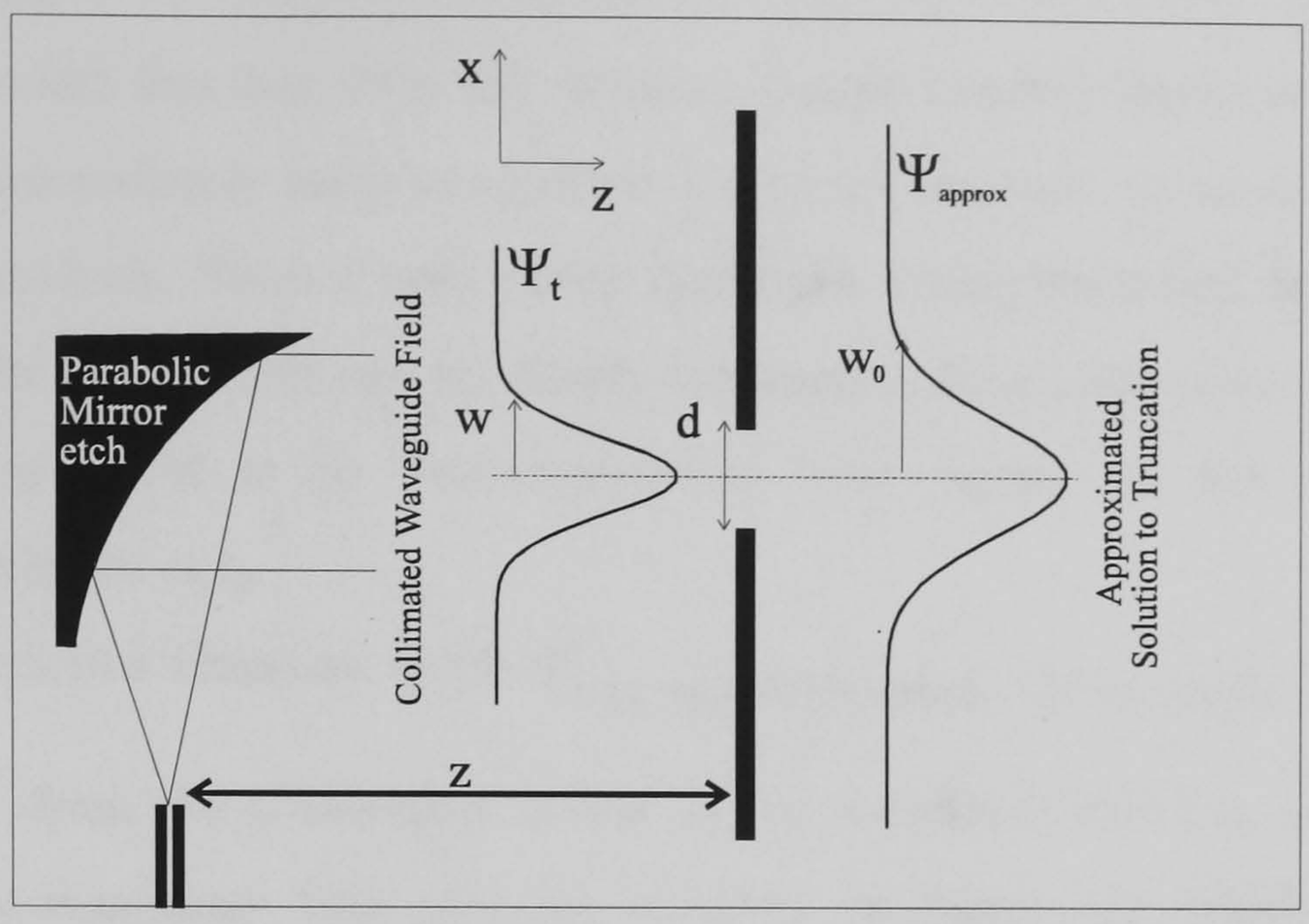

Figure 3.5 Zero order Gaussian approximation to a mirror truncation

Consider now a more realistic field propagating in the slab structure such as a zero order waveguide mode collimated by a parabolic mirror, Ψ_t, illustrated by Figure *3.5*. As with the plane wave analysis, the truncation can also be reduced, as a first approximation, to a normalised Hermite Gaussian beam Ψ_{approx}, with beam waist , w_0, calculated from equation 3.1. This simple approximation may be used to optimise the mirror matrix design. However, the accuracy of the approximation and range of validity is unknown. Thus the MPM is used to compare the actual propagation after truncation, with the zero order Gaussian approximation. The divergence angle, θ, together with the ratio $w_{0/w}$, where w is the beam waste of Ψ_t, are used as figures of merit in this comparison. The results can be summarised in figure 3.6.

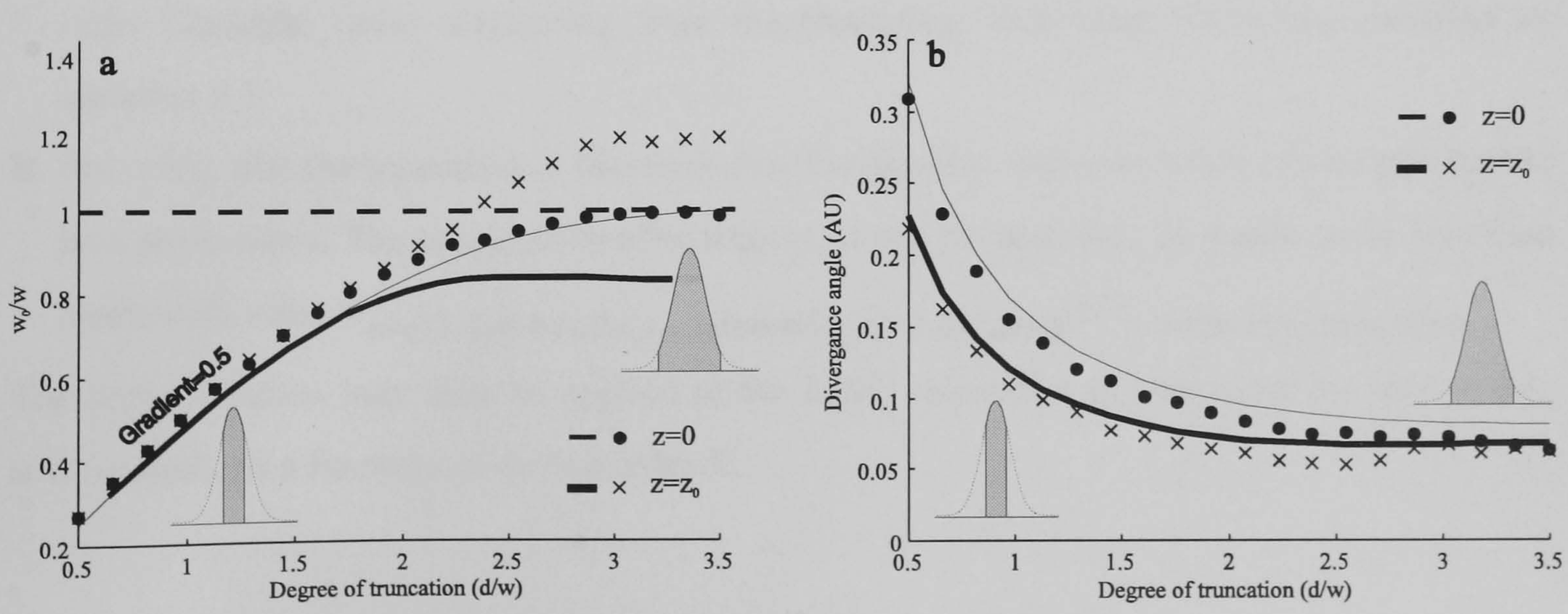

Figure 3.6 Comparison of the MPM with the Gaussian approximation solid line approximation, points - MPM calculation
a Variation of beam width after truncation
b Variation of beam divergence after truncation

Firstly consider the truncation of a collimated Gaussian i.e. at its waist with $z=0$ in figure 3.5. Figure 3.6 shows that the approximation accurately describes the propagating field for both θ and $w_{0/w}$ for all degrees of truncation. It can also be noted from figure 3.6a that for an aperture with width less than $d=w$, the variation is approximately linear with a gradient of a half. This result immediately leads to equation 3.2 which has been shown to be the result for the plane wave analysis. **Thus a zero order Gaussian mode truncated by an aperture of width less than its beam waist can be simply assumed to be a plane wave**. The propagation after truncation is found to be indistinguishable from figure 3.4 and also exhibits the characteristic maximum at z_p.

If the truncated Gaussian beam Ψ_t is not collimated, for example it has travelled a distance $z_0 > \frac{\pi}{\lambda_{eff}} w^2$ from the collimating mirror to the truncation, there is a reduction in the accuracy of approximation. This may be observed in figure 3.6 which shows that the approximation is only accurate for truncation widths less than $d \approx 2w$. Therefore, the truncation cannot be solely described by Ψ_{approx}. Higher Hermite Gaussian orders are required to approximate the solution satisfactorily and account for the extra divergence incurred to the truncated beam. A further increase in z leads to a further reduction in accuracy at lower values of d/w.

3.5.3 Application of Gaussian approximation to the 2DIO crosspoint design.

The above analysis can be summarised in two statements.

A. Providing that a zero order Gaussian beam is truncated by a slit of width less than $d \approx 2w$ before travelling a distance z_0 from its waist, its propagation can be described by a zero order Gaussian beam originating from the truncation with beam waist, w_0, satisfied by equation 3.1.

B. Providing that the truncation is less than $d \approx w$ the incident Gaussian beam can be assumed to be a plane wave. The propagation after truncation can be described by a zero order Gaussian beam with waist w_0=d/2 and exhibits a narrowing at a distance $z=z_p$ from the truncation.

The approximation may then be applied to the 2DIO crosspoint to determine the device size and crosstalk as a function of device order N.

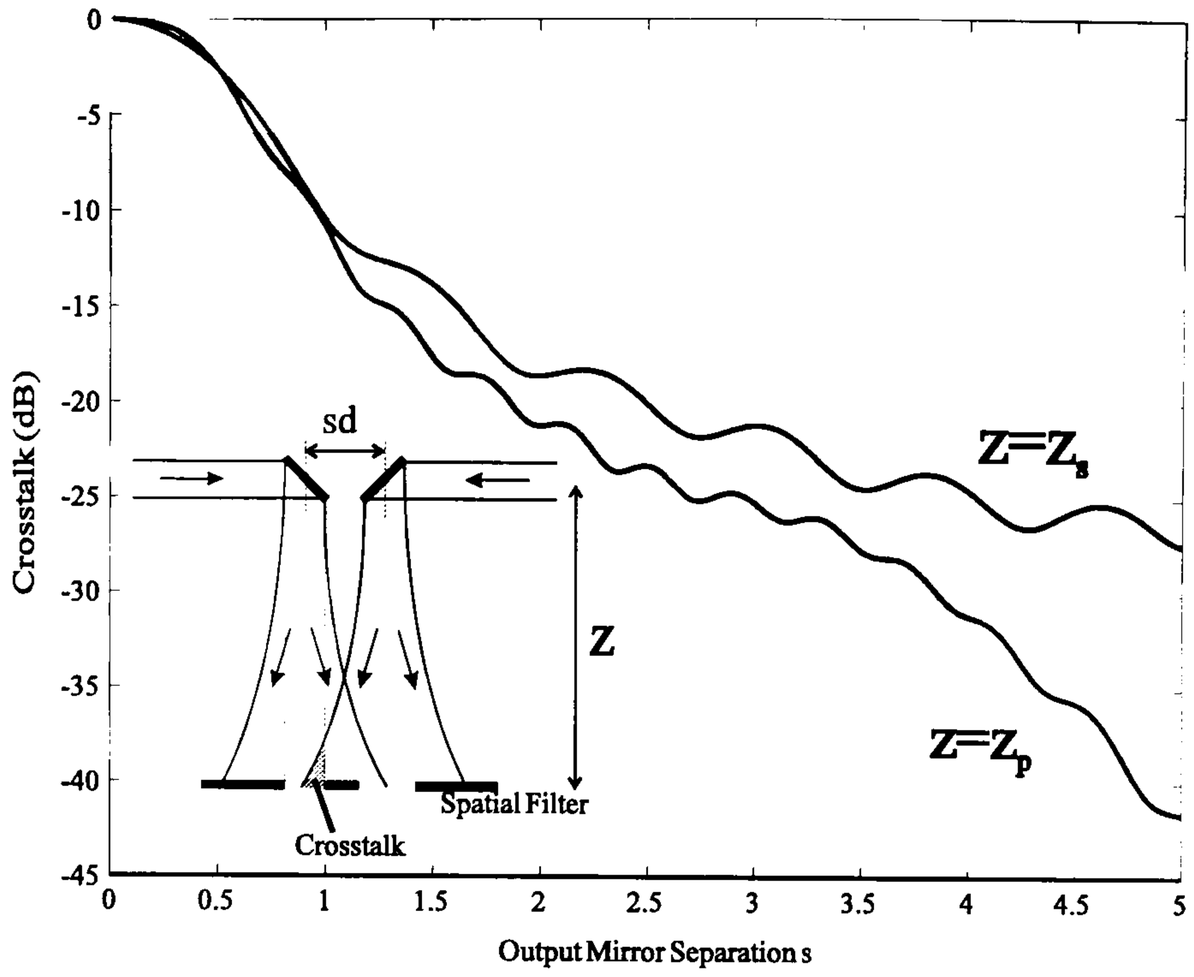

Figure 3.7 Variation of the amplifier separation, s, with the mirror/amplifier separation.

Firstly it can be observed from figure 3.1b that the approximate device size, D_x by D_y is given by the equations

$$D_x = N^2(1+s)d \tag{3.5a}$$

$$D_y = 2(dN^2 + l) \tag{3.5b}$$

where l is the switch length and sd is the switch separation. The variable s is a parameter introduced to increase the amplifier switch separation, which ultimately determines the crosstalk of the device. This is observed in figure 3.7 where the MPM is used to calculated the crosstalk between two neighbouring amplifiers as a function of their separation s. It may be observed that a switch separation of $s=5$ yields a device crosstalk of the order of -40dB for a key mirror/spatial filter separation of z_p i.e. $M_2=z_p$ (figure 3.3). This equation immediately determines the key mirror size

$$d = \frac{8\lambda_{eff}N^2}{\pi} \tag{3.6}$$

However, in order for the input beam to remain collimated over the length of the matrix two extra requirements are imposed on d. Firstly, in order for the beam to remain collimated over the entire length of the matrix (the region denoted by M_1 in figure 3.3), it is required from statement **A** that $2w_{in}=Nd$ and $M_1<z_0$, where w_{in} is the beam waist of the input collimated mode. This sets a lower limit on the truncation mirror size

$$d > \frac{4\lambda_{eff}}{\pi}(s+\frac{1}{2}) \qquad (3.7)$$

Also, in order for the input beam to remain collimated between successive truncations (from statement **B)** it is required that the distance between successive truncations in the matrix, M_3, is less than z_s.

hence $$d > \frac{4\lambda_{eff} Ns}{\pi} \qquad (3.8)$$

which follows from equation 3.6 that $N>s/2$. Thus given l, $s=5$ and $\lambda_{eff=(1.55/3.2)}\mu m$ the device size can be calculated and is shown in figure 3.8. It may be shown the device size increases as a function of N^4, D_x increasing more rapidly owing to the switch separation, ^{s}, required to reduce device crosstalk. The results show that for a device order of $N=4$ a device size of approximately $1.5x1.5mm^2$ is required when a switching region of length $l=500\mu m$ is assumed, which is typical [3]. This equates to a key mirror size of approximately $20\mu m$.

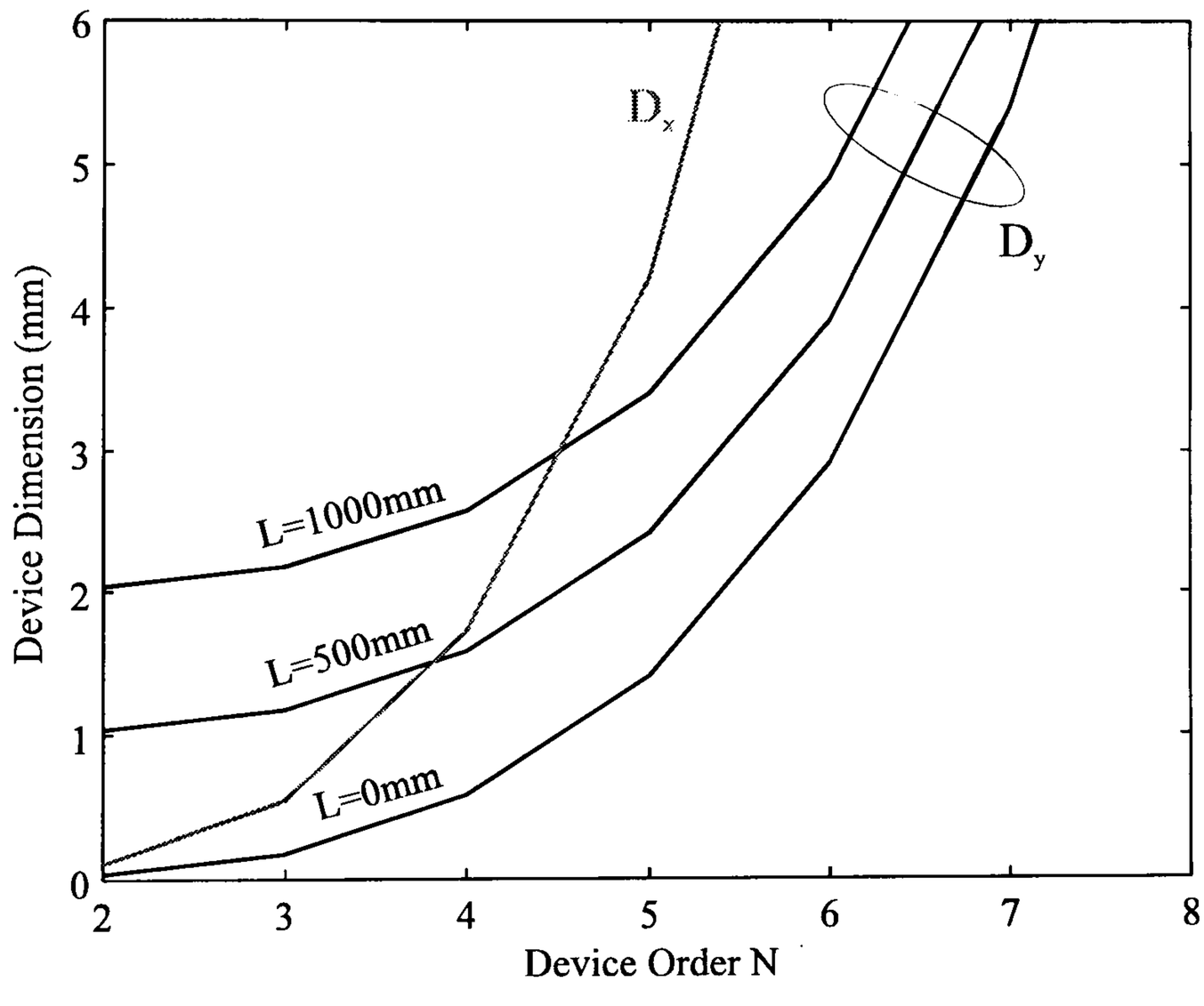

Figure 3.8 Calculation of device size using the Gaussian approximation.

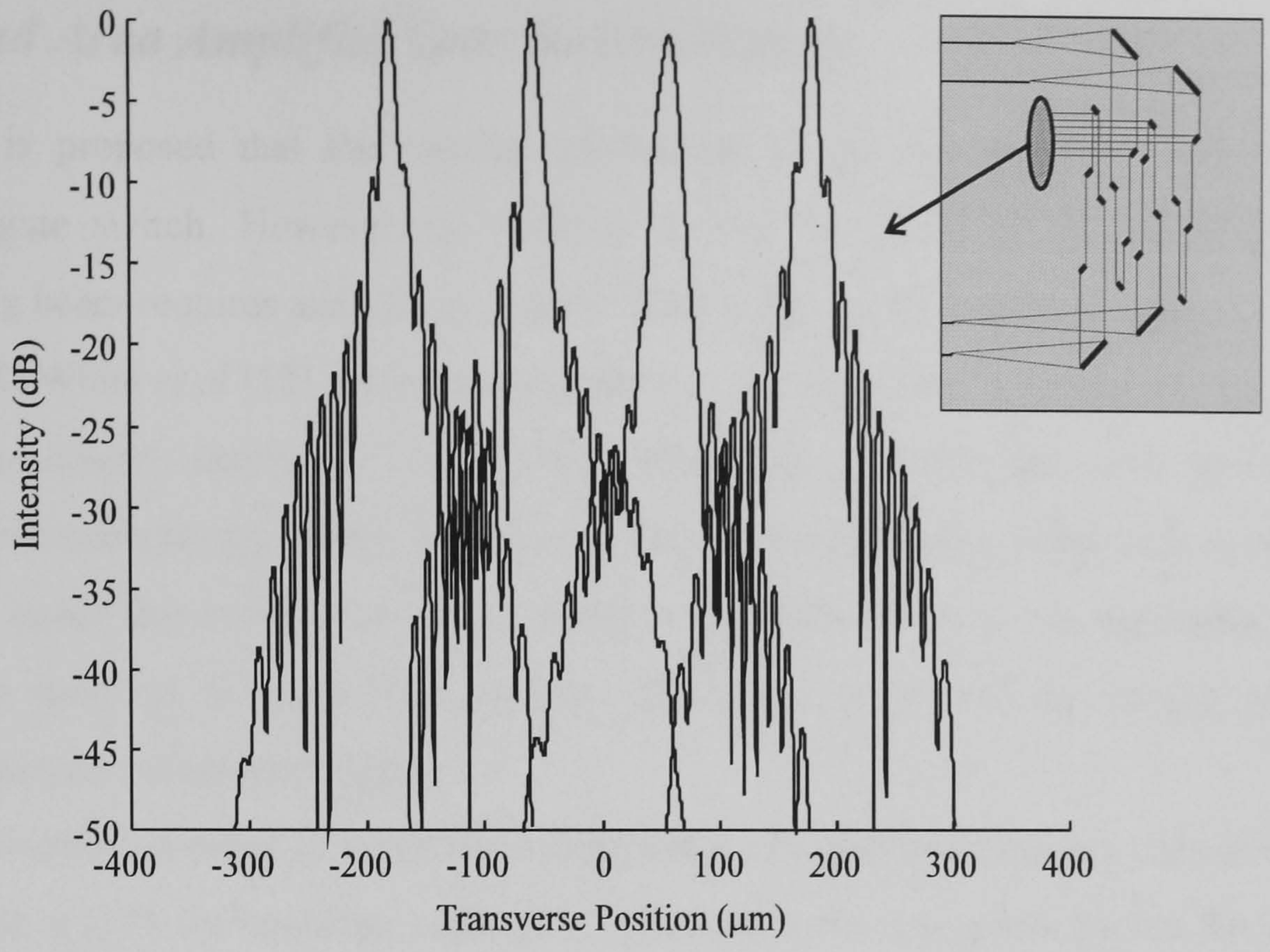

Figure 3.9 MPM simulation of the worst case field at one output of 4x4 mirror matrix

The MPM is then used to determine the actual theoretical performance of the optimised 4th order mirror matrix. This is achieved by calculating the actual field propagation from each of the four inputs, through the mirror matrix, to a single output of the device. Figure 3.9 shows the resulting intensity on one such output arm. This plot indicates that the crosstalk between the inputs is of the order of -40dB, as designed. The splitting and shuffling action of the mirror matrix is calculated in figure 3.10, where it can be observed that the input beam does remain collimated whilst travelling across the mirror matrix.

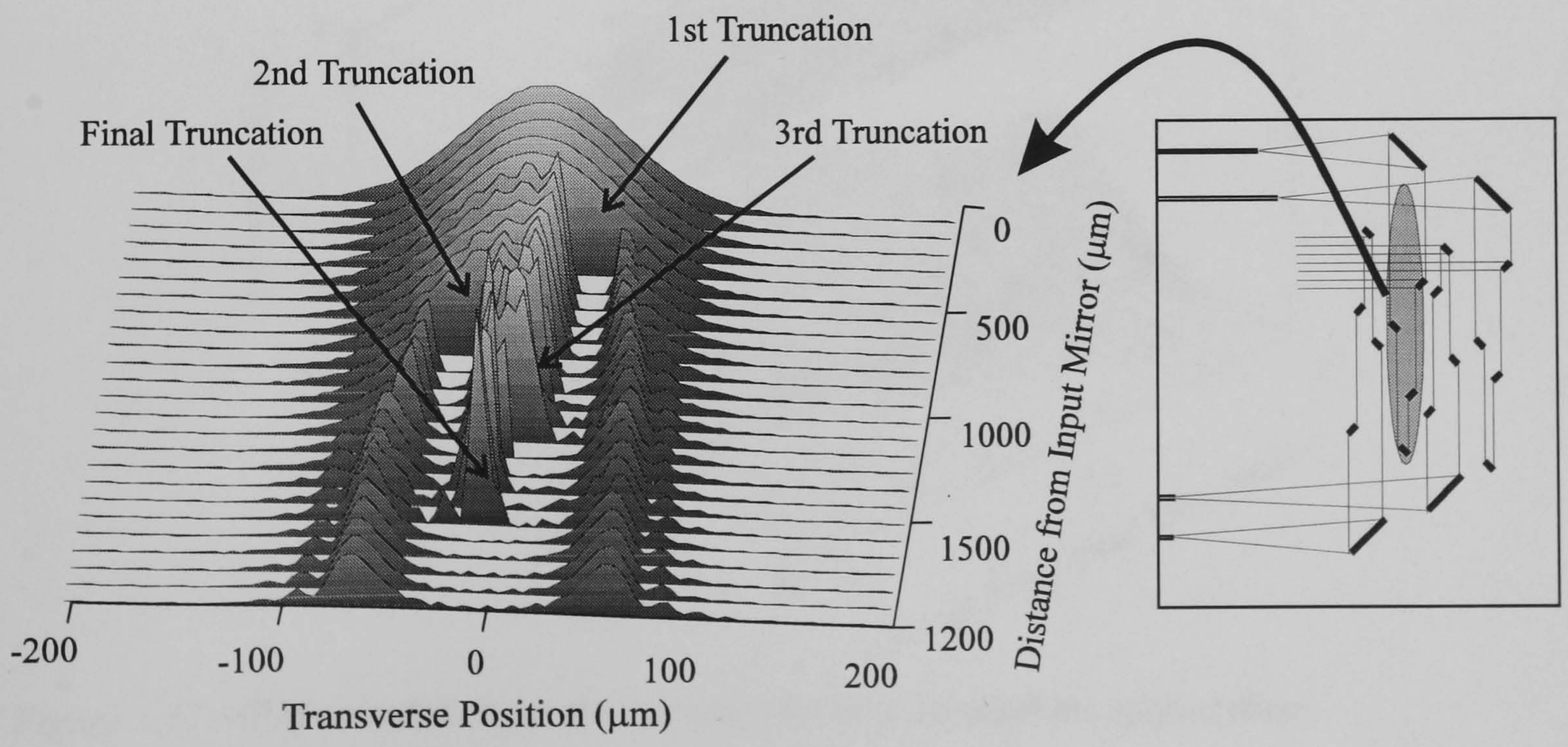

Figure 3.10 MPM of the beam splitting action of a proposed 4x4 2DIO crosspoint.

3.6 Broad Area Amplifier Gate Switch Design

It is proposed that the routing mechanism of the crosspoint is performed by the amplifier gate switch. However, as outlined earlier, the effect of the phase front on the propagating beam requires analysis in order to justify the viability of the device.

J.K. White *et al* [12] perform a detailed two dimensional analysis of a single pass broad area semiconductor amplifier. Their results show that provided the input aperture of the amplifier is broad enough, so that there is no truncation of the input beam both at the amplifier input and inside the cavity, the carrier density distribution across the amplifier becomes a predictable function of transverse position. Therefore, there will be smooth phase delay superimposed on the emitted signal.

However, in order to avoid the complexities of a full two dimensional travelling wave treatment as in [12], the amplifier analysis is separated into to two parts. Firstly the propagation of the beam through the amplifier length is studied by the modal propagation model. The gain and carrier density distribution within the amplifier is then calculated by a multi-section rate equation model (Appendix A). This method assumes that the beam propagates in a purely homogeneous medium and therefore ignores the gain guiding effect of the propagating mode. It does, however, approximately calculate the effect of the carrier distribution on the emitted wavefront. Hence the effect on power coupling to the output waveguide can be approximately calculated (as discussed in *Section 3.7)*.

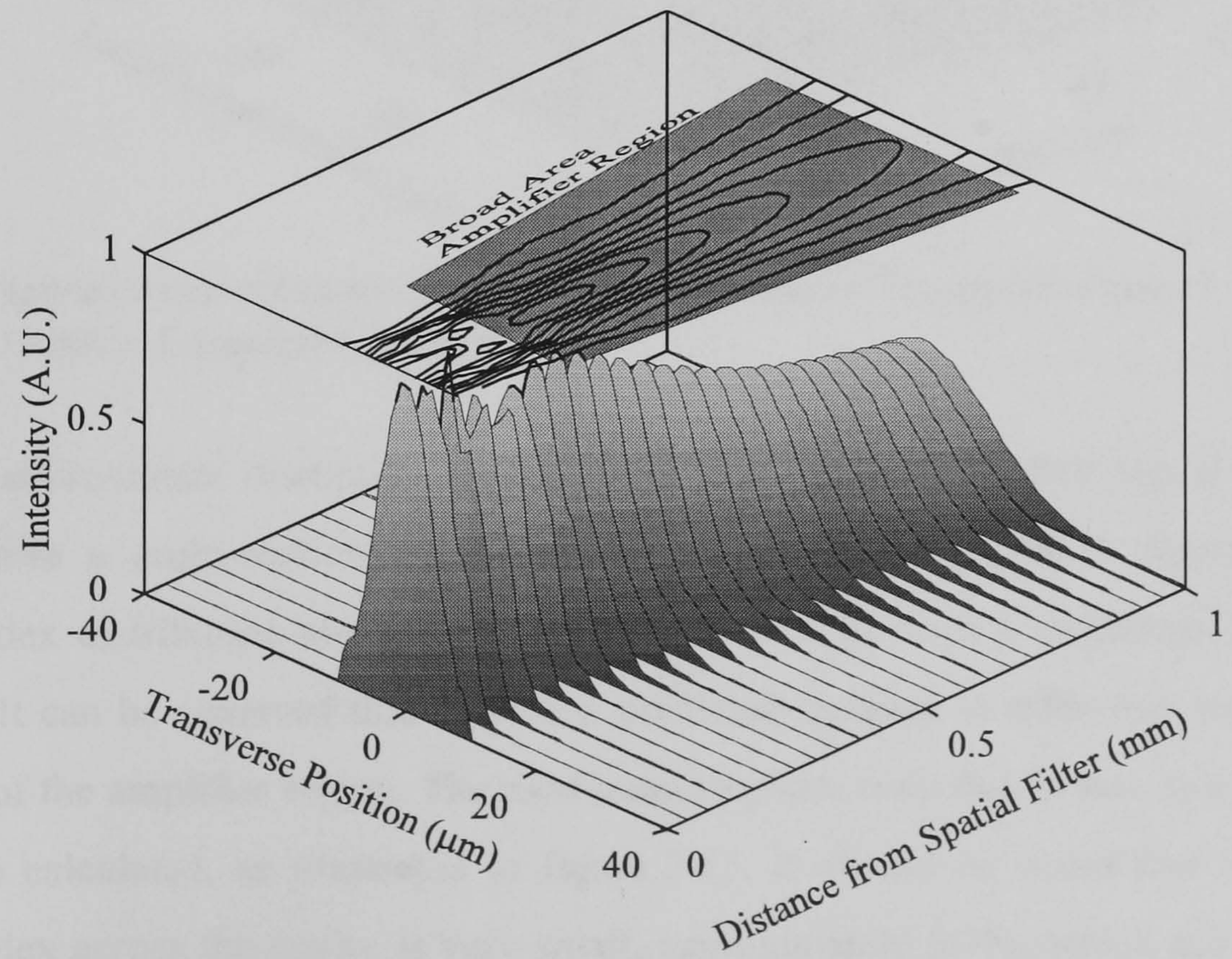

Figure 3.11 MPM calculation for the intensity distribution after the spatial filter

Firstly let us consider the MPM through the cavity. The path of an input to a single output through the device has been summarised by the block diagram shown schematically in figure 3.3. Spatial filters are placed between the mirror matrix and amplifiers. This not only reduces the crosstalk of the switch by preventing stray light from entering each amplifier gate switch, but with correct design forces the power distribution across the amplifier facet to be approximately Gaussian. This can be observed in figure 3.11, where the MPM has been used to calculate the effect of the filter (20μm aperture) for the optimised 4x4 crosspoint, ***after*** the input has passed through the mirror matrix. It can be observed from the contour plot that although diffraction ripples appear in the first 200μm after the truncation, the approximate propagation thereafter is approximately zero order Gaussian. It is found that this method of filtering only results in further signal loss of 0.93dB. The optimum amplifier design also requires a small taper angle of 2^0 in order to avoid truncation of the propagating field inside the amplifier cavity.

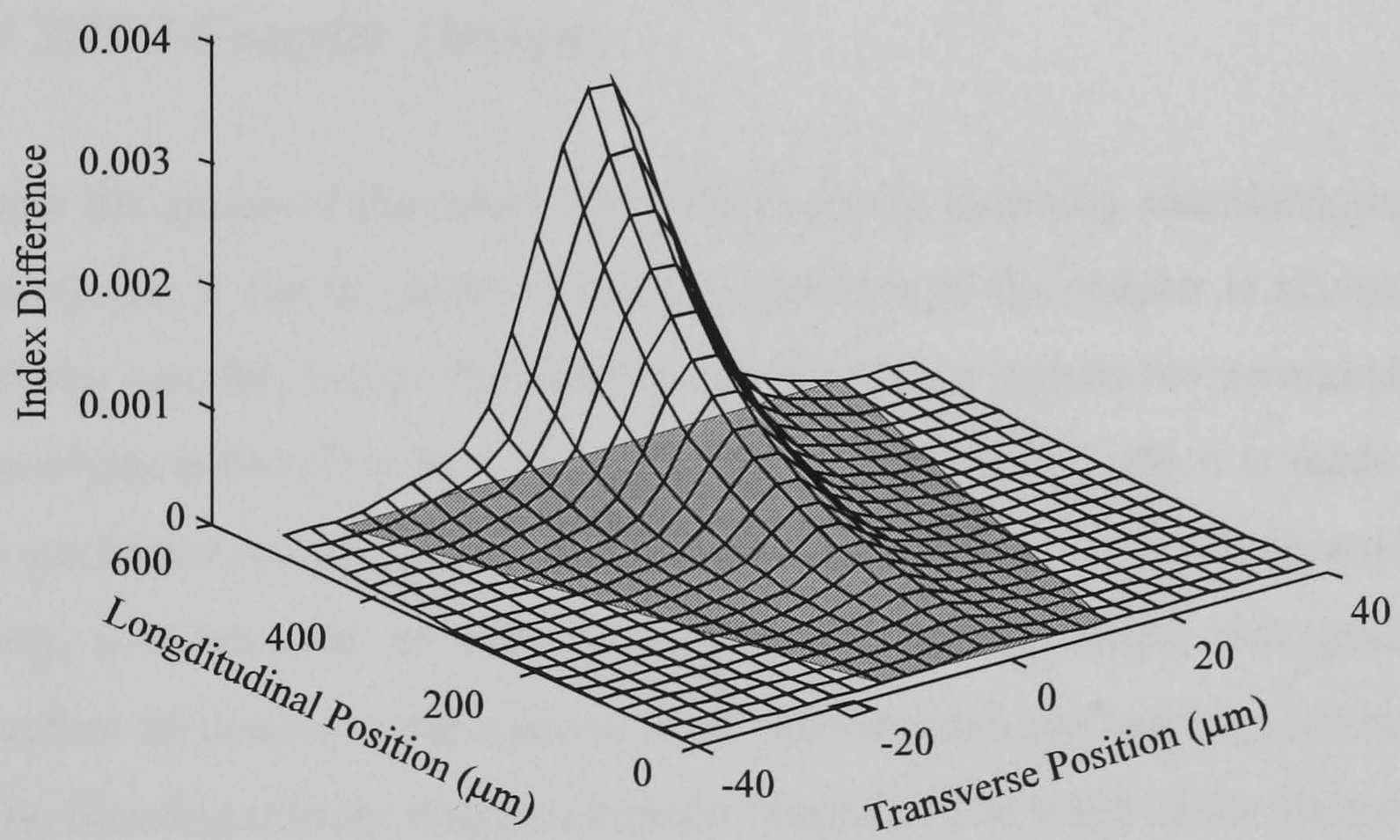

Figure 3.12 Approximate refractive index distribution across the amplifier cavity I=800mA Amplifier gain 25dB.

The approximate disruption on the phase front of the amplified signal may then be calculated from a multi-section rate equation analysis as described in Appendix A. The refractive index distribution along the amplifier cavity from such a calculation is plotted in figure 3.12. It can be observed that there is a predicted increase in refractive index down the central axis of the amplifier region. The total induced phase front due to this index distribution may then be calculated, as illustrated in figure 3.13. It should be noted that the change in refractive index across the cavity is very small, approximately 0.1%, which acts to focus the propagating mode. The induced phase front can then be used in conjunction with the MPM model to determine its effect when coupling to the output waveguide, as discussed in *Section 3.7.*

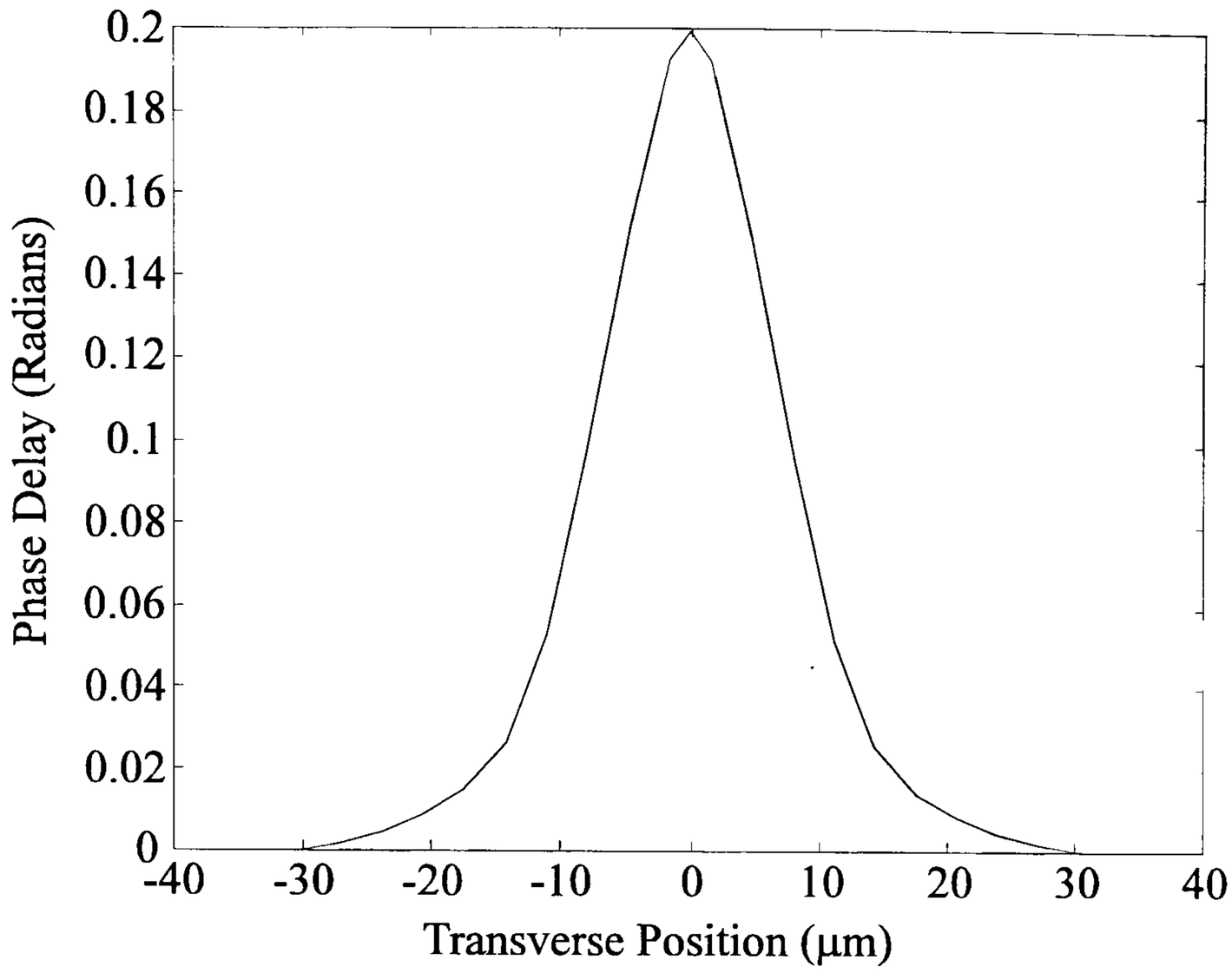

Figure 3.13 Total phase distribution across the amplifier output facet

3.7 Novel 2DIO Coupler Design

Finally the action of the novel Nx1 2DIO coupler is briefly examined, and optimised for a 4x4 crosspoint. It can be observed that the operation of the coupler is almost identical to that of a 1xN star coupler, except that parabolic mirror etches replace the waveguide array. The theoretical analysis is therefore very similar to that of a star [15], which is made easier if its operation as a coherent splitter rather than an incoherent combiner is initially considered.

Firstly, it is assumed, as with the input guide, that the output waveguide is weakly guided. Therefore an optical mode injected backwards through the output guide onto the array of N parabolic focusing mirrors is approximately Gaussian. The waist of the Gaussian beam, w, can be adjusted by changing the waveguide/mirror array separation. Assuming each parabolic focusing mirror has an aperture $d=20\mu m$ and $2w=Nd$, the field contribution on each mirror, χ_m, may then be calculated (dotted line figure 3.14). The diverging field which misses the parabolic mirror array results in a **coupler splitting** loss S of 1.6dB.

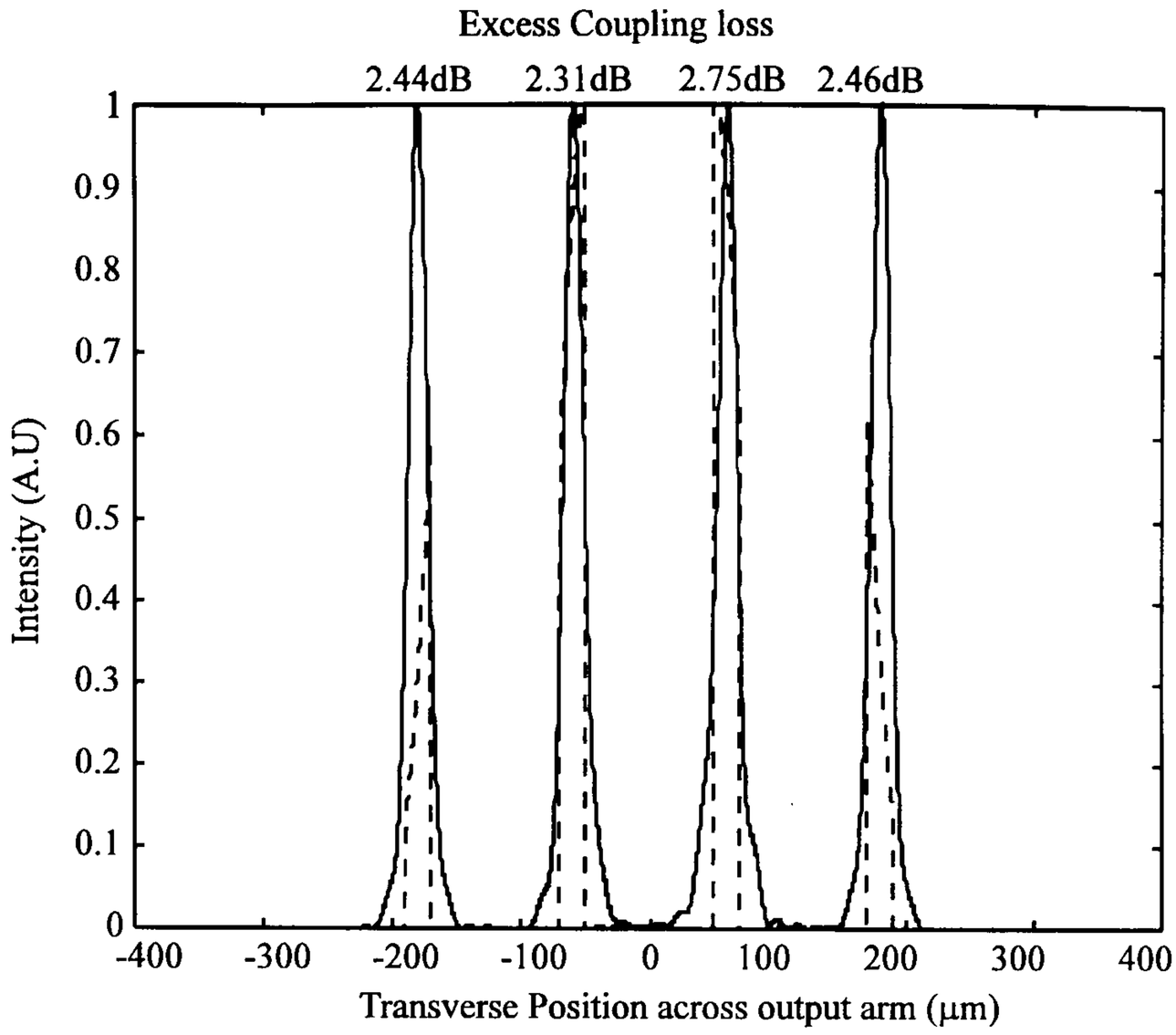

Figure 3.14 Calculation of channel loss of a 2DIO 1x4 coupler.
Solid line - Forward propagation of the signal from each input x_m.
Dashed line - Back Propagation of the output waveguide mode X_m.

Secondly, the field contribution incident on the parabolic mirrors from the opposite direction (through the device from the input guide), X_m, has already been calculated using the MPM and rate-equation analysis (a combination figures *3.9*, *3.11* & *3.12*). By applying the overlap integral between χ_m and X_m the **individual channel** loss, C_m, may then be calculated (figure 3.14). It is found that the gain guiding effect of the amplifier gate switch has a negligible contribution to C_m, the loss is almost all due to the mode mismatch and finite aperture of the mirrors *d*. The total 2DIO coupler *excess* loss (which does not include the intrinsic $10log_{10N}$ combine/split loss) may then be estimated by $S+C_m \approx 4dB$.

3.8 Device Loss And Crosstalk

The total device loss, α, for an NxN 2DIO crosspoint architecture, may now be estimated from the equation

$$\alpha = -20\log_{10} N + I + 3M + F + (S + C_m)\ \ dB \tag{3.9}$$

where the first term describes the inherent splitting and coupling loss of any broadcast crosspoint architecture, and

M is the mirror loss due to mirror roughness and wall verticality, typically -1.5dB per mirror [16].

I is the scattered field in the mirror matrix not directed to the outputs which has been estimated using the MPM to be of the order of -1.6dB, **which is independent of device order***

F is the spatial filter loss calculated to 0.93dB **which is independent of device order*.**

$S+C_m$ is the 2DIO coupler loss between the output parabolic focusing mirrors and the output single mode waveguides, this has been estimated to 4dB **which is independent of device order*.**

It may be observed that the dominant loss is due to the first term (split & combine) which is the theoretical minimum loss of any broadcast architecture. The device order, N, will be limited when this term exceeds the device amplification. However, unlike similar expressions for waveguide based architectures [1], it should be noted that the other terms are largely independent of N. This scalability with no excess increase in loss is a major advantage of this architecture. For an optimised 4x4 crosspoint the total device loss (including split and combine) can be estimated to 24dB. However, it should be noted that this loss is compensated for by the amplifier gate switches, thus the device performance is predicted to be lossless.

The crosstalk of the device at the output has been estimated to -40dB. However, this does not include crosstalk due to light scattering (off several mirrors) inside the device. However, the judicious placement of spatial filters at the input and output waveguides may be used to overcome this problem (figure *3.1*).

3.9 Conclusions

A novel 2DIO crosspoint architecture has been proposed which has been optimised using a Hermite-Gaussian modal propagation model and multi-section rate equation analysis. A zero order Gaussian approximation has been used to ease device design and the limits of the approximation have been discussed by comparison with the modal propagation model. Theoretical calculations show that a 1.55μm InGaAsP-InP 4x4 lossless crosspoint switch with a theoretical crosstalk of approximately -40dB could be integrated on a InGaAsP-InP wafer less than 2x2mm² in size. However, a more rigorous analysis is required in order to assess the design tolerance from variations between and across an InP wafer (for example refractive index), in order to completely justify the design.

* It should be noted that although all preceding loss calculations were performed for a 4x4 crosspoint they are still approximately valid for an NxN device. This is due to the way each calculation has been scaled to the key mirror width, d, and optimum position z_p.

3.10 References

[1] R.A.Spanke, "Architectures for Guided-Wave Optical Space Switching Systems", IEEE Communications Magazine, Vol.25, No. 5, pp 44-48, May 1987.

[2] I.H. White, J.J.S. Watts, J.E. Carroll, C.J. Armistead, D.J. Moule, J.A. Champolovier, "InGaAsP 400x200μm Active Crosspoint Switch Operating at 1.5μm using Novel reflective Y-Coupler Components", Electron Letters, Vol. 26, No.10, pp 617-618, 1990.

[3] G. Sherlock, J.D. Burton, P.J. Fiddyment, P.C. Scully, A.E. Kelly, M.J. Robertson, "Integrated 2x2 Optical Switch with Gain", Electronic Letters,Vol. 30, No. 2, pp 137-138, 1994.

[4] Wim van Berlo, M. Janson, L. Lundgren, A. Morner, J. Terlecki, M. Gustavsson, P. Granestrand, P. Svensson, "Polarization-Insentive, Monolithic 4x4 InGaAsP-InP Laser Amplifier Gate Switch Matrix", IEEE Photonics Tech. Letters, Vol. 7, No.11, pp1291-1293, 1995.

[5] K. Komatsu, K. Hamamoto, M. sugimoto, A. Ajisawa, Y. Kohga, A. Suzuki, "4x4 GaAs/AlGaAs Optical Matrix Switches with Uniform Device Characteristics using Alternating Δβ Electrooptic Guided-Wave Directional Couplers", JLT, Vol. 9, No. 7, pp 871-878, 1991.

[6] H. Nishimoto, S. Suzuki, M. Kondo, "Polarisation-Independent $LiNbO_3$ 4x4 Matrix Switch", Electronic Letters, Vol.24, No. 18, pp 1122-1123, 1988.

[7] J.D. Love, F. Ladouceur, "Excess Loss in Singlemode Right -Angled X Junctions", Electronic Letters., Vol. 28, No. 3, pp 221-222, 1992.

[8] M.Gibbon, G.H.B Thompson, S.J. Clements, D.J. Moule, C.B. Rogers, C.G. Cureton "Optical Performance of Integrated 1.5μm Grating Wavelength-Demultiplexer on InP-Based Waveguide" Electronic Letters, Vol. 25, No. 21 pp 1441-1442, 1989.

[9] S.E. Hicks, C.D.W Wilkinson, G.F. Doughty, A.L. Burness, I. Henning, M.Asgahri, I.H. White, "Reactive Ion Etching of Low-Loss Mirrors in Inp/InGaAsP/InP Heterostructures Using $CH_4/H_2/O_2$ Chemistry" Proc ECIO '93.

[10] M. Born, E. Wolf, "Principles of Optics - Third Edition", Pergamon Press 1965.

[11] D. Marcuse "Theory of Dielectric Optical waveguides - Second Edition" Academic Press Inc.

[12] J.K. White, J.G. McInereney, J.V. Moloney, "Formation of Sharply Peaked sidelobes in Large Aperture Single-pass Semiconductor Laser Amplifiers" Electronic Letters, Vol. 31 No. 1, pp 39, 1995.

[13] J.C.G. Lesurf, "Millimeter-wave Optics, Devices & Systems", Adam Hilger 1990. pp 34-42.

[14] Hecht, "Optics - Second Edition", Addison -Wesley Publishing Company, Inc 1987. Chapter 10.

[15] C. Dragone, "Efficient NxN Star Couplers Using Fourier Optics", JLT, Vol. 7, No. 3, pp 479-489, 1989.

[16] S.M. Ojha, G.H.B. Thompson, C.G. Cureton, C.B. Rogers, S.J. Clements, M. Asghari, I.H. White, "Demonstration of Low Loss Integrated InGaAsP/InP Demultiplexer Device with Low Polarisation Sensitivity", Electronic Letters, Vol. 29, No. 9, pp 805-806, 1993.

Monolithic Integration of Optical Space Switches

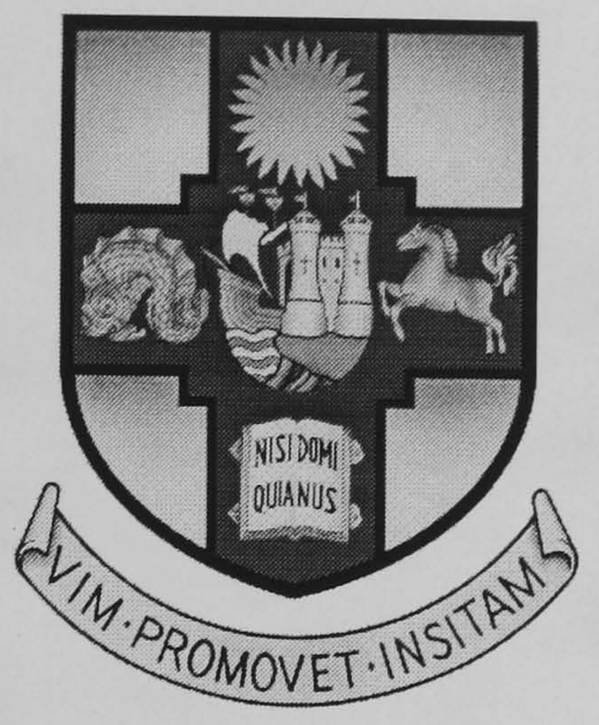

Chapter 4

4.1 Theoretical Optimisation of the Waveguide Crosspoint Switch

Chapter 2 has introduced the basic concept of the waveguide crosspoint switch. It has been shown that by using TIR mirrors, electroabsorption modulators and deep etched MMI couplers the device size can be reduced to a minimum. In this chapter the basic design is analysed theoretically in order to achieve an acceptable device performance. This will allow a calculation of device size with device order. It will be shown that an 8x8 InP device is feasible with a size of approximately 3x2mm^2. This will lead to the fabrication of several test structures in order to verify the theoretical calculations given in this chapter. These test structures will be discussed further in chapters 5 and 6.

4.2 Outline of device structure

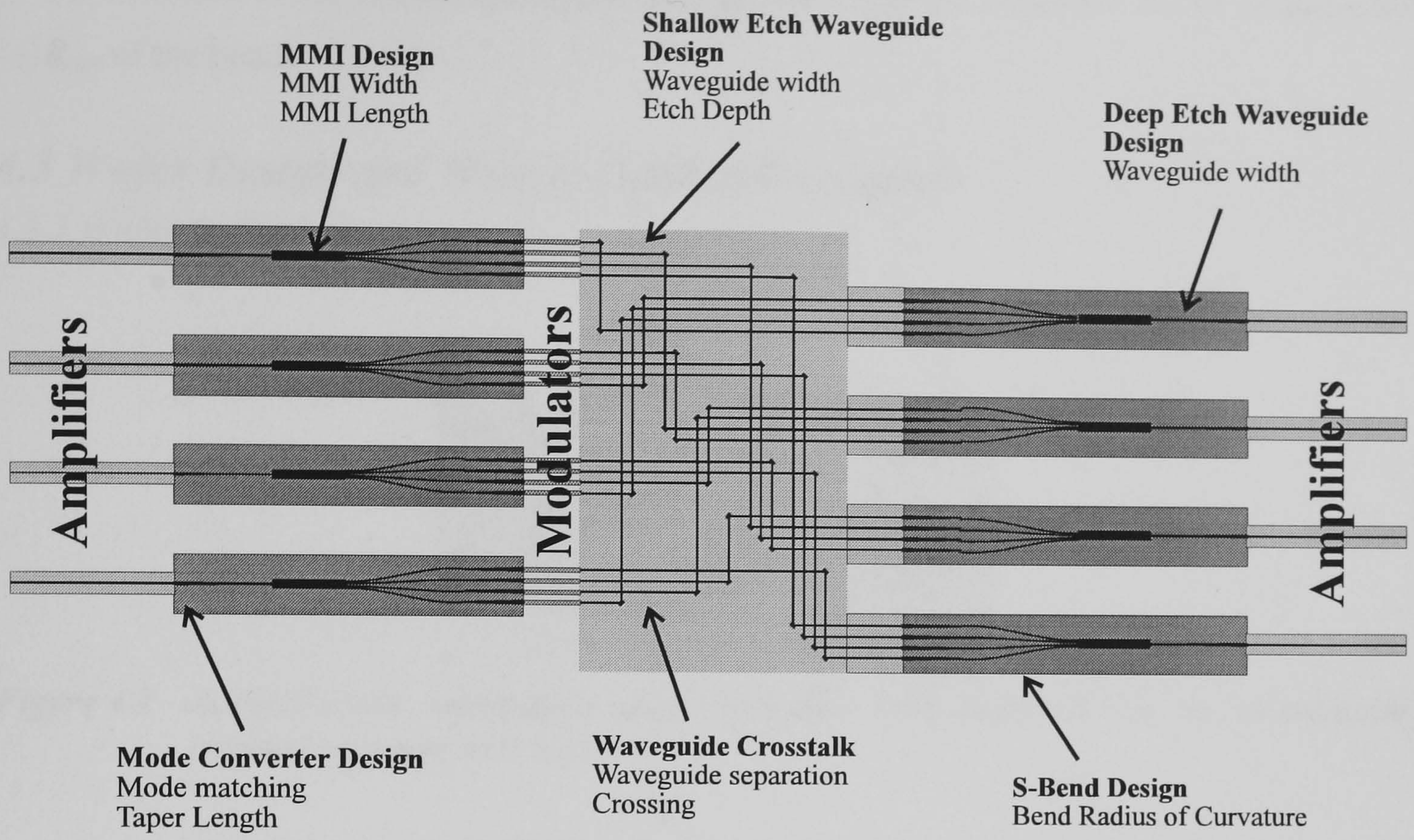

Figure 4.1 Schematic diagram of the proposed 4x4 InP Crosspoint design

A schematic diagram of the proposed device is shown conceptually in figure 4.1. The inputs are first split N ways by input couplers, switched, then shuffled to each output via the waveguide matrix. Finally they are collected together by with N output couplers. It has already been briefly discussed that in order to reduce the size of the coupler stages whilst maintaining low crosstalk and loss in the matrix it is necessary to have separated regions with strong and weak guiding. This chapter will be concerned with analysing in detail all aspects of the switch design. From the choice of waveguide which leads to coupler design and finally the mode converters which are required for a low loss transition between the strong and weak guided regions.

Figure 4.1 highlights the various features of the device which need to optimised before the crosspoint may be fabricated. These will be discussed separately in the following sections as follows

1. Discussion of the InP wafer on which the device will be fabricated.
2. Optimisation of the shallow etch waveguide width, ***d,*** and etch depth, ***e***.
3. Calculation of the device crosstalk by optimisation of the waveguide separation, ***s***, in the matrix.
4. Mode converter design which allows a low loss transition between the deep and shallow etched regions. Calculation of the taper width, ***D***, and length ***L***.

5. Designing of a deep etched fabrication tolerant Multimode Interference coupler (MMI), MMI width, W, and length L_{MMI}.
6. Optimisation of the S-Bend waveguide and calculation of the minimum radius of curvature, R_{co}, of the bends.

4.3 Wafer Design and Weakly Guided Waveguide

4.3.1 Wafer Optimisation

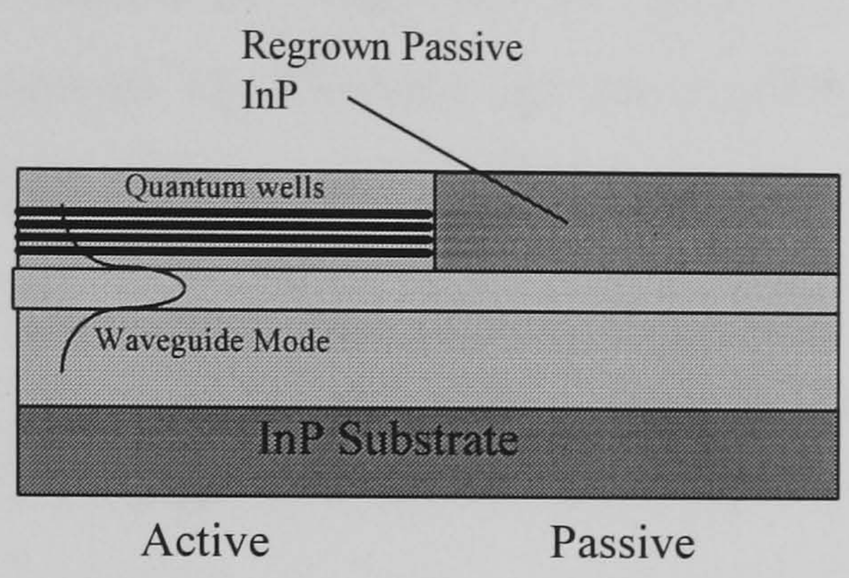

Figure 4.2 Active/Passive integration using selective area regrowth on an evanescently coupled quantum well wafer

In order to optimise each of the components in the crosspoint switch, a wafer design is required onto which the device will be finally fabricated. Therefore it is first necessary to have a basic understanding of how the finally device will be fabricated. The device requires integration of active amplifiers/modulators and passive waveguides which can be achieved by many different methods, such as laser intermixing [1], hybrid integration [2-5], bandgap selective growth [6] and selective area regrowth [7]. It has been proposed that this device will be fabricated by the latter process of selective area regrowth, following a process very close to an earlier BT 2x2 crosspoint design as discussed in [8,9]. The process involves designing an evanescently coupled MQW (multi-quantum well) wafer as shown schematically in figure 4.2 The first processing step involves masking the amplifier/modulator areas of the device and etching away the active MQW. The passive regions are then formed by a second regrowth step to create a low loss passive waveguide. An example of this technique is discussed in [8] and shown schematically in figure 4.2. The passive waveguide structure assumed for the crosspoint is therefore chosen to be compatible with selective area regrowth and is drawn schematically in figure 4.3.

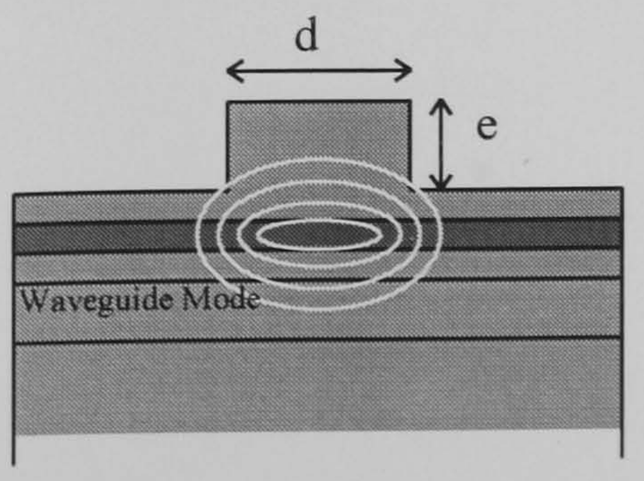

	Material	Width (μm)	Index
Cladding	InP	1.5μm	3.157
Guide	Q1.1	0.4μm	3.288
Cladding	InP	0.5 μm	3.157
Buffer	InP	1.0 μm	3.157
Substrate	InP		3.157

Figure 4.3 Passive waveguide structure using selective area regrowth on an evanescently coupled quantum well wafer (after [8]).

4.3.2 Weakly Guided Waveguide Optimisation

Chapter 2 has briefly discussed the reasons why weak guides are required in the waveguide matrix of the crosspoint. This is because of the large numbers of crossings in the matrix will yield an unacceptable loss owing to the field diffracting across each crossing. The weakly guided waveguides must be single moded - to ensure good coupling to input/output single mode fibres. Also it should be noted that the weak guides mean large waveguide separations at the coupler outputs to minimise optical coupling from the parallel running waveguides in the matrix. This increases device size, thus the final waveguide design must balance waveguide separation with the loss of the waveguide crossings. Before proceeding with this optimisation, the single mode nature of a ridge waveguide will be discussed as this will impose the primary limits of waveguide geometries that are feasible.

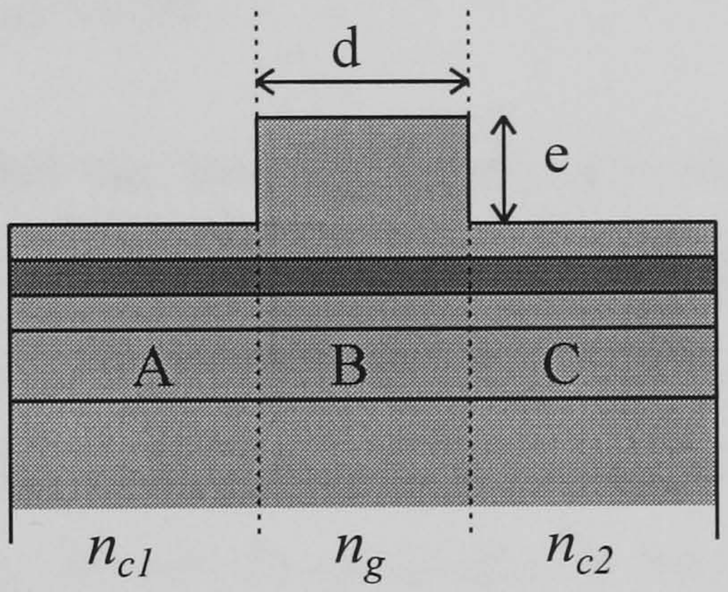

Figure 4.4 Effective Index Representation of a 3 Dimensional waveguide.

A ridge waveguide geometry is considered for the passive waveguide matrix as shown in figure *4.4*. The guiding strength of the waveguide is determined by the etch depth, *e*, in the upper cladding layer. Since the waveguide must be single moded, this sets a maximum waveguide width, $d_{cutoff\ p=1}$ for a given etch depth, *e*, below which the first order mode is cutoff. There are many ways calculating $d_{cutoff\ p=1}$ *(e)* for the above wafer design, here an effective index method [10-.12] is used. Although the calculation is approximate [13], the method simplifies the device optimisation in the later sections.

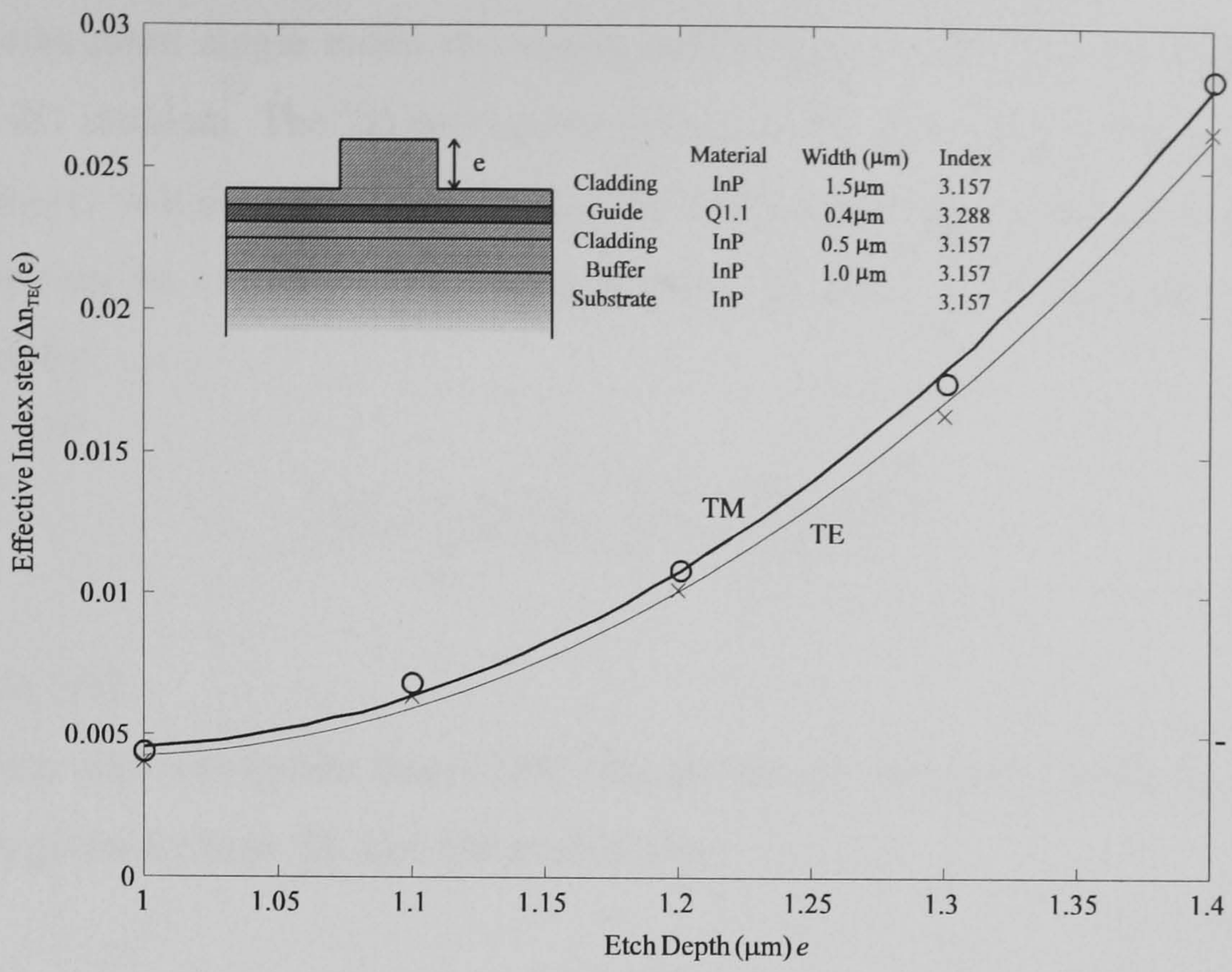

Figure 4.5 Effective Index Step $\Delta n_{TE}(e)$ and $\Delta n_{TE}(e)$ as a function of etch depth e. $n_{g\_TE}=3.197$; $n_{g\_TM}=3.194$

It is first assumed that the mode propagating down the structure can be resolved separately into the horizontal and vertical directions. The 3 dimensional problem can then be reduce to a much simpler 2D calculation which is discussed in [14]. By solving the wave-equation first in the vertical plane independently in the three regions A, B and C (figure *4.4*) the effective indices $n_{c1}(e)$, n_g, $n_{c2}(e)$ can be calculated. In this case, the problem is symmetric $n_{c1}(e)=n_{c2}(e)=n_c(e)$. As such the effective guiding strength in the horizontal direction may then be determined from the equation

$$\Delta n(e) = n_g - n_c(e) \tag{4.1}$$

A multi-layer 2D waveguide mode solver has been used [15] in order to calculate the effective indices of n_g, $n_c(e)$, and hence $\Delta n_{TE}(e)$ and $\Delta n_{TM}(e)$ for both the TE and TM polarisations. This is plotted in figure 4.5 as a function of etch depth e.

aside It is found that when calculating information about the waveguide, such as 1st order cutoff, crossing loss etc. it is easier to deal in terms of the effective index step, $\Delta n(e)$ of the guide rather than the etch depth. Therefore the rest of the chapter will deal in terms of the effective index step of the waveguide. The etch depth, e, required for fabrication may then be determined after the optimum index step, $\Delta n(e)$, has been found.

The maximum single mode waveguide width $d_{cutoff\ p=1}$ (for the 3D structure) is then reduced to a 2D problem. The 2D waveguide formed in the horizontal plane by the effective index step $\Delta n_{TE}(e)$ will determine the 1st order TE mode cutoff for the 3D guide [16], likewise for TM. This may be calculated algebraically from the normalised frequency parameter V, which is given by

$$V = \frac{1}{2} kd \sqrt{2n_g \Delta n(e) - \Delta n(e)^2} \tag{4.2}$$

as discussed in [17].

It is found from slab waveguide theory [18] that the cutoff waveguide width $d_{cutoff\ p}$ of the p^{th} order mode is given for both TE and TM modes when

$$V = \frac{p\pi}{2} \tag{4.3}$$

Thus the maximum single mode waveguide width for the weakly guided structure can be calculated in terms of the effective index step $\Delta n(e)$ from equations 4.2 and 4.3, this is plotted in figure 4.6. It should be noted that in terms of effective index step $\Delta n(e)$ the cutoff point is identical for both TE and TM polarisations (this is a result derived theoretically by Marcuse [19]). However, it should be noted from figure *4.5* that for a given etch depth, *e,* the index step, $\Delta n(e)$, is different for each polarisation. Therefore, both TE and TM polarisations will indeed have different cutoff waveguide widths which may be deduced from both figures *4.5* and *4.6*.

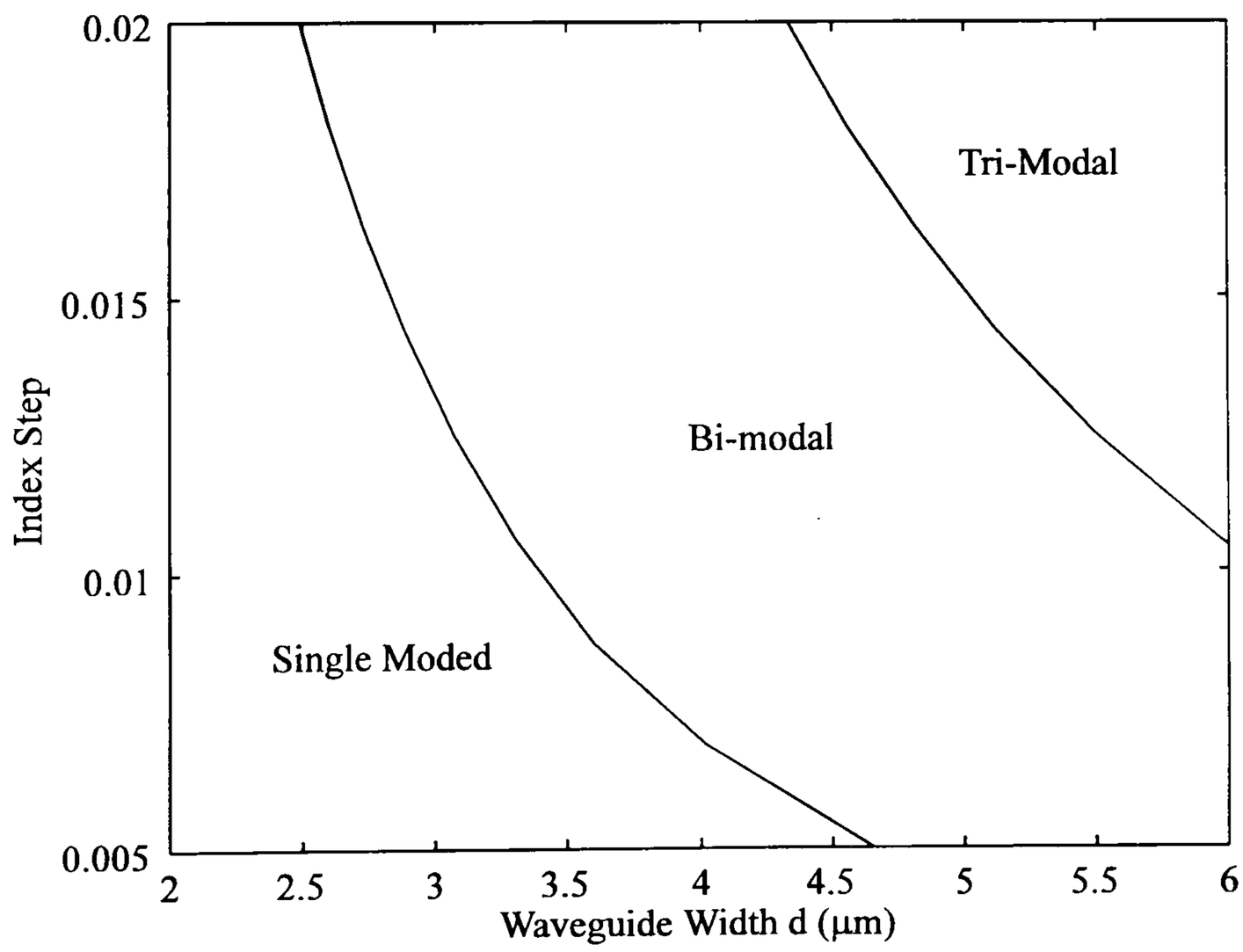

Figure 4.6 Number of Modes propagating in a shallow etched waveguide as a function of width and index step.

Thus the single mode nature of a ridge waveguide has been determined in terms of the effective index step and waveguide width (Figure 4.6). However, an optimum waveguide cannot yet be determined until the following factors have been investigated

1. Crossing loss in the waveguide matrix
2. Crosstalk in the waveguide matrix

as these will both be affected by the waveguide design. These factors will now be discussed in the next section in order to finalise the weak guided waveguide design.

4.3.3 Waveguide Crossing Loss and Crosstalk

Chapter 2 has given a brief description of how the number of waveguide crossings will limit the device performance. In this section a more rigours calculation of the crossing loss and crosstalk will be calculated. This information will then be used to optimise the final waveguide design.

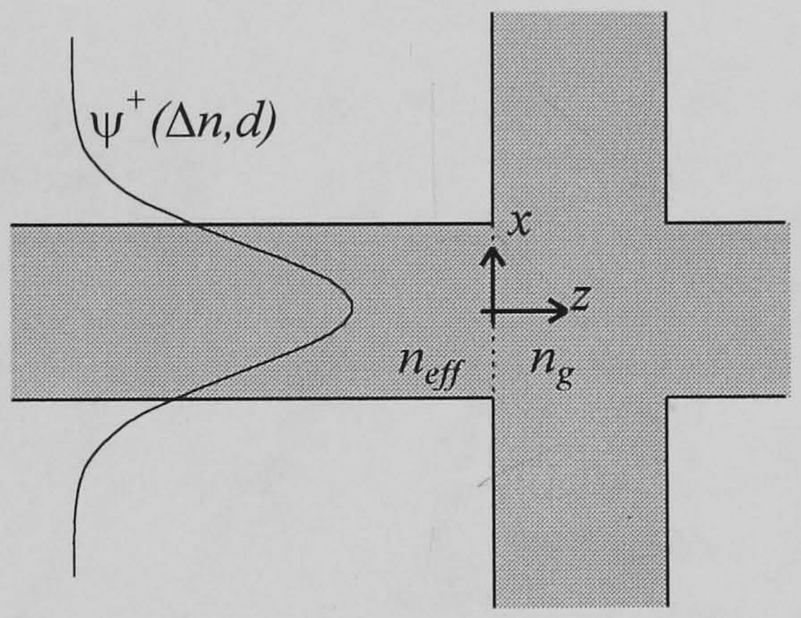

Figure 4.7 Calculation of loss and crosstalk of a waveguide crossing.

Firstly the crossing loss will be discussed. Consider a 2D waveguide mode $\psi(\Delta n,d)$ propagating towards a waveguide crossing. From figure 4.7 it may be shown that the boundary conditions at the crossing lead to

$$\psi^{+}(\Delta n,d) = r\psi^{-}(\Delta n,d) + \sum_{n=0}^{n=\infty} C_n G_n(w, z=0) \qquad (4.4)$$

where the first term describes the reflection at the interface (r is the field reflectivity). The second term represents a complete basis set of Hermite-Gaussian modes $G_n(w,z)$ which describes the light coupling into the 2DIO region right of the boundary. This calculation has already been discussed in chapter 3. The superscripts ± indicate the direction of which $\psi(\Delta n,d)$ propagates.

The back reflection from the crossing is due to the refractive index step n_g- n_{eff}, where n_{eff} is the effective refractive index of the propagating mode left of the boundary. The

reflectivity, $R=|r|^2$, can be estimated by the Fresnel reflection equation at normal incidence [20] which is given by

$$R = \left(\frac{n_g - n_{eff}}{n_g + n_{eff}} \right)^2 \tag{4.5}$$

The value of n_{eff} depends on the waveguide width and effective index step of the waveguide. It's value can be determined from the eigen-value equation [21]

$$\tan(\kappa) = \frac{\gamma}{\kappa} \tag{4.6}$$

where, κ and γ are constants as discussed in [21]

It's solution is plotted in figure 4.8 which along with the crossing reflectivity R which has calculated from equation 4.5 (figure 4.6 has also been used to indicate the mode cutoff boundaries).

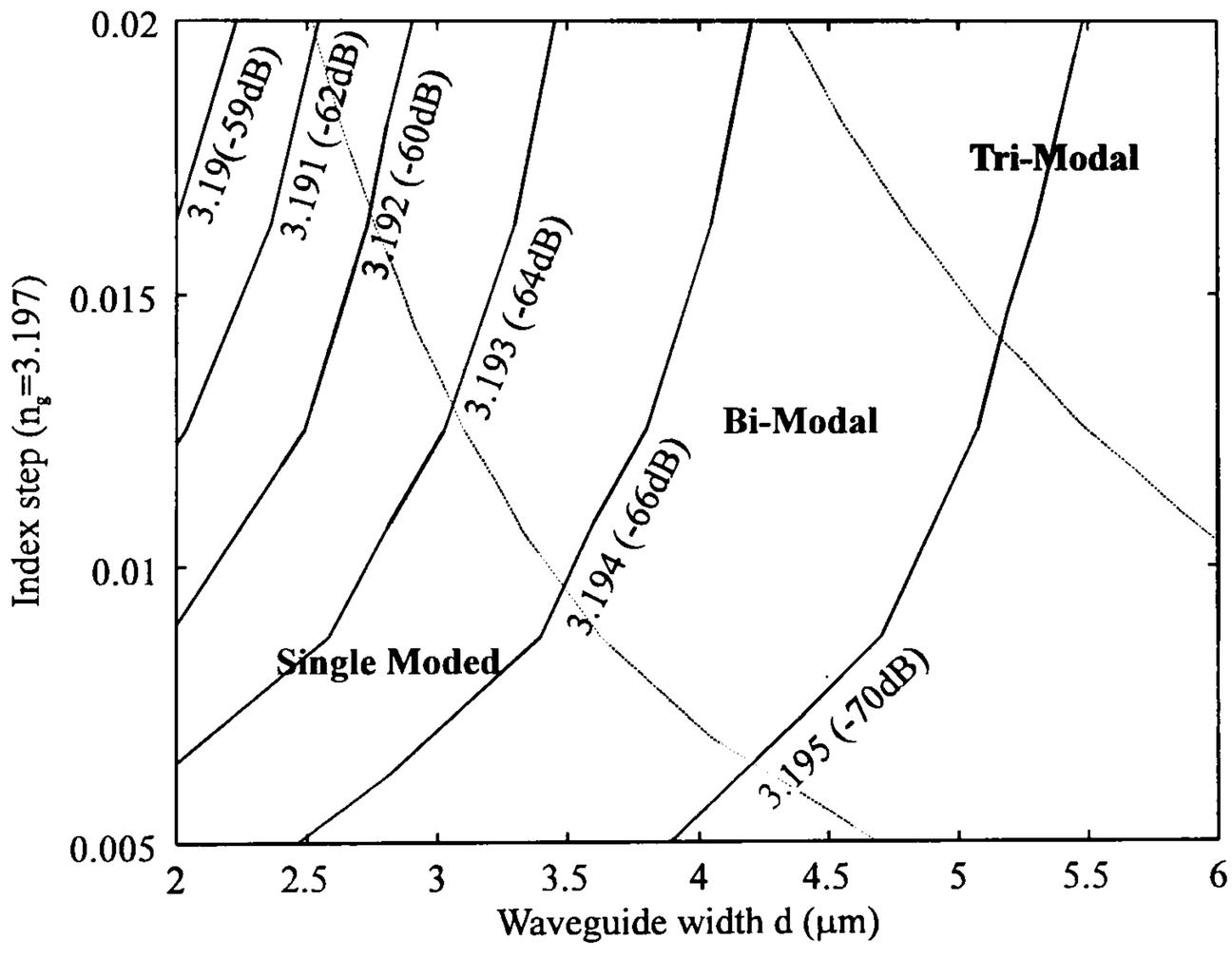

Figure 4.8 Calculation of n_{eff} and hence R from equations 4.5 and 4.6

It may be observed that the reflectivity is very small (<-59dB). As such the first term in equation 4.4 can be ignored, and the crossing loss, $L(\Delta n,d)$, may be determined by only considering the light diffracting across the crossing. This is described mathematically by the overlap integral

$$L(\Delta n,d) = \left| \int_{-\infty}^{\infty} \varphi(\Delta n,d)^* \sum_{n=0}^{n=\infty} C_n G_n(w, z=d) dx \right|^2 \tag{4.7}$$

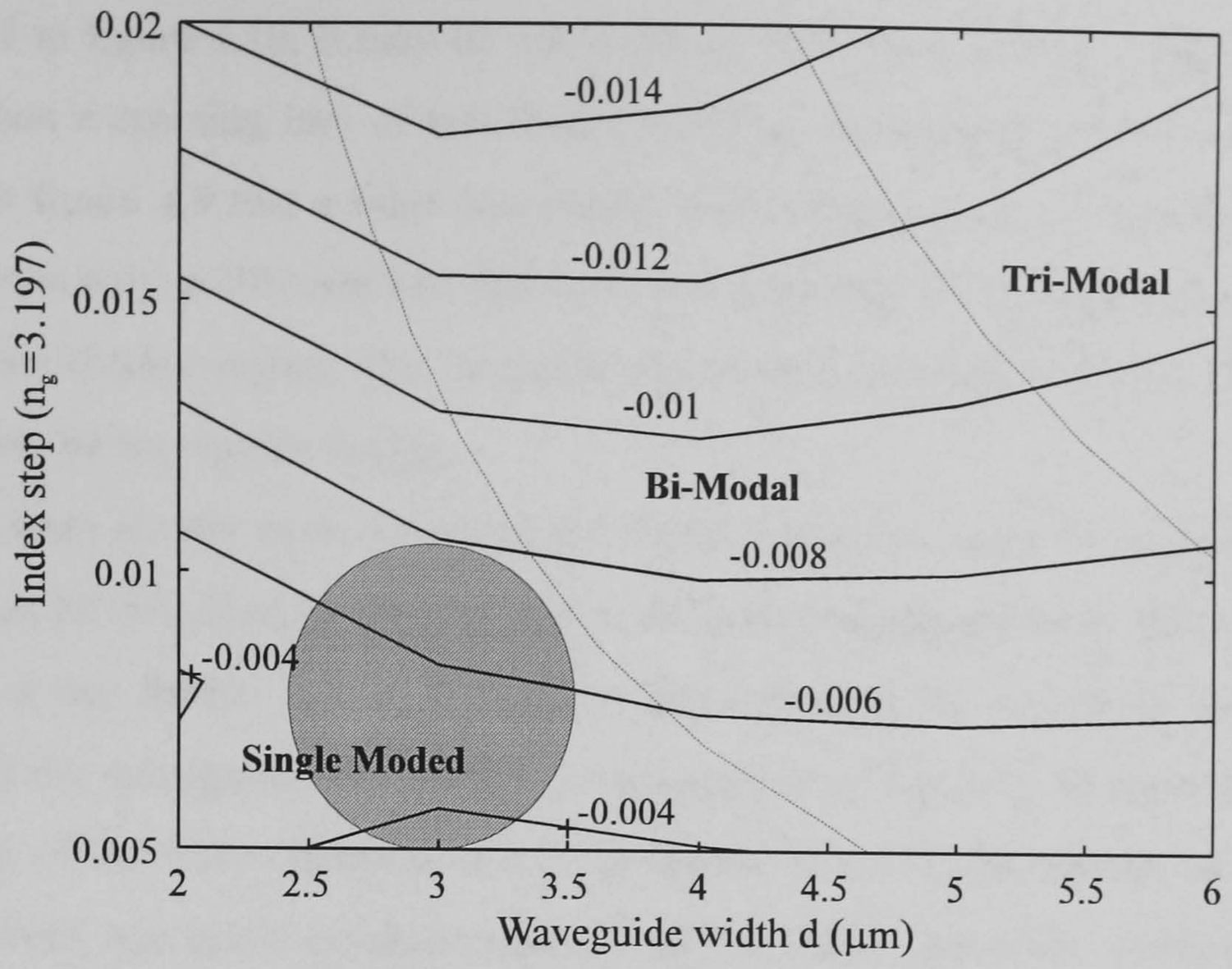

Figure 4.9 Calculation of crossing loss L(Δn,d) in dBs for various waveguide designs

The beam propagation model discussed in Chapter 3 has been used in order to calculate the above equation (for the TE mode only). The result is shown in figure 4.9, where figure *4.6* has been used to indicate the mode cutoff boundaries. It should be noted that strictly the term 'crossing loss' is only accurate in the 'Single Mode' region. Outside this boundary the light coupling into the higher order modes at the other side of the crossing is not considered. Therefore the calculation indicates the amount of power coupled into the zero order mode rather than a 'crossing loss'.

Assuming that the number of waveguide crossings in the architecture is proportional to N^2-N (which is an over estimate), the total crossing loss may be determined as a function of N.

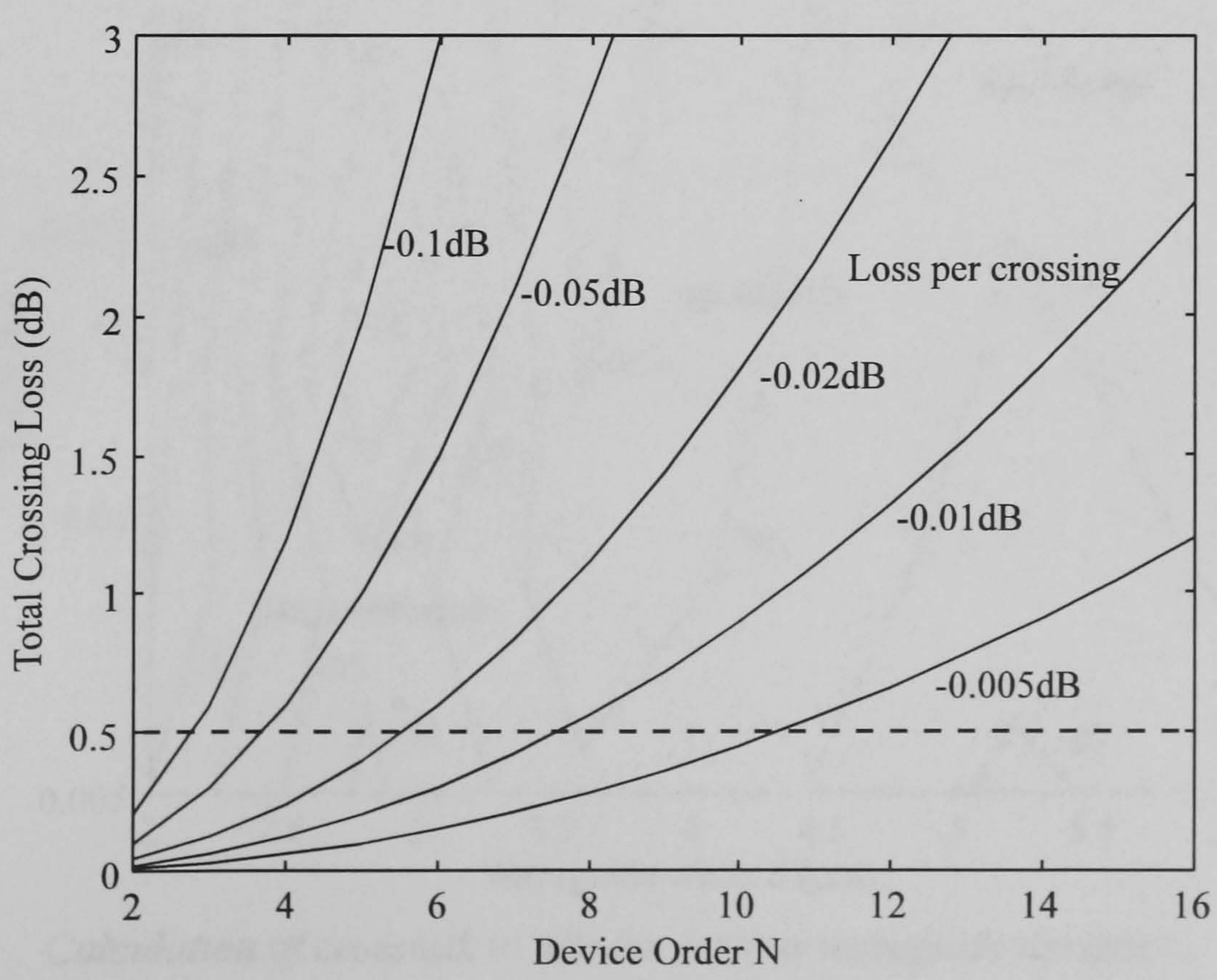

Figure 4.10 Variation of crossing loss as a function of device order, N.

This is plotted in figure 4.10, it may be noted that in order to achieve a 0.5dB penalty for an 8x8 device, then a crossing loss of less than 0.01dB per crossing is required. Thus it can be observed from figure *4.9* that a ridge waveguide of the order of 3μm wide and with an index step of approximately $0.005<\Delta n<0.01$ has both low crossing loss and is mono-mode, this is indicated by the shaded region. The crosstalk due to each crossing will now be discussed in order to finalise the waveguide design.

It has been already been discussed in Chapter 2 that the origin for crosstalk in crossing waveguides can be described by the ray picture of light propagating down the guide. This idea may be taken a step further in a more rigorous calculation by the use of the overlap integral. Assuming that the waveguides are weakly guided such that they may be approximated by the scalar solution of the wave-equation, it may be shown [22] that the amount of optical power which leaks from one guide (eigenfunction $\psi(\Delta n,d,x)e^{-kz}$) to the other guide (eigenfunction $\psi(\Delta n,d,z)e^{-kx}$) may be deduced from the equation

$$\chi(\Delta n,d)=\left|\int_{-\infty}^{\infty}\int_{-\infty}^{\infty}\varphi(\Delta n,d,z)e^{-ikx}\varphi(\Delta n,d,x)e^{-ikz}dxdz\right|^2 \qquad (4.8)$$

where $\chi(\Delta n,d)$ is the fraction of power which leaks into the crossing waveguide. Hence, assuming that the maximum number of crossings in an NxN cross-connect is N^2-N, the maximum crosstalk penalty can be estimated from $(N^2-N)\chi(\Delta n,d)$. This is plotted in figure *4.11* for an 8x8 device. It can be observed that for the majority of waveguide geometries the crosstalk is negligible (<-60dB).

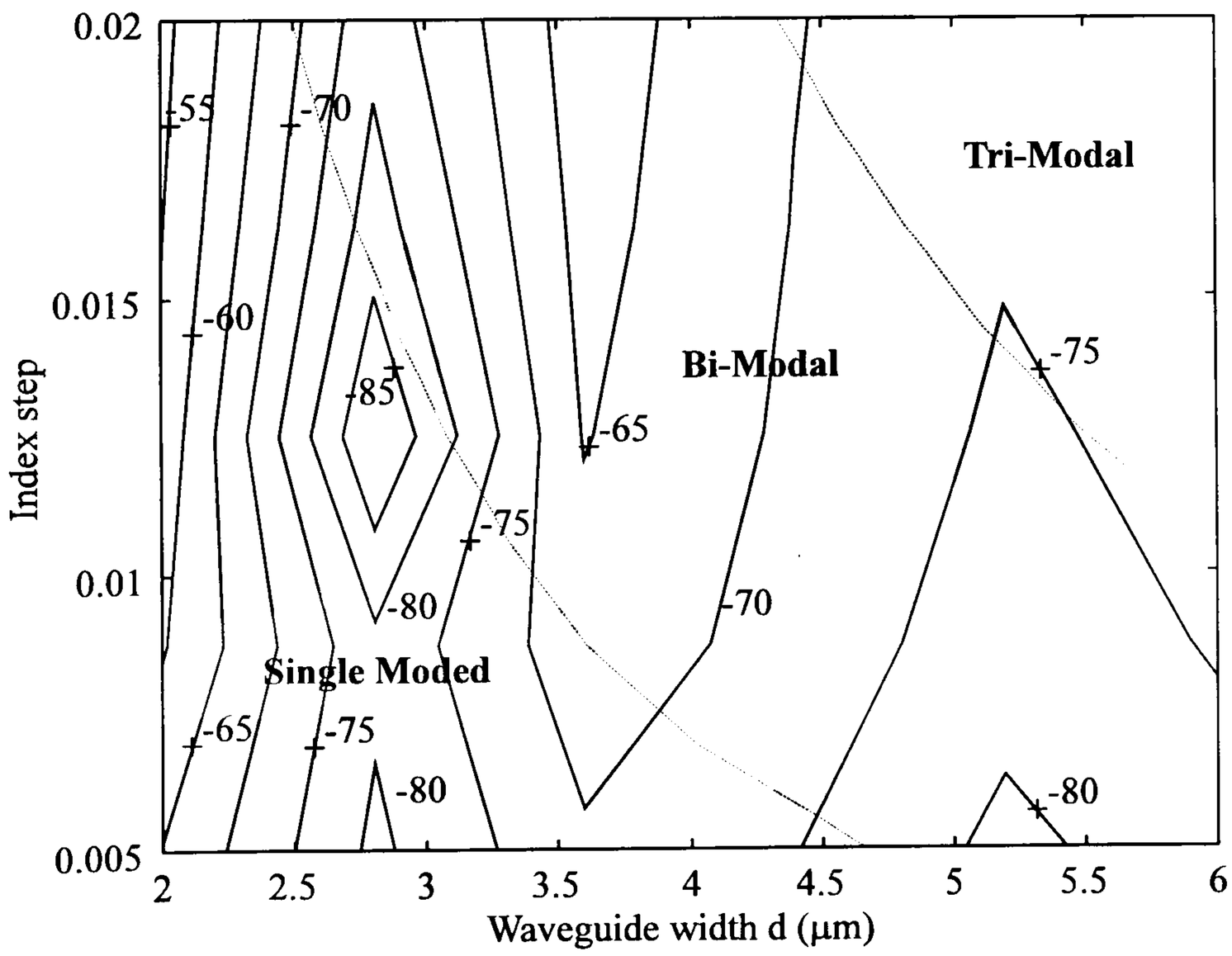

Figure 4.11 *Calculation of crosstalk in dBs for various waveguide designs*

Thus it is concluded that the most suitable ridge guide for the crosspoint design consists of a ***d=3±0.25μm*** wide guiding ridge with an index step of approximately ***Δn=0.010±0.005***. From figure 4.5 it may be observed that this equates to an etch depth of approximately ***e=1.20±0.05μm***. This results in a crossing loss of approximately -0.008dB per crossing and with a crosstalk penalty of the order of -75dB across the total waveguide matrix.

4.3.4 Crosstalk in the waveguide matrix

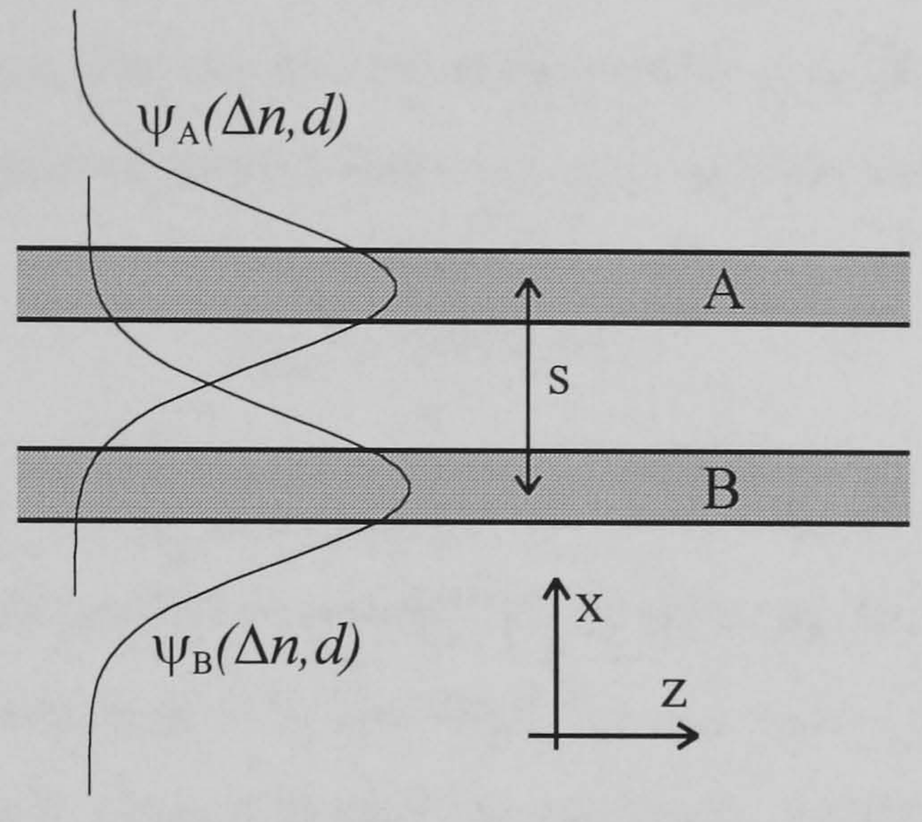

Figure 4.12 Waveguide coupling between two parallel running waveguides A and B.

Crosstalk from the numerous waveguide crossings in the waveguide matrix is not the only source of crosstalk in the device. Unwanted power may also be transferred between two parallel running waveguides, *A* and *B*, via their evanescent tails. This is shown schematically in figure 4.12. The power coupling therefore determines the minimum separation, *s*, which two parallel running waveguides may be separated by in the waveguide matrix. The power coupling can be determined by coupled mode theory [23]. In order to simplify the calculation it assumed that the waveguides are identical and far enough apart such that the solution of the wave-equation can be represented by the local modes propagating in each waveguide. If all the optical power is initially in guide *B,* the power coupled into guide *A, P_A*, can be shown to be of the form [24]

$$P_A = P_B \sin^2 C_{AB} z \tag{4.9}$$

where C_{AB} is the coupling factor between mode *A* and *B*, which is given by

$$C_{AB} = \frac{\varepsilon_0 \omega}{2}(2n_g \Delta n - \Delta n^2) \int_{-\frac{d}{2}}^{\frac{d}{2}} \psi(x - \frac{s}{2}) \psi^*(x + \frac{s}{2}) dx \tag{4.10}$$

where *s* is the centre to centre waveguide separation and ε_0 is the electric permitivity in free space. The coupling length, z_c, the distance over which all the power in waveguide B is

transferred to waveguide A, may be determined from C_{AB} and is given by $2\pi/C_{AB}$. This has been plotted as a function of the waveguide separation, *s*, in figure 4.13 for the optimum shallow etched waveguide design discussed in the previous section (i.e. $d=3.00\pm0.25\mu m$, $\Delta n=0.010\pm0.005$).

For a given waveguide separation, it is apparent from equation 4.9 that the longer two waveguides travel next to each other, the greater the power coupling between them and hence the greater the crosstalk. Thus in order to calculate the device crosstalk the total distance, z_{max}, that two waveguides run along side one another in the device is required. It may be shown that in the case of the *NxN* crosspoint discussed here, z_{max} may be estimated from

$$z_{\max} = 2N^2 s + L \tag{4.11}$$

where *N* is the switch order, which is assumed to be $N=8$, and the length of the modulator region, *L*, is approximately $500\mu m$. The coupling length required for a crosstalk value of -30,-40 and -50dB may then be calculated from equations 4.9 and 4.11. This is also shown in figure 4.13, the intersection of both lines indicates the optimum waveguide separation for the required crosstalk value. It can be observed from figure 4.13 that a waveguide fabricated to within $d=3.0\pm0.5\mu m$ and an etch depth $e=1.20\pm0.05\mu m$ requires waveguide separations, *s*, of the order of 10-15μm to reduce the crosstalk to below -50dB. A final value of *s* is chosen to be 20μm, in order to accommodate the TIR (total internal reflecting) mirrors in the waveguide matrix. The design of these mirrors will now be discussed in the next section.

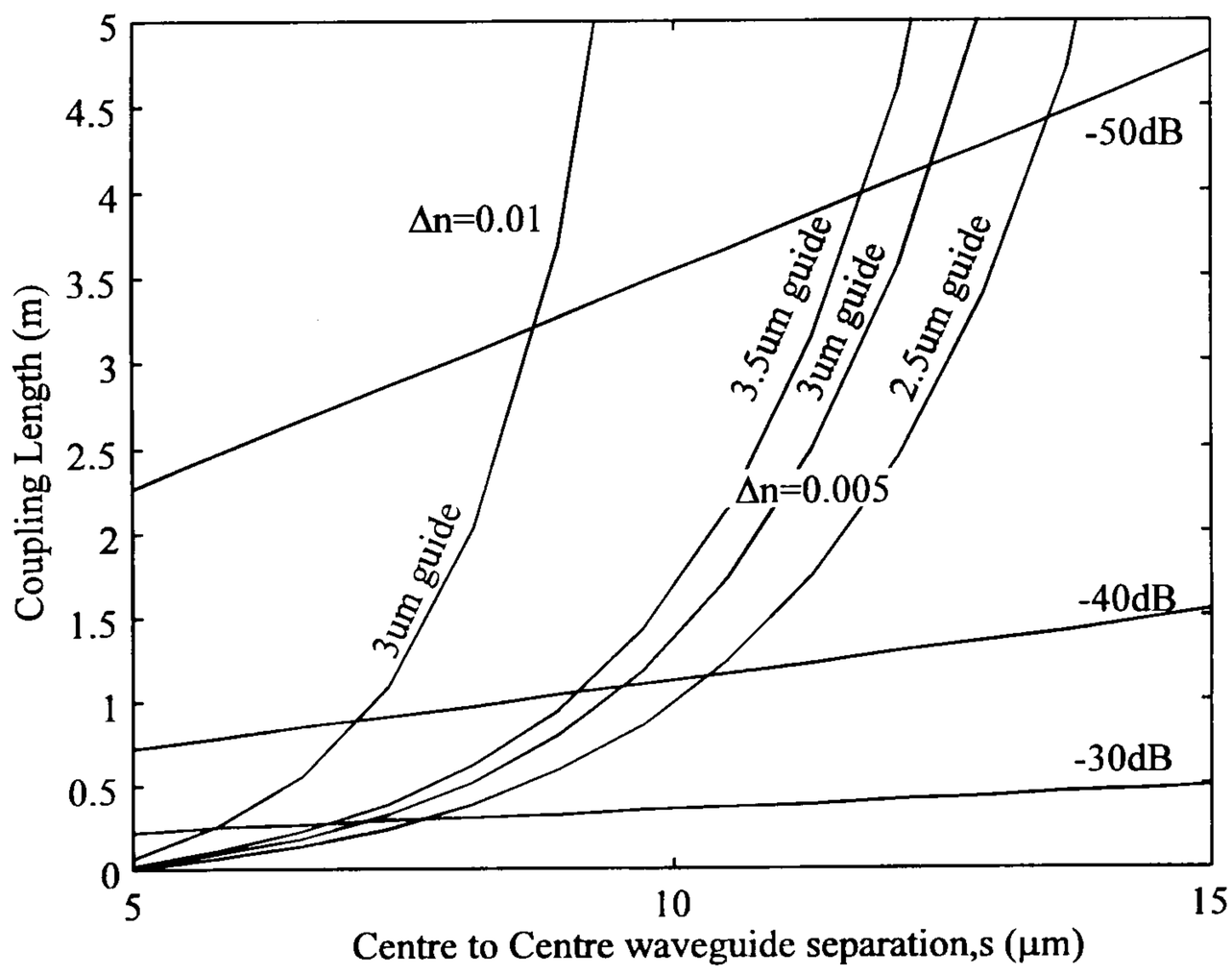

Figure 4.13 Calculation of waveguide crosstalk between two parallel running waveguides

4.3.5 Total Internal Reflecting Mirror Operation

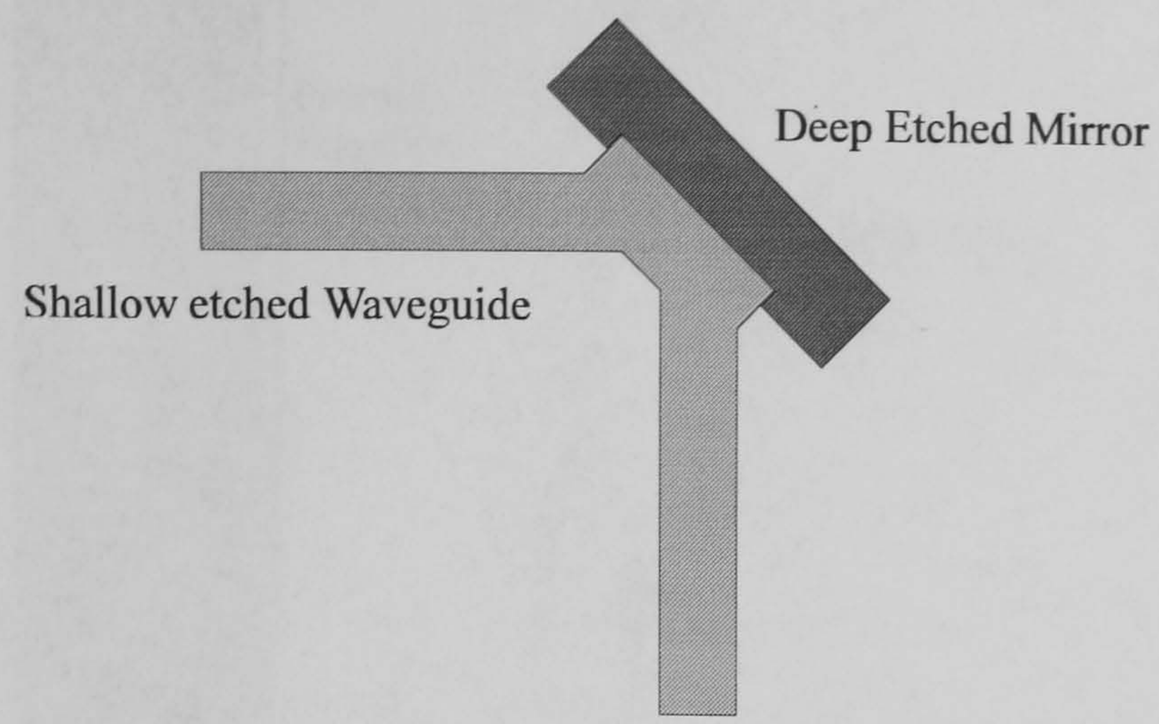

Figure 4.14 Self Alignment of the deep Mirror Etch with the Shallow etched ridge waveguide

The compact size of the waveguide crosspoint is achieved by the use of the Total Internal Reflecting (TIR) mirror [25]. The mirror is capable of steering the beam by 90^0 by virtue of the large refractive index step from InP to air formed by the deep etched mirror. The critical angle, θ_c, may be calculated for the InP/Air interface from the equation

$$\sin\theta_c = \frac{1}{n_{eff}} \tag{4.12}$$

where n_{eff} is the effective index of the propagating mode in shallow etched waveguide. This has been calculated previously to 3.197 for TE_{00} and 3.195 for TM_{00}. This equation predicts a critical angle of approximately 17° for both polarisations. According to the Fresnel equations [20] plane waves incident on the interface above the critical angle will be reflected off the mirror. It is well understood that the distribution of plane waves contained within the incident waveguide mode may be deduced from the fourier transform of the propagating eigenmode. This has been calculated in figure 4.15 and compared with the Fresnel reflection equation for parallel electric field (TE). It may be observed that classically the eigenmode consists of a spread of planes waves propagating approximately 20° above and below the incidence angle. Furthermore, for a 45° turning mirror almost all the incident power is above the critical angle and can therefore be reflected off the mirror.

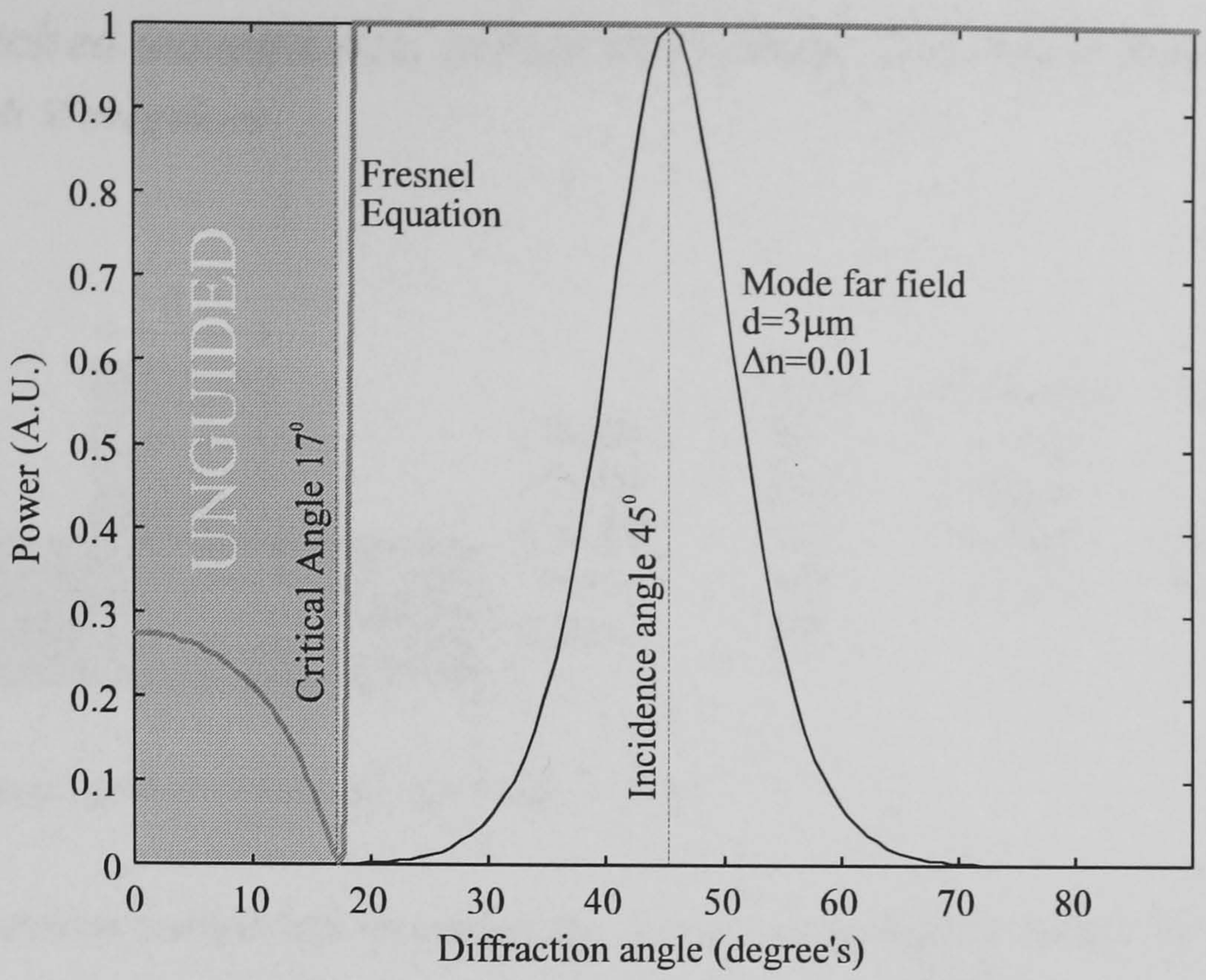

Figure 4.15 Estimation of the TIR mirror performance

A more rigorous theoretical calculation has shown that potentially a very low loss TIR mirror can be realised, <0.08dB [26]. However, it is found that practically it is currently impossible to achieve such a low loss. This is due to three fabrication limitations

1. It is very difficult to achieve a perfectly vertical side wall to form the deep mirror etch [27]. Typically a wall angle of approximately 1° can be achieved.
2. The Roughness on the sidewall due to the quality of the mask used during the dry etching of the mirror also introduces a scattering loss to the reflected field [28].
3. Photolithographic misalignment errors between the deep and shallow etches contributes other losses to the TIR mirror [26].

As such it is found that practically that the losses expected by such a mirror is of the order of 1.0-1.5dB [29]. No theoretical calculations have been made to optimise the mirror design here. Instead a TIR mirror design optimised experimentally by BT research laboratories has been used in the crosspoint design.

4.4 Deep Etched waveguides, MMIs and Mode Converter Design

4.4.1 Deep Etch Waveguides

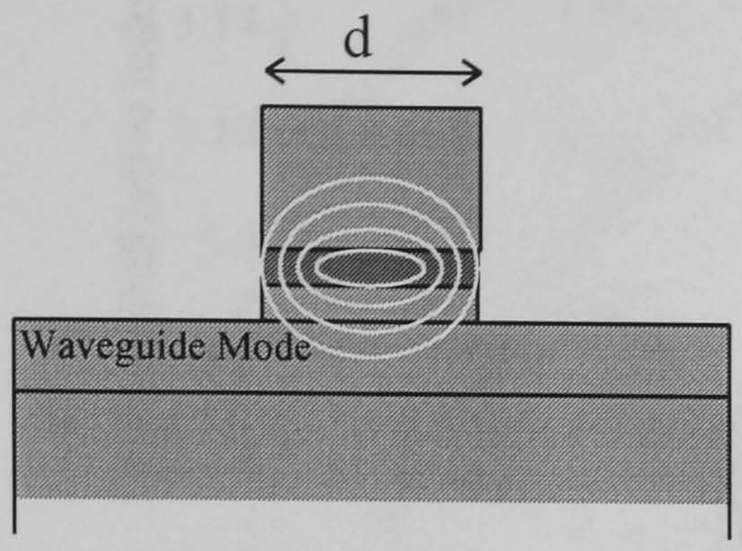

	Material	Width (μm)	Index
Cladding	InP	1.5μm	3.157
Guide	Q1.1	0.4μm	3.282
Cladding	InP	0.5 μm	3.157
Buffer	InP	1.0 μm	3.157
Substrate	InP		3.157

Figure 4.16 Deep etched waveguide sections

The previous section has discussed the optimum waveguide design for the waveguide matrix section of the crosspoint. This section will now discuss the deeply etched regions which allow the compact splitting and combining of the input and output signals. Also, an analysis of the mode converters which allow low loss coupling between the deep and shallow etched sections are also considered.

Firstly the zero order modal cutoff is investigated for the deep etched waveguide shown schematically in figure 4.16. This calculation is slightly different to modal cutoff for the shallow etched waveguide previously discussed in section 4.3.2. In a shallow etched waveguide, the cutoff waveguide width, d_{cutoff}, is determined when the effective index of the first order mode drops below cladding index, n_c (as shown in figure *4.4*). At this point the mode leaks out laterally into the slab and is no longer guided. However, in a deep etched waveguide, n_c is effectively air which is equal to 1 and therefore has no chance of leaking laterally. Instead, cutoff is determined by an effect called substrate leakage [30]. This may be more clearly examined by considering figure 4.17, where the effective indices of the higher order TE and TM modes have been calculated as a function of waveguide width, *d*, using the effective index method previously described in section 4.3.2. It may be observed that as the waveguide width is reduced, the effective index of each mode tends to $n_c=1$ which is expected. However, when the effective index of the mode drops below the substrate index ($n_{sub}=3.157$) the mode is no longer guided since total internal reflection is not satisfied vertically. As such it may be observed from figure 4.17 that the first order TE and TM modes are cutoff with waveguide widths approximately less than 2.8μm, similarly 4.6μm for TE_{02} and TM_{02}. Therefore in order to ensure that the deep etched sections remain single moded, a conservative value of 2μm is chosen for the deep etched waveguide width.

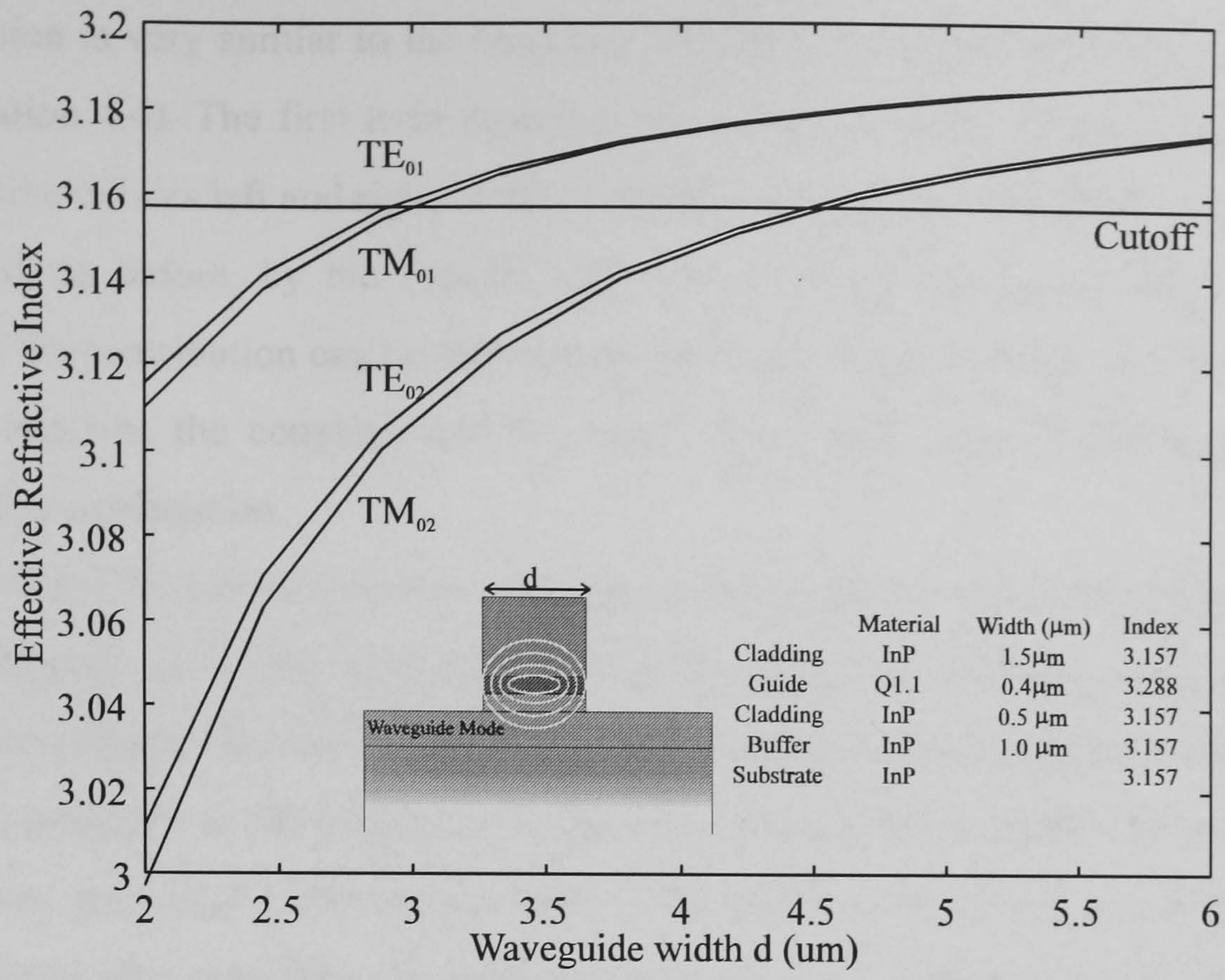

Figure 4.17 Cutoff of a deep etched waveguide

A low loss transition is therefore required between the shallow etched ridge waveguide of width 3μm with an index step of 0.01±0.005 and the deep etched waveguide of width 2μm. This can be achieved by a tapered waveguide structure, of which there are many kinds, notably linear [31], parabolic [32],and exponential [33]. The idea is simply to vary the waveguide width by the corresponding mathematical function in order to reduce the loss over the transition. Here a linear taper is considered as shown schematically in figure 4.18.

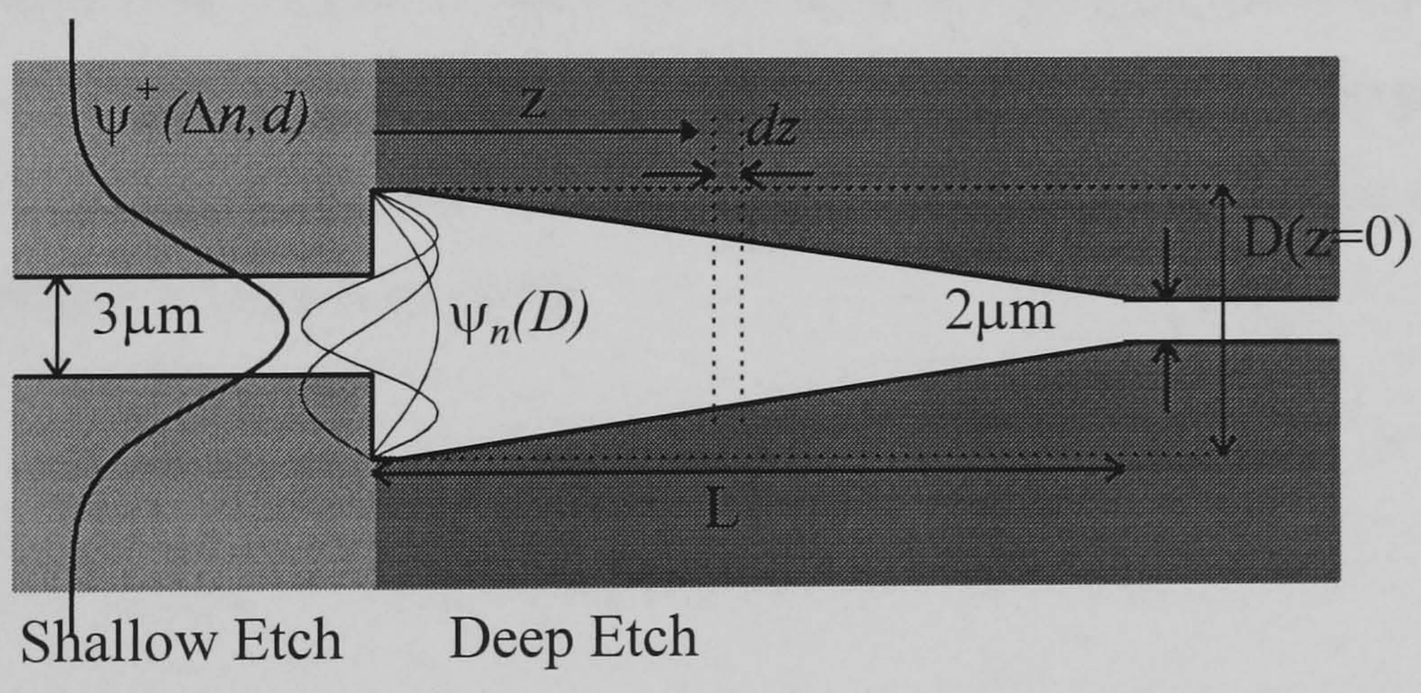

Figure 4.18 Linear Tapered mode converters

If the shallow etched mode propagating from left to right is described by the function $\psi^{+}(\Delta n,d)$, and $\psi_n(D)$ describes the n^{th} order mode propagating in the deep etched section, the boundary condition at the interface is given by

$$\psi^{+}(\Delta n,d) = r\psi^{-}(\Delta n,d) + \sum_{0}^{N} C_n \psi_n(D) + \sum_{m=0}^{\infty} C_m \psi_m \qquad (4.13)$$

This expression is very similar to the boundary condition for a waveguide crossing discussed earlier (equation 4.4). The first term describes the reflection at the interface due to differing modal effective indices left and right of the boundary, where *r* is the field reflectivity. It can be approximated, as before, by the Fresnel reflection at normal incidence which is given by equation 4.5. Its contribution can be shown negligible and therefore is ignored. The second and third terms describe the coupling into the deep etched taper right of the boundary, which requires further explanation.

Marcuse [34] has shown that a waveguide taper can be approximated by a staircase. Provided each step, *dz*, is very small such that the 'local' waveguide width, *D(z)*, in each step is approximately constant and the 'local' waveguide modes can be calculated in each section. If the 'local' waveguide at the beginning of the taper (which has a width *D(z=0)*) supports *N* **guided** modes, then $|C_n|^2$ in the second term is the power coupled into the n^{th} guided mode. $|C_m|^2$ in the third term represents the power coupled into each **radiation** mode. Hence ignoring the interface reflection (which is very small - see figure *4.4*) the percentage power loss across the boundary is given by

$$\sum_{m=0}^{\infty}|C_m|^2 = 1 - \sum_{0}^{N}|C_n|^2 \qquad (4.14)$$

In order to analyse the taper structure rigorously, equation 4.13 may then be applied to every section, *dz*, along the taper [35]. The total taper loss may then be deduced from the summation of losses in each section (in the limit $dz \rightarrow 0$) which may then be calculated from equation 4.14. No attempt is made here in order to optimise the taper loss. Instead, a more intuitive approach is taken where the initial loss from the 3μm shallow etched waveguide to the *fundamental* deep etched waveguide mode is maximised (by optimising *D*). This loss may be deduce from the boundary condition 4.13, and is given by

$$C_{n=0} = \int_{-\infty}^{\infty}\psi^{+}(\Delta n, d)\psi_{n=0}(D)dx \qquad (4.15)$$

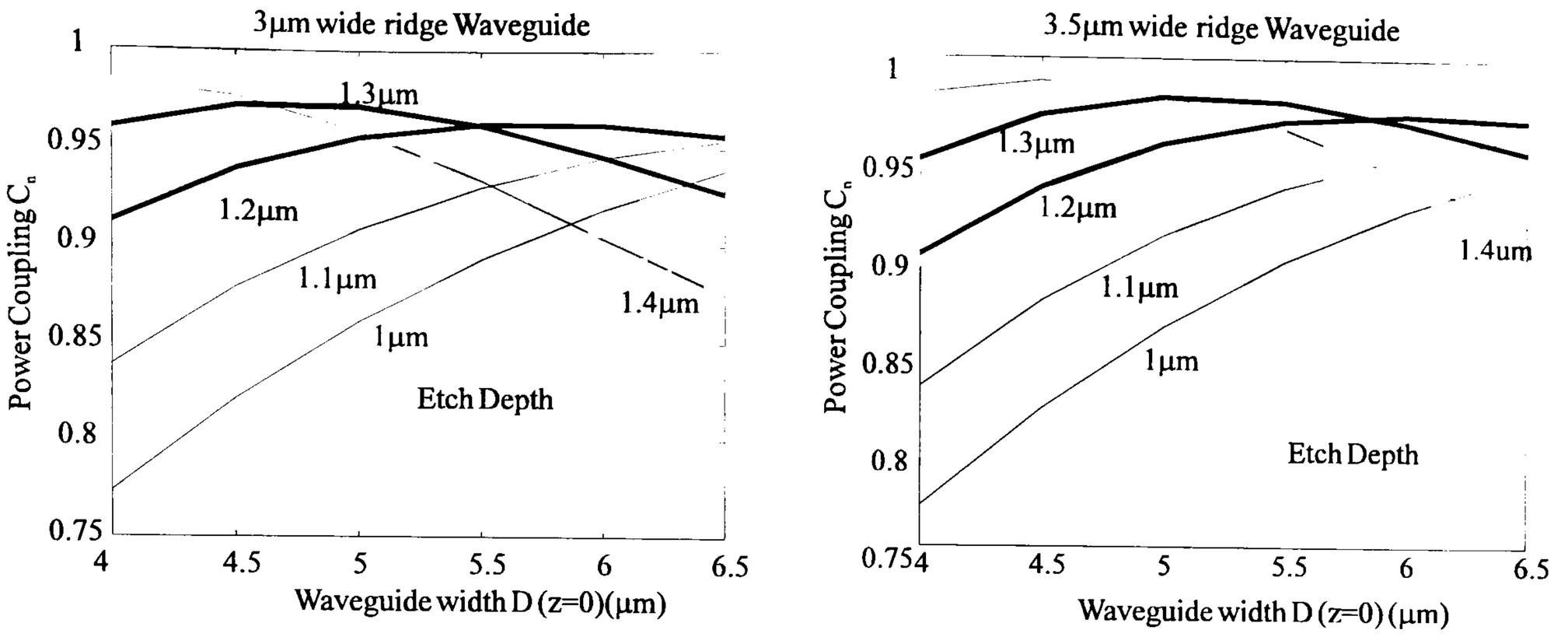

Figure 4.19 Optimisation of Initial taper width, D(z=0), for two shallow etched ridge widths.

This function is plotted in figure 4.19 for two shallow etched waveguide widths, 3.25±0.25μm. It may be observed that the coupling coefficient is maximised for *D(z=0)=5.5±0.5μm*. The waveguide width, *D*, may then tapered down to a 2μm single mode guide. To provide a low loss transition, the taper must operate adibatically. In other words, the zero order 'local' mode must propagate through the taper without a cumulative power transfer to the higher order 'local' modes. It has been suggested by Milton *et al* [32] that adiabatic operation is obtained when

$$\theta(z) < \frac{\lambda_{eff}(z)}{2D_{eff}(z)} \tag{4.16}$$

where, θ is the taper wall angle, λ_{eff} is the effective wavelength (λ_0/n_{eff}) of the zero order mode at a position *z* along the taper, and D_{eff} is the effective width of the mode. This function has been plotted in figure 4.20 for various deep etched waveguide widths, *D*. It should be noted from figure 4.20 that the linear taper angle is constrained by the adiabatic operation of the widest end of the mode converter. An optimum taper would initially vary slowly with a gradual increase in taper angle towards the narrow end (a taper function given by the integral of figure 4.20). Indeed, this is why the parabolic and exponential tapers are found in the literature, and have been shown to require shorter taper lengths compared with linear tapers [32]. However, since only a taper of the order of 5μm to 2μm is required in this application, the extra complexities involved in fabricating these more advanced taper structures complicate the design. Therefore, it may be observed from figure 4.20 that the mode converter discussed here requires a taper angle of the order of 2-3°. It has been shown experimentally that deep etched tapers on InP, with taper angles of less than 2° have yield negligible losses (<<0.5dB) [36]. This results in taper lengths, *L*, of the order of a 100μm.

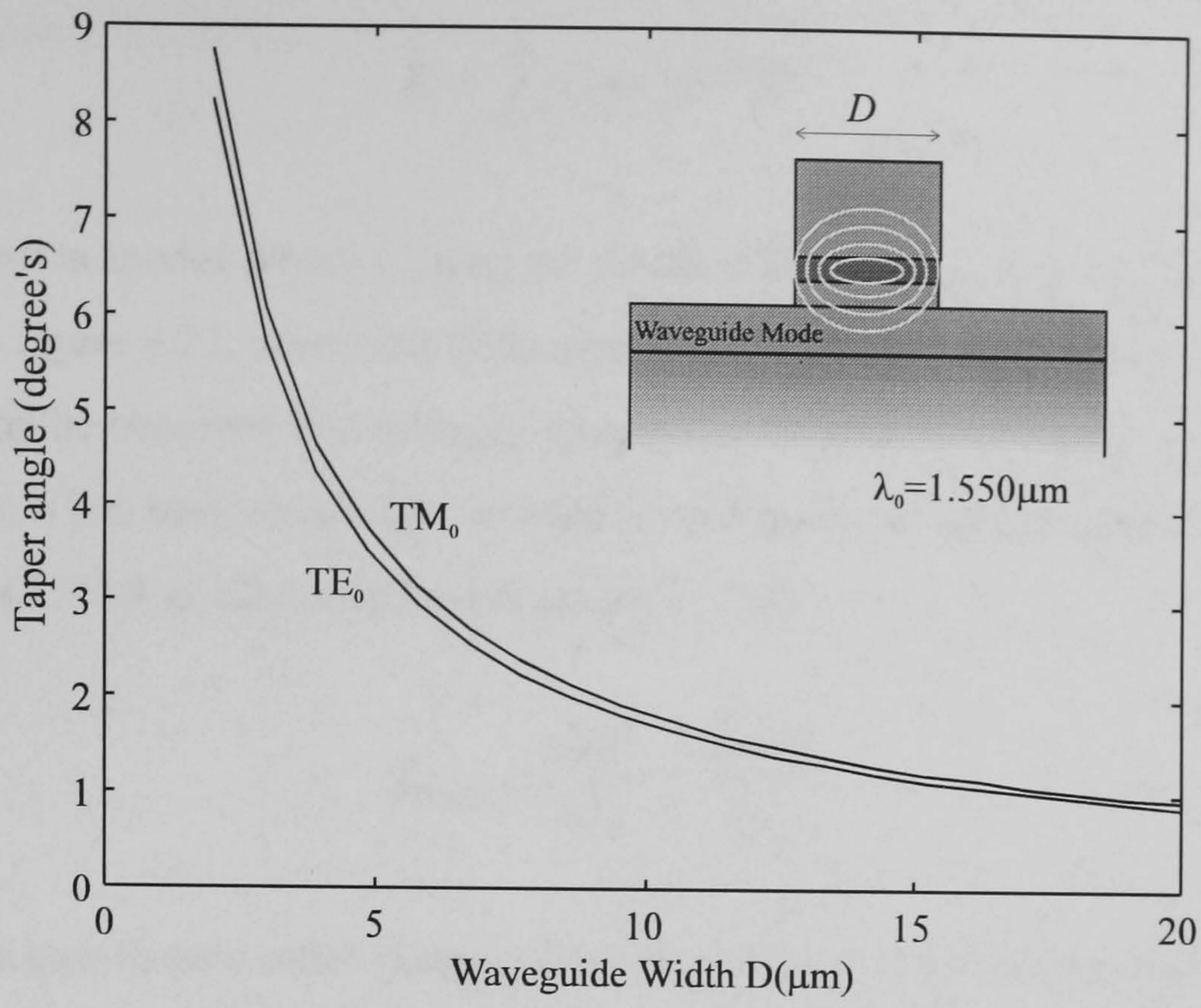

Figure 4.20 Adiabatic Operation of a taper for TE and TM Polarisations

4.4.2 Multimode Interference coupler (MMI) design

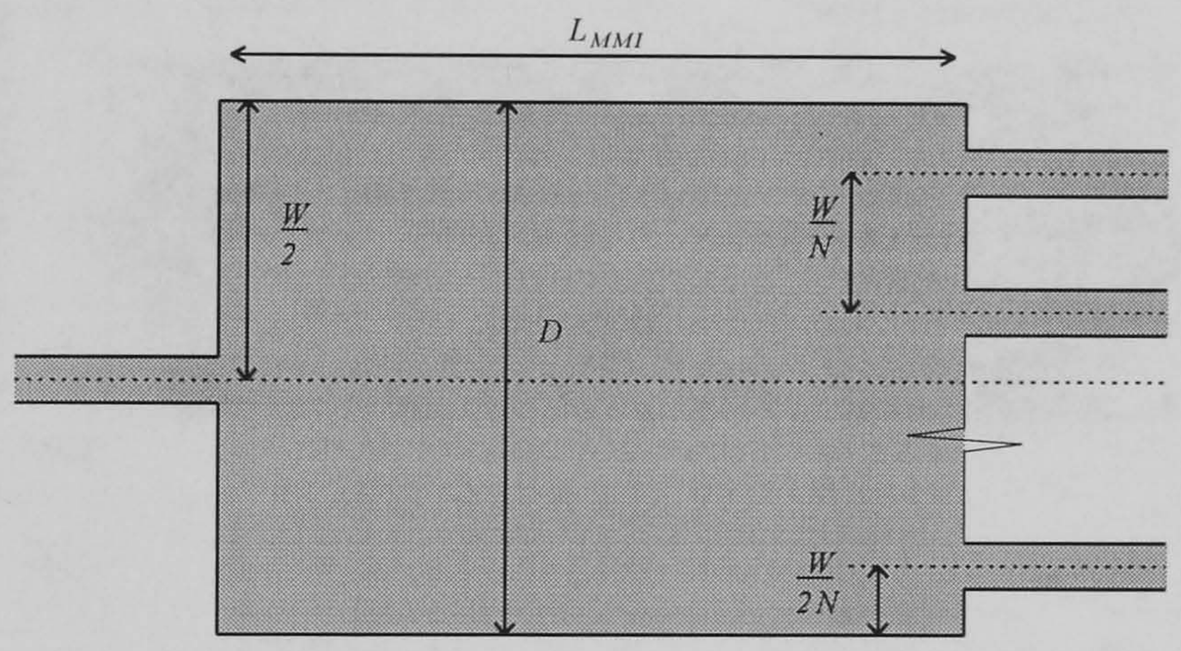

Figure 4.21 Schematic Diagram of a 1xN Multimode Interference Coupler

The proposed method of splitting in the crosspoint is achieved by the use of Multimode Interference couplers (MMIs), as shown schematically in figure 4.21. The coupler consists of one input waveguide and *N* output waveguides joined via a multimoded waveguide of length L_{MMI} and width *W*. Provided the length, L_{MMI}, is accurately controlled, efficient *1xN* coupling can be achieved. This can be shown by analysing the performance of the MMI mathematically, a description of which is not discussed here. The reader is directed towards several excellent papers on the subject [37-40]. However, the field distribution inside the MMI may be calculated by calculating the effective index, $n_{eff\,n}$ of each guided mode, ψ_n, in the multimode waveguide. The field at each section along the cavity, *E(z)* may then be deduced from the equation [37]

$$E = \sum_{0}^{N} C_n \psi_n e^{-ik_0 n_{eff\,n} z} \tag{4.17}$$

(ignoring radiation modes where C_n may be deduced from equation 4.13). This function has been plotted in figure 4.22, where the field intensity along a $W=16\mu m$ MMI coupler has been calculated. It can be observed that multiple images can be formed along the coupler at discrete coupler lengths. It has been shown that in order to split power N ways a coupler length L_{1xN} for a strongly guided MMI as discussed here is given by, [37]

$$L_{1xN} = \frac{nW^2}{N\lambda_0} \pm \frac{\pi n w_0^2}{4\lambda_0} \tag{4.18}$$

where, w_0 is the best fit zero order Hermite-Gaussian mode to the MMIs optical input, and λ_0 is the free space operating wavelength.

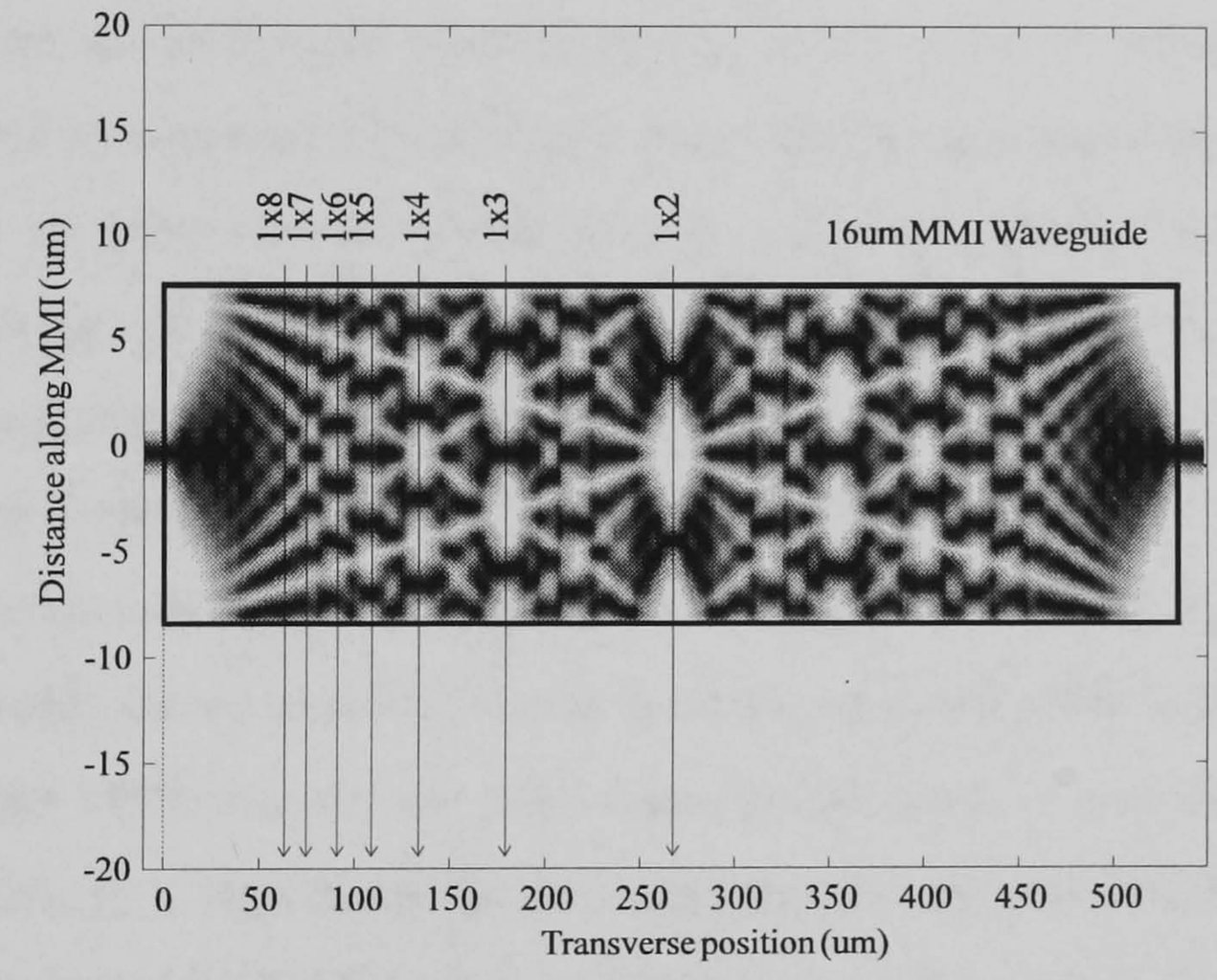

Figure 4.22 Splitting operation of an InP deep etched Multimode Interference Coupler

A tolerance factor has been introduced in equation 4.18. This is the length over which efficient 1xN power splitting may be achieved to within 0.5dB [39]. It may also be observed that there is a quadratic dependence of the MMI waveguide width, W, with length. It is found that this dependence imposes strict limitations on what MMI designs may be fabricated. Equation 4.18 may be written in terms of the width tolerance, δW which is described by

$$\delta W = \frac{N\pi w_0^2}{2W} \tag{4.19}$$

Hence, given that with current photolithographic processes the line width control of current resists is of the order of 0.2μm [41], the design of a MMI coupler is fundamentally limited when $\delta W > 0.2\mu m$. Equation 4.18 may also be rewritten in terms of wavelength bandwidth, $\delta\lambda$. This is the operating wavelength over which the coupler will operate with a 0.5dB penalty [39].

$$\delta\lambda = \frac{N\pi w_0^2}{2W^2}\lambda \tag{4.20}$$

Equations [4.18-4.20] are extremely important in MMI design. They will now be used in order to optimise a *fabrication tolerant* coupler for the crosspoint.

It has already been shown that the output waveguides of the coupler are to be spaced by 20μm. The MMI coupler could be used to both simultaneously split the input and space the output waveguides (such that the waveguide width is given by $W=20N\ \mu m$). The quadratic dependence of the MMI width on the length has already been highlighted. As such it may be shown that designing the MMI in this way would lead to coupler lengths in excess of 5mm. Also the fabrication difficulties in maintaining the MMI width to sub-micron accuraracies (which are predicted by equation 4.19) for such long MMI lengths make the coupler unfeasible. In order to design an MMI coupler which is a lot more fabrication tolerant, the MMI width must be reduced along with the output waveguide separation. S-Bend waveguides may then be used in order to separate the output waveguides to the required 20μm. The design of these bends are discussed in the next section.

It may be observed from equations 4.19 and 4.20 that both the width tolerance, δW, and wavelength bandwidth, $\delta\lambda$, of an MMI coupler is increased as the MMI width, W, tends to zero. Thus the smaller the MMI is made the more fabrication tolerant it becomes and the larger its operating bandwidth. It is also extremely advantageous to make the MMI width as small as possible in order to make the MMI length as small as possible, as described by equation 4.18. The limiting factor in reducing the MMI width has been shown to be that at least N modes are required to propagate in coupler to achieve efficient splitting to the outputs [37]. Since, here the MMI waveguide is so strongly guided this criteria is almost always satisfied, and the limiting factor imposed on the MMI width is the photolithigraphic process in fabricating the output waveguides. If it is assumed that 2μm is the minimum gap between output waveguides in the coupler (1μm is achievable with current g-line resists [42], however this is extremely difficult), then a 1x4 coupler requires an MMI width of exactly 16μm. This leads to an MMI length of 132±3.3μm over which a width tolerance of $\delta W=0.25\mu m$ is required and results in a wavelength bandwidth of $\delta\lambda=80nm$.

4.4.3 Bend design and optimisation

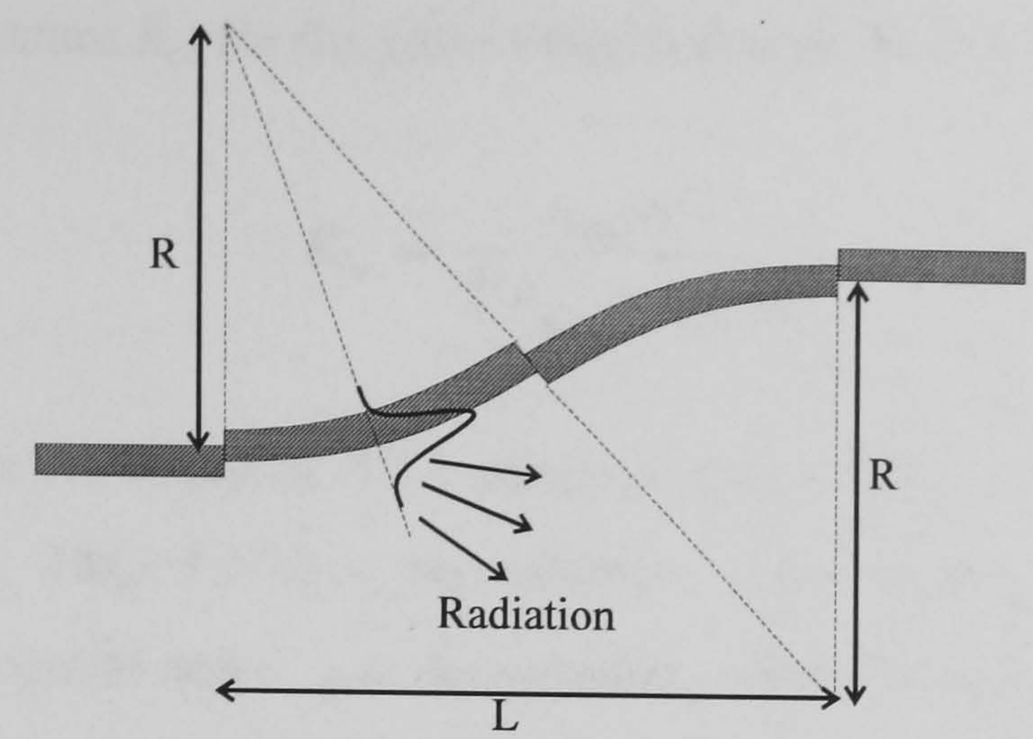

Figure 4.23 S-bend design and optimisation

The use of S-bends is a standard technique for separating the outputs from an MMI coupler. Two arcs of equal radii, *R*, can form an S-shaped curve as shown schematically in figure 4.23. However, a waveguide bend formed by the arc of a circle is a very complicated structure that requires careful optimisation.

Firstly it can be shown that the optical mode propagating in a curved waveguide is skewed towards the outer edge of the bend [43], as shown in figure 4.23. Thus in order to design low loss S-Bends, so that there is efficient coupling between each bend, it is necessary to calculate the amount of skew and offset each waveguide by the correct amount [44]. Alternatively, S-bend designs may be used that do not require offsets (such as Cosine and Linear/Sine [45]) which work by gradually changing the radius of curvature adiabatically. In this case, since the S-bends are so strongly guided, the waveguide offset required to improve the coupling efficiency drops below 0.1μm [40]. This offset is too small to be fabricated by current photolithographic methods, as such a may be ignored.

Secondly, unlike a straight waveguide a bend will always incur an optical loss apart from material absorption [46]. In order for the optical mode to propagate around the bend, the outer tail of the modal field must travel a further distance in order to remain in phase with propagating mode. This is not possible unless the radial refractive index profile is optimised to compensate for the extra path length [47]. In practice changing the refractive index radially is not possible, thus the outer tail radiates as the mode propagates around the bend. The amount of radiation depends on the amount of power in the tail (which depends on the guiding strength and waveguide width) and radius of curvature of the bend. Indeed, if the radius of curvature is below a critical value, R_{co}, known as the cutoff radius of curvature, even the zero order mode of the guide may be cutoff and no light may travel around the bend. However, providing the radius of curvature is large compared with R_{co} the propagation losses can be reduce to an acceptable level. Several methods may be found in the literature in order to calculate the bend loss [46,48-50]. No attempt is made to calculate the exact losses of waveguide bends using the

methods referenced above. Instead a calculation described by [51] is used in order to determine the cutoff radius of curvature R_{co} for the guide described here. This is given by [51]

$$R_{co} = \frac{n_{core} d}{2(n_{eff} - n_{sub})} \tag{4.21}$$

where n_{core} is the refractive index of the waveguide core (*3.282*), d is the waveguide width ($2\mu m$), n_{eff} (TE_0=*3.177*, TM_0=*3.174*) is the effective index of the zero order mode in the equivalent straight waveguide and n_{sub} is the substrate refractive index (*3.157*). Equation 4.21 leads to a cutoff radius of curvature of approximately *190*μm for both TE and TM polarisations. As such S-bends with radii of curvature varying from 100μm to 500μm have been used in the crosspoint designs.

4.5 Device Size

Parameter	Optimised Value
Shallow Etched Waveguide Depth, e	1.20±0.05μm
Shallow Etched Waveguide Width, d	3.0±0.25μm
Waveguide Separation in the matrix, s	20μm
Deep Etched Waveguide width, d	2μm
Mode Converter Width, D	5.5±0.5μm
Mode Converter Taper Length, L	100μm
MMI Width, W	16.00±0.25μm
MMI Length, L_{MMI}	132±3μm
S-Bend Radius of Curvature, R_{co}	>190μm

Table 4.1 Summary of optimised device parameters

The various device parameters discussed in the preceding sections have been summarised in table 4.1. These parameters may then be used to determine the theoretically predicted size of an *NxN* device. It may be shown that the approximate device width, D_y, may be described very simply by the equation

$$D_y = sN^2 \tag{4.22}$$

It should be noted however, that although this is the minimum possible cross-connect size, practically devices are fabricated with a 250μm centre to centre input/output waveguide separation. This eases fibre coupling since ribbon fibre may be used to couple in and out of the device. Thus this equation only holds when $D_y > 250N$ (μm), which has been plotted in figure 4.24. The device length however, cannot be described by such a simple formula and requires more explanation. It may be shown that D_x may be approximated by the equation

$$D_x = 2A + E + 4L + 2\frac{n_{eff}(2Nd)^2}{N\lambda} + 2\sqrt{2R\left[\frac{sN}{2}\right] + \left[\frac{sN}{2}\right]^2} + sN^2 \tag{4.23}$$

where the first and second terms containing A and E represent the length of the semiconductor amplifier and electroabsorption modulator sections (assuming $A=500\mu m$, $E=100\mu m$). The third and fourth terms represent the lengths of the mode converter and a 1xN MMI coupler. It may be shown that the fifth term corresponds to total S-bend length as a function of N ($R=500\mu m$), and the final term represents the approximate length of the waveguide matrix. This function has been plotted together with D_y in figure 4.24.

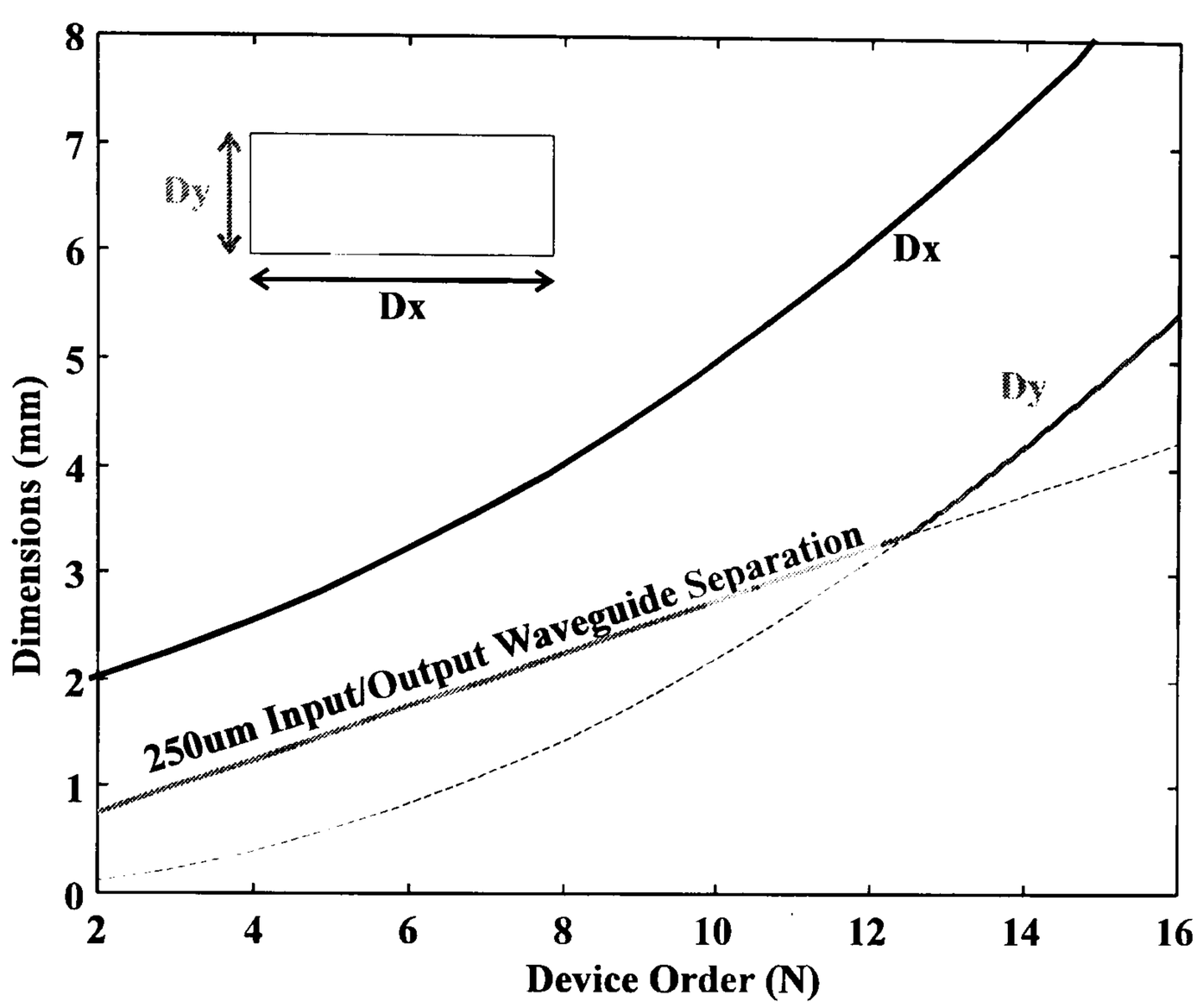

Figure 4.24 Theoretical prediction of device size with device order

It should be noted that in this architecture both the device width and length increase as the square of device order N. Also, as discussed in Chapter 2, the smallest InP based 4x4 broadcast switch reported to date measures $7x3mm^2$, an order of magnitude in area larger than the device reported here. Indeed, ten (and a half) 4x4s or a 12x12 cross-connect implemented using this architecture would occupy a similar wafer area.

4.6 Conclusions

The NxN crosspoint design parameters have been optimised in the preceding sections, which have been summarised in table 4.1. These parameters have been used in order to predict the device size as a function of device order, N, as plotted in figure 4.24. They have also been used to fabricate several test structures in order to validate the theoretical calculations made in this chapter, a discussion of which is given in chapter 5. These test structures allow the losses of each of the components in the device to be analysed independently and enable a prediction of the final device performance to be given in chapter 6.

4.7 References

[1] A. McKee, C.J. McLean, G. Lullo, A.C. Bryce, R.M. De La Rue, J.H. Marsh, C.C. Button, "Monolithic Integration in InGaAs-InGaAsP multiple-Quantum-Well Structures Using Laser Intermiximg" IEEE JQE, Vol. 33, No. 1, January 1997, pp45-55.

[2] N. Bouadma, J. Liang, R. Levenson, S. Grosmaire, P. Boulet, S. Sainson, "Integration of a Laser Diode with a Polymer-Based Waveguide for Photonic Integrated Circuits" IEEE PTL, Vol. 6, No. 10, October 1994, pp118-1190.

[3] S. Mino, K. Yoshino, Y. Yamada, T. Terui, M. Yasu, K. Moriwaki, "Planar Lightwave Circuit Platform with Coplanar Waveguide for Opto-Electronic Hybrid Integration", JLT Vol. 13, No. 12 December 1995, pp2321-2325.

[4] T. Hashimoto *et al*, "Hybrid Integration of Spot-Size Converted Laser Diode on Planar Lightwave Circuit Platform by Passive Alighnment Technique", IEEE PTL Vol. 8, No. 11, November 1996, pp1505-1507.

[5] Y. Yamada, H. Terui, Y. Ohmori, *et al* "Hybrid Integrated 4x4 Optical Gate Matrix Switch Using Silica-Based optical waveguides and LD array Chips", JLT Vol. 10, No. 3, March 1992 pp383-389.

[6] K. Hamamoto, K. Komatsu, "Insertion-loss free 2x2 InGaAsP/InP optical Switch Fabricated using Bandgap Energy Controlled Selective MOVPE", Elec. Lett Vol. 31 No. 20, Spetember 1995, pp 1779-1781.

[7] A. W. Nelson *et al* "The role of MOVPE in the Manufacture of High Performnace InP Based Optoelectronic Devices", J. Crystal Growth, Vol. 93, 1988, pp792-802.

[8] J.D. Burton, P.J. Fiddyment, M.J. Robertson, P.C. Sully, "Monolithic InGaAsP-InP Laser Amplifier Gate switch Matrix", IEE JQE, Vol. 29, No. 6, June 1993, pp2023-2027.

[9] G. Sherlock, J.D. Burton, , P.J. Fiddyment, P.C. Sully, A.E. Kelly, M.J. Robertson " Integrated 2x2 Optical Switch with Gain", Elec. Lett. Vol. 30, No.2, January 1994, pp137-138.

[10] Dietricht Marcuse "Light Transmission Optics Second Edition" Van Nostrand Reinhold Company

[11] T.M. Benson, R.J. Bozeat, P.C. Kendall, "Rigorous Effective Index Method For Semiconductor Rib Wave-Guides", IEE Proceedings-J Optoelectronics, 1992, Vol.139, No.1, pp.67-70.

[12] K.S. Chiang, "Performance Of The Effective-Index Method For The Analysis Of Dielectric Wave-Guides", Optics Letters, 1991, Vol.16, No.10, pp.714-716.

[13] J.S. Lee, S.Y. Shin,"On The Validity Of The Effective-Index Method For Rectangular Dielectric Wave-Guides", Journal Of Lightwave Technology, 1993, Vol.11, No.8, pp.1320-1324.

[14] Dietricht Marcuse "Theory of Dielectric Optical waveguides - Second Edition" Academic Press Inc. pp330.

[15] 'Guides' Pascal Program, University of Glasgow 1990.

[16] Dietricht Marcuse "Light Transmission Optics Second Edition" Van Nostrand Reinhold Company pp310

[17] D.L. Lee, "Electromagnetic Principles of Integrated Optics", John Wiley & Sons 1986.

[18] A.W. Snyder, J.D. Love "Optical Waveguide theory" Chapman and Hall pp704

[19] Dietricht Marcuse "Light Transmission Optics Second Edition" Van Nostrand Reinhold Company pp327

[20] E. Hecht, "Optics- Second Edition", Addison-Wesley Publishing Co. 1989, Chapters 4.

[21] Dietricht Marcuse "Light Transmission Optics Second Edition" Van Nostrand Reinhold Company pp308

[22] J.D. Love, F. Lacouceur, "Excess Loss in singlemode Right-Angled X Junctions", Electronics Letters, Vol. 28, No. 3, January 1992, pp 221-223.

[23] Dietricht Marcuse "Light Transmission Optics Second Edition" Van Nostrand Reinhold Company.

[24] D.L. Lee, "Electromagnetic Principles of Integrated Optics", John Wiley & Sons 1986 pp221-231.

[25] P. Bachmann, H. Kaufman, "GaAs Single-mode rib Waveguides with Reactive Ion-Etched Totally Reflecting Corner Mirrors", JLT, 1985, No. 3, pp785-788.

[26] L. Faustini, C. Coriasso, A. Stano, C. Cacciatore, D. Campi, "Loss Analysis and Interference Effect in Semiconductor Integrated Waveguide Turning Mirrors", IEEE PTL, Vol. 8, No. 10, October 1996 pp1355-1357.

[27] S.E. Hicks, C.D.W. Wilkinson, G.F. Doughty, *et al* "Reactive Ion etching of Low-Loss Mirrors in InP/InGaAsP/InP Heterostructures Using $CH_4/H_2/O_2$ Chemistry", PROC ECIO '93.

[28] U.K. Chakrabarti, S.J. Pearton, F. Ren, "Sidewall Roughness During Dry Etching of InP", Semicond. Sci. Tech. No. 6, 1991pp408-410.

[29] E. Gini, G. Guekos, H. Melchior, "Low Loss Corner Mirrors with 45° deflection Angle for Integrated Optics", Elec. Lett. Vol. 28, No. 5, Febuary 1992, pp 499-500.

[30] L.H. Speikman, Y.S. Oei, E.G. Metaal, F.H. Groen, P. Demeester, M.K. Smit, "Ultrasmall waveguide bends : the corner mirrors of the future ?" IEE Proc Opt. Vol. 142, No. 1, Febuary 1995 pp61-65.

[31] R.K. Winn, J.H. Harris, "Coupling from Multimode to Single-Mode Linear Waveguides Using Horn-Shaped Structures", IEEE trans on Microwave Theory and Techniques Vol. MTT-23, No. 1 January 1975, pp93-97.

[32] A.F. Milton, W.K. Burns,"Optical Waveguide Parabolic Coupling Horns", Appl Phys Lett. Vol.30 Jan 1977 pp28-30.

[33] G.R. Hadley, "Design of tapered waveguides for improved output coupling", IEEE PTL, Vol. 5 September 1993, pp1068-1070.

[34] D. Marcuse, "Radiation losses of Tapered Dielectric Slab Waveguides", BSTJ, Vol. 49, No. 2, Febuary 19070, pp273-290; Erratum BSTJ Vol. 49, No. 5, May-June 1970, p919.

[35] R.K. Winn, J.H. Harris, "Coupling from Multimode to Single-Mode Linear Waveguides Using Horn-Shaped Structures", IEEE trans on Microwave Theory and Techniques Vol. MTT-23, No. 1 January 1975, pp93-97.

[36] L.H. Spiekman, Y.S. Oei, E.G. Metaal, F.H. Groen, P. Demeester, M.K. Smit, "Ultrasmall waveguide bends : the corner mirrors fo the future ?" IEE Proc Opt. Vol. 142, No. 1, Febuary 1995 pp61-65.

[37] L.B. Soldano, E.C.M. Pennings, "Optical Multi-Mode Interference Devices Based on Self-Imaging: Principles and Applications" JLT Vol. 13, No. 4 April 1995, pp615-627.

[38] M. Bachmann, P.A. Besse and H. Melchior, "Overlapping-image multimode interference couplers with a reduced number of self-images for uniform and nonuniform power splitting" Applied Optics Vol.34 No. 30 1995, pp6898-6910.

[39] P.A. Besse, M. Bachmann, H. Melchior, L.B. Soldano, M.K. Smit "Optical Bandwidth and Fabrication Tolerances of Multimode Interference Couplers" JLT Vol. 12 No. 6 1994, pp1004-1007.

[40] L.H. Spiekmann, Y.S. Oei, E.G. Metaal, F.H. Groen, I. Moerman, M.K. Smit, "Extremely small Multimode Interference couplers and Ultrashort Bends on InP by Deep Etching", IEEE PTL Vol. 6, No. 8 August 1994 pp1008-1010.

[41] Private communication with BT Research Laboratories, Martlesham Heath, January 1996.

[42] Microposit Technical Information, "Shipley S1800 Series Photoresist", Shipley Europe Ltd, Herald Way, Coventry, CV3 2RQ.

[43] M. Heinlium, J.H. Harris, "Analysis of Curved Optical Waveguides by Conformal Transformation" IEEE JQE Vol. QE-11, No. 2 Febuary 1975 pp75-83.

[44] T. Kitoh *et al* "Bending Loss reduction in Silica-Based Waveguides by using Lateral Offsets", JLT Vol. 13, No. 4, April 1995 pp 555-562.

[45] P. Liu, B. Li, P.J. Cressman, J.R. Debesis, S. Stoller," Comparison of Measured Losses of Ti:$LiNbO_3$ Channel Waveguide Bends", IEEE PTL Vol. 3 No. 8 August 1991 pp755-756.

[46] M. Heinlium, J.H. Harris, "Analysis of Curved Optical Waveguides by Conformal Transformation" IEEE JQE Vol. QE-11, No. 2 Febuary 1975 pp75-83.

[47] E.A.J. Marcatili, "Dielectric Tapers with Curved Axis and no Loss", IEEE JQE, Vol. 21, No. 4, April 1985, pp307-314.

[48] D. Marcuse, "Bending losses of the assymetric slab waveguide", Bell Sys. Tech. J., Vol. 50, No.8, 1971, pp2551-2563.

[49] E.A.J. Marcatili, "Bends in optical dielectric guides", Bell Sys. Tech. J., Vol. 48, 1969, pp2103-2132.

[50] M. Miyagi, S. Nishida, "Bending losses of Dielectric Rectangular Waveguides for Integrated Optics", J. Opt. Soc. Am., Vol. 68, No. 3, 1978, pp316-319.

[51] E.C.M Pennings, R.J. Deri, R.J. Hawkins "Simple Method for Estimating Usable bend Radii of deeply etched optical rib waveguides", Electronics letters Vol. 27 No. 17 August 1991 pp 1532-1533.

Monolithic Integration of Optical Space Switches

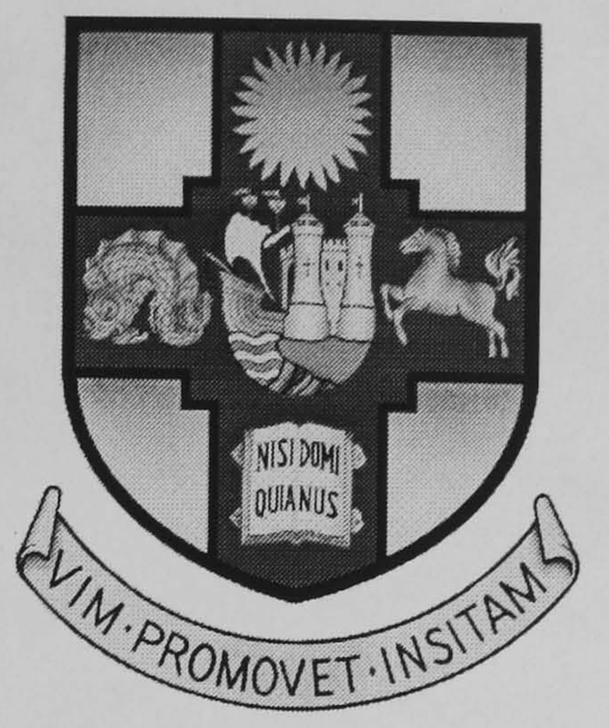

Chapter 5

5.1 Passive 4x4 Waveguide Crosspoint Fabrication

Chapter 4 has theoretically analysed the waveguide crosspoint switch architecture proposed in chapter 2. In this chapter several test structures are discussed which have been designed and fabricated in order to justify the theoretical calculations made in chapter 4. The fabrication procedure is first discussed, outlining the problems associated with multi-level mask alignment and dry etching of InP waveguide turning mirrors. Various test structures are proposed which separate out the various aspects of the device design. Finally the process used to fabricate the test structures will be given, along with the results of vertical deep etching.

5.2 Fabrication Tolerant Processes design

5.2.1 The Self Alignment Process - the TIR waveguide mirror

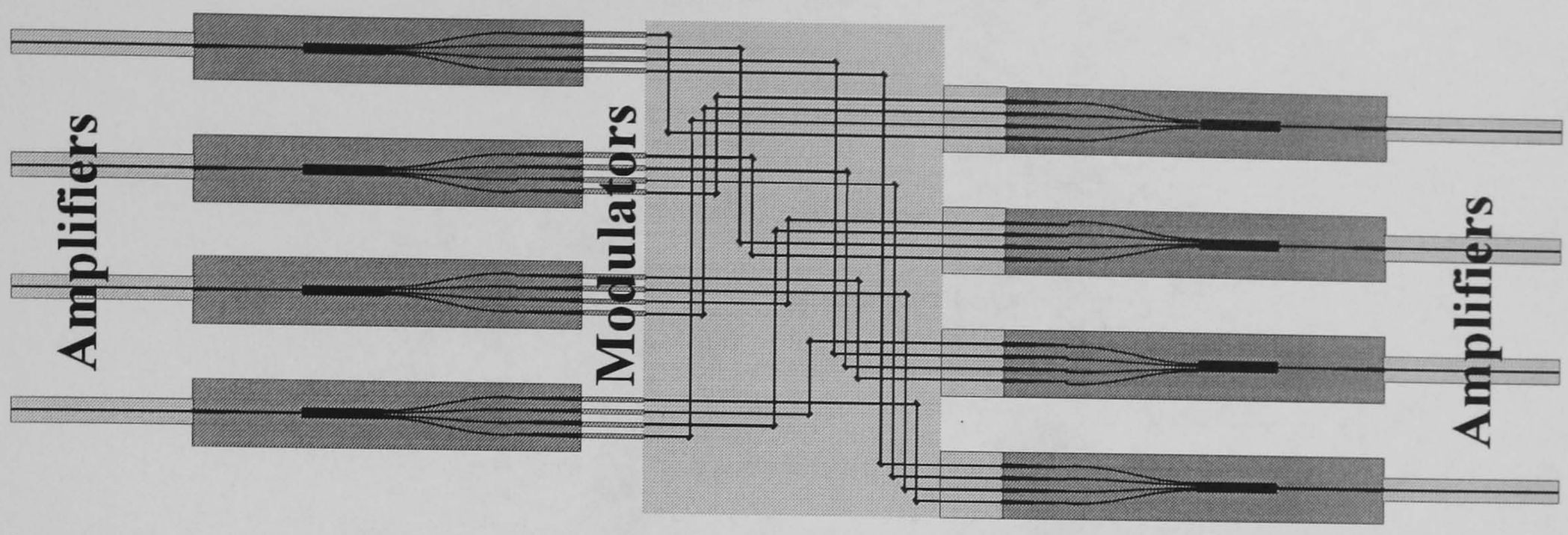

Figure 5.1 Schematic diagram of proposed 4x4 InP Crosspoint design

It has already been discussed that the device drawn schematically in figure 5.1 requires regions of both shallow (light grey) and deep etching (dark grey). Theoretically it has been assumed that the alignment between these regions is exact, however practically this is not the case. Thus, before developing a photolithographic mask and fabrication process for the crosspoint, the problems associated with multi-level mask alignment need to be addressed. These issues may be discussed more clearly by examining the fabrication of the waveguide turning mirrors [1] in the waveguide matrix (figure 5.2).

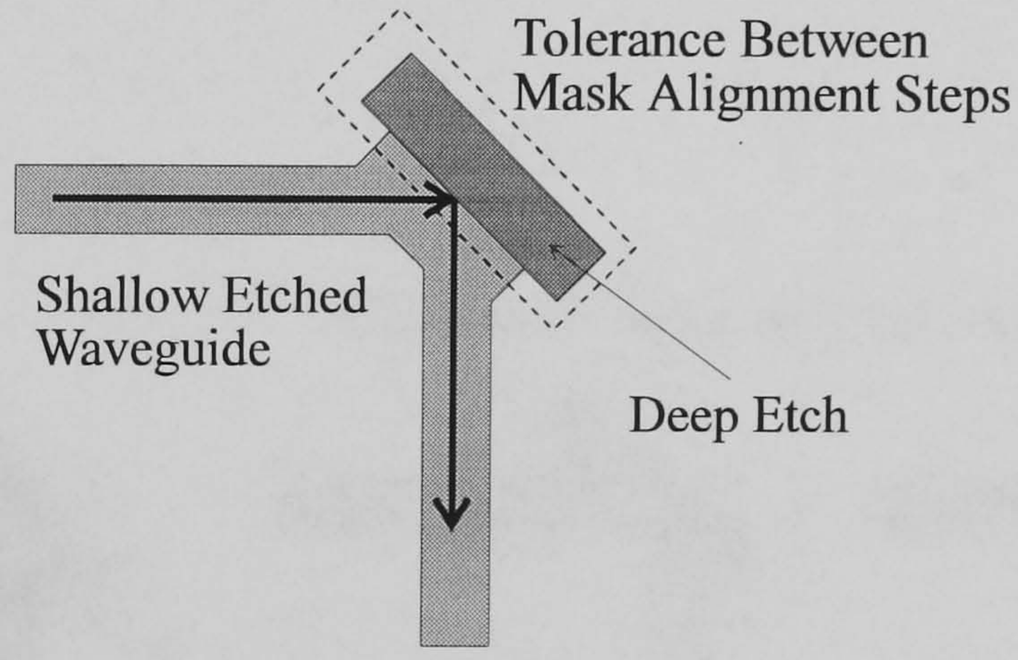

Figure 5.2 Self Alignment of the deep Mirror Etch with the Shallow etched ridge waveguide

The performance of the TIR waveguide turning mirror has already been given in chapter 4. It has been discussed that theoretically if the deep etch is aligned perfectly with the shallow etched ridge waveguide with no roughness, then the loss of the mirror can be as low as 0.08dB [2]. However, practically because both the shallow etch and deep etches must be done in two separate processing steps, the accuracy to which both etches may be aligned to one another is limited to the mask alignment used in the second step. Currently, photolithographic mask alignment is limited to of the order ±0.5μm. Therefore, after processing, the deep etch

may lie anywhere within the area indicated by the dashed line shown schematically in figure 5.3. Thus it may be observed that the incident mode is reflected off axis to the output waveguide and a loss of many dBs may be incurred [2, 9,11].

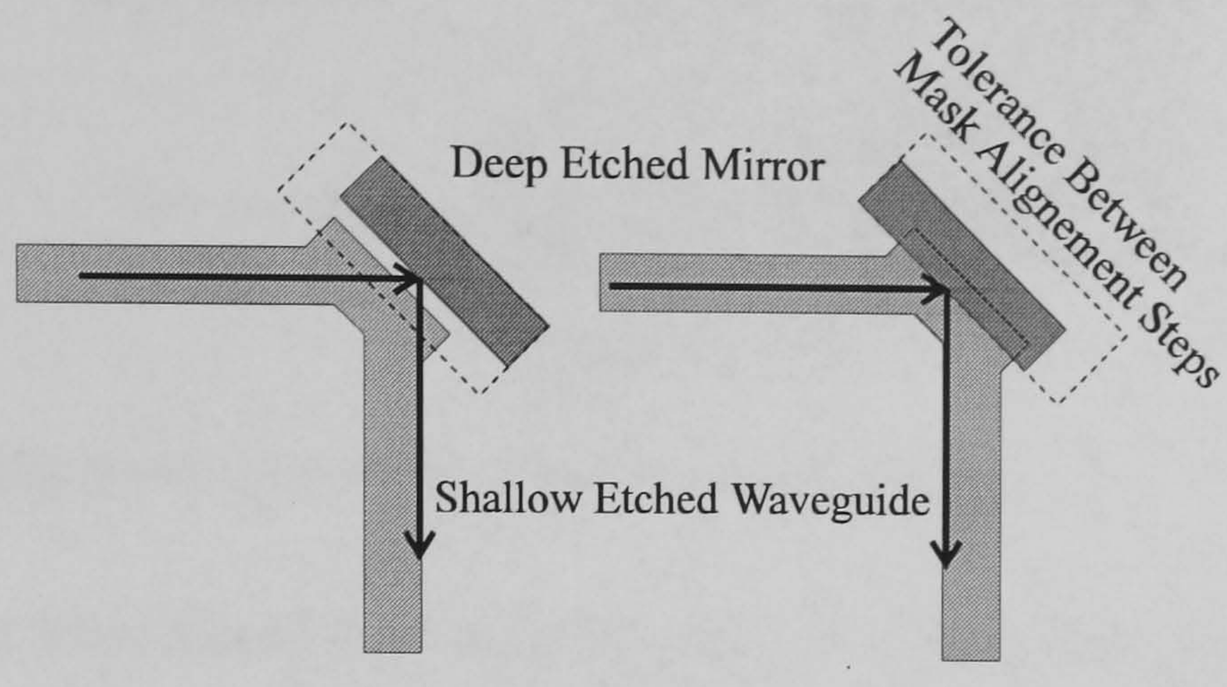

Figure 5.3 Loss incurred to a TIR mirror due to Mask Alignment error.

This problem can be resolved by the use of a process called self alignment [3]. In this method of fabrication a mask is first patterned on the wafer which is resistant to both the shallow and deep etch, as shown schematically in figure 5.4. This 'self alignment mask' remains on the wafer through the entire fabrication process. Thus by etching *over* the resistant mask, self alignment can be achieved between different separate processing steps. This is demonstrated schematically in figure 5.4 in the case of the TIR mirror. During the mask design the deep etch window is positioned such that it is offset by the expected mask alignment error. Thus after fabrication, the deep etch is always aligned to ridge waveguide.

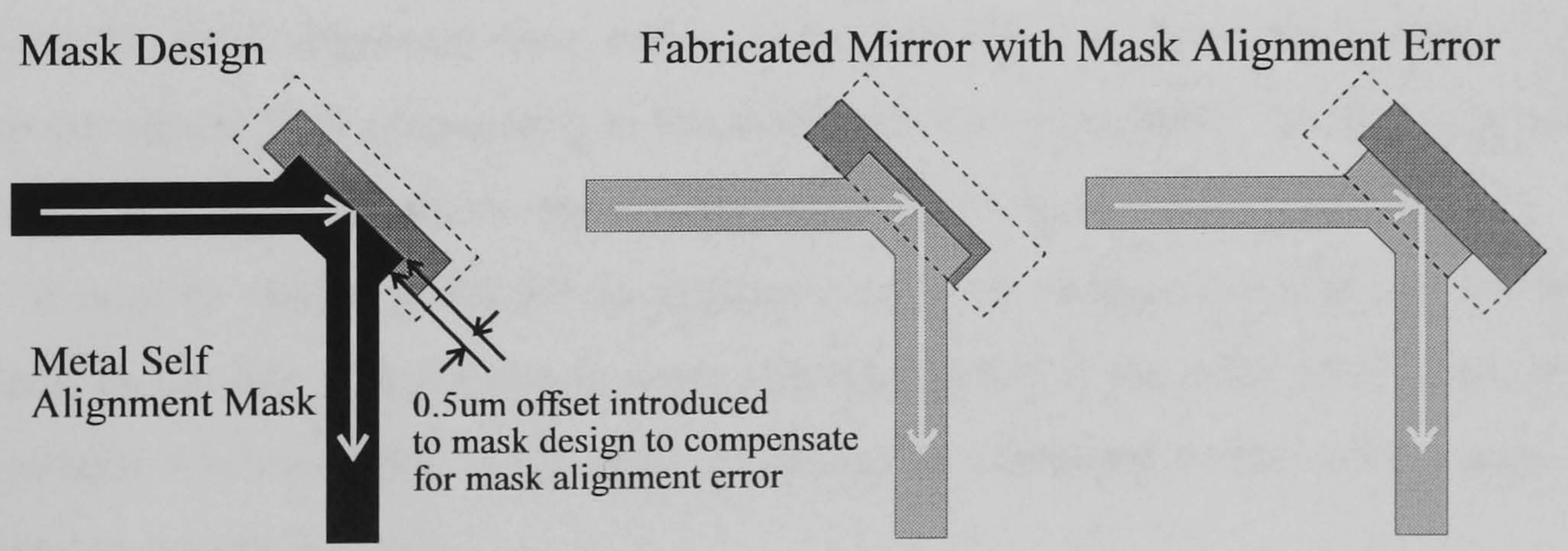

Figure 5.4 TIR mirror design using a self alignment mask.

5.2.2 The Self Alignment Process - the Tapered Mode Converter

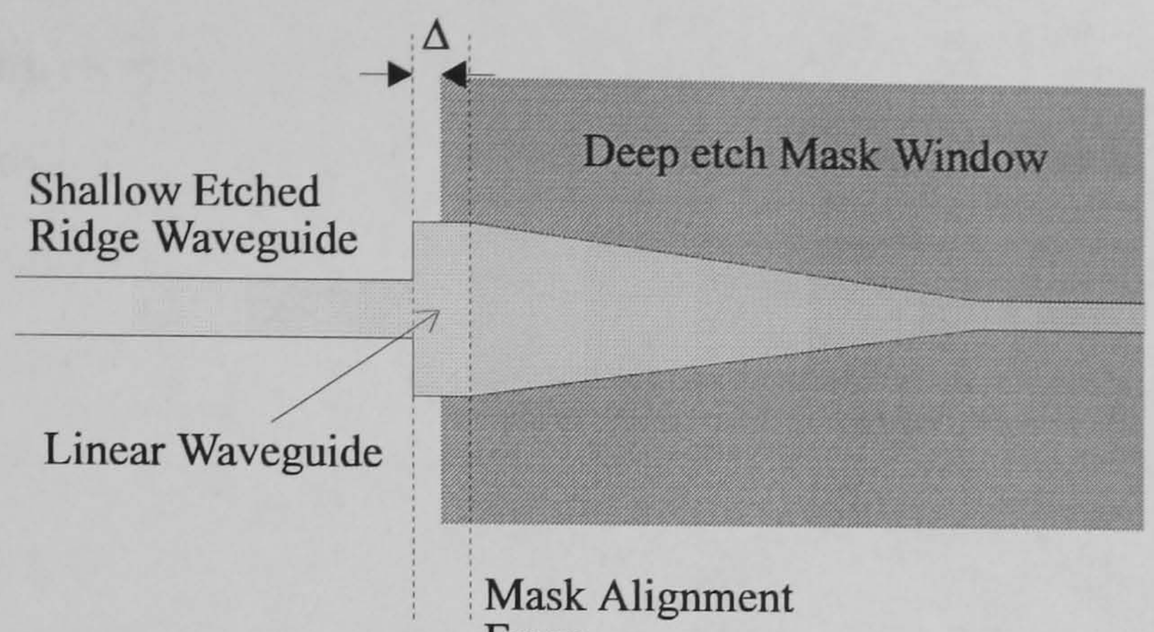

Figure 5.5 Self Alignment used in the tapered mode converter

There is one other area of the crosspoint where exact alignment is required between the deep and shallow etch. This is in the taper mode converter which provides low loss coupling between the regions of strong and weak guiding. Self alignment can also be used here to good effect in order to alleviate the problems due to mask alignment error as shown schematically in figure 5.5. A small linear waveguide region is used in-between the shallow and deep etch region. The deep etch mask's length is reduced such that the edge of the deep etch window will always be positioned somewhere on the linear waveguide owing to mask misalignment. This misalignment will introduce a small loss, *L*, owing to the field initially coupling to a shallow etched multimode waveguide, instead of the deep etched waveguide, which may be estimated from the equation [4]

$$L = 1 - \frac{\sqrt{1+4Z^2}}{\sqrt{1+5Z^2+4Z^4}} \text{ where } Z = \frac{2\lambda\Delta}{\pi n_{eff}\omega_0^2} \tag{5.1}$$

where Δ is the mask alignment error, and w_0 is the best matched zero order Hermite Gaussian beam to the optical field propagating in the shallow etched waveguide. This function has been plotted for TE_{00} mode for various waveguide parameters in figure *5.6*.

It may be observed that for an alignment error of ±0.5μm and hence $0<\Delta<1\mu m$, the theoretical excess loss incurred due to mask misalignment is of the order of -0.01dB, over the entire erbium window. This contribution is negligible compared to the other losses in the device and so may be ignored.

It has therefore been shown in this section, that by a combination of self alignment and the use of subtle alterations to the deep etch mask design, a fabrication tolerant process can be developed in order to overcome the limits of mask misalignment. The next section discusses in more detail test structures that have been fabricated in order to analyse the design of the device, after which the exact fabrication procedure used to construct the test structures will be discussed.

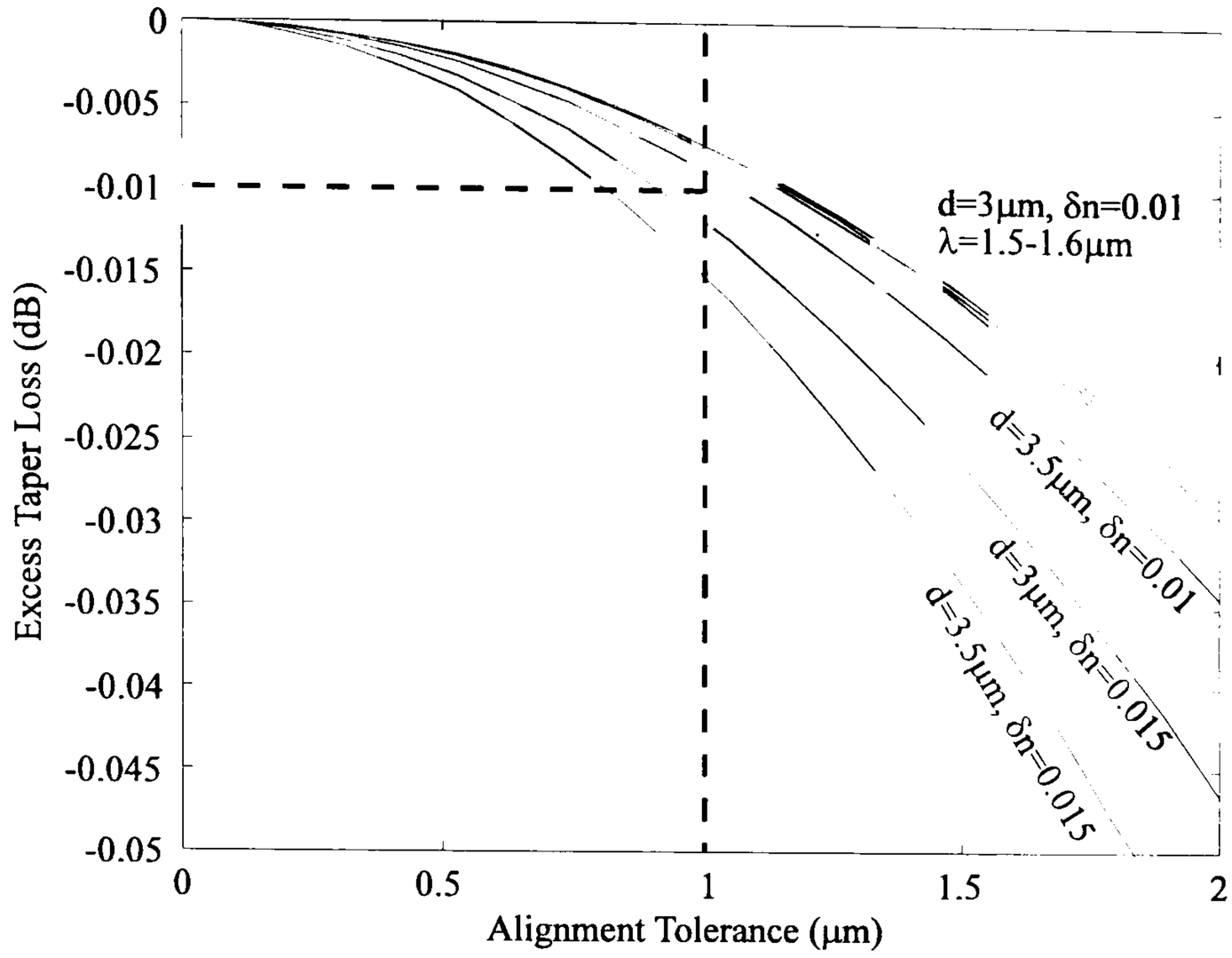

Figure 5.6 Excess Loss of the Mode Converter Owing to Mask Misalignment (TE_{00})

5.3 Outline of test structure components

Test Structure	Technical Specification
Crossing Loss	Waveguides with various numbers of crossings 5,10,15,20,25.....45,50. Crosstalk Analysis, waveguide separations 5, 10, 15, 20, 25μm
TIR Mirrors	8 TIR mirrors BT design 20μm centre to centre waveguide separations
MMIs	1x4 Waveguide Length 131, 134, 136, 138, 141μm 1x8 Waveguide Length 265, 268, 270, 272, 275μm (Mode Converter width 5.5μm, Taper Length 100μm)
Tapers	Taper Lengths 20,50,70&100μm (Mode Converter Width 5.5μm) Mode Converter widths 4.5, 5, 5.5, 6,6.5μm (Taper Length 100μm)
S-Bends	S-Bend radius of curvature 100, 200, 300, 400, 500μm (Mode Converter width 5.5μm, Taper Length 100μm)

Table 5.1 Summary of the Test Structure Designs

The final crosspoint device requires the monolithic integration of many integrated optical components which have been optimised theoretically in chapter 4. However in order to validate these theoretical predictions, several test structures have been fabricated in order to separate out the various aspects of the device design. The following paragraphs outline in more detail the purpose of each individual passive component with the technical specifications outlined in table 5.1. The main aim of the components is optimise two aspects of the crosspoint. These are firstly the MMI couplers which include the mode converters and S-bend waveguides and secondly the waveguide matrix which consists of a large number of waveguide crossings and TIR waveguide mirrors.

5.3.1 Optimisation of the waveguide matrix

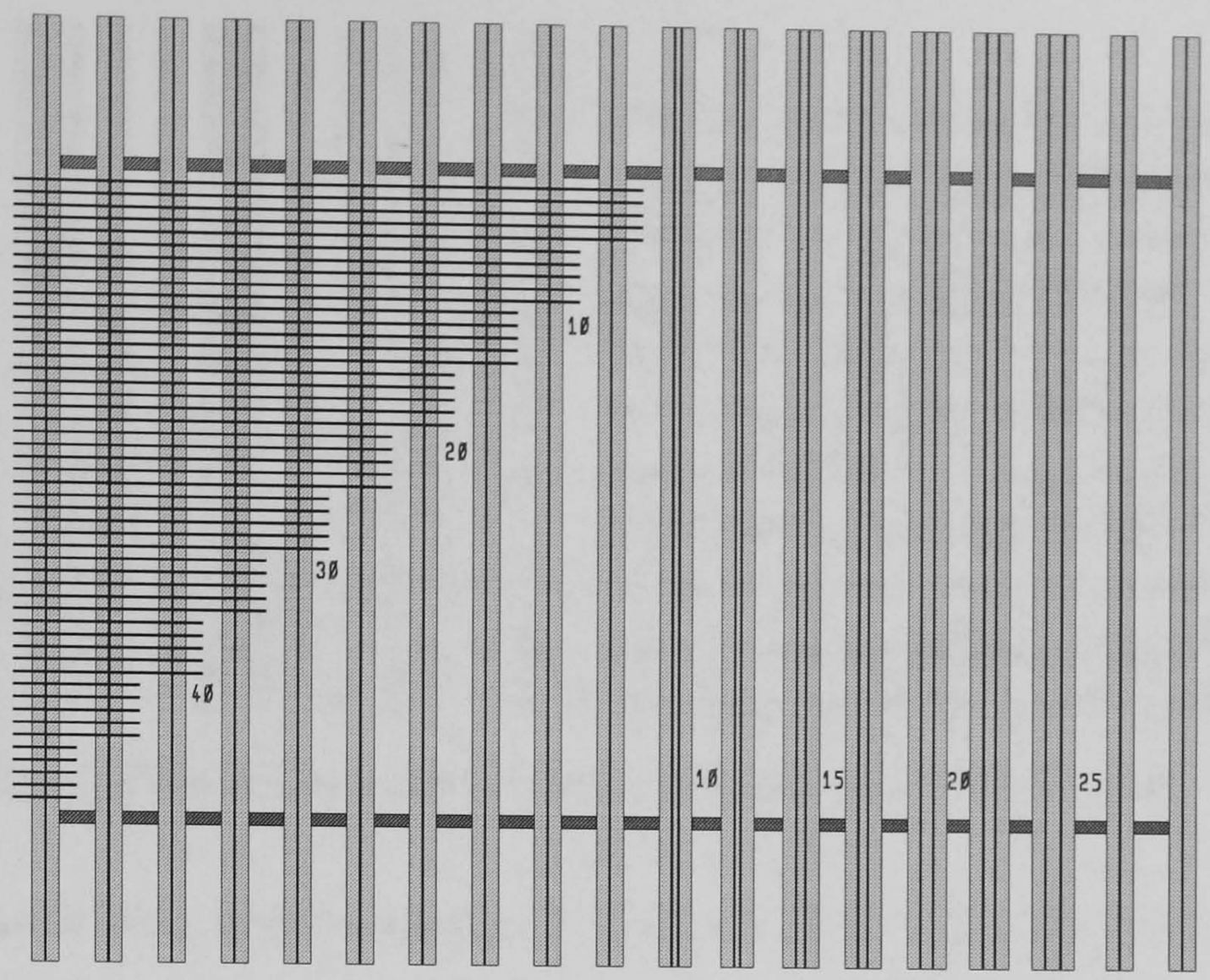

Figure 5.7 Mask Design for the assessment of crossing loss and waveguide crosstalk

The waveguide matrix consist of two basic components which may have an effect on the crosspoint performance, namely waveguide crossings (of which there are many) and the waveguide turning mirror. Firstly the crossing loss in the matrix is examined by the test structure shown in figure 5.7. The component consists of many straight waveguides with an increasing number of 90° crossings varying from 5 to 50 in increments of 5. Also included are waveguides with different centre to centre separations (5, 10, 15, 20, 25μm) in order to calculate the optical coupling between the guides. With respect to the waveguide turning mirrors, figure 5.8 outlines a test structure which allows measurement of mirror loss, but also whether the mirror can be placed between two parallel running waveguides. It may be noted from the mask design of the complete device (figure 5.1), that mirrors have been placed in order to maximise the number of waveguide crossings. This has been done since the truncation effect of placing mirrors between guides is unknown. This test structure therefore allows calculation of any detrimental performance on the mirror position.

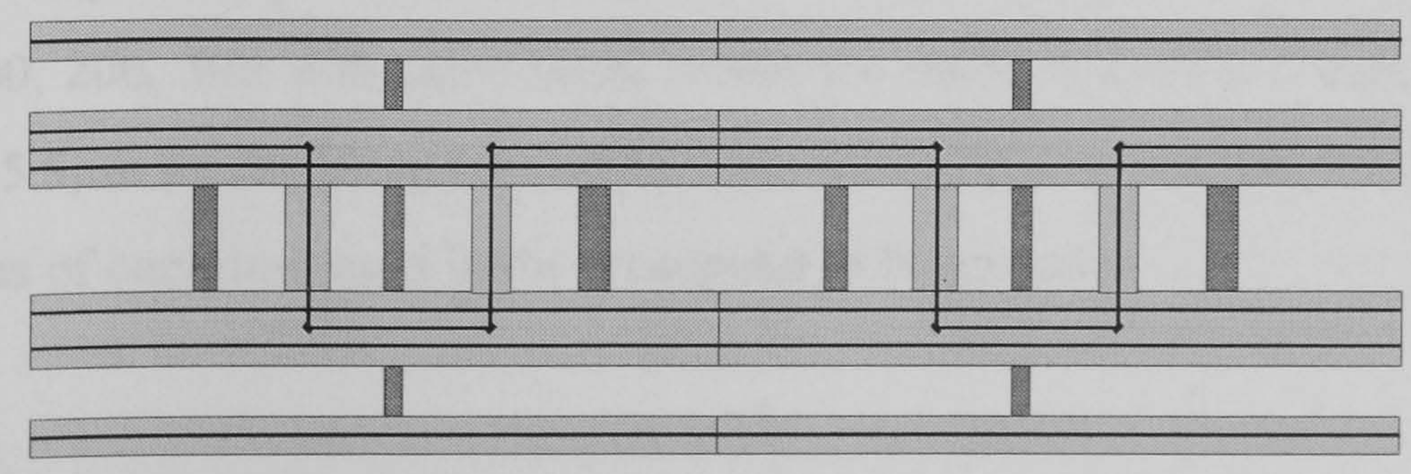

Figure 5.8 TIR Mirror/Waveguide Proximity Effects

5.3.2 Multi-Mode Interference couplers

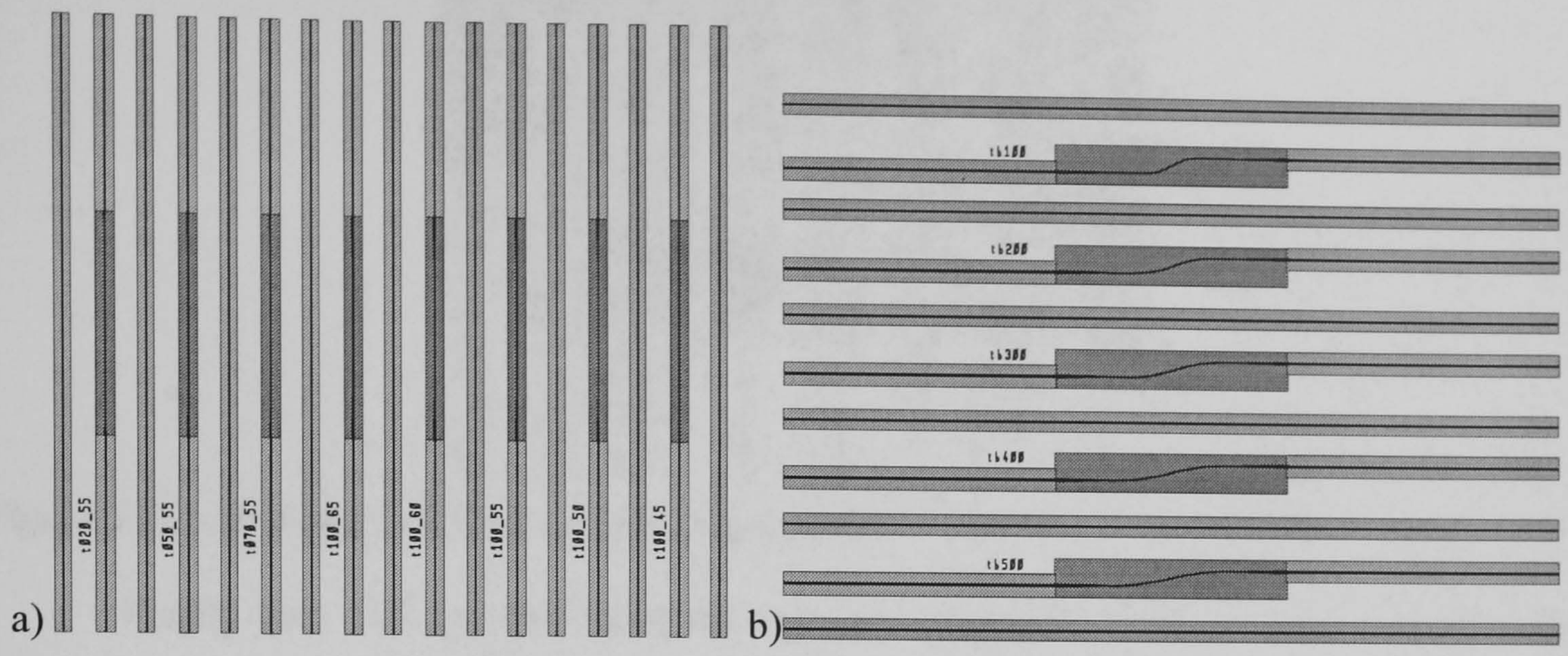

Figure 5.9 Tapered Mode Converter test structure (left) and S-Bend (right)

The second most important aspect of the crosspoint is the MMI splitter used on the input and output of the device. The coupler is a very complicated structure since it consist of three main components namely the tapered mode converters, S-Bend waveguides and of course the MMI itself. These three constituent parts have therefore been separated into different test structures in order to analyse the contribution from each component. Firstly figure 5.9a outlines the mask design for the tapered mode converter optimisation. The components simply consist of a 1mm long deep etched 2μm waveguide, which are addressed either side by a straight ridge waveguide followed by a deep etched tapered waveguide (as drawn schematically in figure 5.6). Taper lengths varying from 20 to 100μm are included along with different mode converter widths which range from 4.5 to 6.5μm in 0.5μm steps. These structures therefore allow optimisation of the mode converter design. A large number of straight waveguides are also included between each mode converter design so that the straight ridge waveguide losses may be determined.

The radius of curvature used in the MMI S-bend waveguides may be optimised by using the components drawn in figure 5.9b. Each test structure is almost identical to the tapered mode converters discussed above, however an offset of 20μm is introduced between input and output ridge waveguides by a 2μm waveguide bend. The radius of curvature of each bend is varied from 100, 200, 300, 400 and 500μm whilst the mode converter design is kept constant (100μm taper, 5.5μm mode converter width). Loss measurements on this component allow the minimum radius of curvature used in the crosspoint to be assessed.

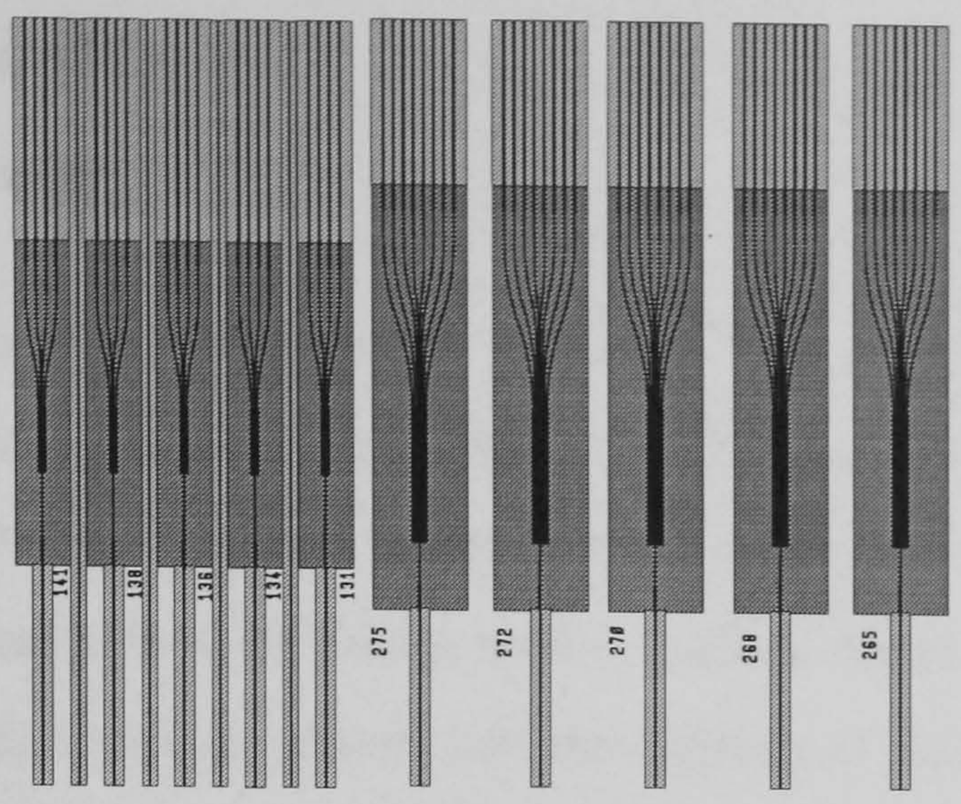

Figure 5.10 1x4 and 1x8 MMI Length optimisation

Finally both 1x4 and 1x8 MMI designs have been fabricated, in order to predict the performance of both a 4x4 and 8x8 crosspoint switch (as shown in figure 5.10). The same mode converter design and S-bend radius of curvature is used in all coupler designs (as defined in table 5.1) so that the sole loss contribution from the MMI may be calculated. A standard technique for determining the optimum MMI coupler design is to vary the MMI length whilst keep the MMI width constant [5]. This 'tuning' is required since the absolute refractive index of the wafer and the MMI etched width tolerance is unknown. Therefore MMIs with various lengths are included on the mask ranging from 141-131μm for the 1x4 coupler and 265-275μm for the 1x8 coupler. These length tolerances have been determined by assuming a 10% error in refractive index and a 0.5μm error in MMI width.

5.3.3 Passive 4x4 Crosspoint Switch

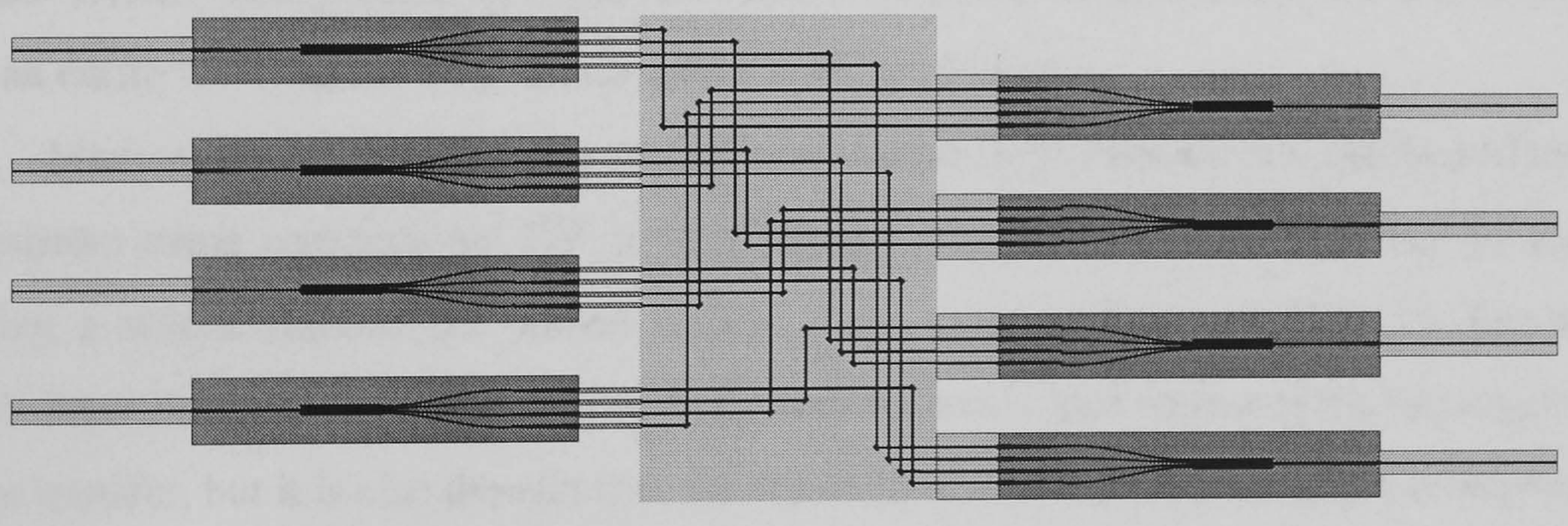

Figure 5.11 Passive 4x4 crosspoint splitter

Finally, the complete passive 4x4 crosspoint drawn in figure 5.11 is included on the mask plate in order to assess any fabrication problems associated with the final device. Four copies of the device are included, each with a different MMI length. This allows an exact determination of the fibre to fibre loss incurred by the architecture, which may then be compared with sole loss contribution from each constituent component. A discussion of these loss measurements will be given in chapter 6, however for now, the remaining aim of this chapter will be to discuss the fabrication of the passive devices along with the etching tolerances achieved.

5.4 Fabrication Procedure

5.4.1 Background Information

The procedure used to fabricate the test structures is an extension of a process developed by BT Research Laboratories, Nortel and Glasgow University under the EPSRC 2DIO grant in the mid 1990's [6]. It was found that the difficulty in fabricating low loss InP mirrors is achieving vertical side-walls with a smooth surface. Verticality may be achieved by dry etching with a methane hydrogen mixture and the addition of small quantities of Oxygen to remove polymer deposition [7]. However, roughness introduced onto the mirror is much more of a problem. It was found that the method used to initially transfer the waveguide pattern to the wafer, is critical in determining the sidewall roughness of the fabricated mirror [8]. Any kind of corrugation or roughness in the etch mask immediately superimposes itself on the etched mirror which increases the loss of the mirror dramatically [9, 2, 11]. Unfortunately many types of commercially available photoresist produce rough corrugation of the order of 0.1μm on their edges (for example AZ-1350J [8]). In the electronic fabrication industry (for which they were developed) this poses no problem. However, when fabricating optical waveguides where the wavelength of light in the InP is of the order of 0.5μm, the losses incurred by scattering prohibit their use. As such, existing processes have used direct write in order to alleviate mask roughness. A thin layer of PMMA (~200nm) is used as the photo-reactive material and the waveguide pattern is transferred to the wafer by direct write with an E-Beam Writer. This process is extremely labour intensive, since it may take many hours to write an entire wafer and is no good for larger scale production.

Many authors have however, recently succeeded in fabricating deep etched MMIs and TIR mirrors using conventional UV contact lithography. This has been achieved by initially applying a silicon dioxide (or silicon nitride) mask prior to exposure [10-13]. The silicon dioxide layer not only acts as an Anti-Reflection (AR) coat which improves the accuracy of the pattern transfer, but it is also thought that the dry etching of the SiO_2 prior to the semiconductor minimises the mask induced roughness. Recently, it has also been found that dry etching a metal Titanium film and Silicon Nitride as a combined mask for deep etching provides better sidewall smoothness [14]. Figure 5.12 therefore illustrates a process which has been developed for the crosspoint in order to accommodate UV contact lithography with the self alignment. Initial process development and fabrication of the test structures was carried out during a three month placement at Department of Electrical Engineering at Glasgow University. However, owing to logistical and time constraints the final devices were completed by Dr. Yahong Qian. The exact fabrication process has been discussed in more detail in the following section.

5.4.2 Fabrication Procedure Developed for the passive test structures

Define waveguide pattern

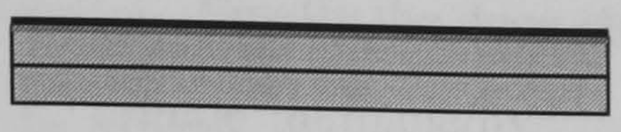

1. Clean samples
2. Deposit 500nm Silicon Nitride
3. E-Beam evapourate 150nm Ti

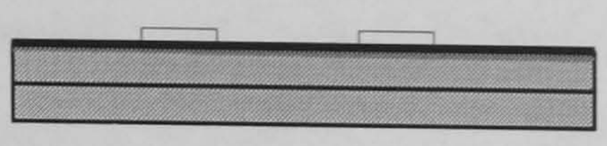

4. Define waveguide pattern by UV exposure
5. Develop.

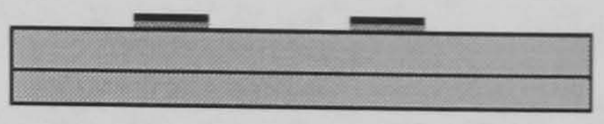

6. SF_6 dry etch Titanium
7

Deep etch mirrors and MMIs

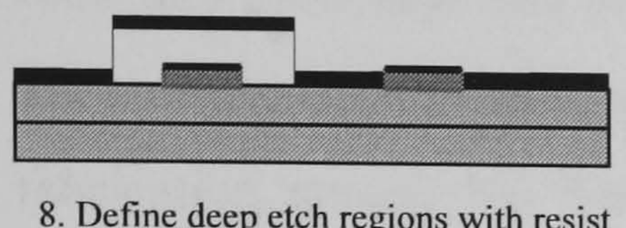

8. Define deep etch regions with resist
9. Evapourate Titanium mask

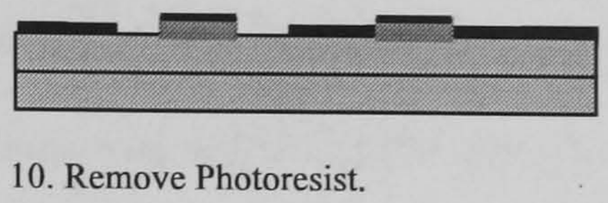

10. Remove Photoresist.

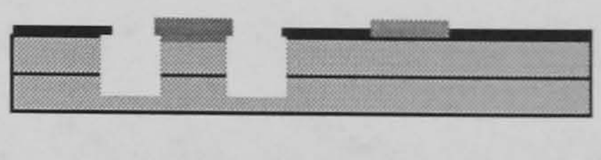

11. $CH_4/H_2/O_2$ dry etch samples

Shallow etch waveguides

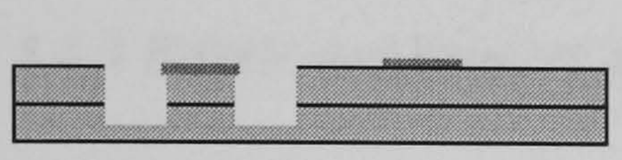

12. $SiCl_4$ dry etch Titanium

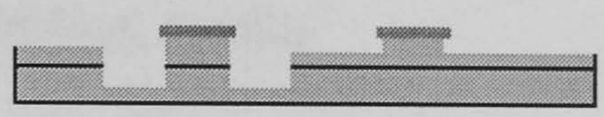

13. $CH_4/H_2/O_2$ dry etch samples

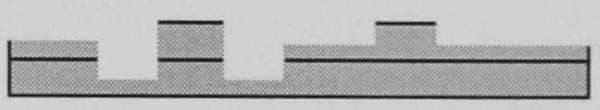

14. Remove Silicon Nitride by wet etch (HF)

Figure 5.12 Fabrication procedure developed for the Crosspoint Test Structures.

A MOVPE wafer grown at Sheffield University (wafer No. MR1007 specification given in chapter 4) was cleaved into approximately 10mm square pieces. The samples were cleaned in an ultra-sonic bath for 5 minutes with three independent solvent steps (Optoclear, Acetone, Methanol), followed by a 5 minute de-ionised water rinse. After blow drying with a filtered air gun, the samples were baked on a hot plate (100°C) for 10 minutes to remove any residual water. 500nm of silicon nitride was deposited by PECVD (Plasma Enhanced Vapour Chemical Deposition) followed by electron beam evaporation of 150nm of Titanium. A further hot plate bake (100°C 10 minutes) was used to dry the samples before 0.5μm of Shipley series 1800 resist was deposited onto the wafer by spinning (Primer; 10 second 4000rpm, S1805 30 seconds 4000rpm). The resist was then baked (90°C 30 minutes) before the light field waveguide mask was used to expose the resist at 450nm for 4 seconds on a Karl Suss MJB3HP-UV400 Mask Aligner. Standard Shipley developer was used to form the waveguide pattern (50:50 Developer/H_2O, 75 seconds) followed by a 5 minute de-ionised water rinse, blow dry and post bake (120°C 30 minutes). A subsequent SF_6 and C_2F_6 dry etch step were used to etch the Ti and SiN respectively which completed the self alignment waveguide mask.

The deep etched regions of the components were then fabricated as follows. A titanium mask was first deposited by lift off to protect the shallow etched regions of the wafer during the deep etch run. This was achieved by a UV contact lithographic process step using S1813, with the light field deep etch mask was used to highlight the deep etch regions. 100nm of evaporated titanium was then deposited on the samples, followed by lift off in acetone to mask the shallow etch regions. The InP wafer was then dry etched (machine ET340, CH_4 3.6sccm; H_2 26.4ccm;

O_2 0.4sccm, pressure unthrottled, power 100W) for 40 minutes to a depth of approximately 2μm (etch rate ~50-55nm/minute).

Finally the deep etch titanium mask was removed by a $SiCl_4$ dry etch step and a second 12 minute methane/hydrogen/oxygen dry etch run defined the shallow etch waveguides. The silicon nitride self alignment mask was then removed by immersion in a silicon dioxide etchant (1:4 Hydrofluoric Acid:Ammonia) for 30 seconds followed by a 5 minute de-ionised water rinse and blow dry. The samples were then cleaved using a RA120 GaAs Karl Suss scriber at the University of Bristol, and tested using the experimental set-up discussed in chapter 6. The fabrication quality has been discussed in the next section along with the etching tolerances achieved and the devices fabricated.

5.4.3 Fabricated Devices and Etching quality

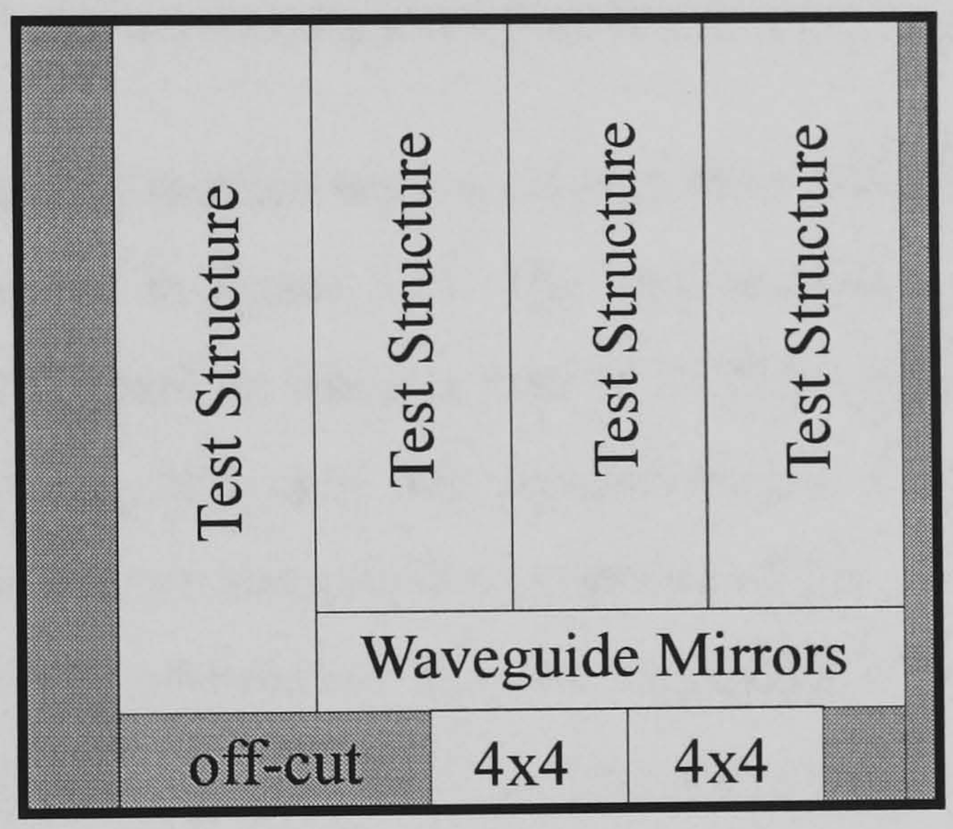

Figure 5.13 Position of InP passive test components on sample MR1007-B

The processed InP sample MR1007-B was cleaved up into three chip types before assessment as outlined in figure 5.13. These InP chips were termed - a) the test structures, b) the waveguide turning mirrors, and finally c) the 4x4 passive crosspoint, which are discussed as follows

a) The test structures

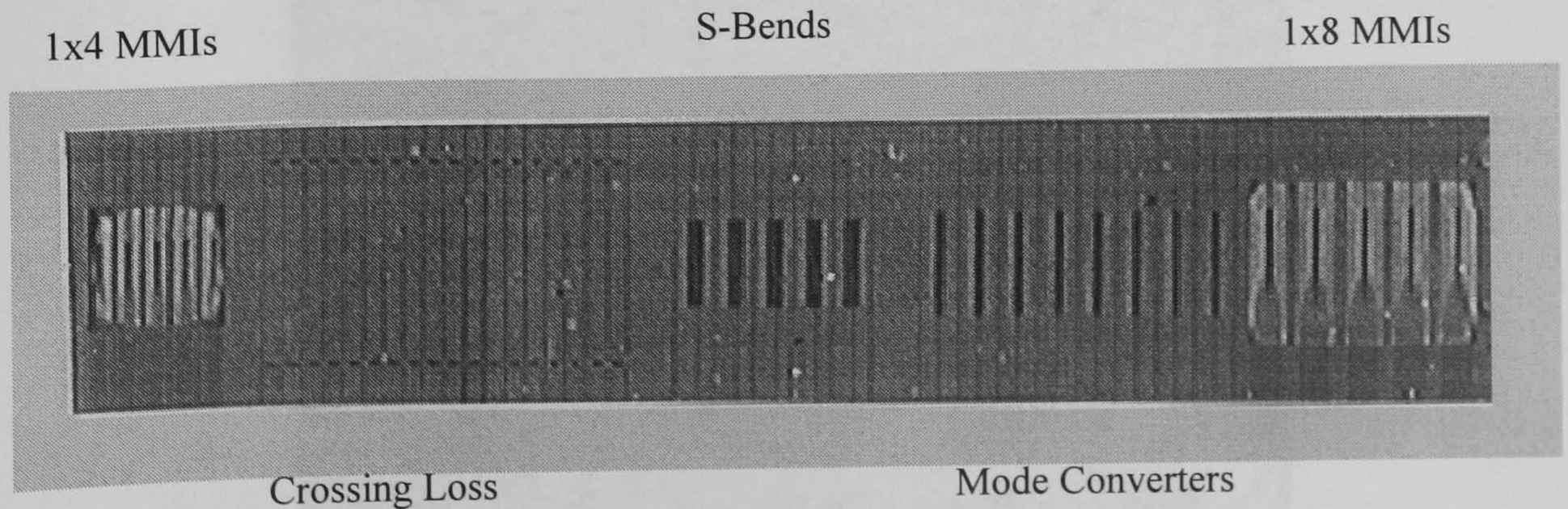

Figure 5.14 Cleaved InP chip containing five test structure components - 'test structures'

The test structures consisted of five different components as labelled in figure 5.14. A complete set of four test structure chips were obtained after cleaving, which measured approximately 1.5mm by 7mm. Combining all five components onto a single chip in this way drastically reduced the amount of cleaving required and also speeded up assessment and allowed easier tweezer handling of each component.

b) The waveguide turning mirrors

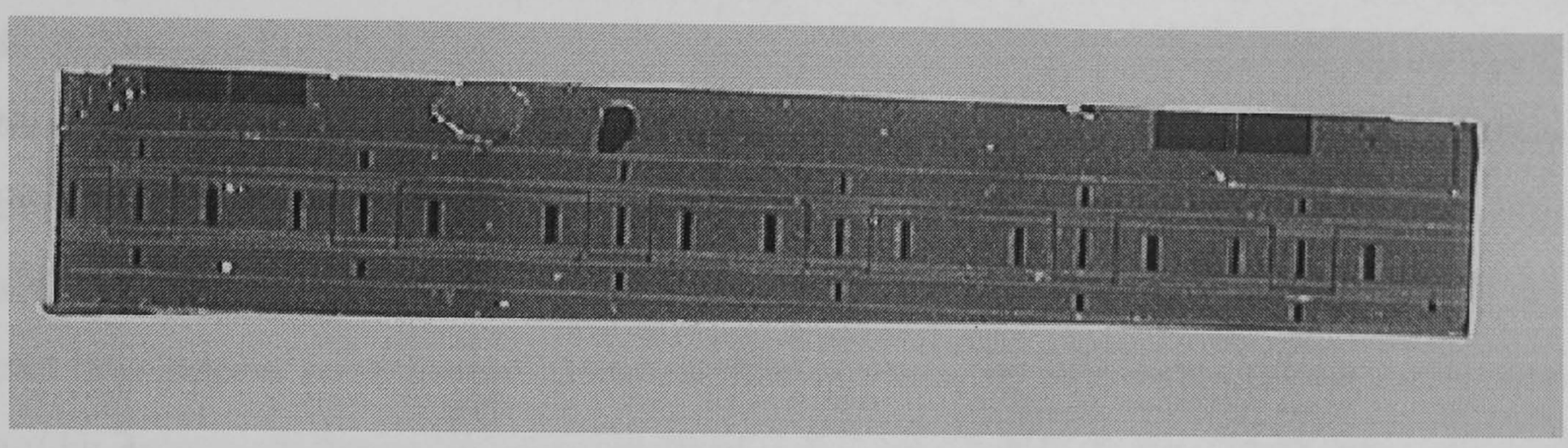

Figure 5.15 Cleaved InP chip containing a total of 24 TIR waveguide mirrors

The waveguide turning mirrors were separated from the above test structures onto a separate chip as photographed in figure 5.15. The chip measured approximately 4.5mm by 0.5mm and contained a single path on which a total of 24 TIR waveguide mirrors were formed in a square tooth. By cleaving this chip into smaller lengths containing 2, 4, 6, 8 and 12 waveguide mirrors allowed a more accurate determination of the TIR mirror loss (as discussed in chapter 6). This method also allowed the absolute waveguide loss (in dBs per centimetre) to be determined from the straight waveguides, which lie along side the mirrors, by the cut-back method [15].

c) The passive 4x4 crosspoint

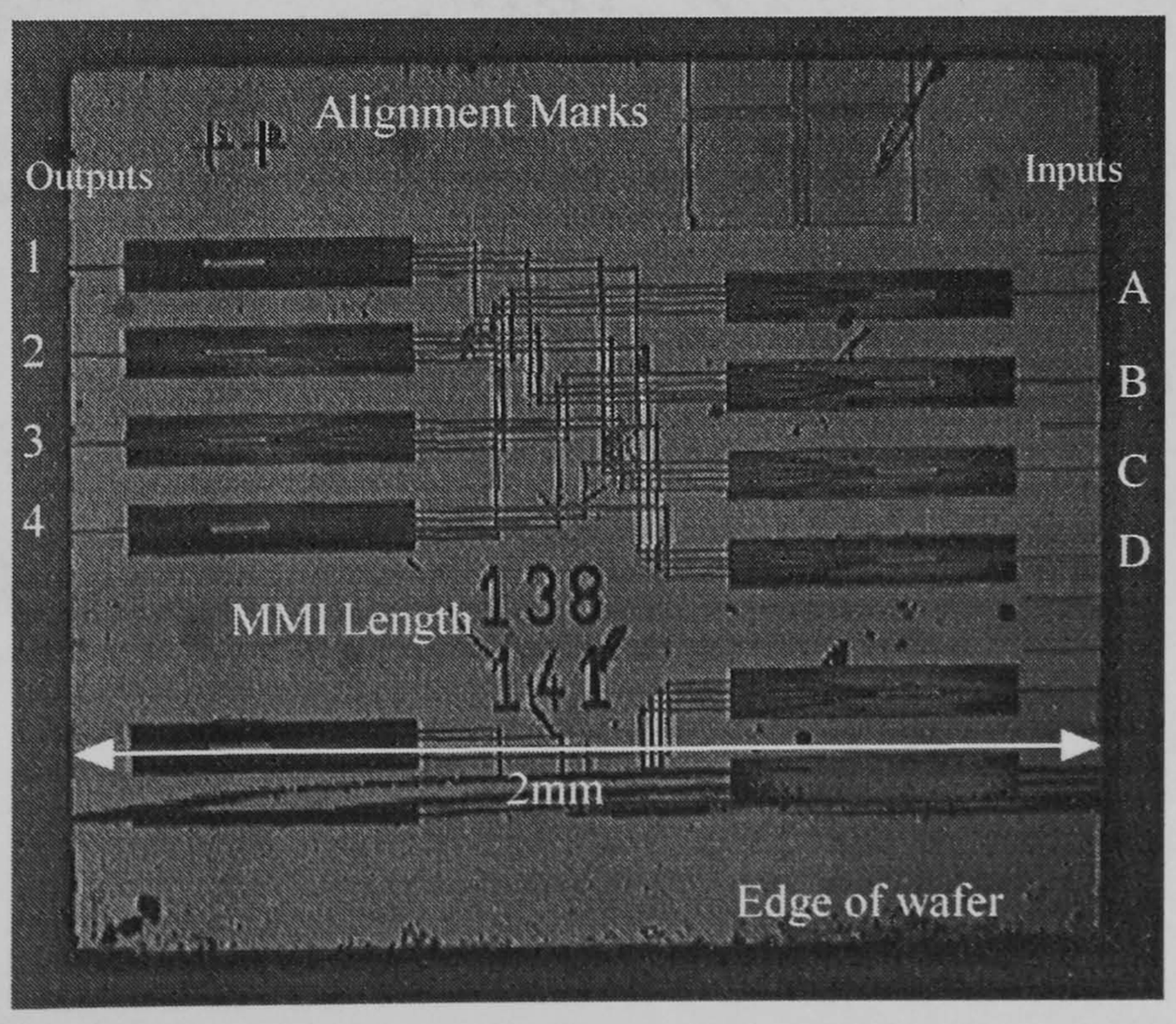

Figure 5.16 Fabricated 4x4 passive test structure

Finally, the full 4x4 passive implementation of the crosspoint was fabricated along side the test components in order to asses any problems associated with its fabrication. Figure 5.16 shows a photograph of the final 4x4 cleaved chip. The device measured approximately 2mm by 1.5mm (which was not optimised). It should be noted that each input has been labelled from A to D, whilst the outputs have been number 1 to 4. This allows the corresponding input/output paths to be discussed more easily in chapter 6, for example A1, B3 etc. Scanning Electron Microscopy (SEM) of this device on an Hitachi S-800, allowed a more accurate determination of the etching quality achieved by the processing. By SEM imaging one of the mode converters in the crosspoint (as shown in figure 5.17), several important features relating to the etch quality may be highlighted. Firstly, there is significant waveguide rounding apparent between the shallow ridge/deep etched taper. This is a consequence of the diffraction limit of the UV contact lithographic process used to transfer the initial waveguide pattern to the substrate which cannot be improved. Secondly, a grassy floor is obtained in the deep etched region owing to the Methane/Hydrogen/Oxygen etch used to fabricate the device [6]. Finally a very thin layer of polymer has also been deposited in a 'fence' around the deep etched window.

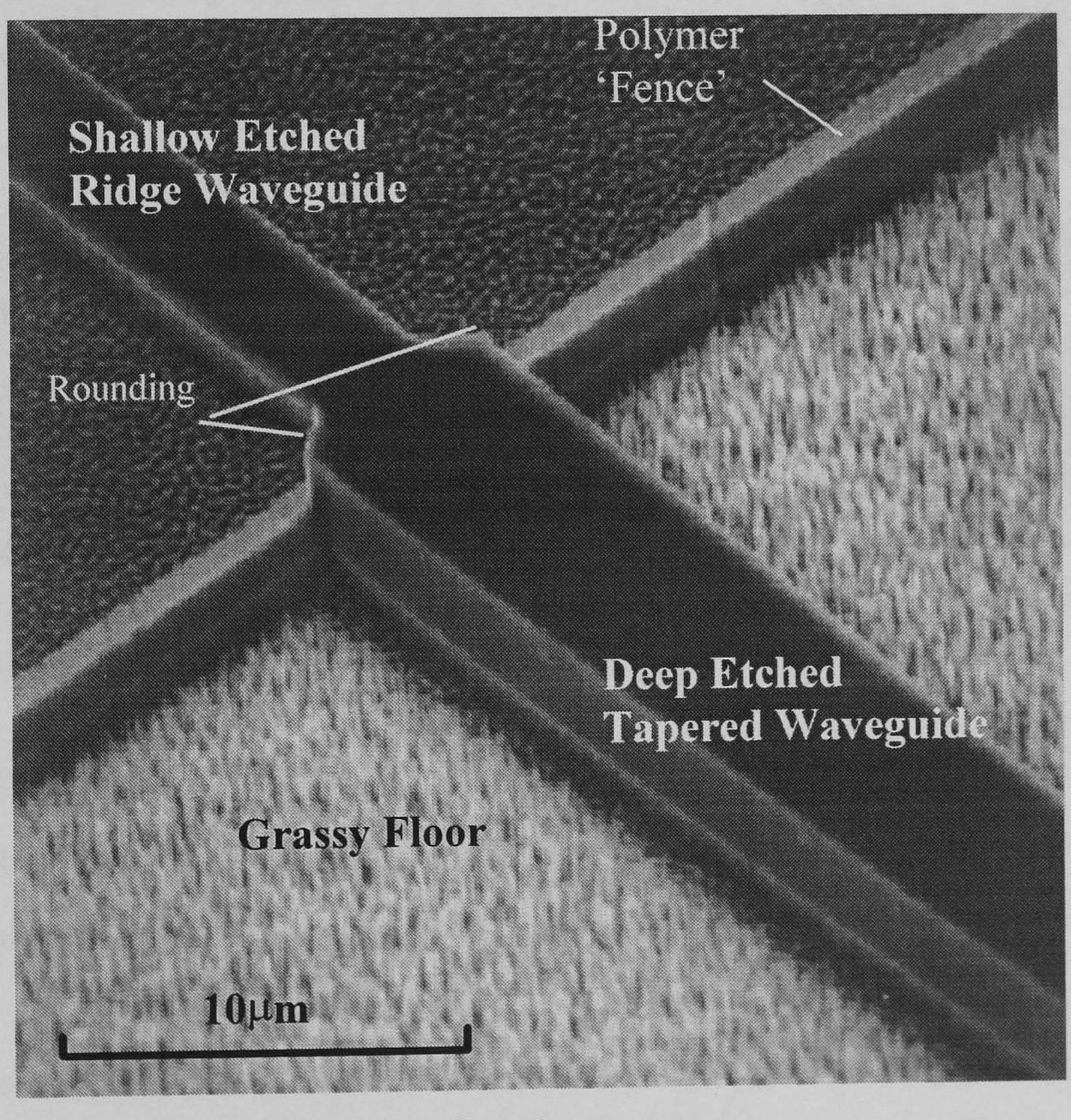

Figure 5.17 SEM of a fabricated tapered mode converter

Initially it may also appear that the waveguide core is clearly visible along the taper and shallow to deep etched boundary. However, it was found that this is in fact, an artefact of the multi-step etching used to fabricate the deep then shallow etched waveguides. This line actually indicates the peaks of the grassy floor which has been 'mowed' along the deep etched walls during the second (shallow) etch step. Indeed it was found that it was impossible to distinguish the core from the cladding by changing the orientation of the samples in the SEM. This indicates good deep etching uniformity, since, in a non optimised etching process, the core is often found protruding from the cladding layers, which makes for lossy TIR mirrors. Other parameters measured using the SEM included the deep etching verticality, which was measured on an off-cut sample to approximately 1° (see figure 5.18a), whilst sidewall roughness was visually comparable to SEMs of TIR mirrors currently reported in the literature [2, 9,11].

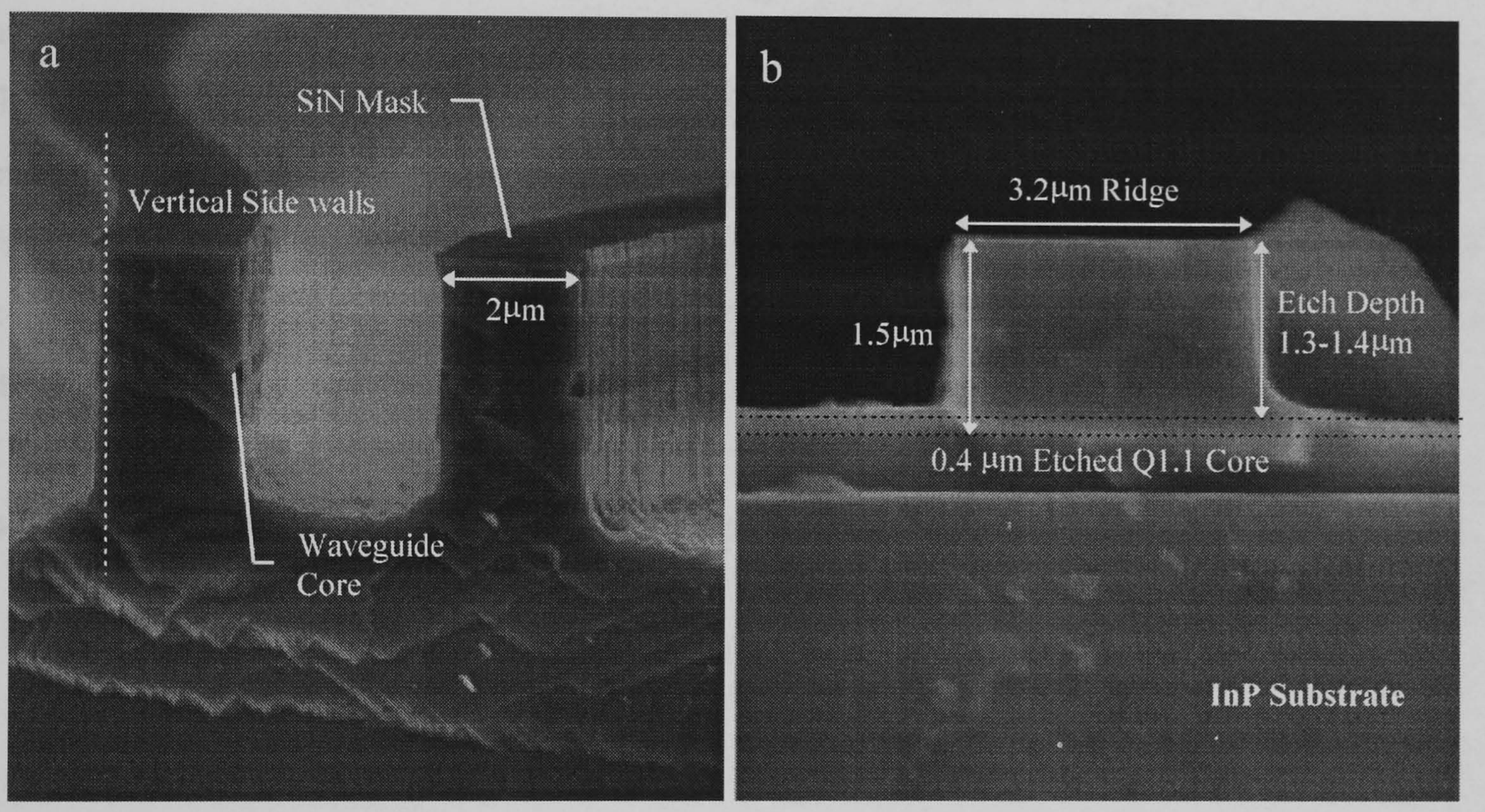

Figure 5.18 SEM of two deep etched 2μm waveguides (left) and a ridge waveguide with wet etched core to reveal guiding layer (right)

Finally the various fabricated waveguide dimensions such as shallow etch depth and waveguide widths were measured using the SEMs shown in figure 5.18. It should be noted that all the mask designs for the passive devices were oversized by 0.5μm. This was done in order to compensate for linewidth errors introduced by the photoresists and undercutting of the etching process. The fabricated shallow etched waveguide width was measured to 3.2μm (which corresponded to a linewidth error of -0.3μm), whilst the deep etched waveguide width was measured to 2μm (which corresponded to a linewidth error of -0.5μm). A more critical waveguide parameter is the ridge waveguide etch depth. However it has already been shown in figure 5.17, that identifying the exact position of the waveguide core is difficult since the etch uniformity is so good. Therefore an off-cut sample was etched for 2 minutes in a proprietary

NiCr etchant (Acetic Acid and Ceric Ammonium Nitrate), which was found to preferentially etch InGaAsP (the waveguide core) compared with InP (the waveguide cladding). This allowed an exact determination of the etch depth above the guide which was then measured using the SEM to between 1.3 to 1.4μm (figure 5.18b). It should be noted that this is slightly deeper than required (theoretical calculations in chapter 4 pointed to an etch depth no greater than 1.2μm).

5.5 Conclusions

In conclusion, it has been shown that a fabrication tolerant process can be developed for the crosspoint in order to overcome the problems associated with multi-level mask alignment. This has been achieved by adopting a self alignment process and optimising the mask design. A number of InP passive test structures have been designed in order to optimise the many components included in the crosspoint architecture. These included waveguide crossings, TIR mirrors, tapered mode converters, S-bend waveguides and MMI couplers. A fabrication process has been developed in order to accommodate self alignment along with UV contact photolithography. Finally the full passive 4x4 crosspoint has been fabricated along with the test structures and the etching quality and tolerances achieved have been highlighted. Chapter 6 will now discuss loss measurements which have been made on the passive devices in order to validate the theoretical predictions made in chapter 4.

5.6 References

[1] P. Bachmann, H. Kaufman, "GaAs Single-mode rib Waveguides with Reactive Ion-Etched Totally Reflecting Corner Mirrors", JLT, 1985, No. 3, pp785-788.

[2] L. Faustini, C. Coriasso, A. Stano, C. Cacciatore, D. Campi, "Loss Analysis and Interference Effect in Semiconductor Integrated Waveguide Turning Mirrors", IEEE PTL, Vol. 8, No. 10, October 1996 pp1355-1357.

[3] U. Niggerbrugge, P. albercht, W. Doldissen, H.P. Nolting, H. Schmid, "Self aligned Low-Loss Totally Reflecting Waveguide Mirrors in InGaAsP/InP", Proc. 4th European Conf. on Integrated Optics, Glasgow, 1987, pp90-93.

[4] P.A. Besse, M. Bachmann, H. Melchior, L.B. Solando, M.K. Smit, "Optical Bandwidth and Fabrication Tolerances of Multimode Interferenceee Couplers", JLT, Vol. 12, No. 6, June 1994 pp 1004-1009.

[5] L.H. Spiekman, Y.S. Oei, E.G. Metaal, F.H. Groen, I. Moerman, M.K. Smit, "Extremely Small Multimode Interference Couplers and Ultrashort Bends on InP by Deep Etching", IEEE PTL, Vo. 6, No. 8, August 1994, pp 1008-1010.

[6] S.E. Hicks, C.D.W. Wilkinson, G.F. Doughty *et al* "Reactive Ion Etching of Low-Loss Mirrors in InP/InGaAsP/InP Heterostructures Using $CH_4/H_2/O_2$ Chemistry", Proc. ECIO '93.

[7] A.L. Burton, P.H. Loosemore, S.N. Judge, I.D. Henning *et al*, "Low Loss Mirrors for InP/InGaAsP Waveguides", Electronic Letters, No. 29, 1993 pp520-521.

[8] U.K. Chakrabarti, S.J. Pearton, F. Ren, "Sidewall Roughnesss During Dry Etching of InP", Semicond. Sci. Technol. No. 6 1991 pp 408-410.

[9] L. Faustini, C. Coriasso, A. Stano, C. Cacciatore, D. Campi, "Loss Analysis and Interference Effect in Semiconductor Integrated Waveguide Turning Mirrors", IEEE PTL, Vol. 8, No. 10, October 1996 pp1355-1357.

[10] E. Gini, G. Guekos, H. Melchior, "Low Loss Corner Mirrors with 45^0 deflection Angle for Integrated Optics", Electronic Letters, Vol. 28, No. 5, Febuary 1992, pp499-501.

[11] L. Faustini, C. Coriasso, A. Stano, C. Cacciatore, D. Campi, "Loss Analysis and Interference Effect in Semiconductor Integrated Waveguide Turning Mirrors", IEEE PTL, Vol. 8, No. 10, October 1996 pp1355-1357.

[12] L.H. Spiekman, Y.S. Oei, E.G. Metaal, F.H. Groen, P. Demeester, M.K. Smit, "Ultrasmall waveguide bends : the corner mirrors fo the future ?" IEE Proc Opt. Vol. 142, No. 1, Febuary 1995 pp61-65.

[13] L.H. Spiekmann, Y.S. Oei, E.G. Metaal, F.H. Groen, I. Moerman, M.K. Smit, "Extremely small Multimode Interference couplers and Ultrashort Bends on InP by Deep Etching", IEEE PTL Vol. 6, No. 8 August 1994 pp1008-1010.

[14] Y.H. Qian, A.C. Bryce, J.H. Marsh, C.D.W. Wilkinson, M.Owen, R.V. Penty, I.H. White, M.J. Robertson, "Fabrication of Test structures for a 4x4 In/InGaAsP Optical Matrix", CLEO Europe 1998.

[15] R.G. Walker, "Simple and accurate loss measurement technique for semiconductor optical waveguides", Electronics Letters, Vol. 21, No. 13, June 1985, pp 281-583.

Monolithic Integration of Optical Space Switches

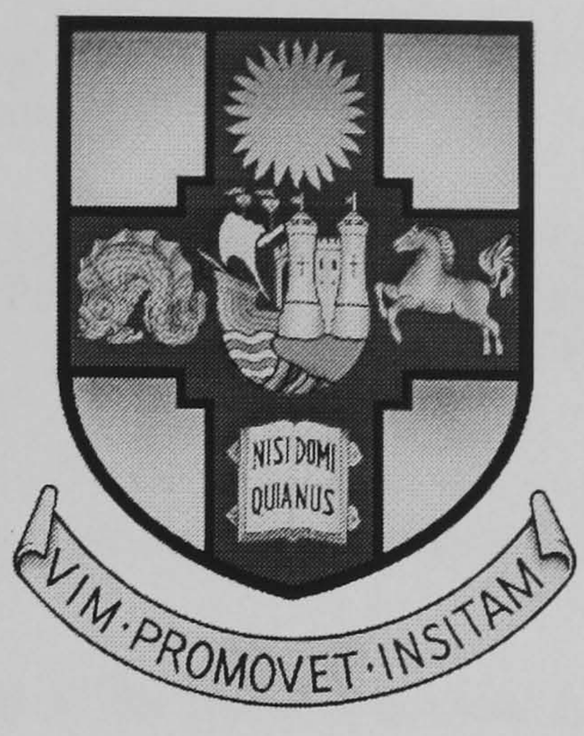

Chapter 6

6.1 Loss Assessment of the Waveguide Crosspoint

Chapter 5 has discussed the design and fabrication of several test structures which have been constructed in order to optimise the waveguide crosspoint switch architecture proposed in Chapter 2. These test structures consisted of waveguide crossings, TIR waveguide turning mirrors, MMI couplers, tapered mode converters, S-bend waveguides and finally the full passive implementation of the 4x4 crosspoint switch. This chapter is concerned with the measurement and assessment of these passive test structures. This is done in order to justify the theoretical calculations made in chapter 4. Finally loss analysis of the test structures allows an estimation of the 4x4 crosspoint performance.

6.1.1 Device loss and Near Field measurement system

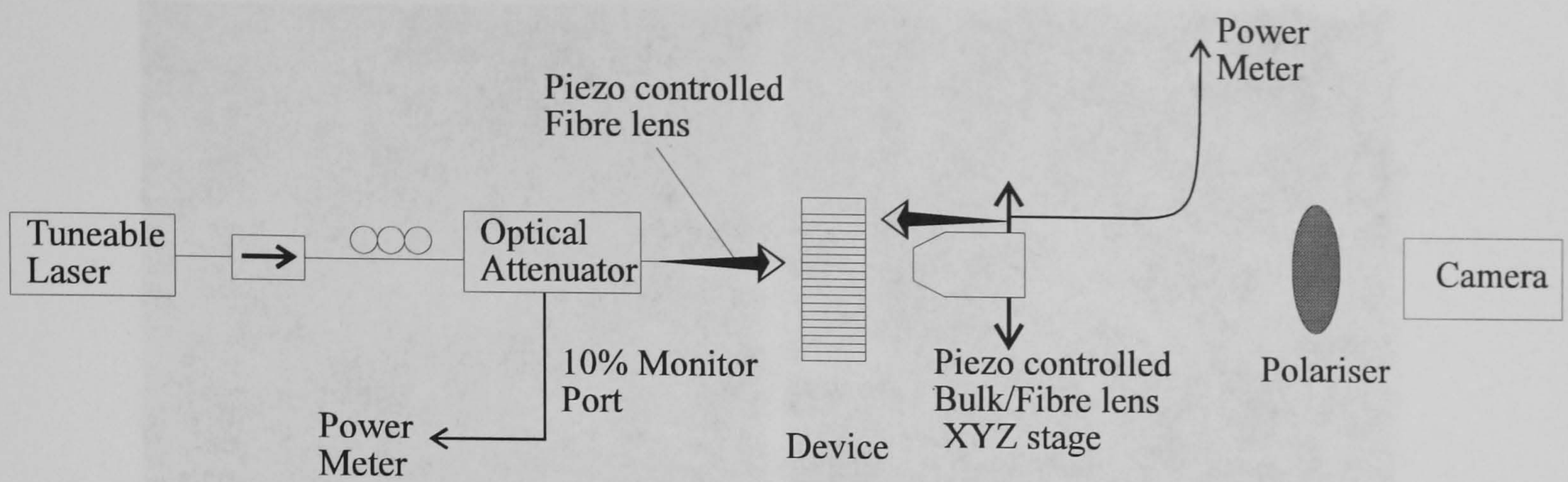

Figure 6.1 Experimental Set-up used to determine passive test structure losses

Although visual inspection of the passive devices (as discussed in chapter 5) gives an indication of the etching quality achieved in the fabrication process, the ultimate test is obtained from optical loss and near field measurements of each of the components. The experimental arrangement used to measure these losses is outlined in figure 6.1. A tuneable laser (HP8168E) was used as the reference input signal and coupled into an optical attenuator (JDS Series 7000) via a fibre isolator and polarisation controller. The attenuator allowed simultaneous measurement of the input power via the 10% monitor port and was required to avoid saturating the IR camera used to measure the near fields of the devices. Light was injected into each device via a fibre lens which was mounted on a Melles Griot piezo controlled XYZ stage. This allowed extremely accurate positioning of the fibre lens with respect to the waveguides under test (measured 6.6μm of travel with a resolution of less than 50nm), thus lowering the error due to fibre alignment. The output light could then be coupled into either a microscope objective or lensed fibre, which were mounted side by side on a secondary piezo controlled XYZ stage. The lens was used in conjunction with an IR camera and a polariser to determine the input polarisation of the tuneable source. A visual picture of the near field of the device also allowed a rough indication to the alignment of the input fibre lens. The bulk lens could then be quickly replaced with the fibre lens by operating a translation stage, and the output piezo control was used to finely align the output waveguide with the use of a second power meter. As such, the throughput fibre-to-fibre loss incurred by the passive components could be accurately determined.

6.1.2 Loss and Near-field measurements of the ridge waveguides

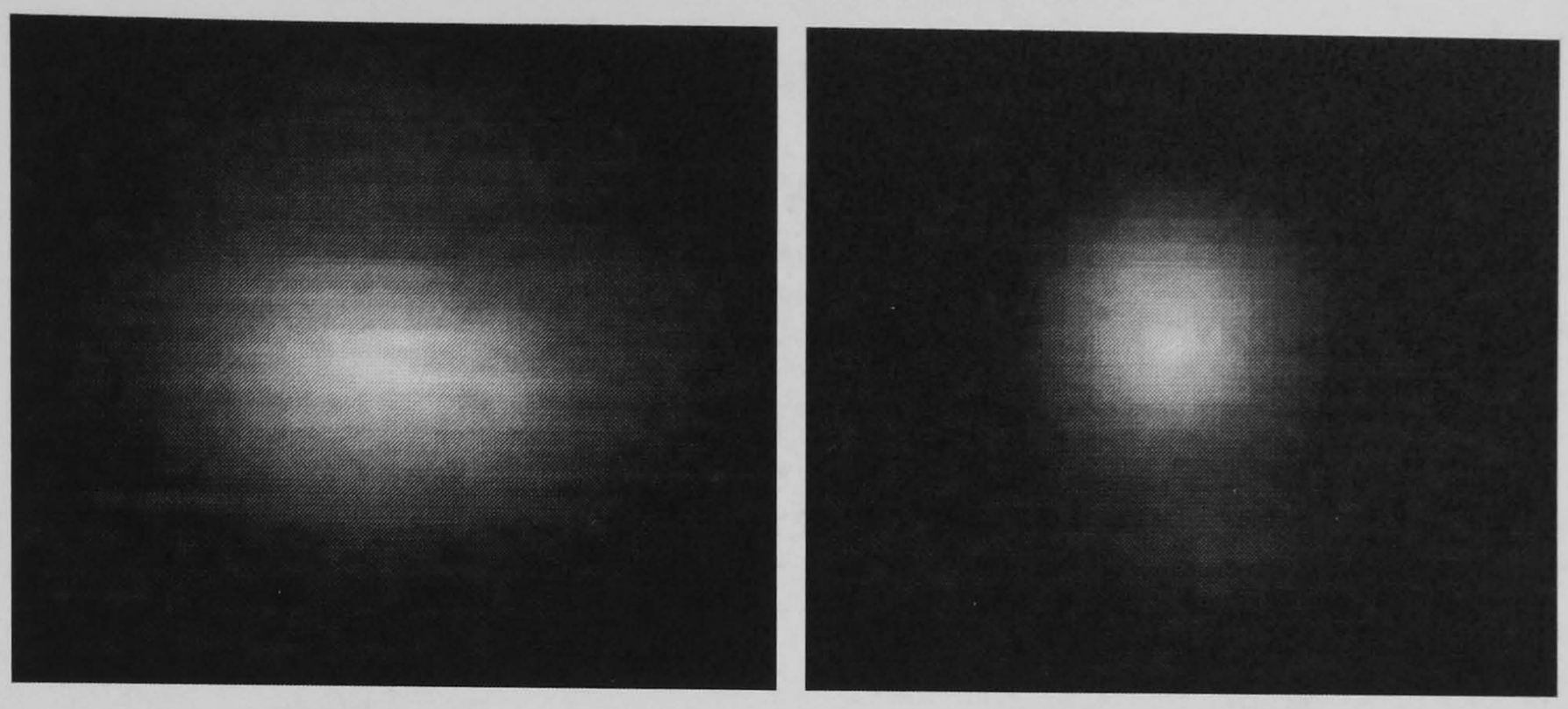

Figure 6.2 Near fields of the 3.2μm wide shallow etched ridge waveguide (left) and 2.0μm wide deep etched waveguide (right) showing single mode TE operation

The first measurements taken with the passive components were near fields of straight waveguides using a x40 Melles Griot microscope objective and the IR camera. This allowed verification that the waveguide designs were single moded as suggested by the theory given in chapter 4. The input polarisation was determined by placing a 1550nm bulk TE orientated polariser in front of the IR camera and adjusting the polarisation controller in order to achieve maximum throughput for TE or minimum in the case of TM. It was found that greater than 13dB isolation could be achieved between TE or TM using this method (>95%), which was calculated by replacing the IR camera with a broad area power meter (HP8153A). A video capture system was used to photograph the near fields of both a 3.2μm wide shallow etched ridge waveguide (left) and a 2.0μm wide deep etched waveguide (right) for a TE optical input at 1550nm. Figure 6.2 indicates that both waveguides were single moded in operation which agrees well with the theoretical calculations made in chapter 4.

The first indication of material and etching quality is given by the loss of a straight ridge waveguide in dBs per centimetre. This figure of merit was determined using the cut-back method [1], whereby the fibre to fibre loss of a straight waveguide was measured as a function of chip length. These measurements were taken at wavelength of 1550nm and are plotted in figure 6.3. A least squares fit to the data resulted in a gradient and waveguide loss of approximately 5±2dB/cm for both polarisations. This is quite a high figure for an InP ridge waveguide, indeed guides have been reported with losses as low as 0.5dB/cm which is an order of magnitude lower [2]. However, it was shown in chapter 5 that non optimum processing resulted in etch depth of almost 1.4μm. This value is very close to the guiding layer and therefore the optical mode, which has increased optical scattering and has resulted in an increased waveguide loss.

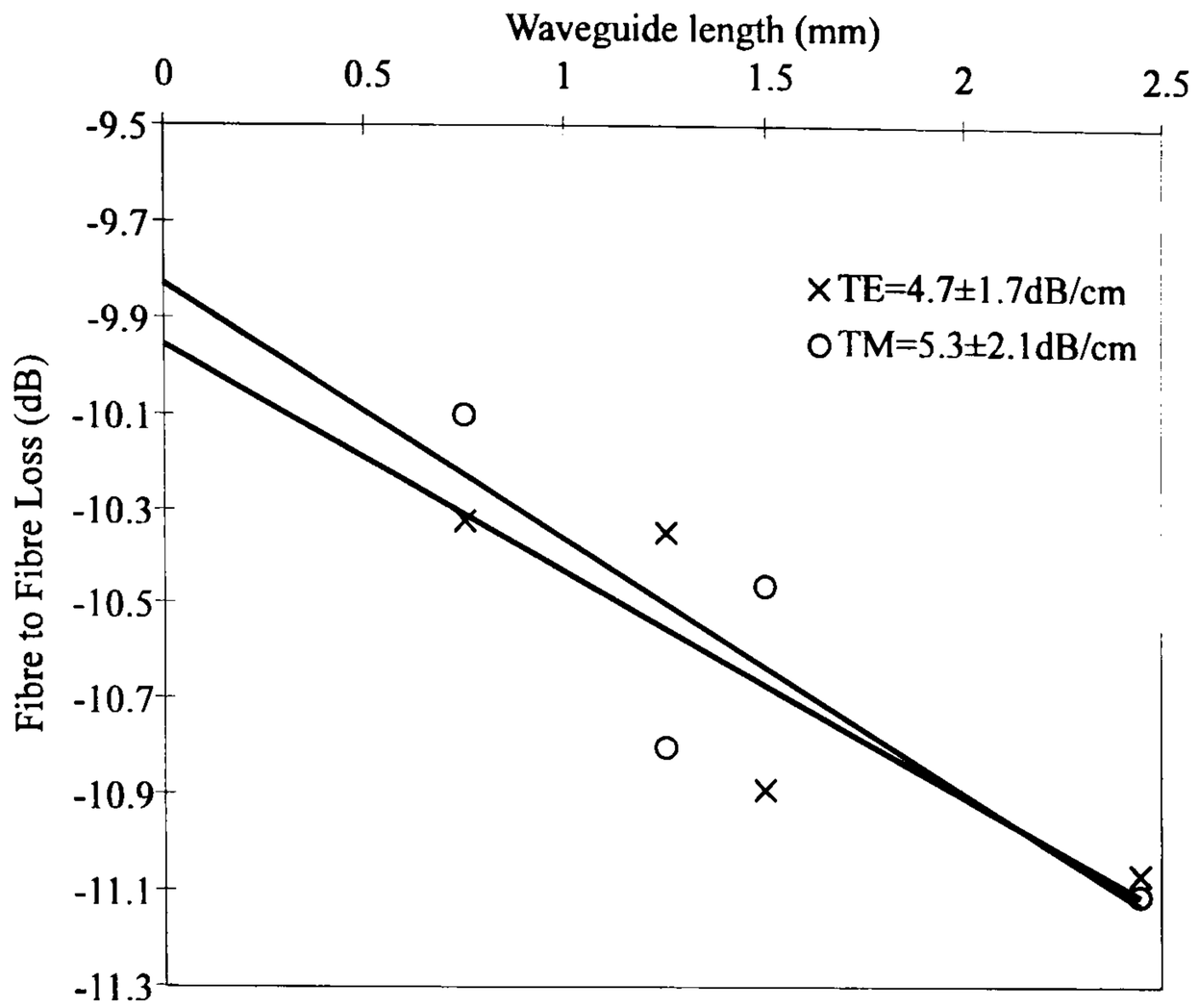

Figure 6.3 Measurement of the straight ridge waveguide loss using the cut-back method.

Two other important details may be noted from figure 6.3. Firstly, it would appear that there is a certain amount of measurement error for each waveguide length tested (although this is more evident in later graphs, especially figure 6.4). Indeed an error on each fibre to fibre measurement of ±0.5dB was estimated from the standard deviation of fifty 1.5mm long waveguides. This uncertainty was attributed to the error in the coupling between the fibre lens and the devices. Secondly, the fibre to fibre coupling loss associated with each measurement may be inferred from the intercept of figure 6.3. This corresponds to a value of 9.9±0.3dB for both TE and TM polarisations. Approximately 3dB of this was associated with the 33% Fresnel reflection at both input and output facets whilst the remaining 3.5dB (x2) was due to the optical mode mismatch between lensed fibre and InP waveguide.

The various other crosspoint components were subsequently tested by comparing the fibre to fibre loss with that of a straight waveguide. This allowed the fibre coupling and losses due to waveguide scattering to be subtracted so that the sole excess loss contribution from each component could be determined. Before discussing the full passive 4x4 crosspoint loss, its constituent components are first examined. This has been discussed in two separate sections, measuring firstly the performance of the waveguide matrix and then secondly the MMI couplers. These measurements will allow an estimation of the performance of the 4x4 crosspoint before finally assessing its overall loss experimentally.

6.2 Analysis of the Waveguide Matrix

6.2.1 Loss measurements of the waveguide crossings

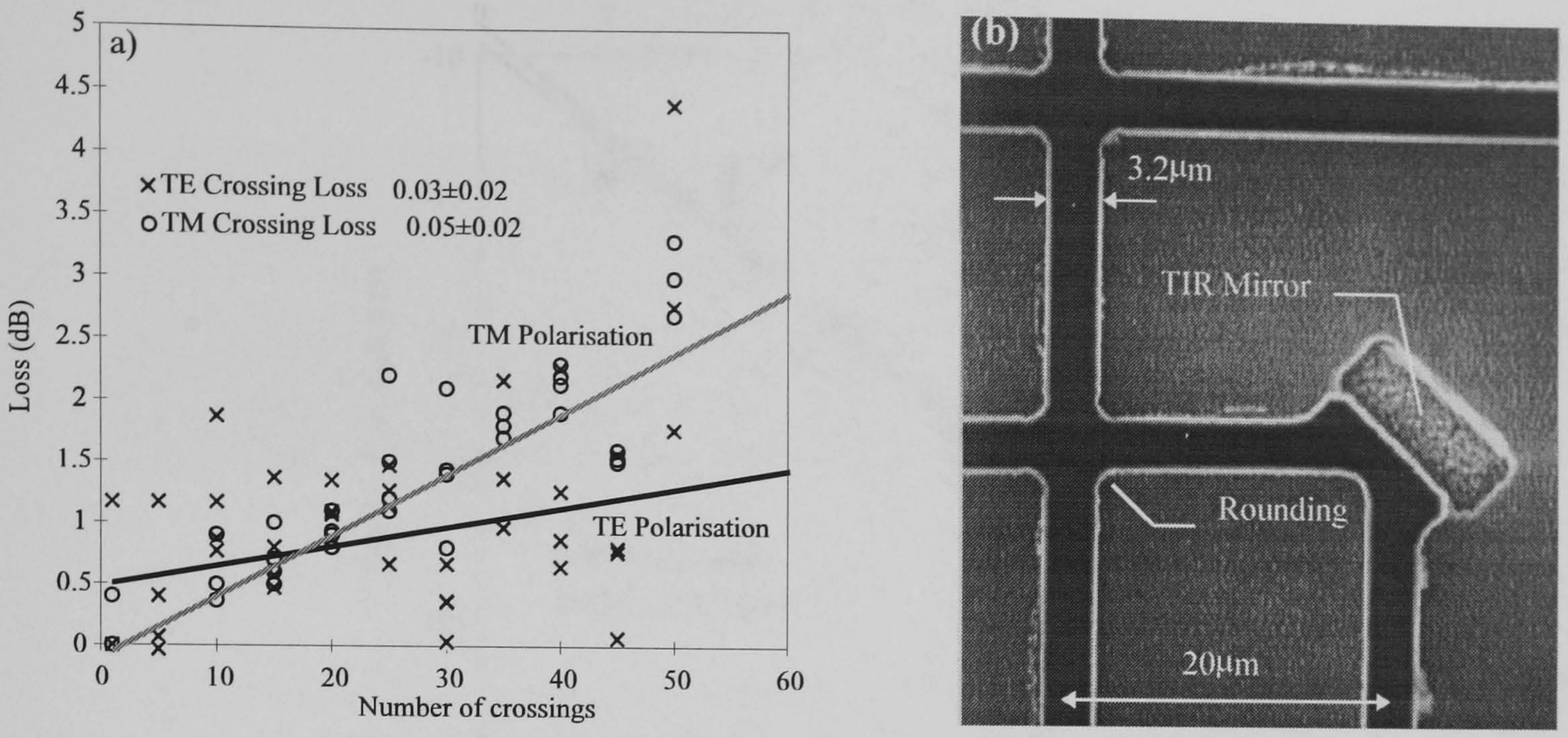

Figure 6.4 Measurement of the waveguide crossing loss (left) and SEM of a waveguide crossing (right) highlighting photolithographic rounding.

The waveguide matrix is central to the crosspoint performance, connecting every input to every output. It consists of a number of straight waveguides, TIR waveguide mirrors and a large number of waveguide crossings (as shown by the SEM in figure 6.4b). Its performance has been investigated with two components, namely the TIR waveguide mirrors and the waveguide crossing test structures. Firstly, figure 6.4a shows the loss measurements on the crossing loss test structure. This figure shows more clearly the error associated with the fibre to fibre loss measurement (±0.5dB). The best fit straight line has been included on the graph for TE (black) and TM (grey). At first sight the TM loss may appear to substantially larger than the TE polarisation. However statistical regression analysis on the data [3] resulted in a loss per crossing of 0.03±0.02dB for TE and 0.05±0.02dB for TM which are statistically consistent.

These losses are slightly higher than the theoretically calculated values made in chapter 4 which predicted a value of approximately 0.015 for the waveguide examined here. This discrepancy was attributed to rounding at the crossing as shown in the SEM in figure 6.4b. An effect caused by the resolution limit of the photolithography process used to fabricate the crossings. The resultant corner rounding causes more of the optical field to be scattered at the crossing, which has not been considered in the theory given in chapter 4. However, it should be noted that this has no detrimental effect on the crosspoint architecture. The measurement still shows that the crossings introduce an excess loss of just 0.8±0.3dB (16 crossings) for the entire 4x4 crosspoint which is negligible.

6.2.2 Loss measurements of the waveguide turning mirrors

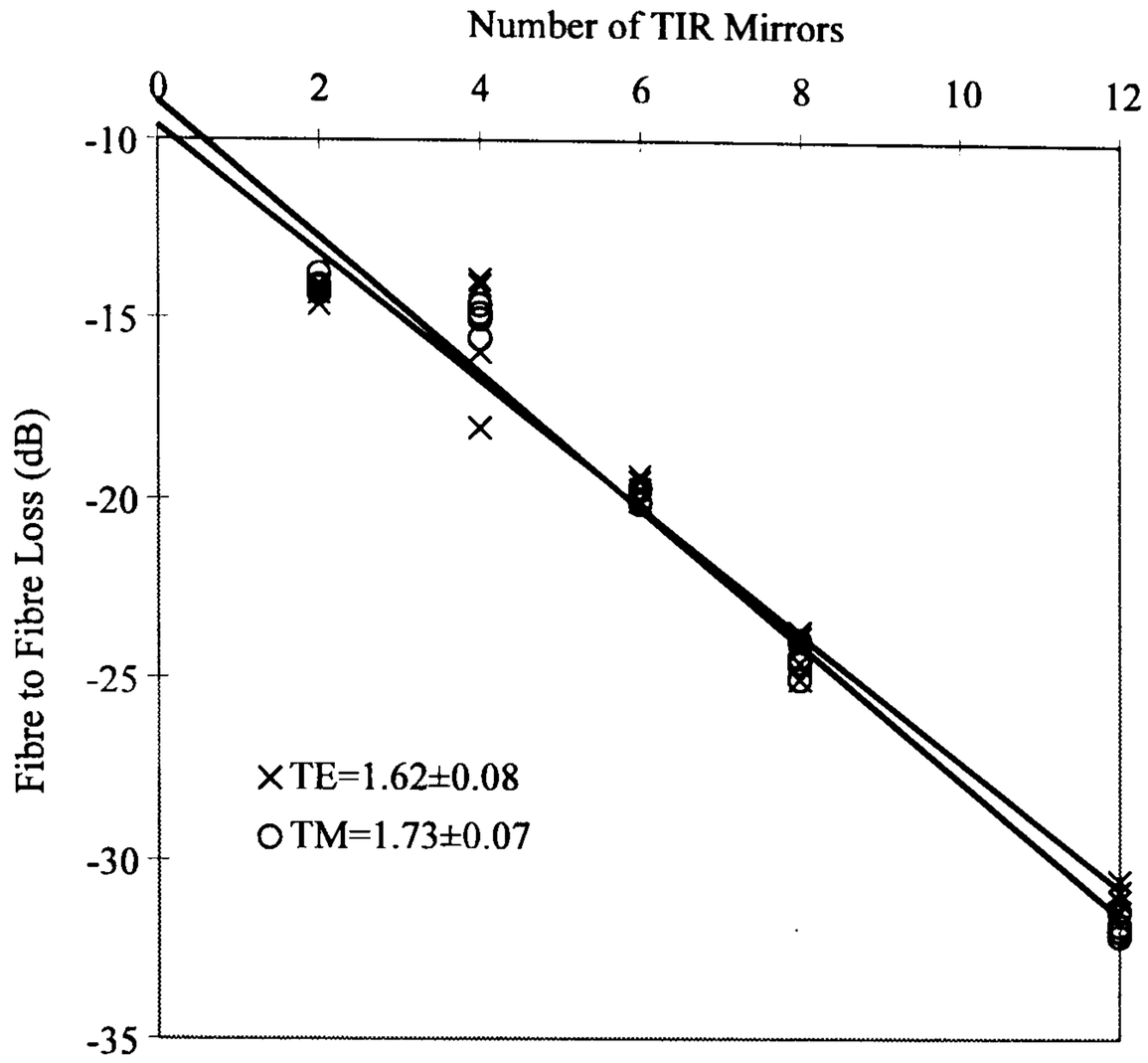

Figure 6.5 Measurement of the waveguide TIR mirror loss for TE and TM Polarisations at 1550nm.

The mirror losses were determined from the waveguide turning mirror device discussed in chapter 5. The chip was cleaved up into several sections so the fibre to fibre loss could be measured in terms of number of waveguide mirrors. These results are plotted in figure 6.5 along with the least squares best line fit for both TE and TM polarisations at 1550nm. The gradient of the line corresponds to the individual mirror loss which was calculated to be 1.62±0.08dB for TE and 1.73±0.07dB for TM. This is a typical value reported in the literature (TE loss 1.5dB from [4]) and indicates that the vertical etching technology is adequate. The y-intercept of each line indicates the fibre to fibre coupling loss which agreed with the previous result of 9.9±0.3dB measured from the straight ridge waveguide analysis.

6.3 Analysis of the MMI Couplers

6.3.1 Near-field measurements of the MMI Couplers

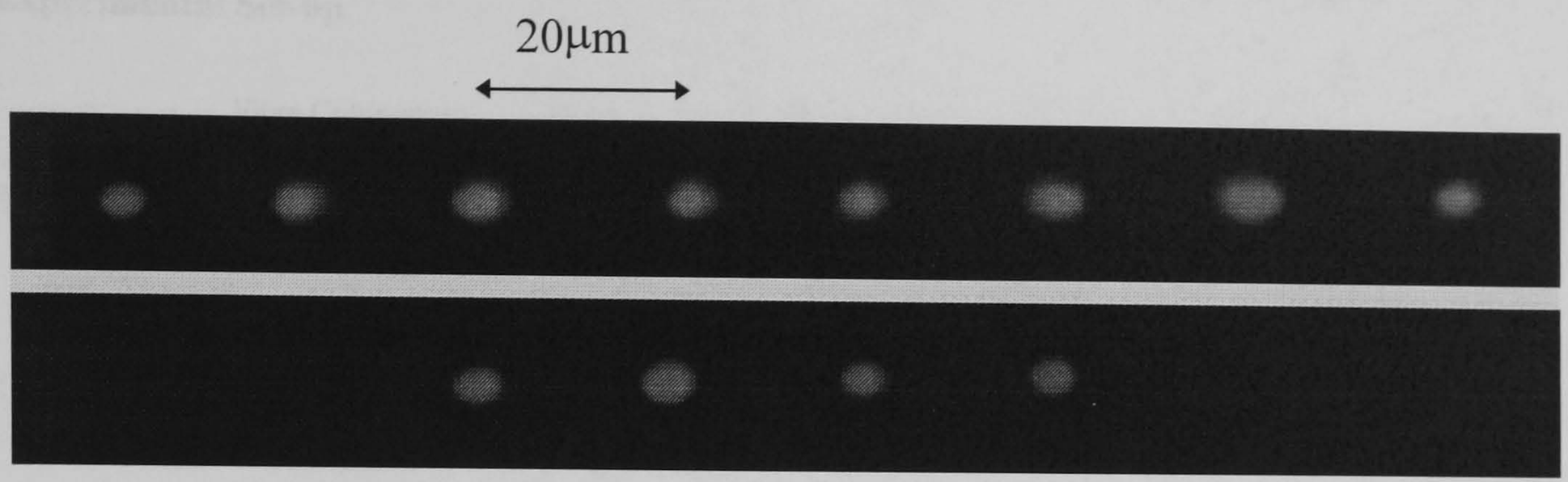

Figure 6.6 Photographed TE near fields of a 1x8 (265μm) and 1x4 (length 138μm) MMI test structures

Assessment of the Multi-Mode Interference couplers began with the measurement of the near field patterns using the same method described in the previous section. Figure 6.6 shows two near field photographs of a 1x4 and 1x8 operating with a TE input polarisation at a wavelength of 1550nm. The results were taken with a x16 Melles Griot microscope objective and correspond to a 265μm long 1x8 coupler and 138μm long 1x4 MMI. The expected number of outputs appear on the camera spaced by exactly 20μm. The observant reader may notice a slight variation in output power on each port. This effect was attributed to Fabry Perot cavities being set up between the input and output cleaved facets. Changing the input wavelength by a few nanometers resulted in a 'twinkling' of the output ports caused by constructive and destructive interference inside the chip. The extinction ratio of these ripples can be used to measure the round trip loss of the device [1]. However, in the case of the MMI this effect implies a non uniform splitting ratio. Thus it was necessary to Anti-reflection (AR) coat the MMI coupler chip facets in order to remove the FP cavities and allow the effective measurement of coupler performance.

6.3.2 AR Coating of the MMI Couplers

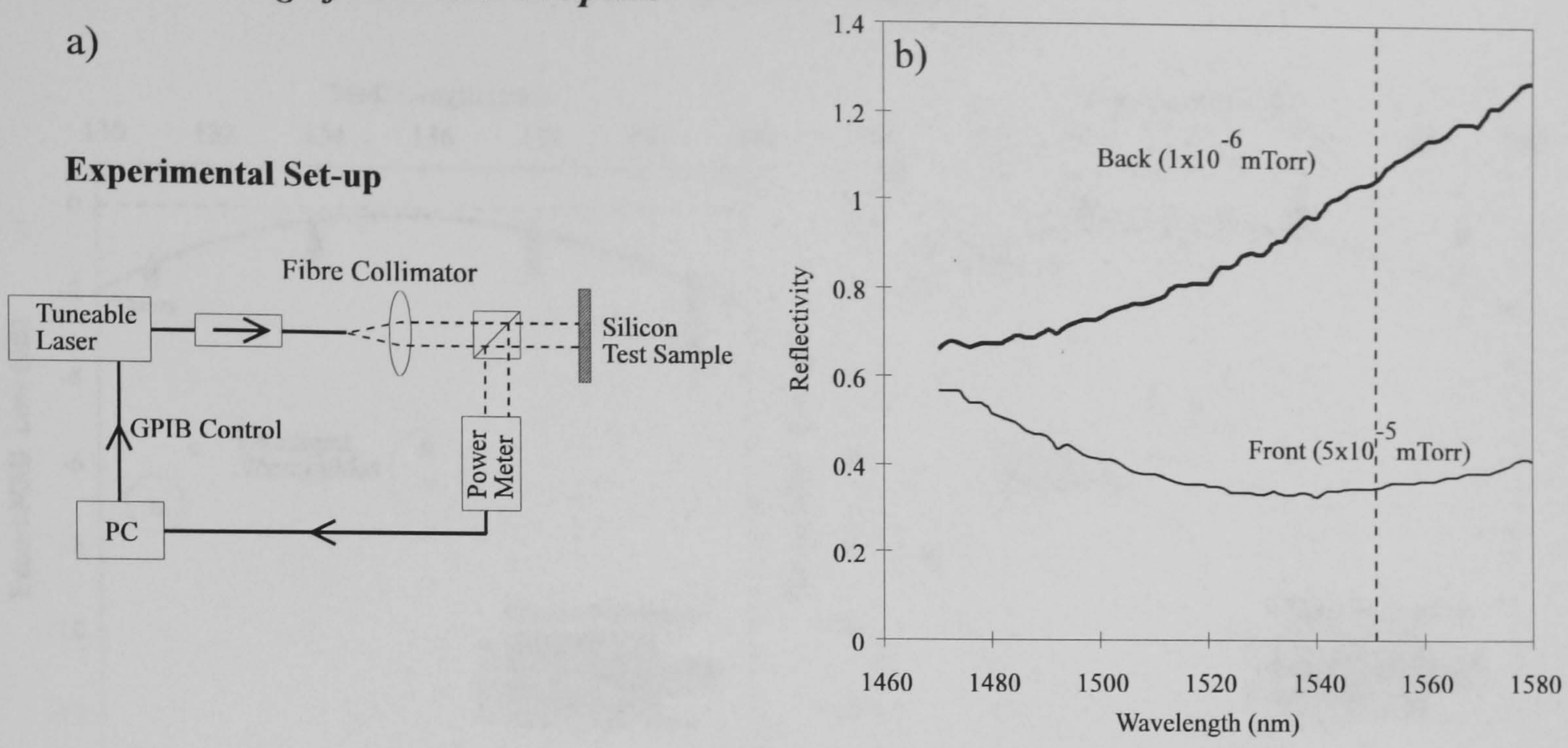

Figure 6.7 AR Coating of test structures in order to test MMI couplers.

Anti-reflection coating may be achieved by depositing a $\lambda/4$ thick film on the device facets such that destructive interference from each interface causes a reduction in reflectivity [5]. Approximately 180nm of TiO_2 (refractive index approximately 2.12) was deposited on each facet with a Leybold-Heraeus electron beam evaporator (at the University of Bristol). A silicon test sample placed in the evaporator during each run allowed an estimation of the achieved reflectivity. This was determined by collimating a tuneable laser source (HP8168E) onto the sample via a 50:50 beam splitter and measuring the reflected power using a HP8153A power meter (figure 6.7a). GPIB control of both instruments allowed a measurement of reflectivity with incident wavelength after the system had been calibrated with a gold plated mirror. It may be observed from figure 6.7b that a zero incidence reflectivity of approximately 0.4% and 1% was achieved on the front and back coated facets at a wavelength of 1550nm. The difference in reflectivity between each coating run was attributed to a different chamber pressure during each evaporation, which resulted in a different film density. It was found that AR coating the MMIs effectively removed the Fabry Perot cavities and therefore allowed component assessment by direct fibre-to-fibre measurements.

6.3.3 Fibre to Fibre Loss Measurements of the 1x4 MMIs

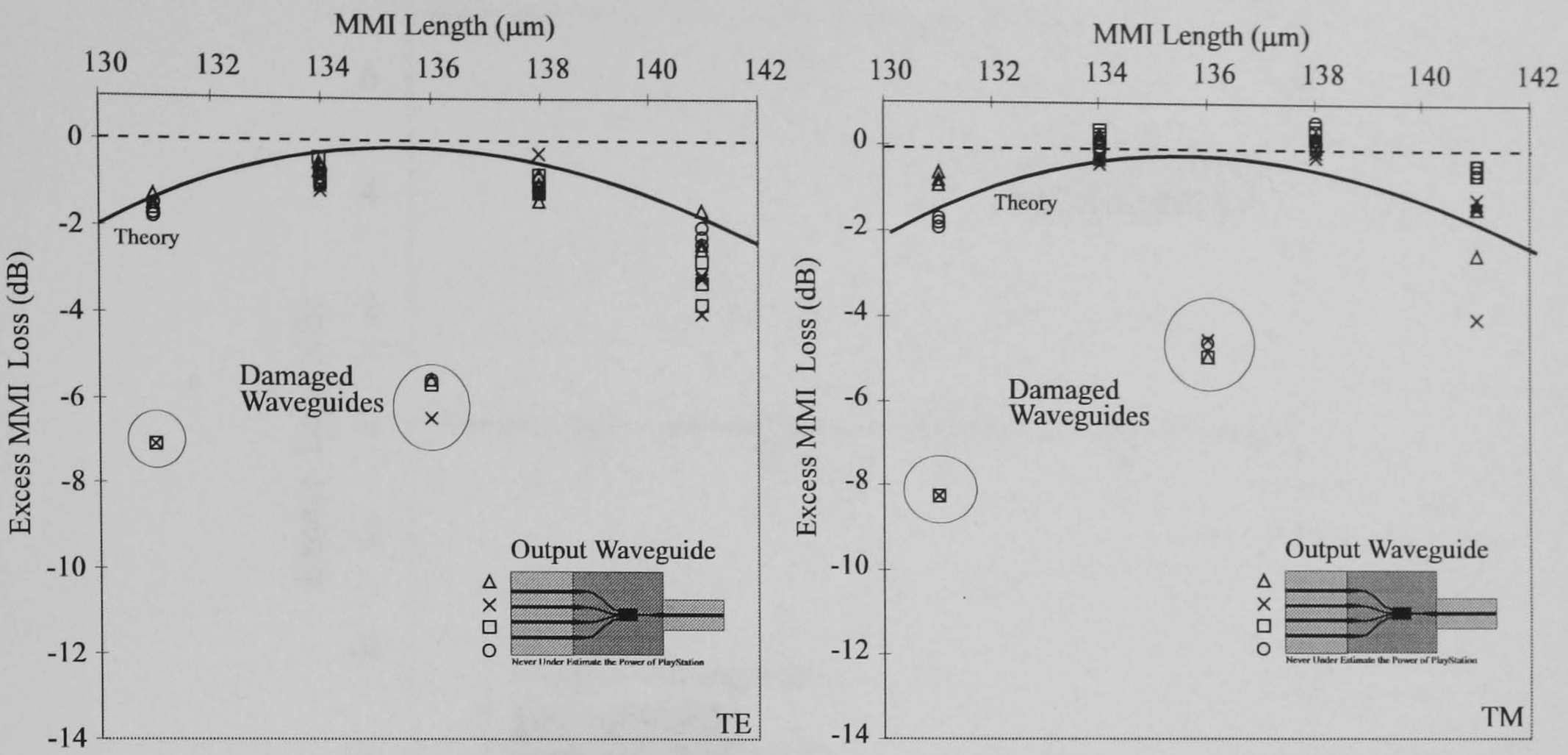

Figure 6.8 MMI Efficiency as a function of MMI length for TE (left) and TM (right) Polarisations

The experimental set-up discussed in section 6.1.1 was used to measure the fibre to fibre loss of each of the five 1x4 test structures discussed in chapter 5. These results were taken for both TE and TM polarisations and for all four of the MMI output waveguides. The measurements were first plotted in terms of MMI length. The straight waveguide loss has been subtracted from the measurements in order to remove the fibre to chip coupling losses. Furthermore the MMIs should incur a minimum of 6dB loss (for a one by four split) which has also been subtracted from the results. This has been done in order to determine the sole *excess* loss contribution from the coupler as shown in figure 6.8. Unfortunately a number of MMI waveguides were damaged and incurred higher losses than expected (circled points).

It may be observed from figure 6.8 that there is a negligible excess loss incurred by the MMI splitter for both TE and TM polarisations. Indeed the figure implies that the TM polarisation performs with a *negative* excess loss. This result is of course impossible, and it is an artefact of the ±0.5dB error on all the fibre to fibre measurements. The optimum MMI length may be observed to be 136μm which is in exact agreement with the theoretical predictions made in chapter 4. Indeed the MMI model discussed in chapter 4 has been used to superimpose a trend line on the measurement points and shows excellent agreement between theory and experiment.

6.3.4 Channel Uniformity and Optical Bandwidth

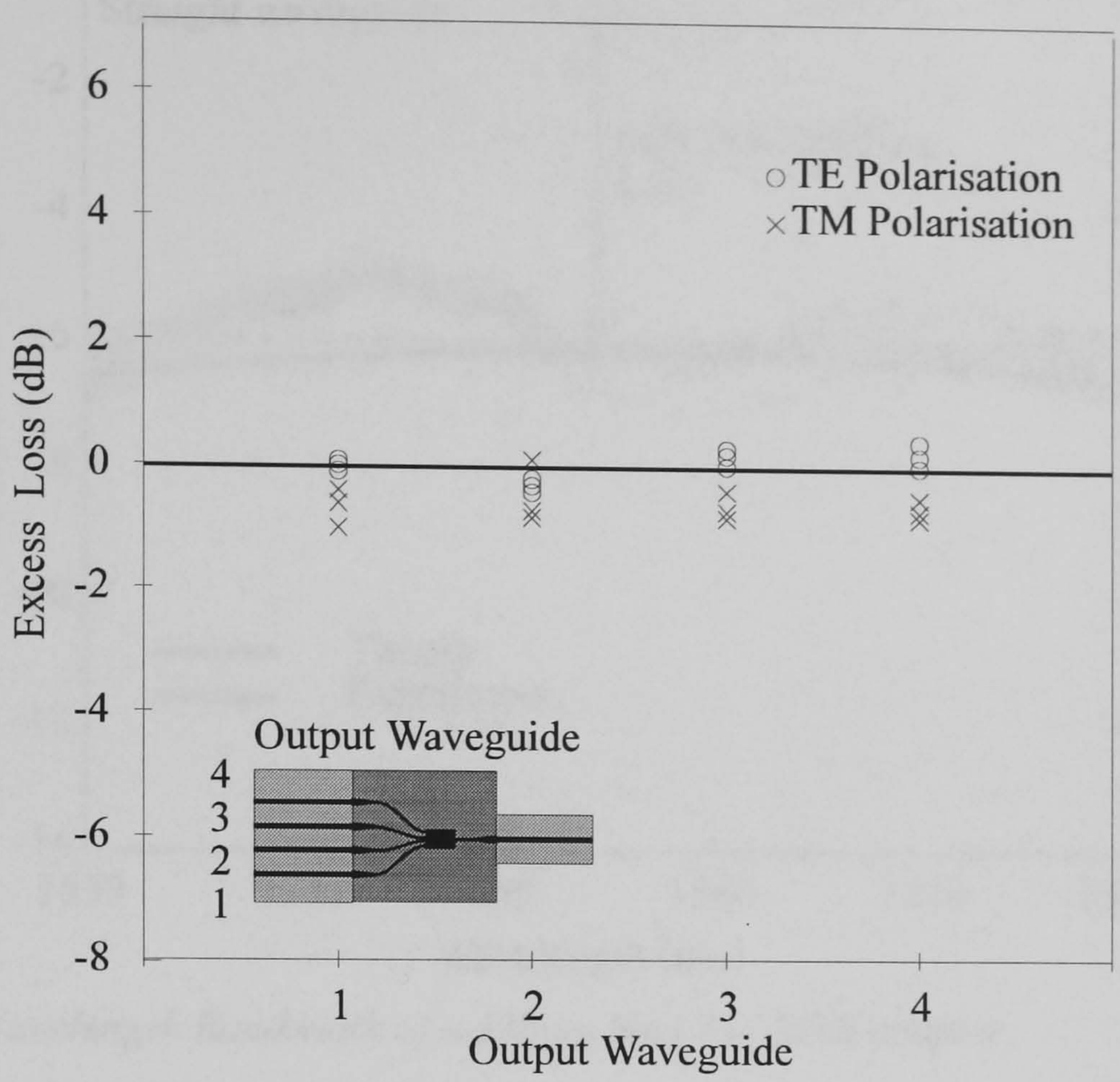

Figure 6.9 Performance of a 138μm long 1x4 MMI coupler for both TE and TM polarisations at 1550nm.

The three most important parameters of an integrated optical splitter are excess loss, output power uniformity and optical wavelength bandwidth. These parameters may be more accurately determined by examining more closely the performance of one of the MMI couplers, namely the 138μm long device which had the best overall performance. Firstly figure 6.9 plots the excess loss of this coupler as a function of the output waveguide. The excess loss incurred by MMI appears to negligible, however taking the measurement uncertainty into account it must be concluded that the excess loss incurred by the coupler is at worst a 1dB, or alternatively 0.5±0.5dB. Secondly, output power uniformity may also be deduced from this figure and is maintained within the experimental measurement error of ±0.5dB for both TE and TM polarisations.

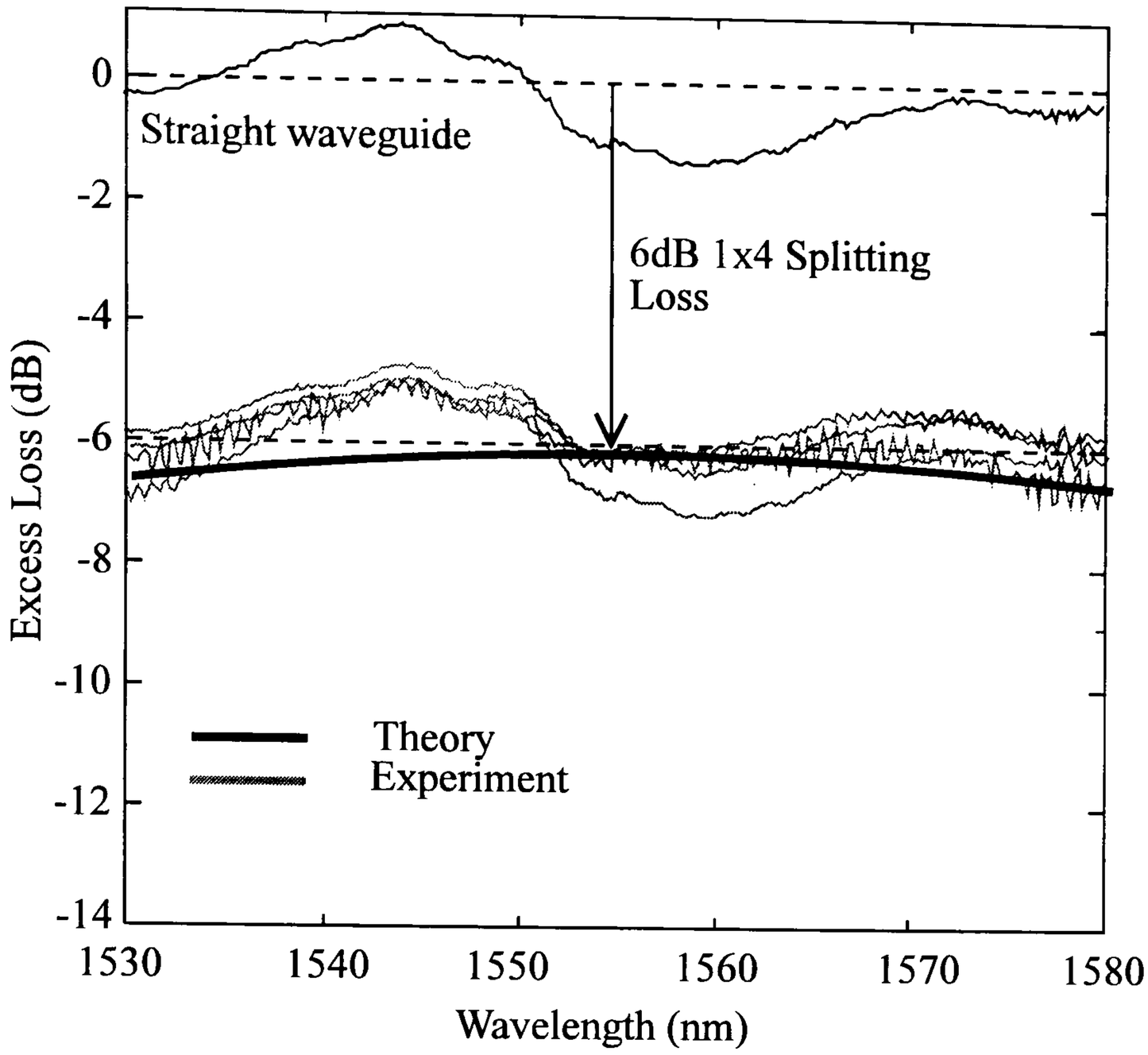

Figure 6.10 Wavelength Bandwidth of a 138μm long 1x4 MMI coupler.

Finally the wavelength bandwidth of the 1x4 MMI coupler was measured by coupling the spontaneous emission of an EDFA (IRE Polus, EAD-60, pump current 500mA) into the 138μm long device. Figure 6.10, shows the transmitted power for each of the four MMI output waveguides as a function of input wavelength which was measured with a HP71450A Optical spectrum analyser (after normalisation). A ripple of approximately 2dB was measured on all the MMI outputs but more importantly was also evident on a straight waveguide. The period of the ripples may be measured to approximately $\Delta\lambda$=30nm which corresponds to a Fabry Perot cavity of length 30μm (in air). This is approximately the distance between the fibre lens and chip when maximum coupling is achieved. Since the ripple response was present for both the straight waveguide and MMI coupler it may therefore be concluded that the effect was a result of the fibre to fibre measurement rather than a wavelength dependence of the MMIs. It was found that the effect of this external cavity could never be removed. However, visually comparing the MMI performance with that of a straight waveguide suggests that the wavelength bandwidth of the MMI is flat over the EDFA window. This agrees well with the theoretical curve which has been calculated from the MMI model presented in chapter 4 and has been superimposed on figure 6.10 (black line).

6.3.5 Tapered Mode converter and S-bend optimisation

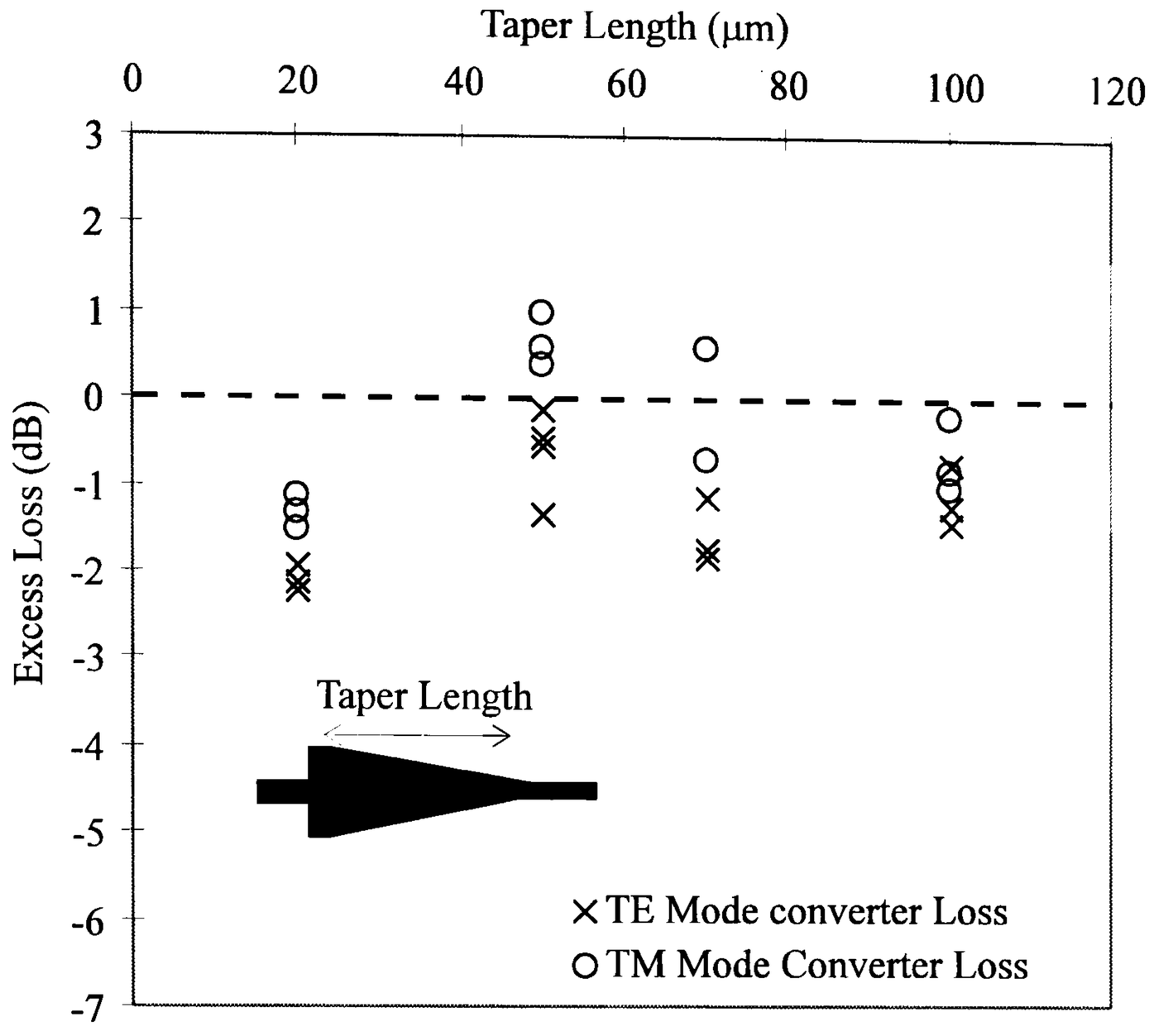

Figure 6.11 Optimisation of the tapered Mode Converter length for both TE and TM polarisations at 1550nm.

The previous section has shown that the MMI couplers have been designed so that they perform with a very low excess loss. However, this has been achieved, in part, by using a mode converter with a very long taper length of 100μm and large radius of curvature S-bends (500μm). The final two test structures, namely the mode converters and S-bends enable these two aspects of the MMI coupler to be studied in more detail. Firstly the tapered mode converter test structure has been used to optimise both the taper length and the taper width. These results are summarised in figures 6.11 and 6.12 for a 1550nm input for both TE and TM polarisations. With respect to the taper length, it may be observed from figure 6.11 that there is a negligible increase in the mode converter loss even if the taper length is halved from 100μm to 50μm. A further reduction to 20μm however, does suggest that the adiabatic condition no longer holds and there is a measurable 1dB increase in loss. This result is very important since a reduction in taper length in each of the four mode converters within the crosspoint would result in a 8% reduction in the device length.

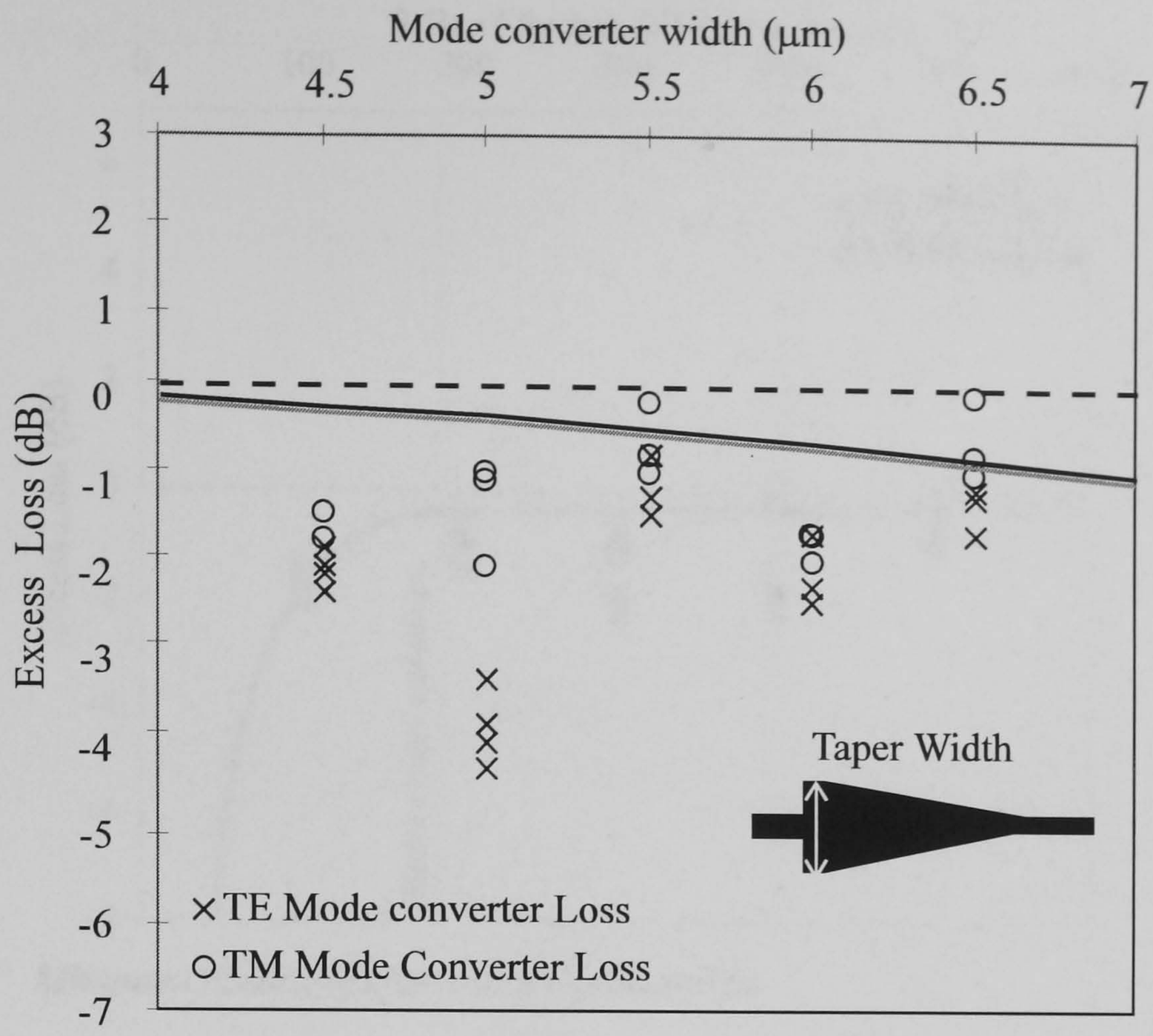

Figure 6.12 Optimisation of the tapered mode converter width for both TE and TM polarisations at 1550nm.

The loss measurements made on the mode converter taper width are plotted in figure 6.12 for both TE and TM polarisations. Also included are the theoretical trends as determined by the analysis presented in chapter 4, with the solid black line representing TE and solid grey line TM. Owing to the experimental error on the measurements it is difficult to ascertain whether the experimental data agrees with theoretical curves. With hindsight a larger spread of mode converter widths should have been fabricated in order to more rigorously justify the theoretical calculations made in chapter 4. However, it should be noted that a loss penalty of less than 1dB was obtained for the 5.5μm wide device. Combined with the low excess loss measurements made on the MMI couplers still indicates very good mode converter performance.

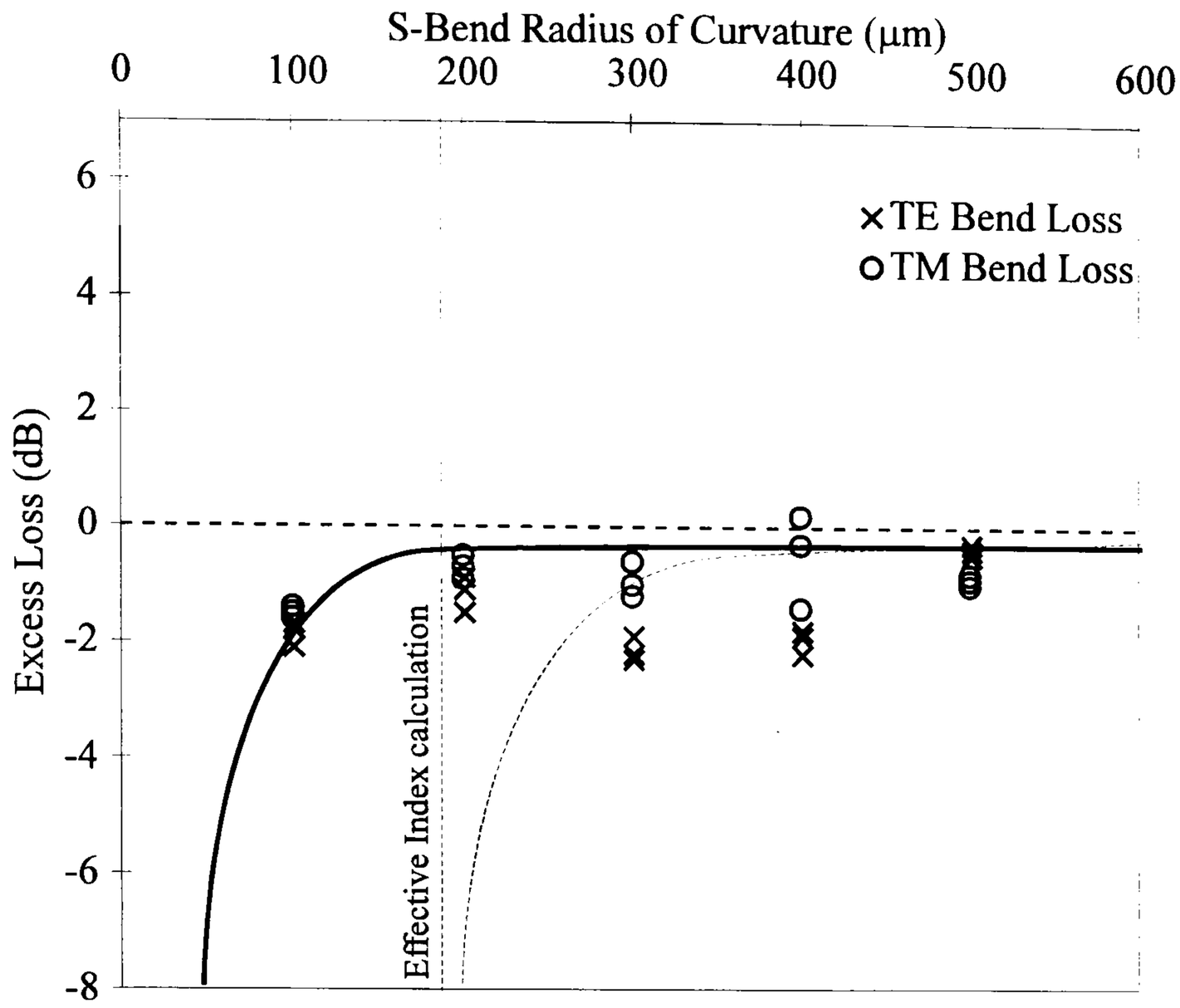

Figure 6.13 Minimum Radius of Curvature Optimisation

Finally, before discussing the performance of the full passive 4x4 crosspoint switch, figure 6.13 summarises the loss measurements made on the S-bend waveguide test structures. The dashed vertical line indicates the theoretical cut-off radius of curvature as calculated from the equation given in [6] and discussed in chapter 4. This represents the waveguide radius below which no light should be guided around the S-bend. During the test structure design it was expected that theoretical trend indicated schematically by the dashed curve would be obtained from experimental measurement. However, it may be observed that a trend shown schematically by the solid curve is more evident. This discrepancy between the theoretical estimate and experimental data was attributed to the simplicity of the calculation given in chapter 4. It should be noted that the equation used was obtained from an effective index approximation for a rib waveguide structure which gave an analytic expression for cut-off. Thus it must be concluded that the theory is not directly applicable for a deep etched waveguide as discussed here. However, more importantly this graph does show that the radius of curvature used for the MMI couplers may be reduced from 500μm to 200μm with a negligible increase in loss. It may be shown that this would equate to a further 4x4 device length saving of 8%.

6.4 Analysis of the Passive 4x4 Crosspoint

6.4.1 Predicted performance of the Passive 4x4 Crosspoint switch

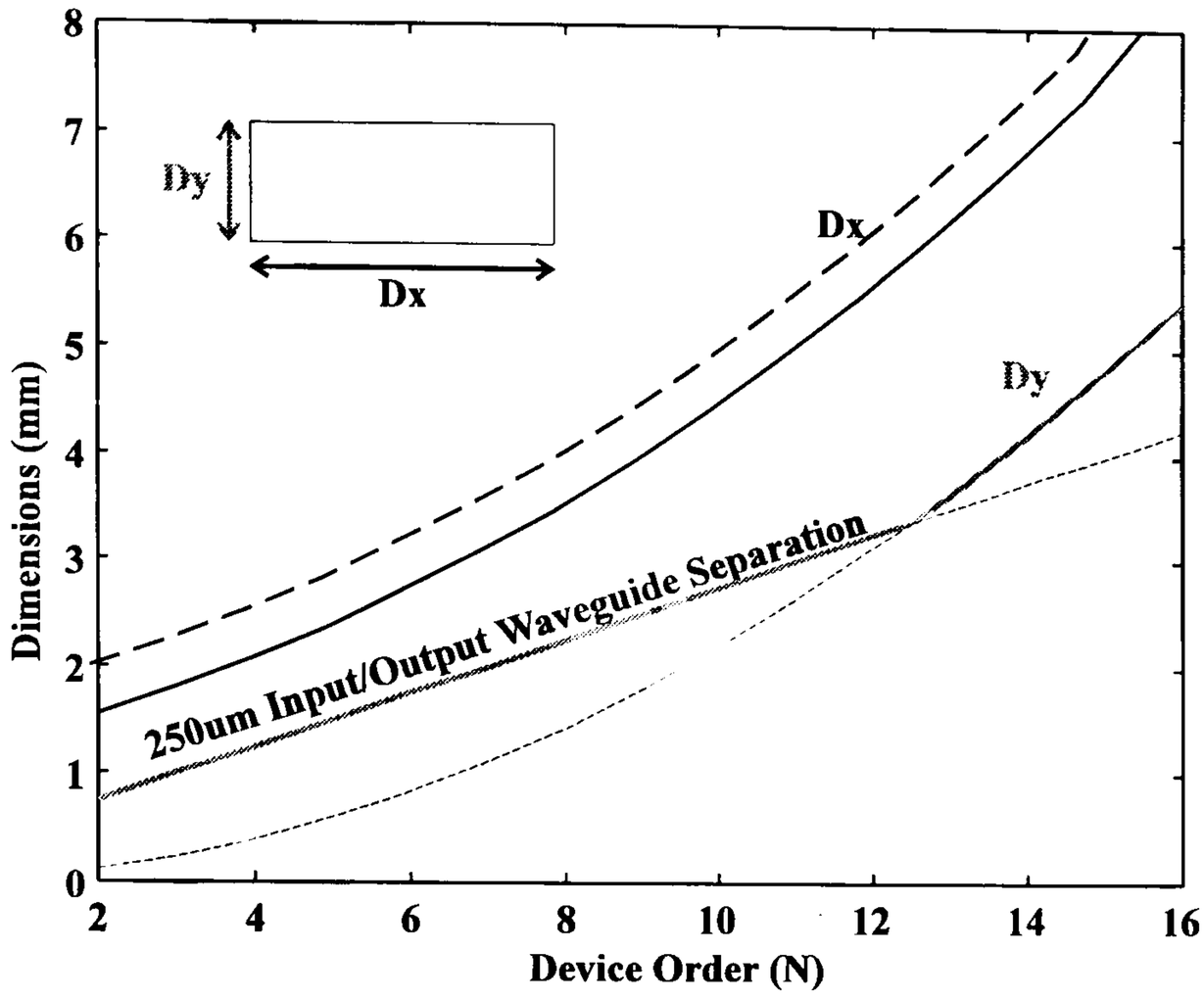

Figure 6.14 *Full active/passive crosspoint switch size as a function of device order.*
Dashed Line : Theoretical prediction made in Chapter 4
Solid Line : Device size calculated from test structure loss measurements.

Two very important conclusions may be drawn from the measurements made on the test structures. The first is the improvement in device size with device order, owing to the reduction in taper length and S-bend radius of curvature. Recalculating the crosspoint length, *Dx,* and width, *Dy,* which are given by the equations 4.22 and 4.23 reported in chapter 4, results in a size reduction of approximately 16%. This is highlighted in figure 6.14 where the recalculated size (solid line) may be visually compared with the theoretical prediction made in chapter 4 (dashed line). These results show a 4x4 crosspoint switch occupies 1x2mm² of an InP wafer. As a comparison this is less than the area occupied by eight typical DFB lasers, or in terms of device density, over 1500 crosspoints per 3 inch wafer, which is considerable.

Component	Loss	
Splitting	6dB	
Combining	6dB	
MMI Excess Loss	1.0±0.5dB	(x2)
TIR Mirror	1.6±0.1dB	(x2)
Waveguide Crossings	0.05±0.02dB	(x16)
Waveguide loss	1.0±0.4dB	(2mm)
	Total 19.0±0.9dB	
	Excess 7.0±0.9dB	

Table 6.1 *Predicted loss performance of a purely **passive** 4x4 crosspoint switch*

A prediction of the total loss of the purely passive 4x4 crosspoint may also be made from the experimental loss measurements discussed in the previous sections. This is summarised in table 6.1 where the key losses in the crosspoint have been highlighted. It should be noted that major loss mechanism is the splitting and combining of inputs signals, which is inherent to a broadcast architecture and cannot be eliminated. The second dominant loss term is incurred by the waveguide turning mirrors which add over 3dB to the excess loss of the device. However, it should be noted that this factor was known well before the device was proposed, and as argued in chapter 2, the mirrors were key to making the architecture so compact. Finally the waveguide crossings, waveguide scattering loss and MMI excess loss contribute a further 3dB to the device loss. Thus, table 6.1 suggests that facet to facet loss of the fabricated passive 4x4 crosspoint architecture should be of the order of 19.0±0.9dB. Ignoring the splitting and combining losses this equates to an excess device loss of 7.0±0.9dB. It should be noted however, that the theoretical results in chapter 4 do indicate that a smaller ridge etch depth of 1.2μm would lower both the waveguide scattering loss and the waveguide crossing loss. This would therefore result in an even lower excess device loss of the order of 5-6dB.

The next section discusses the experimentally measured losses of the 4x4 passive crosspoint test structure. This allows a comparison between the individual component test structure losses as given in table 6.1 and the fully fabricated 4x4 passive device.

6.4.2 Near Field Measurements of the passive 4x4 crosspoint

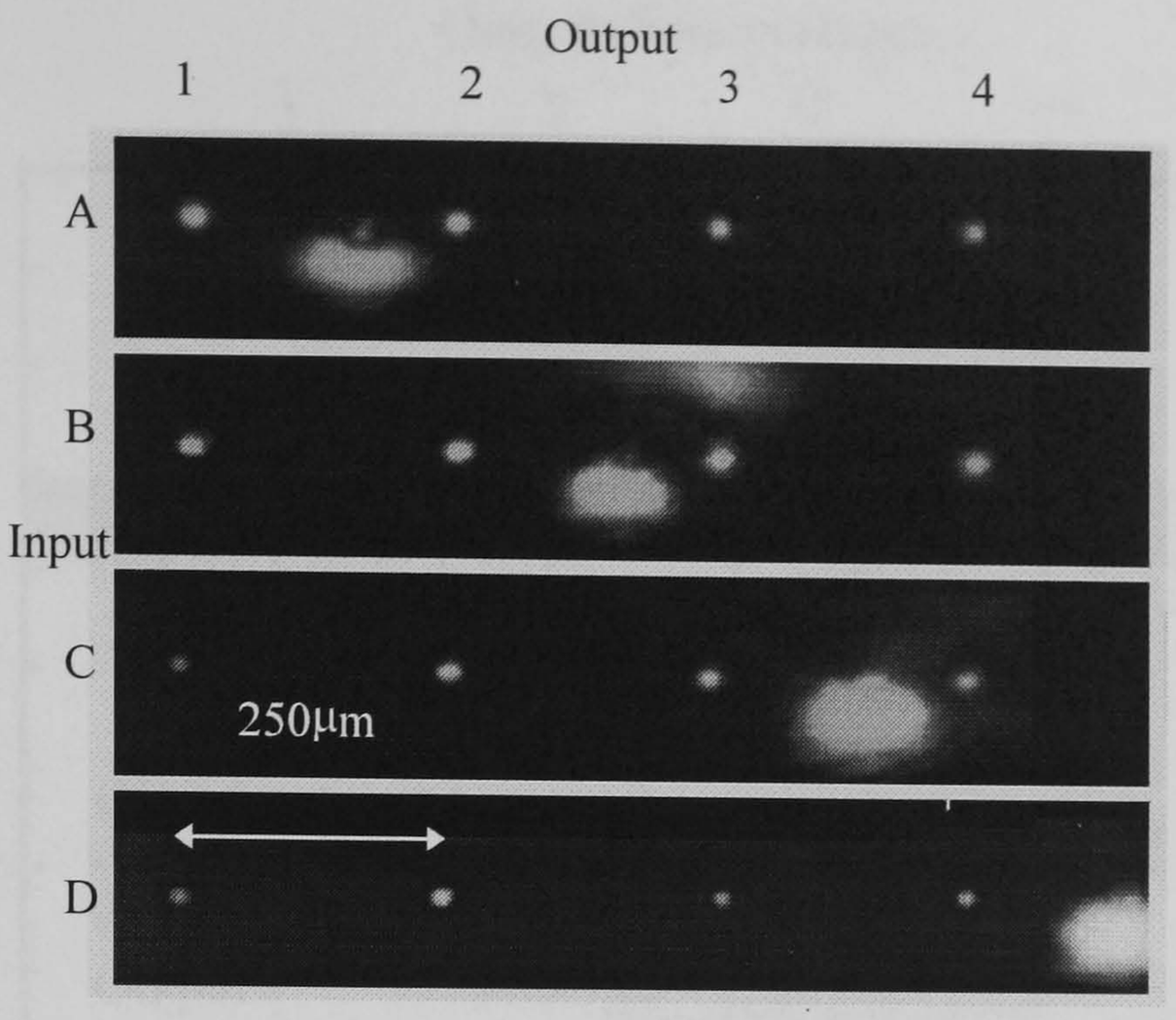

Figure 6.15 Photographed TE near fields of a passive 4x4 crosspoint switch

Near field measurements were first taken of the passive 4x4 crosspoint devices as a first indication of their operating performance. Figure 6.15 shows four separately photographed near fields operating at 1550nm (TE polarisation) which were measured with a low magnification x2.5 microscope objective and IR camera. The position of the optical input at the far end of the chip may be observed from the large circular spots interleaved between the outputs. This is light which has coupled into substrate modes and traversed the chip to the output facet. In terms of channel uniformity, it may be noted that several input/output combinations appear to have high losses, for example C1, D1 and D3. SEM imaging of the device indicated some form of waveguide damage or poor TIR mirror alignment on these paths. Also, it should be noted that it is incorrect to infer the performance of the device by comparing the intensity of the spots on different photographs, since each photograph is subject to different development times and input coupling powers etc. A more accurate measure of the device performance is achieved by a direct fibre to fibre loss measurement as discussed in the next section.

6.4.3 Loss Measurements on the passive 4x4 crosspoint

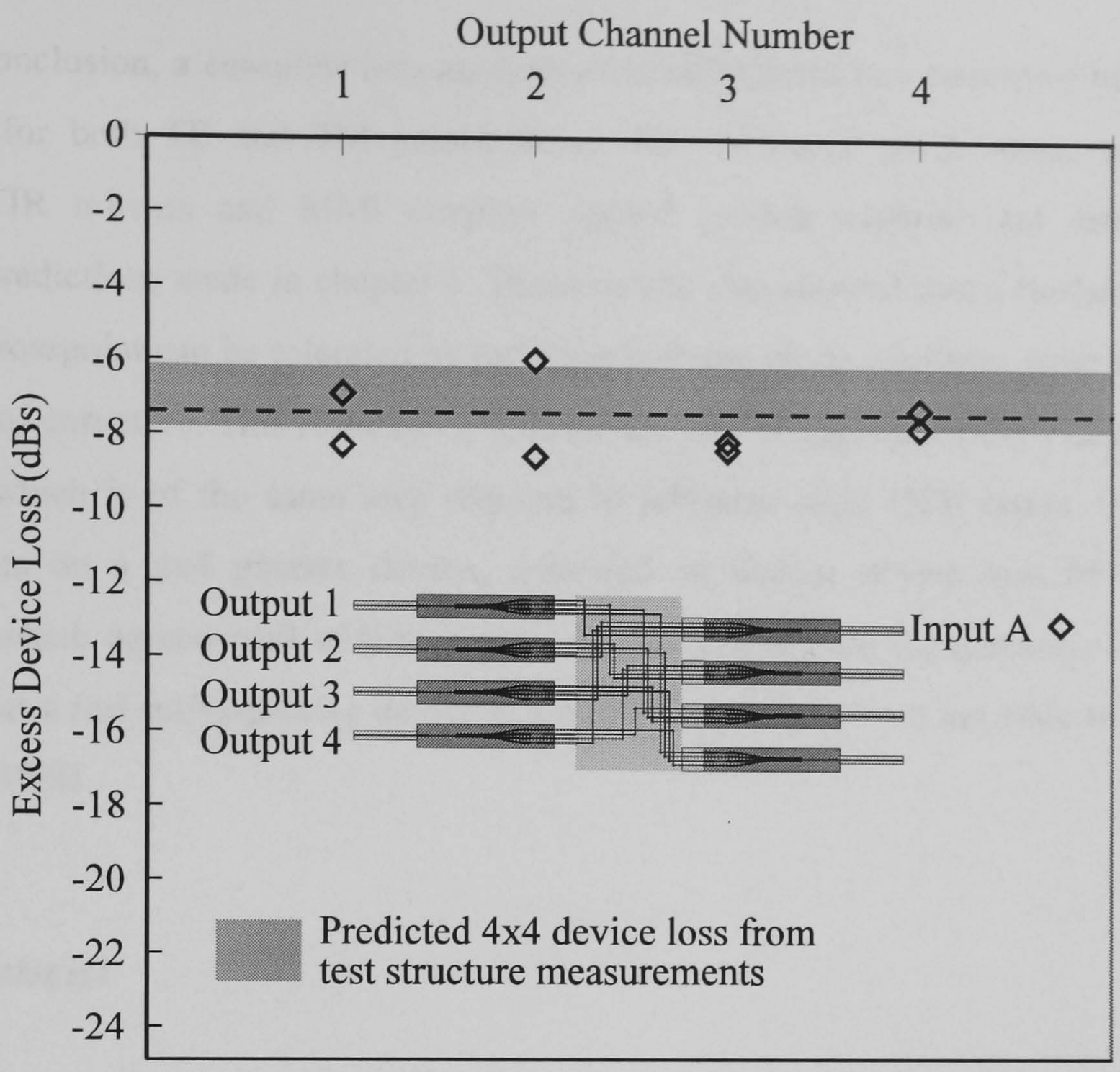

Figure 6.16 Excess loss of a passive 4x4 crosspoint switch for a TE polarised input at 1550nm

Finally, figure 6.16 summarises the loss measurements made on the passive 4x4 crosspoint test structure for a TE input polarisation at 1550nm for input channel A. Each measurement was taken several times and suggests approximately 1dB of error on each measurement as previously reported. A horizontal grey bar has been added to the figure which indicates the predicted crosspoint excess loss of 7.0±0.9dB made in table 6.1. It may be observed that there is good agreement between the 4x4 passive crosspoint loss and losses predicted from measurements made on the individual test structures. The average excess loss from these measurements was calculated to be 7.2±0.5dB and is indicated by the dashed line in figure 6.16. With regard to a full active/passive device, this loss could easily be offset by biasing the two 500μm long amplifiers positioned on both the input and output waveguides (typically more than 20dB gain each, 40dB total). Thus, it is expected that the final device will perform with net fibre to fibre gain of order of 10dB (assuming a 10dB fibre coupling loss).

6.5 Conclusions

In conclusion, a complete loss analysis of the fabricated test structures has been made at 1550nm for both TE and TM polarisations. The measured performance of waveguide crossings, TIR mirrors and MMI couplers agreed (within experimental error) with the theoretical predictions made in chapter 4. These results also showed that a further reduction in size of the crosspoint can be tolerated by reducing both the mode converter taper length and S-bend radius of curvature. This results in a final device size of approximately 1x2mm² for a 4x4 crosspoint, which is of the same area required to fabricate eight DFB lasers. Fibre to Fibre measurements on a 4x4 passive device, indicated an excess device loss of the order of 7.2±0.5dB, which agreed well with measurements on the passive components. It was finally suggested that a full active/passive device is expected to perform with net fibre to fibre gain of the order of 10dB.

6.6 References

[1] R.G. Walker "Simple And Accurate Loss Measurement Technique For Semiconductor Optical Wave-Guides" Electronics Letters, 1985, Vol.21, No.13, pp.581-583.

[2] Private Communication with Dr. M.J. Robertson, Head of Optoelectronic Research BT Laboratories Martlesham Heath, Ipswich.

[3] Microsoft Excel v5.0 User's Guide, "Statistical Analysis of Data", Chapter 31.

[4] E. Gini, G. Guekos, H. Melchior, "Low Loss Corner Mirrors with 45° deflection Angle for Integrated Optics", Elec. Lett. Vol. 28, No. 5, February 1992, pp 499-500.

[5] E. Hecht, "Optics- Second Edition", Addison-Wesley Publishing Co. 1989.

[6] E.C.M. Pennings, R.J. Deri, R.J. Hawkings, "Simple Method of Estimating usable bend radii of deeply etched optical rib waveguides", Electronics Letters Vol. 27, No. 17, August 1991, pp 1532-1533.

Monolithic Integration of Optical Space Switches

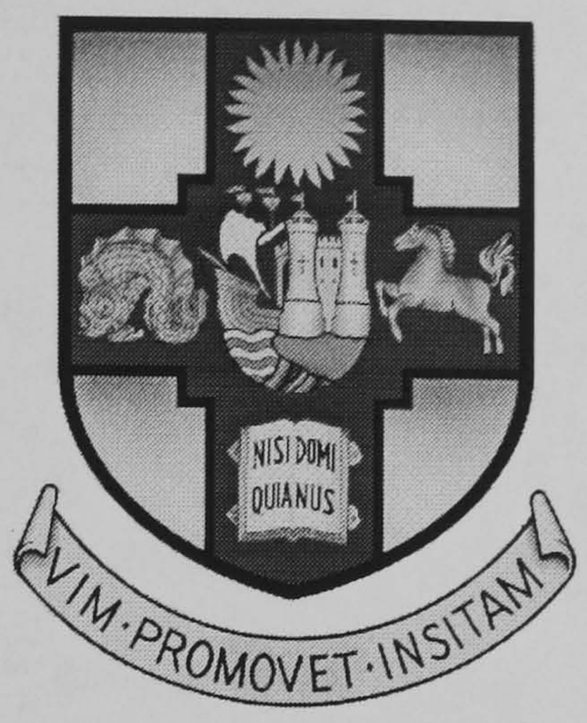

Chapter 7

7.1 The Multi-wavelength Grating Cavity (MGC) Laser

Chapter 1 has briefly introduced the concept of wavelength routing in order to construct an NxN crosspoint switch. In this chapter, the Multi-wavelength Grating Cavity (MGC) Laser fabricated by BT Research Laboratories, Martlesham Heath, is used to demonstrate the functionality of wavelength routing. A brief introduction of the MGC fabrication and method of operation is given. The device is then characterised and the various parameters such as threshold current, grating response and lasing wavelengths are discussed. The temperature stability of the laser will be addressed before finally the device is used to demonstrate multi-wavelength conversion, WDM multiplexing and wavelength routing at 2.488Gbits/s. This figure is currently the highest modulation rate achieved by a monolithic integrated multi-wavelength laser.

7.2 Outline of device structure and fabrication

7.2.1 Selective Area Regrowth

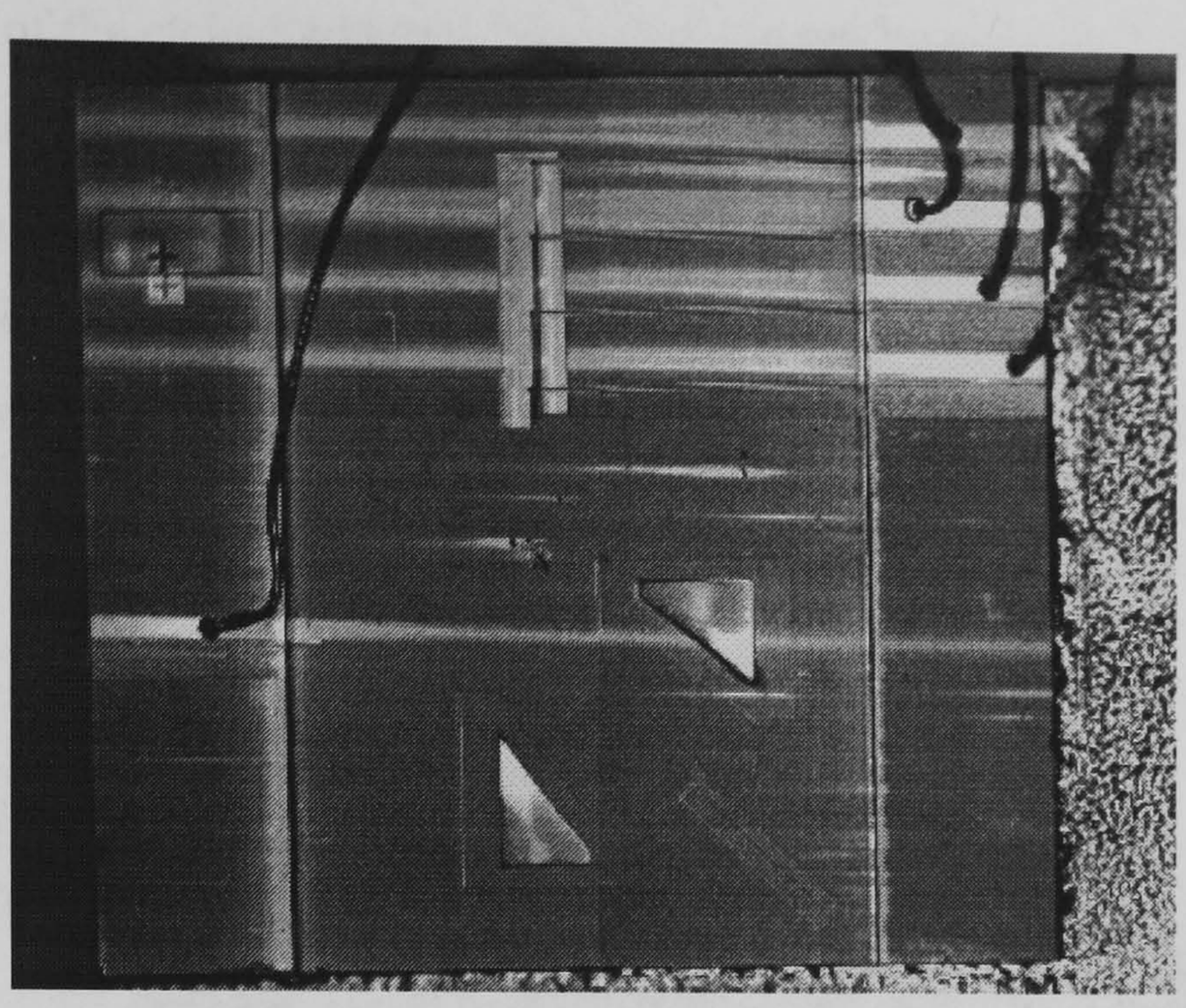

Figure 7.1 The Multi-Grating Cavity (MGC) Laser

The Multi-Grating Channel (MGC) Laser discussed in this chapter is shown in figure 7.1, and drawn schematically in figure 7.3. The device is an integrated InGaAs/InGaAsP/InP multi-wavelength laser operating around 1.55μm. It consists of two active gain regions which sandwich a passive 2DIO slab waveguide fabricated by selective area regrowth [1]. The active regions consist of InGaAsP/InGaAs quantum wells which lie above the quaternary waveguide core (as shown schematically in figure 7.2), and therefore gain is evanescently coupled to the propagating optical mode. In the passive region, the quantum wells have removed by the application of a silicon dioxide mask and the selective wet etching to an 'etch stop'. This consists of a very thin epitaxial grown layer (0.1μm) of n doped InP which is resistant to a selective InGaAs/InGaAsP wet etch used to remove the quantum wells in the upper cladding

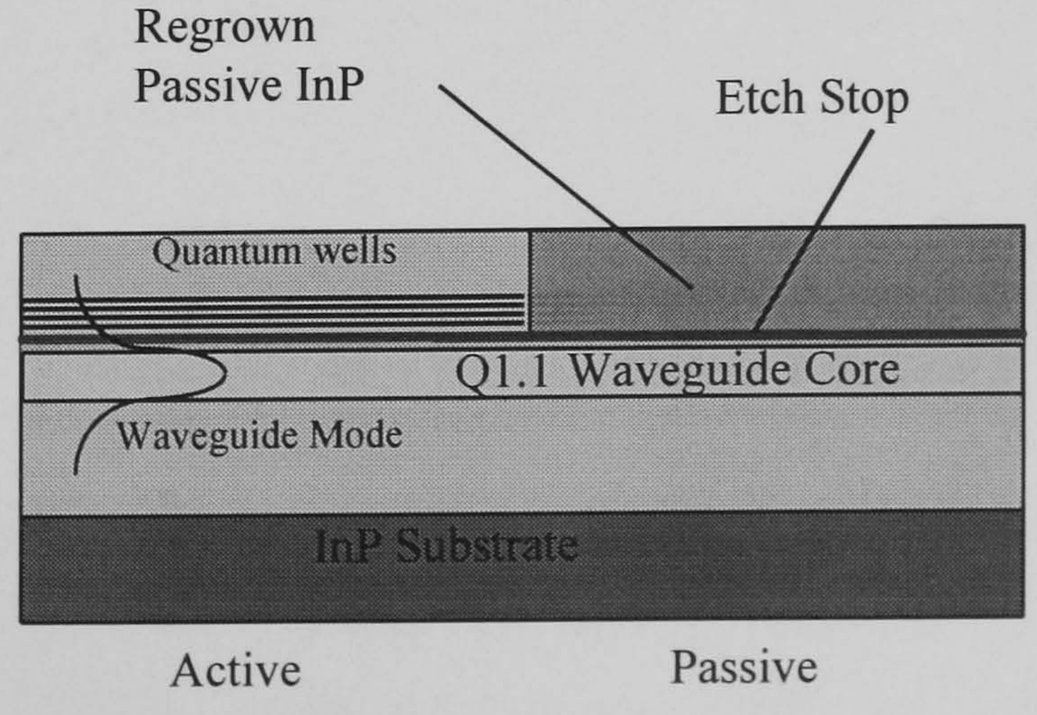

Figure 7.2 Active/Passive integration using selective area regrowth on an evanescently coupled quantum well wafer

layer. This process therefore allows a very accurate etch depth control so that the wells may be removed without etching through to the waveguide core. In order to obtain a low loss transition between the active and passive region (i.e. a small refractive index step) it is necessary to regrow InP in place of the etched material. Since InP cannot be epitaxially grown on the silicon dioxide mask used to remove the quantum wells, regrowth is simply achieved by a subsequent InP epitaxial growth step (by MOVPE [2]) which forms the passive slab waveguide. The stripes and deep etched mirrors (which are discussed in the next section of this chapter) are then patterned onto the wafer. This is achieved by same processes used in the fabrication of the test structures discussed previously in Chapter 5.

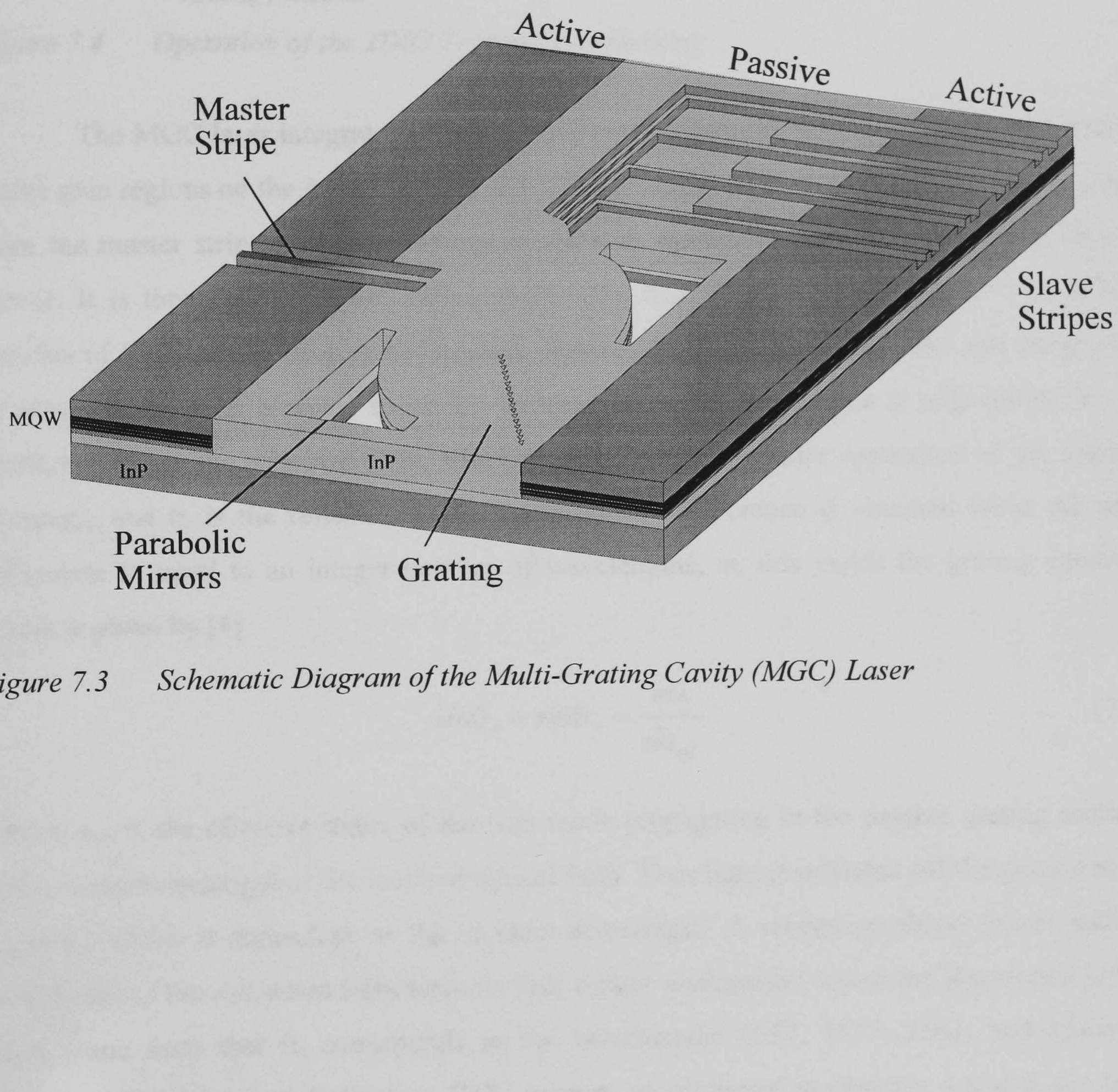

Figure 7.3 Schematic Diagram of the Multi-Grating Cavity (MGC) Laser

7.2.2 Device Operation

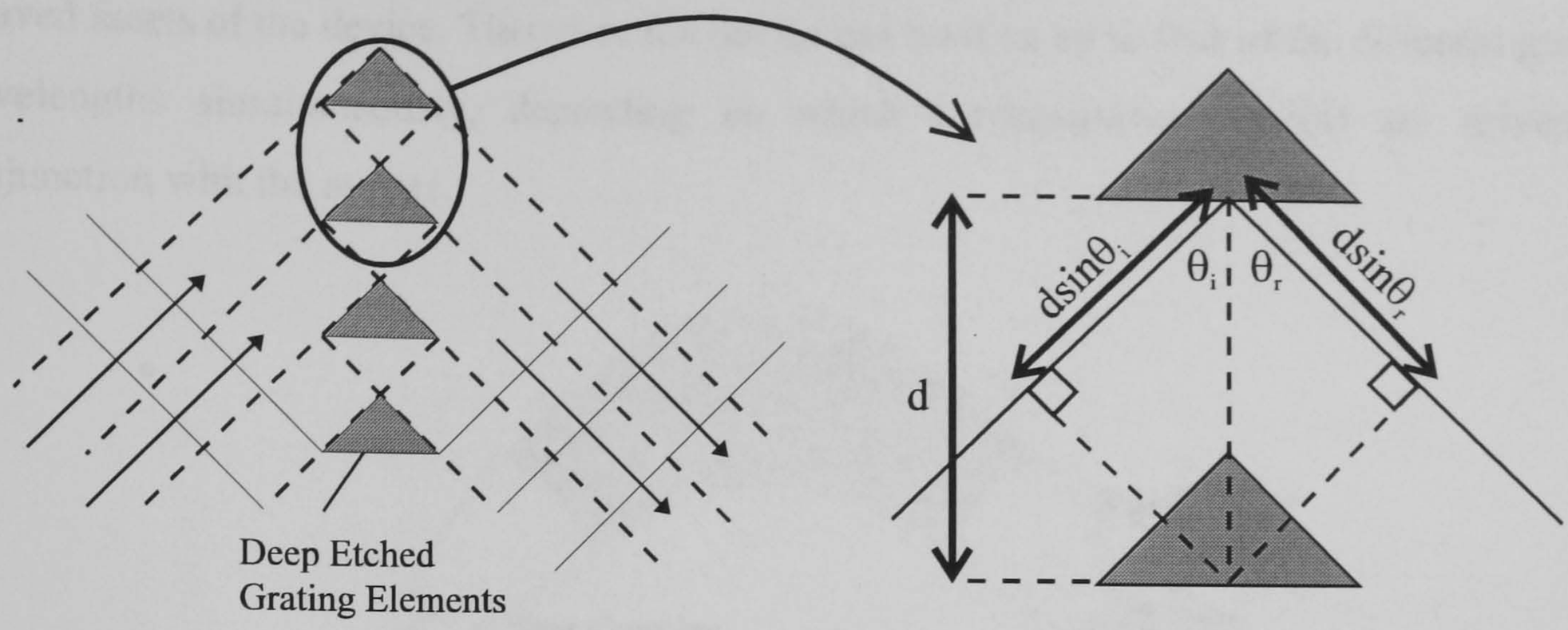

Figure 7.4 Operation of the 2DIO Transmission Grating

The MGC laser integrates an InP passive grating demultiplexer section [3] with MQW active gain regions on the input (Master) and the four output (Slave) waveguides. Light emitted from the master stripe is able to diverge in the slab waveguide until it strikes the parabolic mirror. It is then collimated and reflected onto the transmission grating (figure 7.3). which consists of 32 triangular deep etched mirrors (figure 7.4). If the light is incident onto the grating at angle an θ_i, each element splits the incident beam and introduces a path difference of $dsin\theta_i+dsin\theta_r$ to the reflected field, where d is the centre to centre separation of the grating elements, and θ_r is the reflected angle. Constructive interference is obtained when the path difference is equal to an integer number of wavelengths, m, this yields the grating equation which is given by [4]

$$sin\theta_i + sin\theta_r = \frac{m\lambda}{dn_{eff}} \tag{7.1}$$

where, n_{eff} is the effective index of the slab mode propagating in the passive grating section, and λ is the wavelength of the incident optical field. Thus light is reflected off the grating at an angle θ_r, which is dependent on the incident wavelength. A second parabolic mirror etch is used to focus the diffracted light towards four output waveguides which are positioned in the focal plane such that θ_r corresponds to the wavelengths 1553, 1557, 1561, and 1565nm. Integrated Total Internal Reflecting (TIR) mirrors, as discussed in chapters 4 and 5, are then used to separate the guides from approximately 4-5μm to 250μm apart, into four electrically isolated 500μm long gain regions (the slaves). The total device size is approximately 4mm square.

The grating section therefore introduces four wavelength selective paths between the master and four slave gain regions, determined by the position of each slave on the output focal

plane of the focusing mirror. On biasing, providing there is enough optical gain to compensate for the optical loss in the grating section, lasing cavities may be achieved between the two cleaved facets of the device. Therefore the device can emit on up to four of the different grating wavelengths simultaneously, depending on which corresponding slave(s) are driven in conjunction with the master.

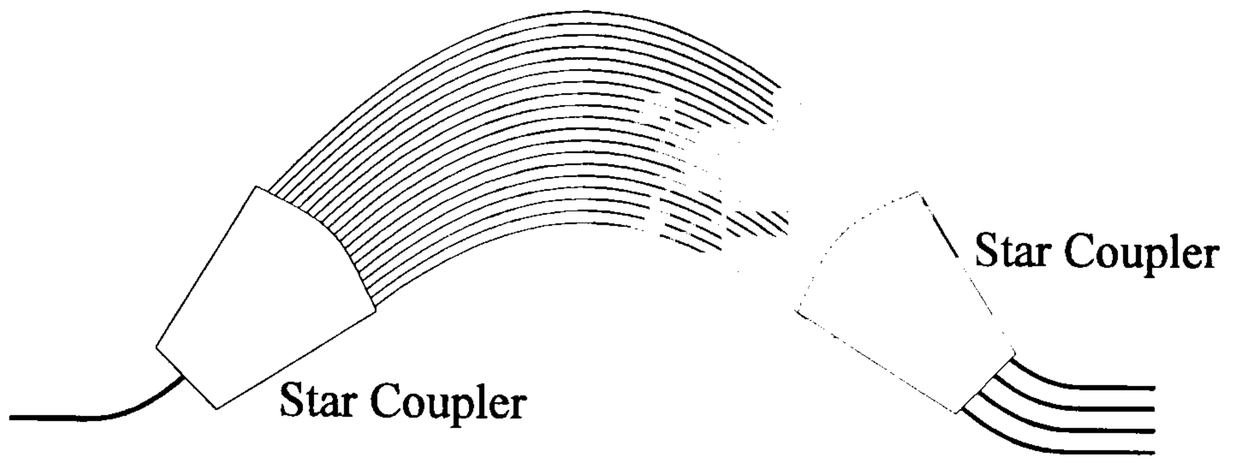

Figure 7.5 Schematic of a phased waveguide array multi-wavelength laser

It should be noted that several other multi-wavelength laser designs have been presented in the literature, which are outlined in table 7.1 for comparison. To date, multi-wavelength laser design has concentrated on the phased waveguide array demultiplexer as drawn schematically in figure 7.5. Its principle of operation is mathematically identical to the transmission grating. However the path differences are achieved using a subtly different technique. An array of waveguides with differing lengths are used to incur a spatial phase delay between two input and output star couplers.

Ref	Year	Channel Spacing	Number of Channels	Multiplexer	Modulation
[5]	1992	~4nm	9	Rowland Grating	-
[6]	1994	2.9nm	4	Phased Array	-
[7]	1994	6.4nm	6	Phased Array	-
[8]	1995	1.6nm	8	Phased Array	-
[9]	1996	0.8nm	18	Phased Array	1.2Gbits/s
[10]	1996	3.2nm	9	Phased Array	-
[11]	1997	1.6nm	16	Phased Array	622Mbits/s
[12]	**1998**	**3.7nm**	**4**	**MGC**	**2.488Gbits/s**

Table 7.1 Multi-wavelength Lasers Fabricated to Date.

It should also be noted that modulation has never been achieved in a multi-wavelength laser above 1.2Gbits/s. Indeed, to date, wavelength conversion has never before been demonstrated in a monolithically integrated multi-wavelength laser. In this chapter wavelength conversion is achieved at 2.488Gbits/s using the MGC laser using three novel configurations. Before giving a detailed description of this operation, the discussion of the various laser parameters will be given. This allows insight into some of the physics behind the laser operation.

7.3 Initial Device Characterisation

7.3.1 Lasing Thresholds and operating wavelengths

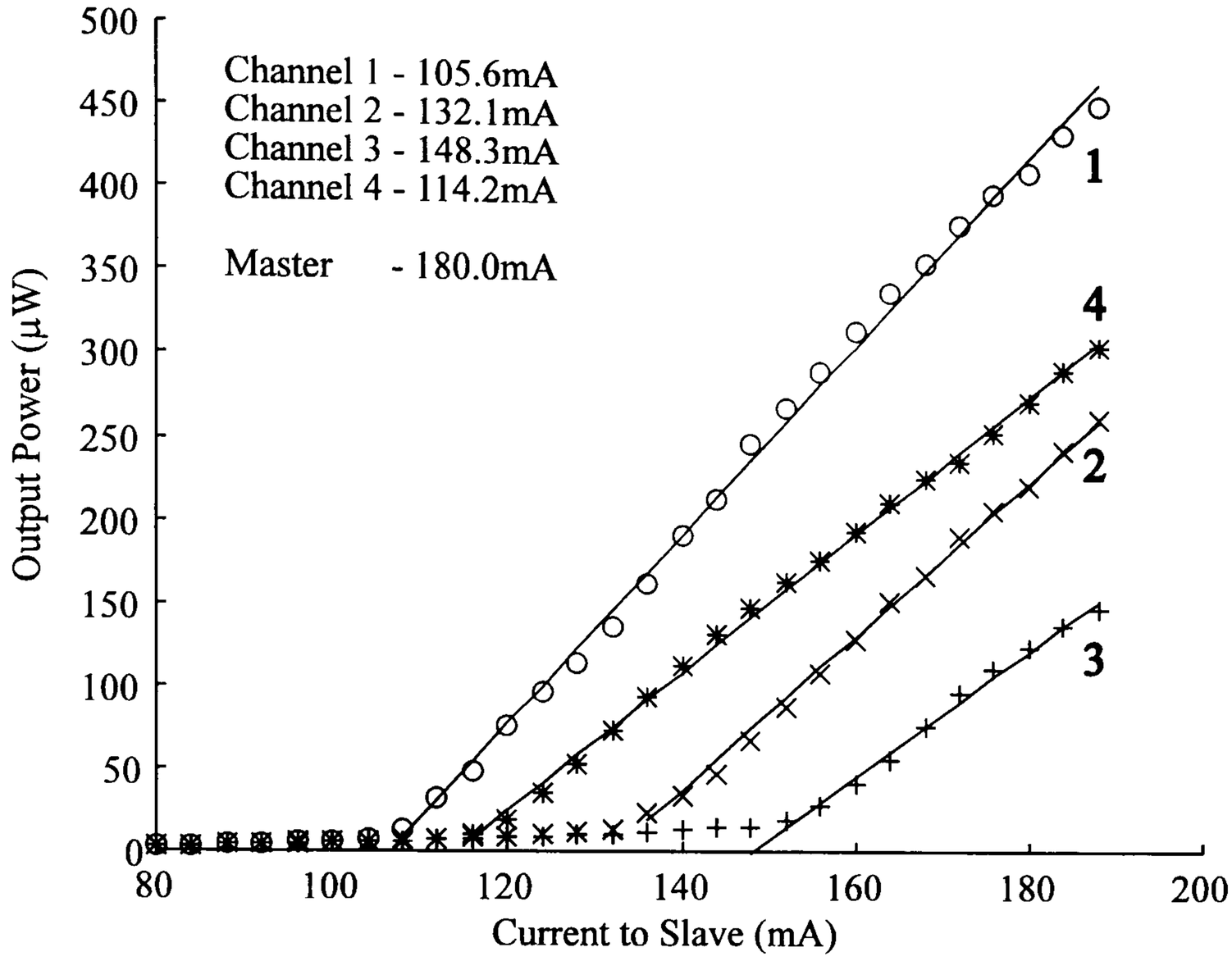

Figure 7.6 Pulsed Light-Current Characteristics of the MGC Laser at 20°C

The MGC laser was donated by BT research Laboratories on an IC submount and bonded p-side up on a diamond heat sink. Initially the device was temperature controlled at 20°C and operated with 50ns pulses and a 200% duty cycle (10μs period) using two HP-214B pulse generators. Forward bias was applied independently to each slave and simultaneously to the master stripe, and a current of 180mA was injected into each stripe and measured using two current probes (Tektronics CT-1). The laser threshold was calculated by plotting the LI of each channel independently (figure 7.6) by addressing the device with a bulk lens and measuring the lasing signal with a power meter (HP-8153A). Rotating a polariser between the bulk lens and power meter when driving each channel independently at 180mA per stripe allowed the determination of the polarisation of the lasing mode (figure 7.7). Each lasing channel of the MGC laser has been labelled from one to four. Subsequently, a fibre lens was addressed to the master facet of the device and CW lasing was observed on an Optical Spectrum Analyser (HP-70951A) independently on all four channels (figure 7.8). These results are summarised in table 7.2 and discussed as follows.

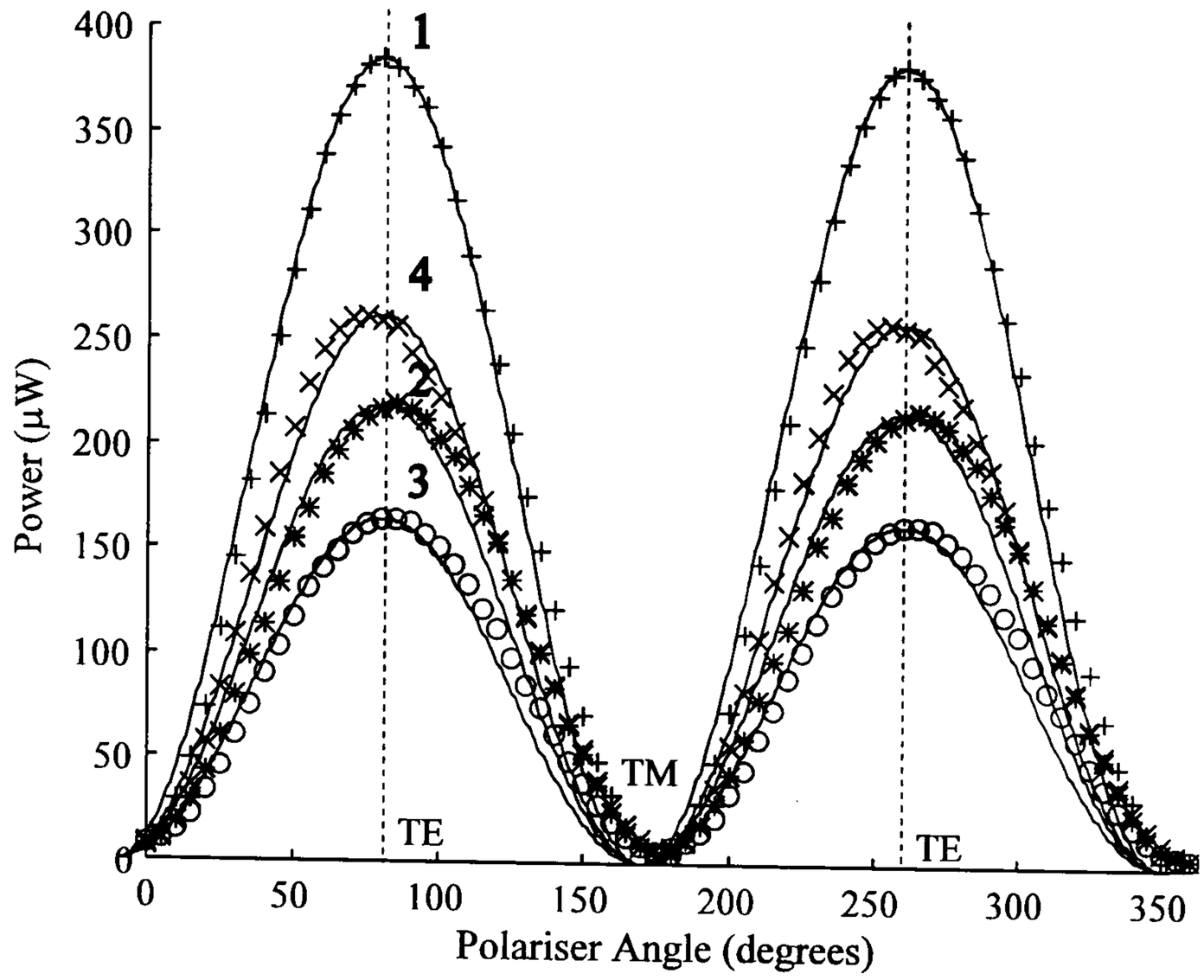

Figure 7.7 *TE Lasing of the pulsed MGC Laser at 20°C*

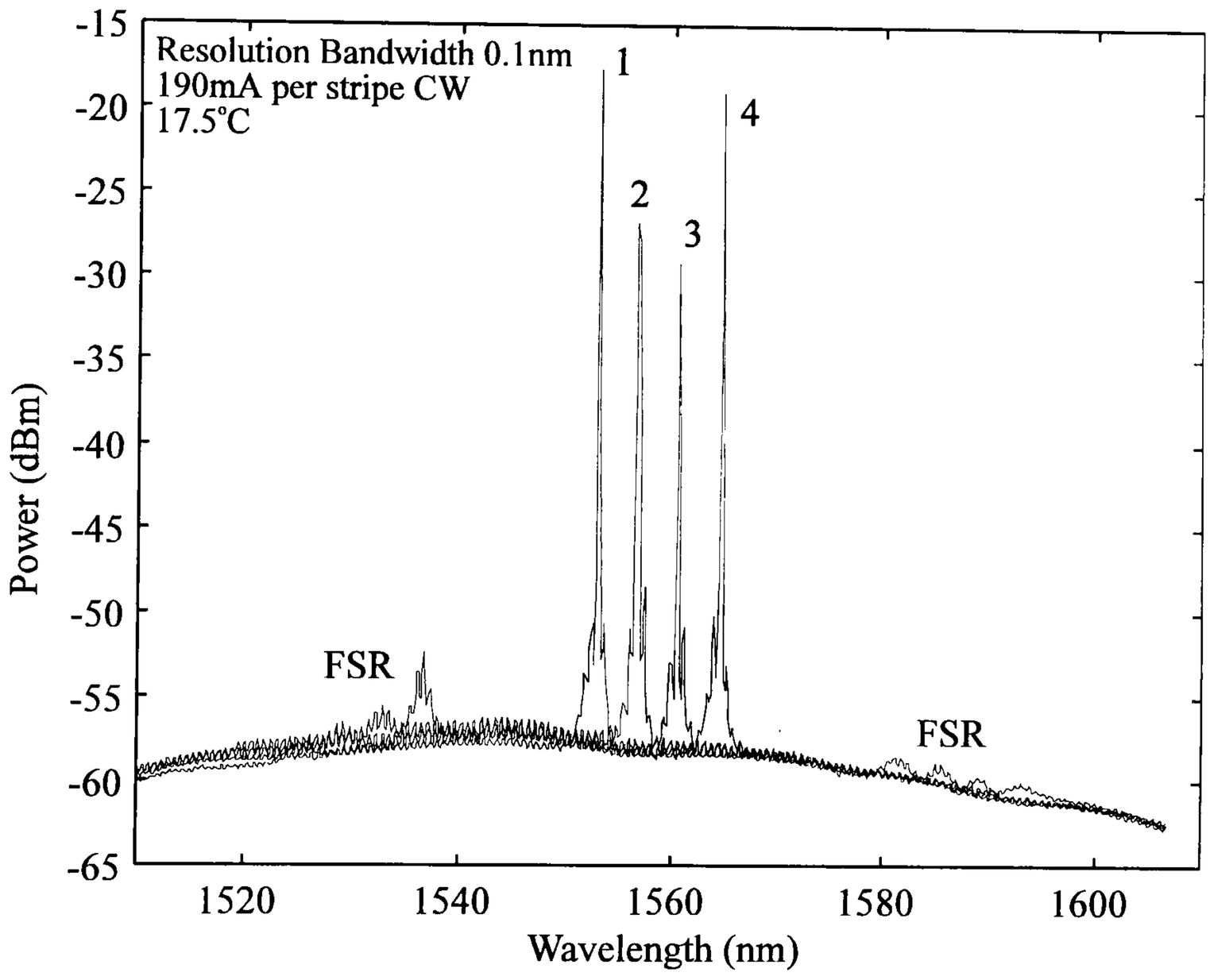

Figure 7.8 *CW Wavelength Emission of the four channels of the MGC laser at 17.5°C I_m=190mA ; I_s=190mA.*

Channel Number	CW Lasing Wavelength(nm)	Master+Slave Threshold (mA)	Threshold per Stripe (mA)	Lasing Polarisation
1	1553.49	285	142.5	100% TE
2	1557.13	312	156.0	100% TE
3	1560.85	328	164.0	100% TE
4	1564.51	294	147.0	100% TE

Table 7.2 *Device Performance of the MGC Laser at 20°C.*

It may be observed from table 7.2 and figure 7.8 that the device operates in four wavelength channels, lasing at wavelengths of 1553.49nm, 1557.13nm, 1560.85nm and 1564.51nm at 17.5°C. Additional peaks buried in the noise floor correspond to the Free Spectra Range (FSR) of the grating [13], or the $(m-1)^{th}$ order in equation 7.1. The device lases 100% TE in all channels, and there was noted an approximate 10mA increase in threshold between pulsed and CW operation. This was attributed to thermal heating of the active layer and therefore a reduction in differential gain. The approximate loss incurred by the passive grating section, α, may be inferred from these calculations of threshold current from the equation (ignoring scattering losses and assuming logarithmic gain) [14]

$$\alpha = 2\Gamma a_0 L \ln\left(\frac{I_{th}\tau_s}{eVn_0}\right) + \ln(R) \tag{7.2}$$

where (assuming typical device parameters [15]), Γ is the total confinement factor (~5%), a_0 is the logarithmic gain coefficient (2000-3000cm^{-1}), L is the master/slave stripe length (500μm), τ_s is the carrier lifetime (1-2ns), e is the charge on the electron, V is the active volume, n_0 is the transparency carrier density (1-2x$10^{18}cm^{-3}$) and finally R is the facet reflectivity (~33%). This yields a cavity loss of approximately 15±3dB. Such a high value is attributed to a 3dB interface loss between active and passive regions which therefore translates to a 9±3dB demultiplexer loss which is typical [3]. It should be noted that this calculation must be regarded as very approximate, a more detailed analysis of the demultiplexer can be obtained by direct measurement when the active stripes are biased to transparency. This is discussed further in the next section.

7.3.2 Transmission Grating Response

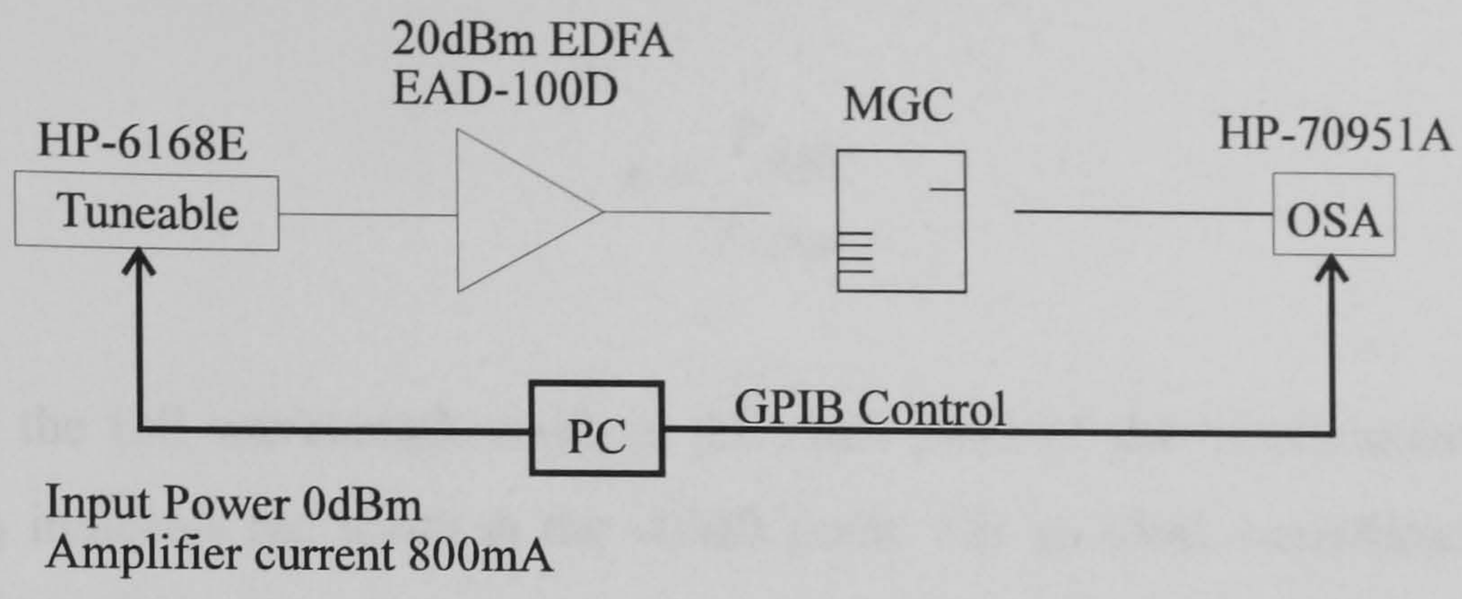

Figure 7.9 *Experimental Set-up for the determination of channel grating loss of the MGC laser*

The transmission grating within the MGC is the key feature to the operation of the device. The grating response, $\alpha(\lambda)$, was calculated in order to determine the input/output filtering of the device. This information is used very effectively later on in this chapter in order to optimise the performance of the MGC as a wavelength converter.

A tuneable laser (HP-6168E), was first pre-amplifier with a 20dBm Erbium Doped Fibre Amplifier (EDFA), as shown schematically in figure 7.9. This optical signal was then injected into the slave side of the MGC laser using a fibre lens, and each stripe was biased independently just below threshold. The input signal which passes through the device was coupled into a second lensed fibre addressed to the master facet and measured on an Optical Spectrum Analyser (OSA). GPIB control of the tuneable laser and OSA allowed a relative measurement of the transmission through the grating section of the device. This is plotted in figure 7.10 (after calibration).

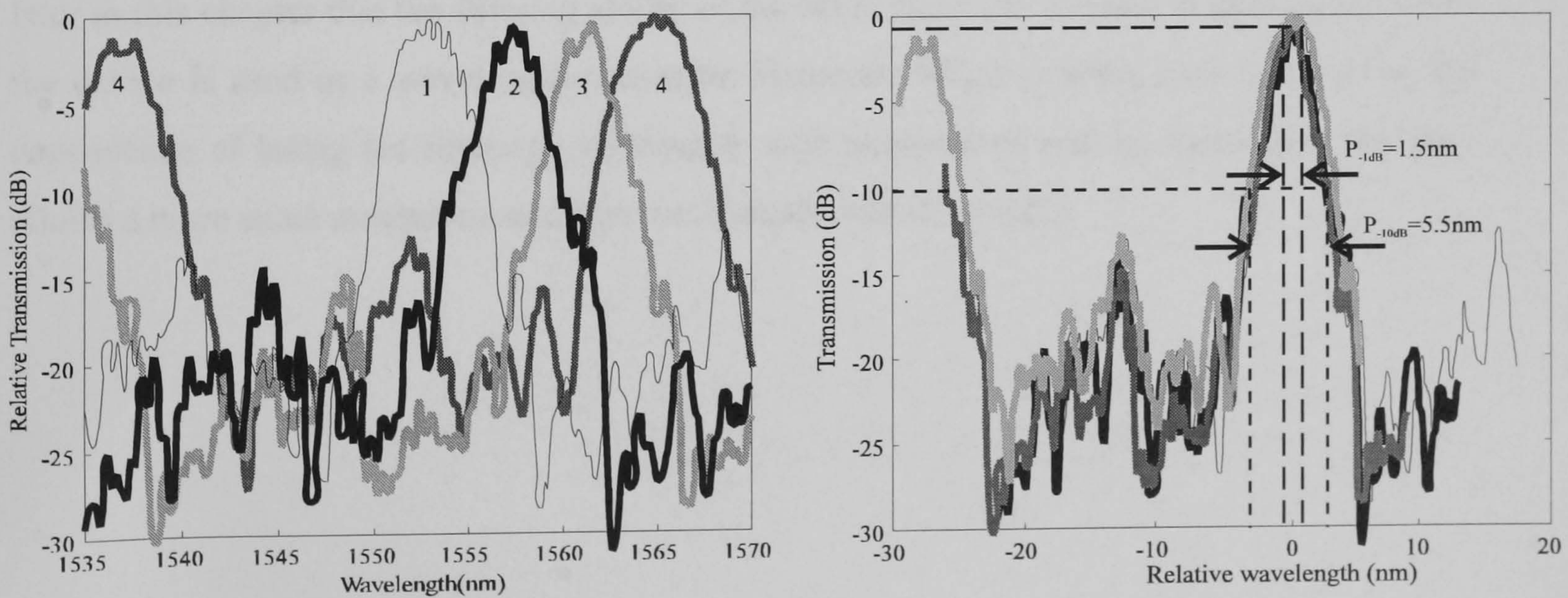

Figure 7.10 *Relative Transmission Grating Loss as a function of Wavelength*

In order to assess the performance of the demultiplexer, a figure of merit is often used which is termed the filter quality factor, *s*, [16] and is given by

$$s = \frac{P_{-1dB}}{P_{-10dB}} \tag{7.3}$$

where P_{-1dB} is the full wavelength width at the -1dB point of the transmission function, and likewise P_{-10dB} indicates the width at the -10dB point. For an ideal demultiplexer the quality factor has a value of 1 which corresponds to a top hat filter distribution. Very low values of *s* (<<0.2) indicate a very poor filtering response. It may be observed from figure 7.10 that the transmission grating discussed here has a calculated quality factor of approximately 0.27 (1.5/5.5). As a comparison, table 7.3 gives a few examples of filter quality factors, such as the 100GHz ITU specification for a passive demultiplexer (0.25 at -30dBs) [17], a Gaussian distribution, and finally the JDS Fitel TB1500B tuneable bandpass filters used in the experiments discussed later in this chapter.

Device	Filter Quality Factor s
100GHz ITU spec. (after[17])	0.50
Gaussian	0.31
MGC	0.27
JDS Fitel TB1500B	0.26

Table 7.3 Comparison of filter quality factors at -10dB point

In terms of filtering response (for which the MGC has not been optimised) the device performs better than a tuneable filter used in many laboratory experiments. It will be shown later in this chapter that the filtering ability of the MGC laser can be used to good effect when the device is used as a wavelength converter. However, before moving onto conversion, the dependence of lasing (or filtering) wavelength with temperature will be discussed. This also allows a more exact measurement of the wavelength channel spacing.

7.3.3 Temperature Stability of the MGC Laser

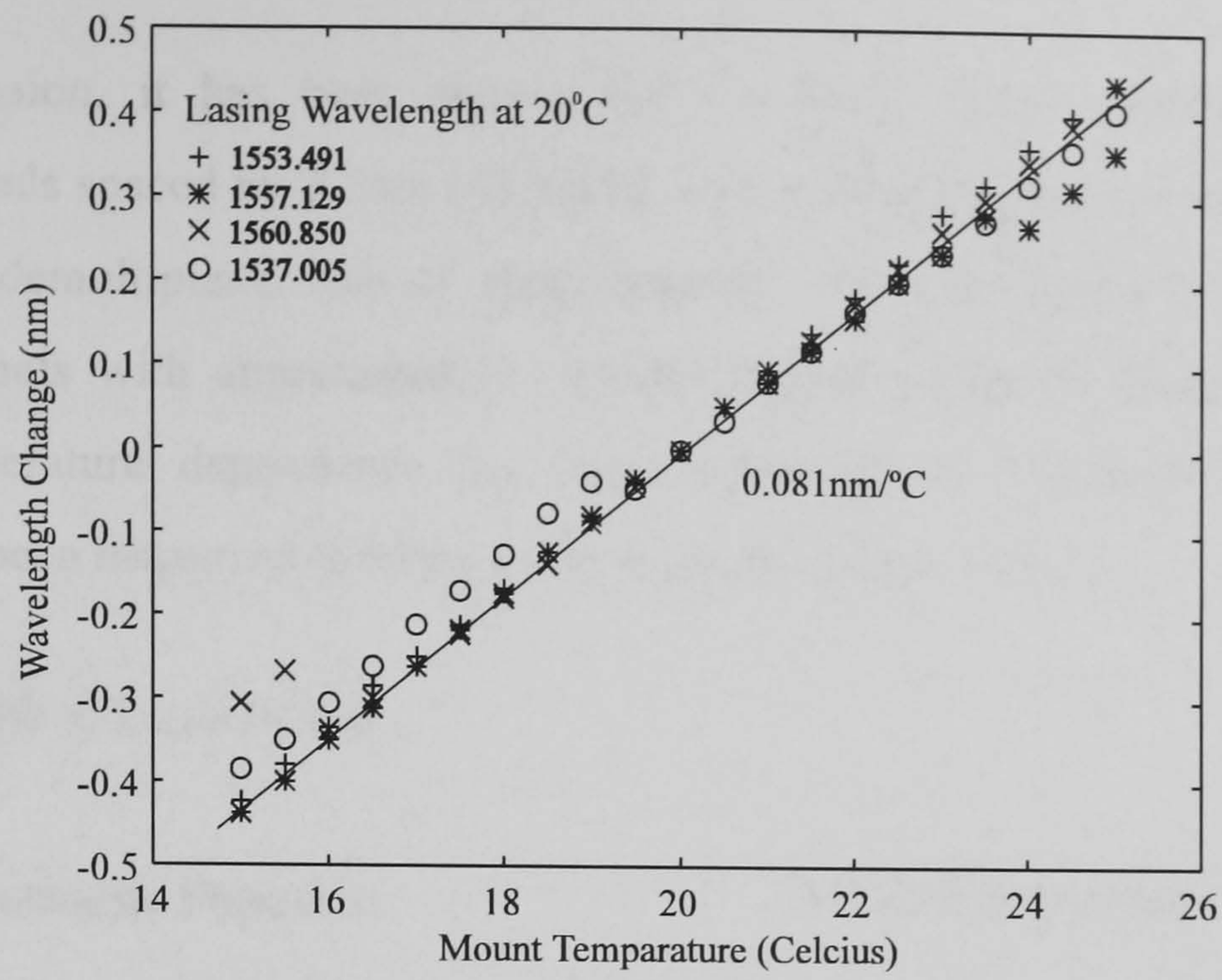

Figure 7.11 Variation of peak lasing wavelength of the MGC laser with temperature

In dense WDM network systems, operating with a channel spacing of 0.8nm on the ITU grid, the dependence of channel wavelength with temperature is of great importance. Thus the variation of the MGC lasing wavelength with temperature has been measured experimentally to check that channel spacing or registration is maintained with temperature (figure *7.11*). It may be observed that there is an average increase in lasing wavelength with temperature of 0.81nm per 10^0C. This is a typical value found with DFB lasers [18], which corresponds to the refractive index change of InP with temperature [19]. The variation of channel spacing with temperature may be determined from this data and is shown in figure 7.12. It may be observed that the average channel spacing of the device is 3.67nm (453GHz) which is maintained within a standard deviation of 50pm between 15 and 25°C.

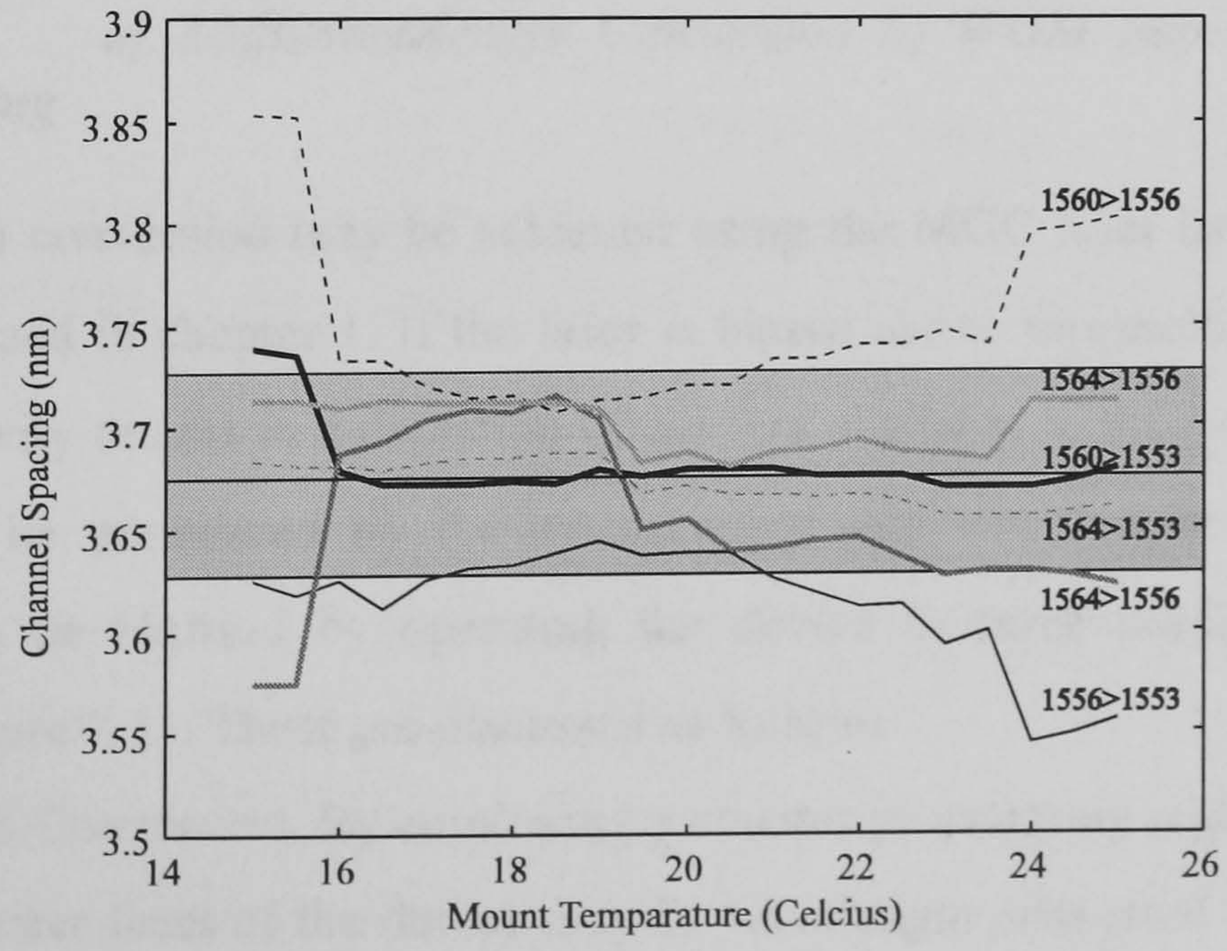

Figure 7.12 Variation of Channel Spacing of the MGC laser with temperature

7.3.4 Summary

In conclusion, it has been shown that the MGC laser operates on four WDM wavelength channels spaced by 3.7nm (453GHz) with a threshold current of 140mA per stripe (9.3kA/cm^2) and demultiplexer loss of approximately 7dB. The device lases TE for all four wavelength channels with approximately -10dBm output power at 200mA per stripe. The wavelength temperature dependence has been measured to 0.081nm/°C and the grating performance has been measured in terms of filter quality factor, *s=0.27*.

7.4 Wavelength Conversion

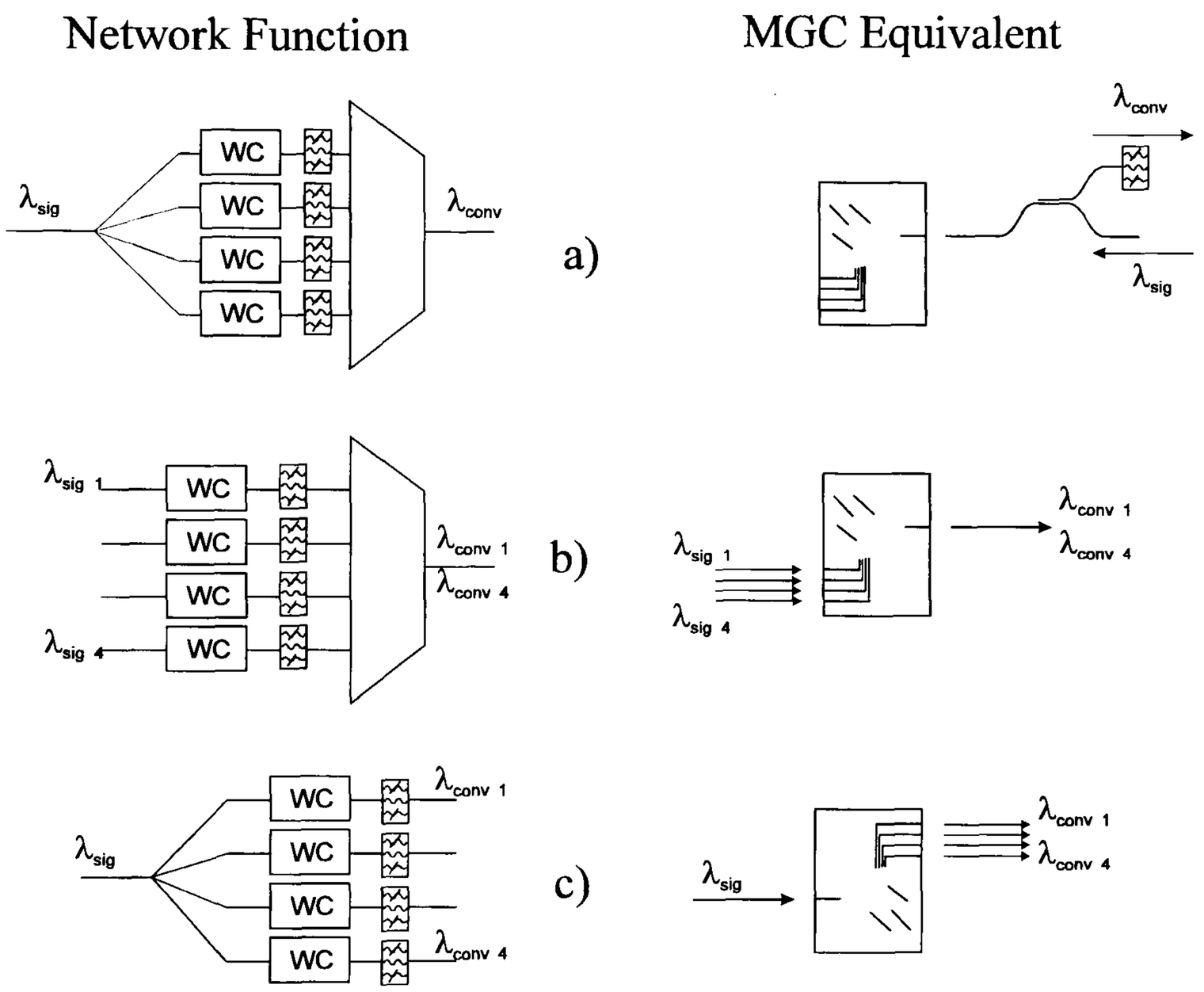

Figure 7.13 Three novel configurations for achieving wavelength conversion with the MGC laser. a) Multi-wavelength Conversion b) WDM Repeater c) Wavelength Routing

Wavelength conversion may be achieved using the MGC laser by the process of gain saturation as discussed in chapter 1. If the laser is biased above threshold, the introduction of photons into the cavity results in a depletion of carriers available to the lasing mode. Thus the MGC output may be modulated by the optical input and wavelength conversion may be achieved. This can be realised by operating the device in three configurations as shown schematically in figure 7.13. These are discussed as follows

a) Multi-wavelength Conversion. By employing a counter propagating regime, an optical input injected into the master facet of the device may be wavelength converted onto any of the four MGC wavelengths, depending on which slave is driven in conjunction with the master. As

discussed in chapter 1, the ability of achieving multi-wavelength conversion is essential for wavelength routing applications.

b) WDM Multiplexing. Injection of an optical input into each slave waveguide allows simultaneous wavelength conversion and multiplexing to the master output stripe. This function is useful if for example a number of optical input signals not standardised to the ITU grid need to aligned before transmitting down a single optical fibre.

c) Wavelength routing. Injection of an optical input into the master stripe of the MGC laser allows space switching to each output stripe, depending on which is biased. Thus a 1x4 crosspoint switch is realised, which offers a full broadcast functionality.

It may be observed from the block diagrams drawn in figure 7.13 the vast component saving offered by the MGC laser. It will be shown that automatic wavelength filtering of the optical input can also achieved along with conversion, owing to the wavelength dependant transmission of the grating section calculated in figure 7.10. Thus the MGC can perform various complex network functions (multiplexing, demultiplexing, splitting, filtering and wavelength conversion) in a single monolithic integrated device.

7.4.1 (a) Multi-Wavelength Conversion using the MGC

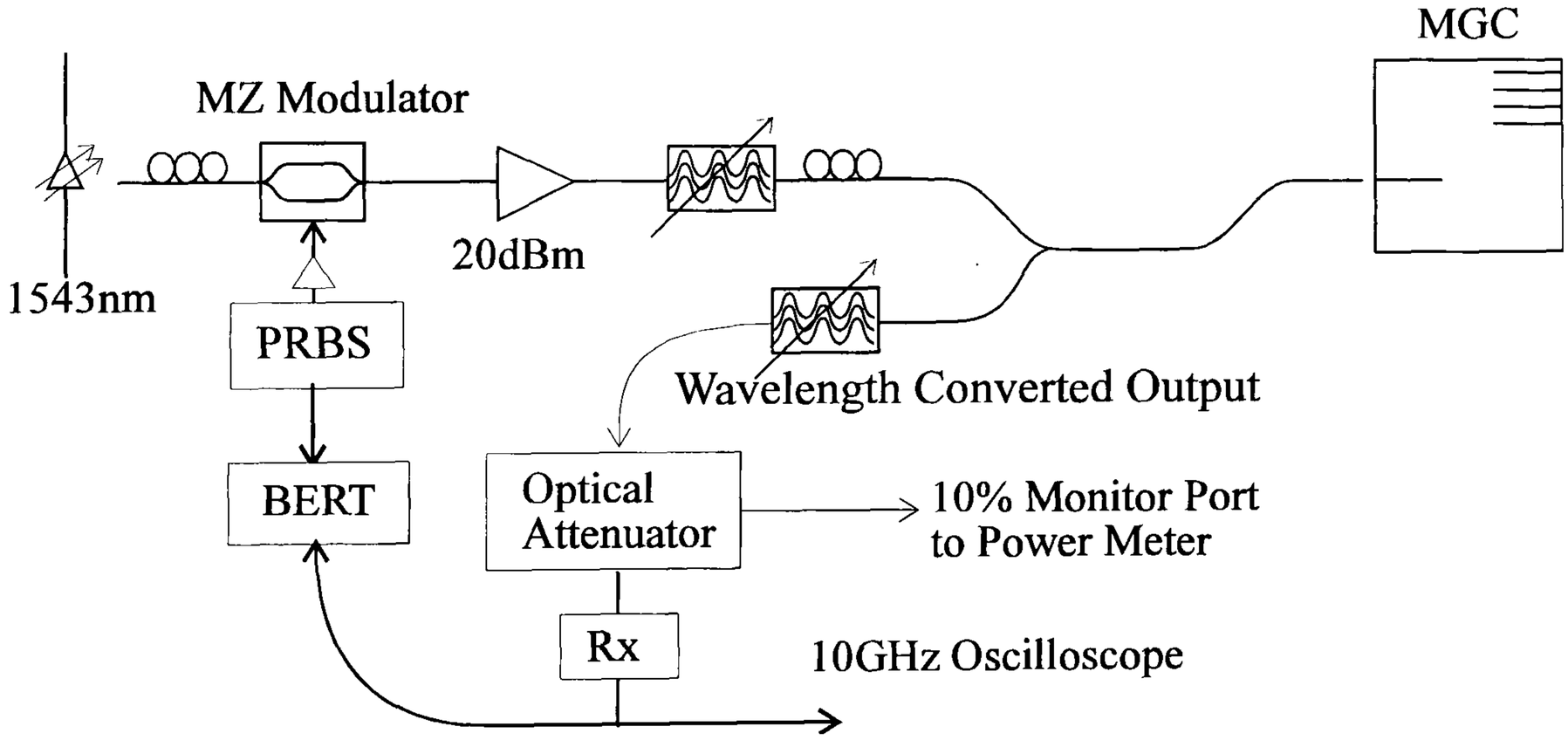

Figure 7.14 Experimental set-up used to demonstrate the MGC laser as a multi-channel wavelength converter.

The experimental set-up used to achieve multi-wavelength conversion using the MGC laser is outlined in figure 7.14. An input signal is first patterned with a PRBS (Pseudo Random Binary Sequence) using a Mach-Zehnder electro-optic modulator. The signal is pre-amplified using a 20dBm EDFA (Polaris EAD-60) and post filtered with a JDS Fitel TB1500B Fabry Perot tuneable bandpass filter (to remove the EDFA spontaneous emission). A polarisation controller was used to maximise the coupling efficiency to the TE lasing mode of the MGC laser, before the optical signal was injected into the master stripe via a 2x2 fibre coupler and

fibre lens. It was necessary to post filter the wavelength converted output to resolve each MGC channel separately during simultaneous conversion to multiple MGC wavelengths. Also post filtering was required owing to the substantial back reflection (approximately 30%) of the optical input off the facet of the device. The wavelength converted output was attenuated by a JDS Series 7000 optical attenuater and detected with a Nortel 2.5GBits/s receiver. This allowed measurement of the received power via a 10% monitor port which was required for Bit Error Rate (BER) measurements. The received wavelength converted eye diagrams were constructed using a HP54122A 10GHz sampling oscilloscope, and BER was measured using a HP708420 3Gbit/s test set.

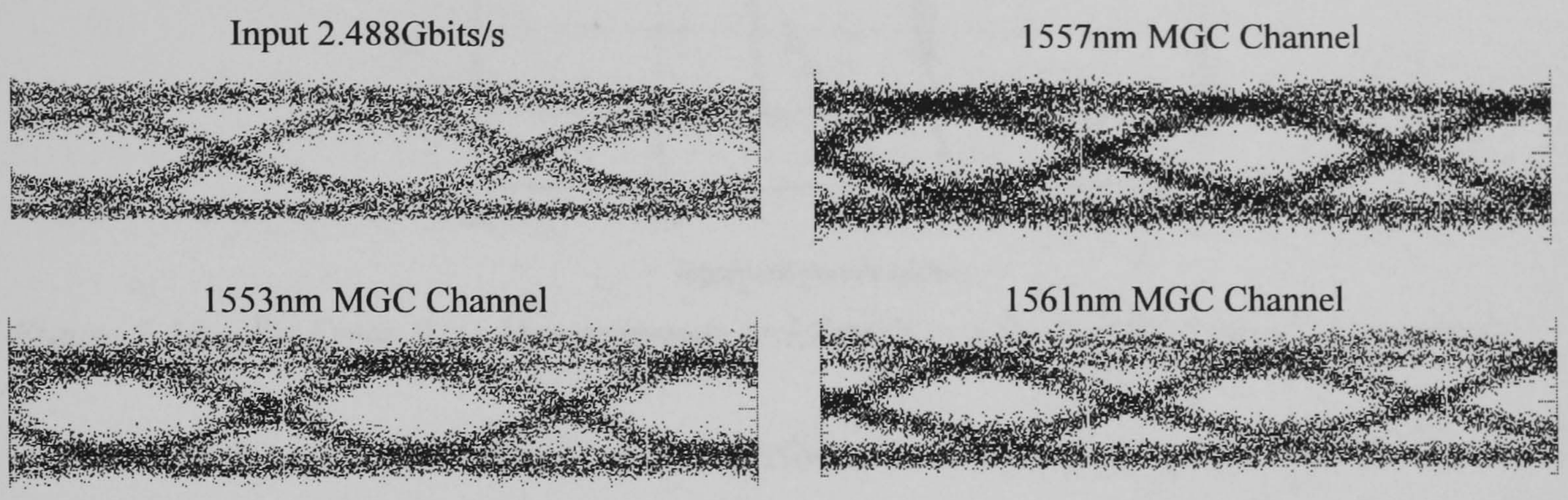

Figure 7.15 Single channel wavelength conversion at 2.488Gbits/s

Channel Number	Optimum Bias Conditions at 2.488Gbits/s	
	Bias to Slave(mA)	Bias to Master(mA)
1 (1553nm)	201	180
2 (1557nm)	243	242
3 (1561nm)	242	239
4 (1565nm)	-	-

Table 7.4 Drive conditions for single channel conversion at 2.488Gbits/s

By biasing each slave stripe independently in conjunction with the master stripe, single channel wavelength conversion was demonstrated at 2.488Gbits/s with a coupled into power of approximately 6dBm. The eye diagrams for this mode of operation are shown in figure 7.15 along with the optimum bias conditions which are given in table 7.4 (PRBS 2^7-1). It was found that bias conditions were critical for achieving an open eye, a change of only a few milli-amps resulted in severe degradation of the converted bit stream. Unfortunately, owing to the bandwidth of the JDS Fitel Optical bandpass filters (1530-1561nm), channel four which lases at 1565nm could not be evaluated. A degradation of extinction ratio of 9dB on the input to approximately 7dB on the output was noted on all channels.

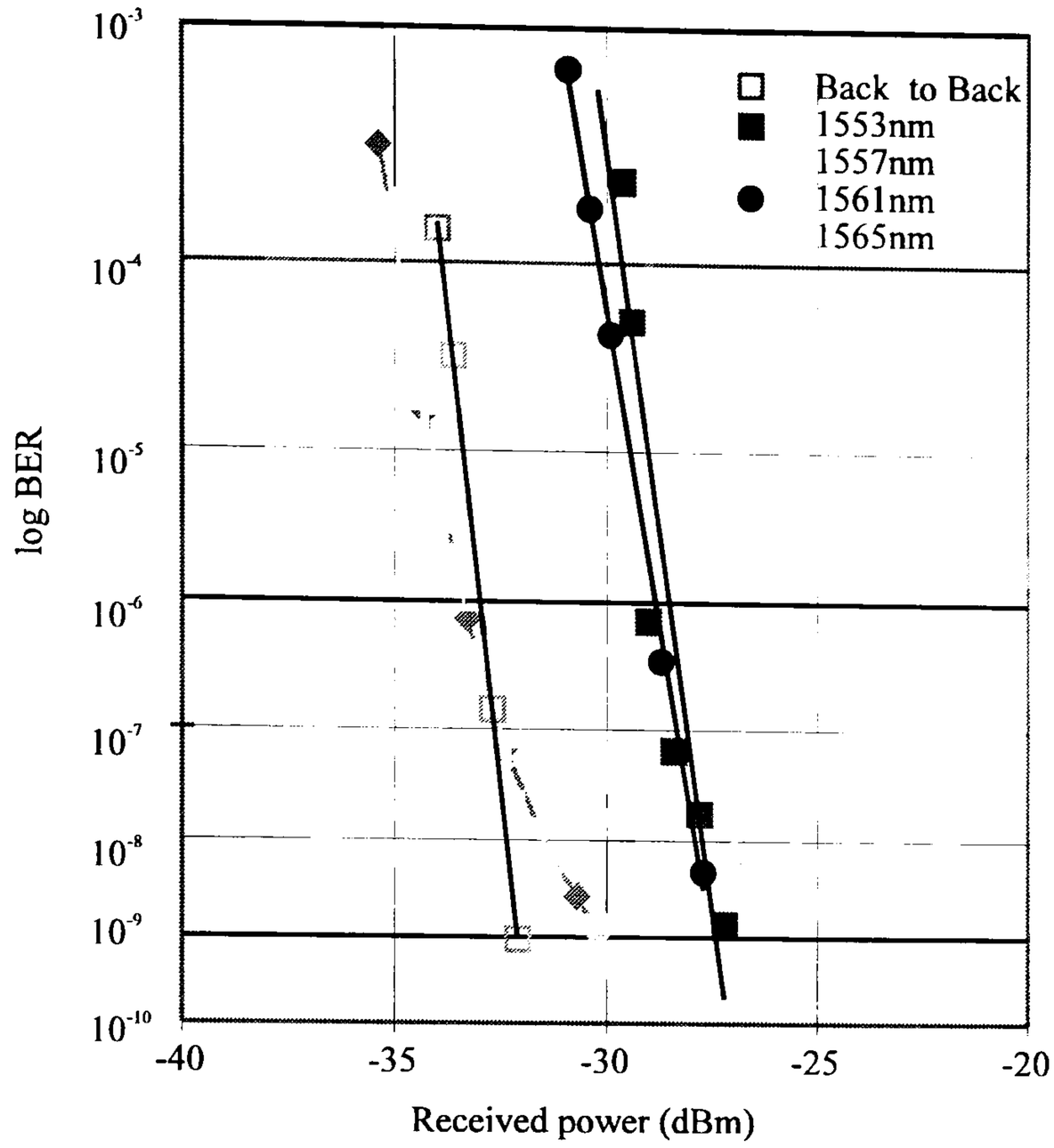

Figure 7.16 Bit Error Rate Measurements at 1.244Gbits/s for Single Channel Conversion

In order to quantify the conversion performance it is essential to calculate the Bit Error Rate penalty introduced by the MGC. This was achieved by plotting the received power versus the error rate count which was determined by a HP708420 error rate detector. Since the Mach Zehnder used to pattern the optical input required six volts of swing in order to operate efficiently, it was necessary to pre amplify the output of the HP70841B pattern generator (maximum voltage output 2v). The 3dB frequency bandwidth of the amplifier used in these experiments was limited to 0.01-4.5GHz. This limited the input data stream to pattern lengths no greater than 2^7-1 and the linearity of the amplifier prohibited the measurement of Bit Error Rate (BER) at 2.488Gbits/s. However, it was found that BER could be effectively measured at the lower data rate of 1.244Gbits/s and is plotted in figure 7.16. It may be observed that a 4dB penalty was introduced on channels 1&3 whilst channel 2 introduced a negligible penalty. No measurable dependence on bit-error rate was found with input wavelength (within the erbium window 1530-1560nm) for a constant coupled input power.

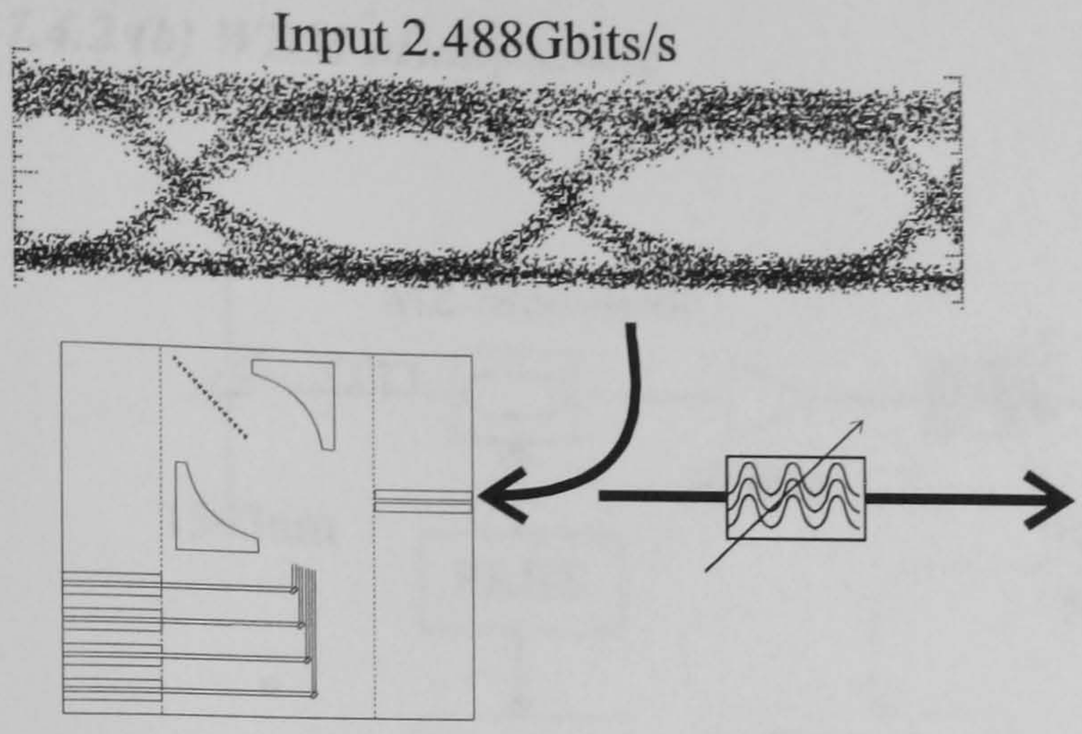

Figure 7.17 *Eye Diagrams showing simultaneous conversion to multiple wavelengths at 2.488Gbits/s*

By biasing two slave channels along with the master, conversion can also be achieved to multiple MGC channels with a small degradation in extinction ratio. This is highlighted in figure 7.17, where conversion is shown simultaneously to both 1557 and 1561nm channels. Since the eye diagrams for all the permutations of outputs are very similar only this combination has been plotted, however conversion has been achieved on all other channel combinations. It was noted that different drive conditions were required for multiple conversion compared with single channel operation in order to achieve an optimised eye with no closure. These drive conditions are summarised in table 7.5. It should be noted that the required bias to each of the slave stripes is substantially lower than for single stripe operation. This was attributed to substantial current leakage between each of the wavelength channels.

Channel Numbers		Optimum Bias Conditions at 2.488Gbits/s		
		Bias to Slave(mA)		Bias to Master(mA)
1 (1553nm)	2 (1557 nm)	141	130	220
2 (1557 nm)	3 (1561 nm)	138	152	242
3 (1561 nm)	1 (1553 nm)	140	143	239

Table 7.5 *Drive conditions for multi channel conversion at 2.488Gbits/s*

7.4.2 (b) WDM Multiplexing

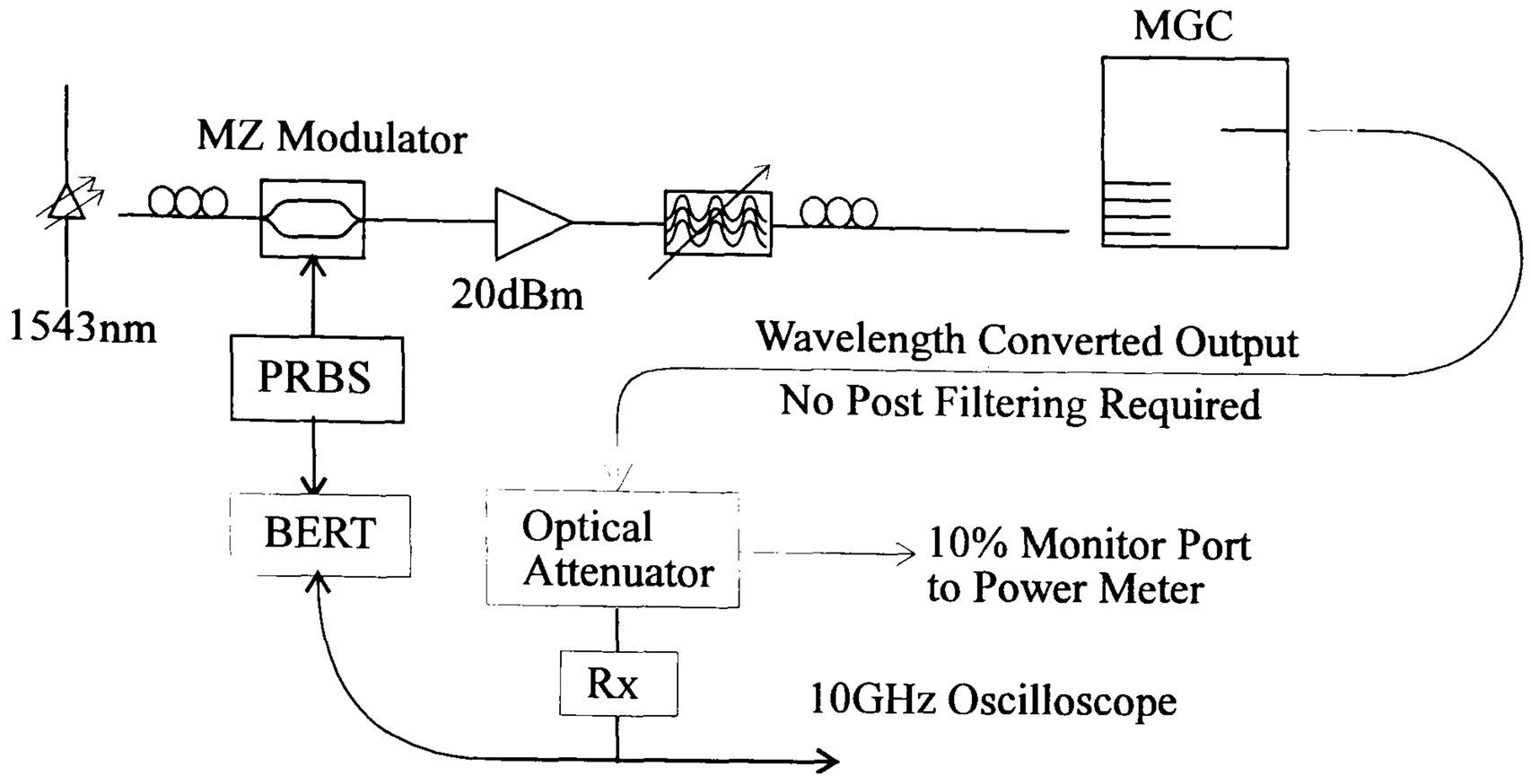

Figure 7.18 Experimental set-up used to demonstrate the MGC laser as a WDM multiplexing

Figure 7.18 outlines the experimental set-up used to demonstrate WDM multiplexing using the integrated MGC laser. The arrangement is almost identical to that used to demonstrate multi-wavelength conversion discussed in the previous section. However, here the 1543nm modulated signal is injected via a fibre lens into the slave side of the device, whilst the optical output is obtained by addressing a second lensed fibre to the master facet.

It has already been highlighted that conversion can be achieve along with WDM multiplexing with this configuration. This is shown in figure 7.19 where the experimental bit patterns have been measured using the HP54122A 10GHz sampling oscilloscope. It may be observed that there is an associated inversion of the wavelength converted channel with respect to the input. Also, there is a small degradation of extinction ratio from 9.2 dB on the optical input to approximately 7dB on all wavelength converted MGC channels. A similar degradation in extinction ratio was observed when operating the device as a multi-wavelength converter which was discussed in the previous section. This suggests that a similar bit error rate penalty is incurred to the converted signal.

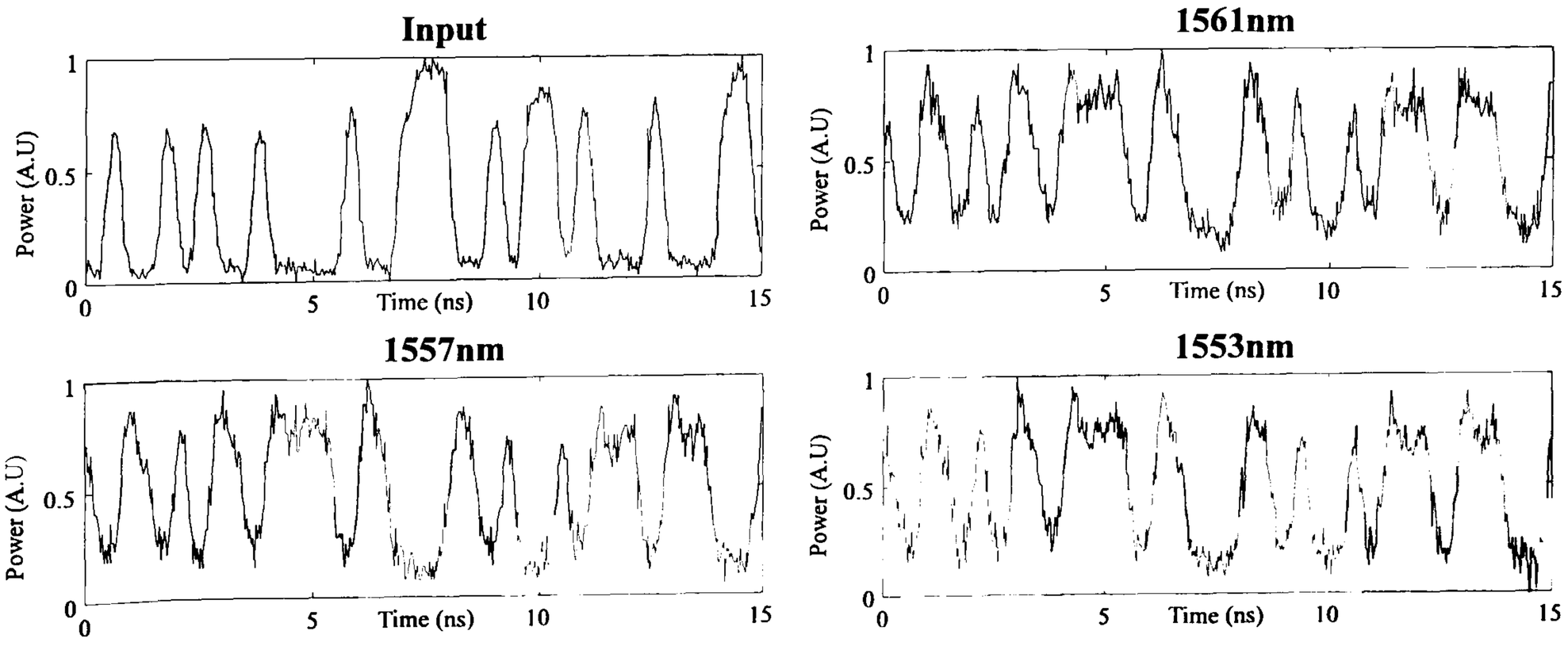

Figure 7.19 Experimental Wavelength Converted bit patterns at 2.488Gbits/s used to demonstrate the MGC laser as a WDM repeater

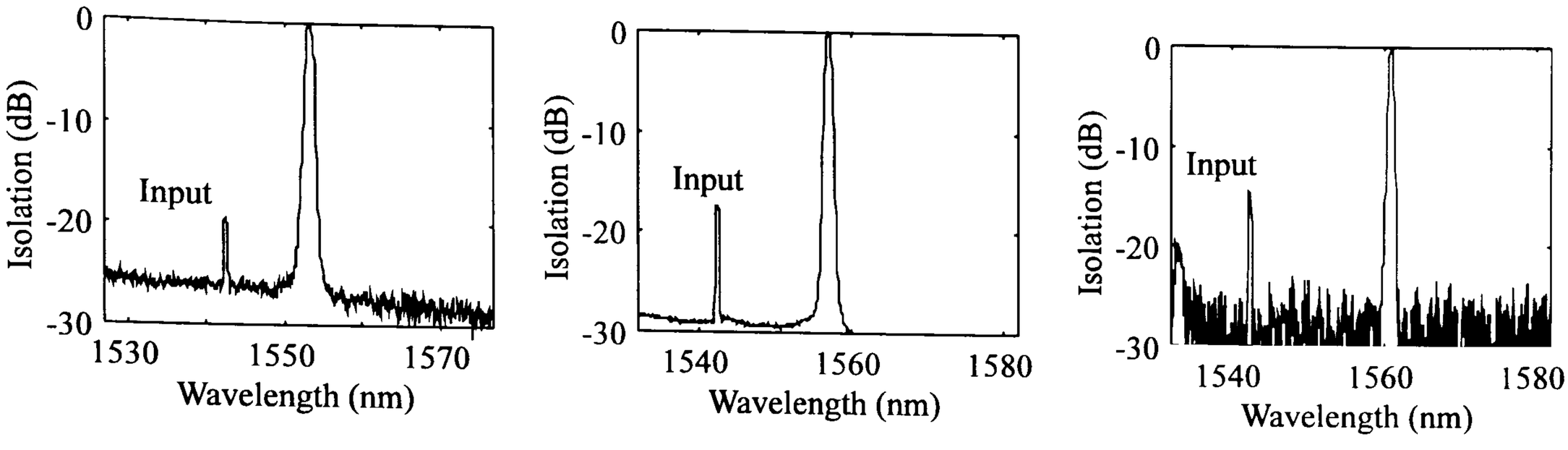

Figure 7.20 Optimised All Optical Filtering of the Input Signal

As with multi-wavelength conversion, no measurable dependence was found with input wavelength. However, it was found the need for post-filtering of the optical output could be eliminated. This was achieved owing to the filtering response of the diffraction grating which isolates the slaves from the master stripe according to wavelength, as calculated previously in figure 7.10. It may be noted from figure 7.10 that a transmission null occurs on all channels when the optical input is approximately 1543nm at 20^0C. Thus, by converting from 1543nm automatic filtering of the converted output could be demonstrated. This is highlighted in figure 7.20, where the optical spectrum of each bit trace plotted in figure 7.19 has been measured using an Optical Spectrum Analyser (HP-70951A). It may be noted that the grating section introduces a 15-20dB isolation from optical input to output under this method of operation.

With other forms of wavelength conversion which were raised in chapter 1, post-filtering is normally an essential part of the converter (unless a counter propagating regime is employed). However in this case, by optimising the optical input, the need for post filtering was eliminated. It may be observed from figure 7.10 that currently there is a substantial phase noise floor at -20dB which only allows automatic filtering at a single optimum input signal at 1543nm. This phase noise floor is attributed to mirror roughness in the grating section. An optimised device would have an improved grating performance so that filtering could be achieved at any input wavelength.

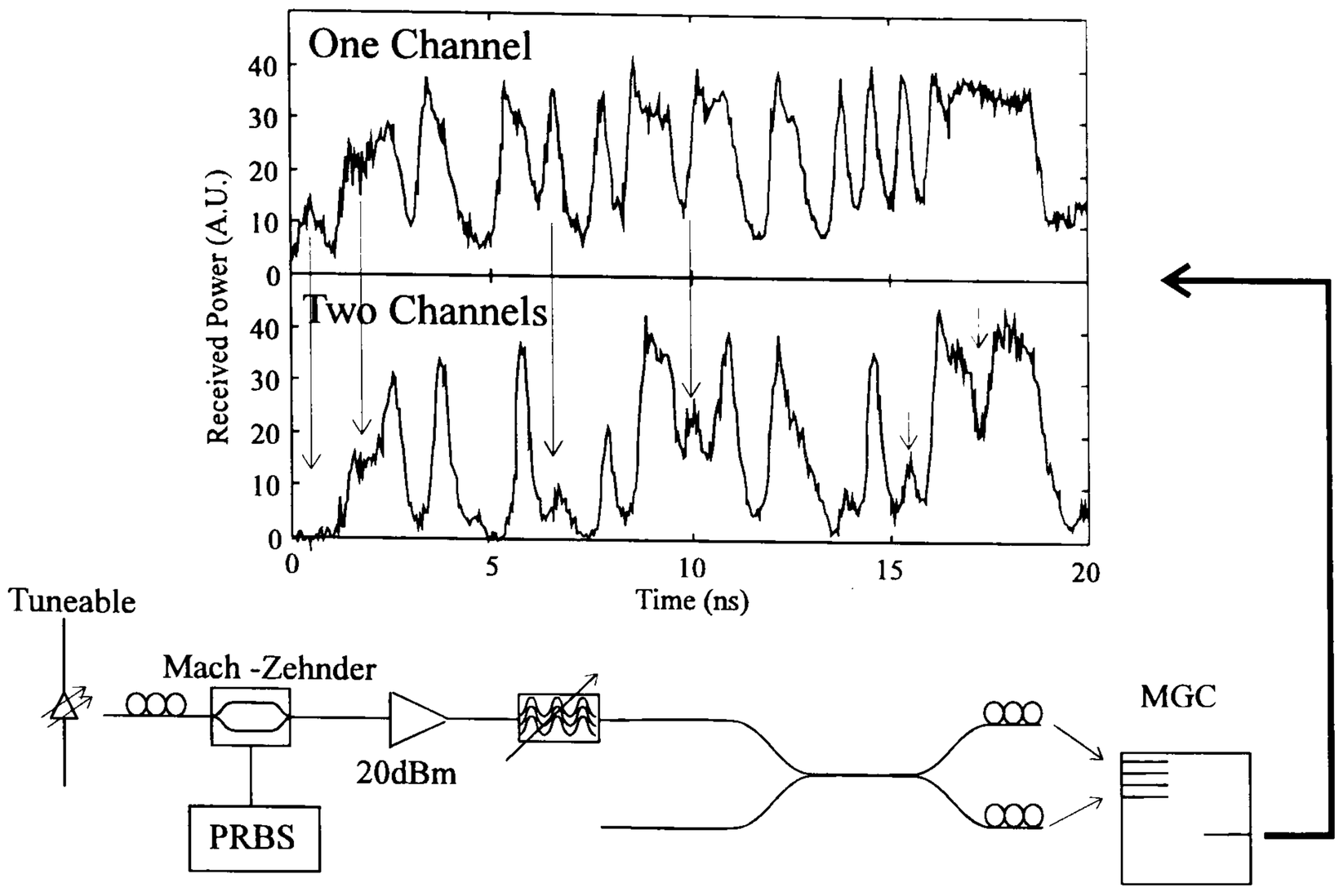

Figure 7.21 *Inter-Channel Crosstalk owing to gain saturation in the master stripe of the MGC Laser (Channel 1)*

Multi-wavelength operation was attempted with channels 1 and 4 driven simultaneously, by splitting the optical input with a 2x2 fibre coupler and injecting the signal into each stripe with a fibre lens (as outlined in figure 7.21). It was found that simultaneous operation could only be achieved if the optical input to each stripe was identical. If a time delay was introduced between inputs (which simulated arbitrary input signals) crosstalk between channels was obtained on the optical output, these results are shown in figure 7.21. It may be observed that substantial patterning was obtained between channels which was attributed to carrier depletion in the master stripe. Ironically, gain saturation in the master stripe (which induced wavelength conversion in the slave stripes), caused detrimental crosstalk on the optical output.

7.4.3 (c) 1x4 Wavelength Routing

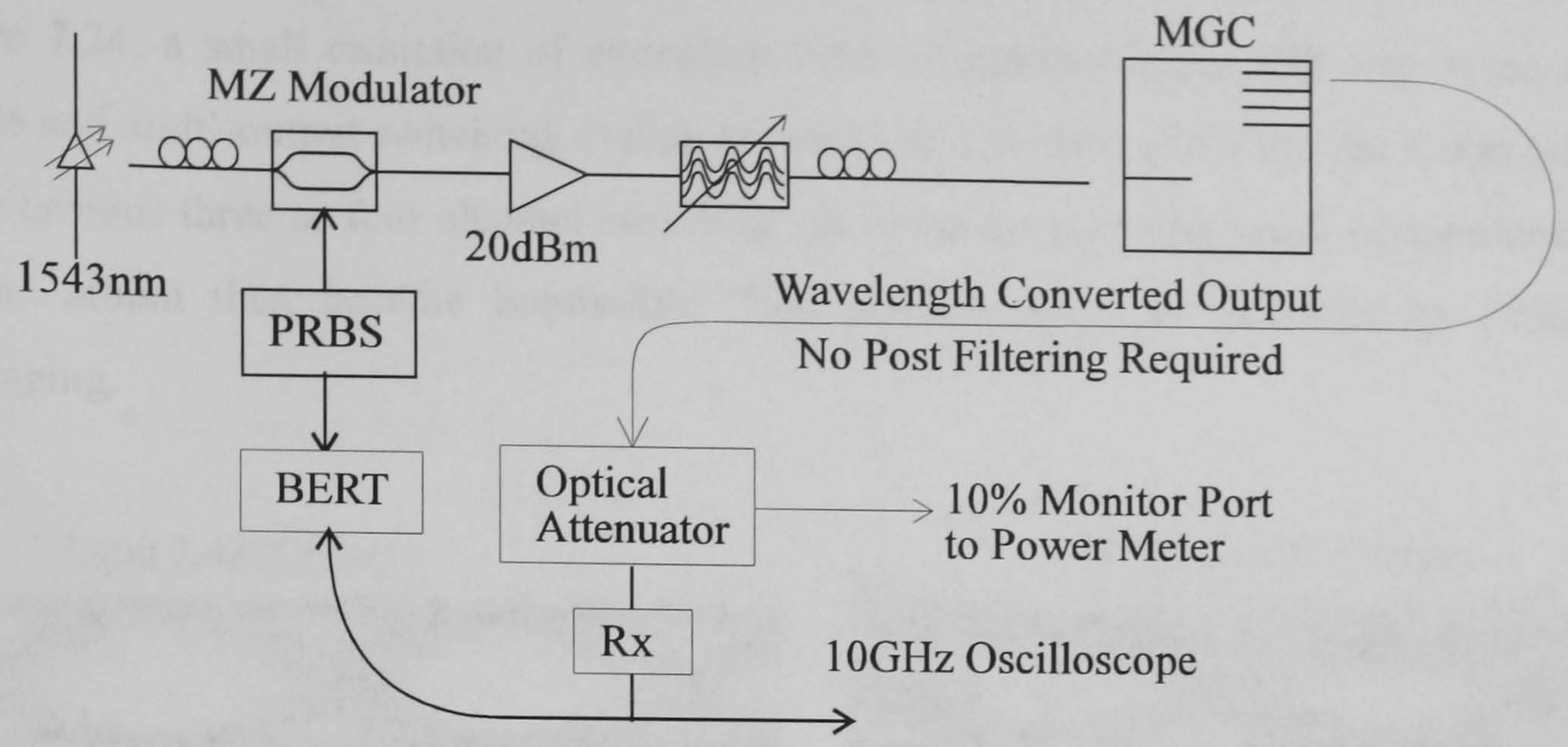

Figure 7.22 1x4 Wavelength routing using the MGC laser at 2.488Gbits/s

Finally, a subtle change in experimental set-up which was used to demonstrate multi-wavelength conversion, can achieve 1x4 space switching at 2.488Gbits/s. By injecting the input signal via a fibre lens into the master facet, the wavelength converted output may be measured from the slave facet as outline in figure 7.22. It was found that 1x4 switching could be demonstrated by biasing the MGC laser under conditions identical to that used to achieve multi-wavelength conversion (outlined in section 6.4.1, in tables 7.4 and 7.5). Indeed, as with WDM multiplexing, it was also found that by optimising the input wavelength no post filtering was required on the MGC output. This therefore allowed channel 4 at 1565nm to be assessed since the measurement was no longer limited by any post filtering. For brevity the eyes diagrams for conversion to each channel have not been included in this thesis, however figure 7.23 does show single channel 1x4 switching to the (so far unreported) 1565nm channel. This was achieved by biasing the master to 200mA and slave to 210mA with a coupled input power estimated to approximately 6dBm. It should be noted that this measurement therefore allows table 7.4 to be completed for the 1565nm channel.

Broadcast switching has also been achieved by biasing more than one stripe simultaneously. Once again bias conditions were found to be identical to that for multi-wavelength conversion as outlined in table 7.5. In order to complete the characterisation of the

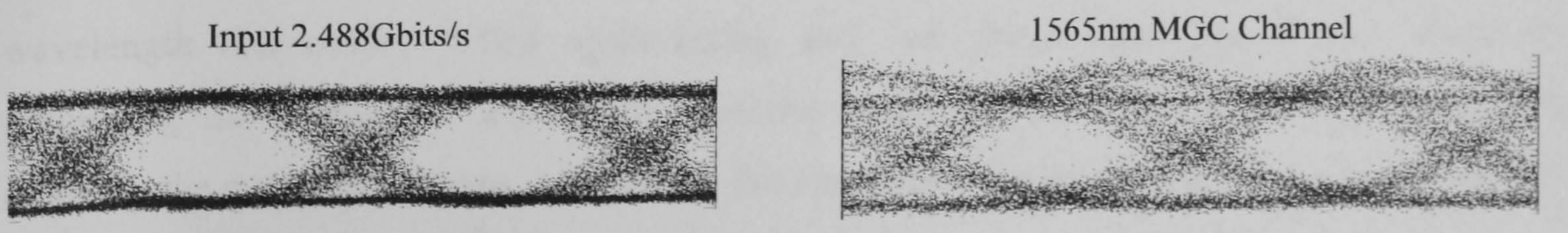

Figure 7.23 1x4 Wavelength routing to the 1565nm MGC channel at 2.488Gbits/s

MGC for multi-wavelength operation table 7.6 outlines the optimum drive conditions required for the 1565nm channel. Eye diagrams demonstrating one such configuration are plotted in figure 7.24, a small reduction of extinction ratio of approximately 1dB was noted between single and multi-output switching. Owing to non ideal mounting of the device, it was found that simultaneous three or four channel switching could not be achieved, since temperature control of the mount then became impossible. This problem could be resolved by proper laser packaging.

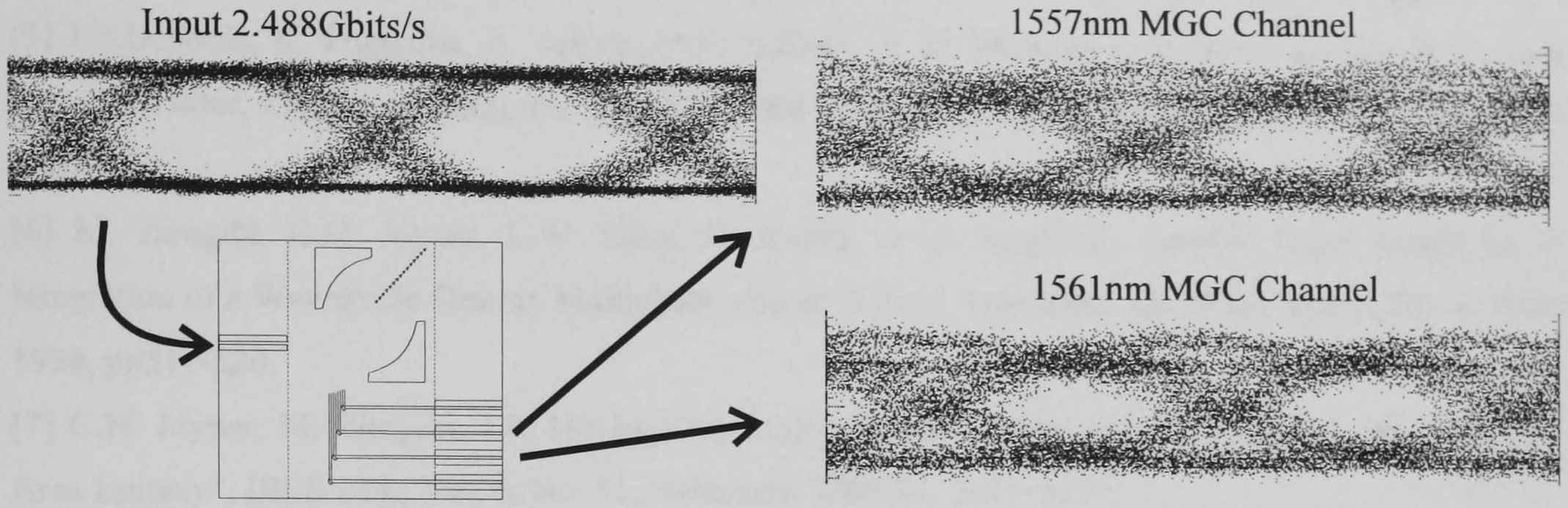

Figure 7.24 Eye Diagrams showing simultaneous space switching and wavelength conversion at 2.488Gbits/s

Channel Numbers		Optimum Bias Conditions at 2.488Gbits/s		
		Bias to Slave(mA)		Bias to Master(mA)
1 (1553nm)	4 (1564nm)	150	147	203
2 (1557nm)	4 (1564nm)	152	173	220
3 (1561nm)	4 (1564nm)	160	163	232

Table 7.6 Drive conditions for multiple 1x4 Space Switching (or multi-wavelength conversion) to the 1564nm channel at 2.488Gbits/s

7.5 Conclusions

In conclusion, wavelength conversion has been achieved for the first time at 2.488Gbits/s with a monolithic integrated multi-wavelength laser. This is currently the highest modulation rate demonstrated by such a device. By operating the laser in many different configurations, three novel network functions have been demonstrated. These included multi-wavelength conversion, WDM multiplexing and 1x4 space switching. It was found by optimising the conversion wavelength that the need for post filtering could be removed, reducing the component count still further. Bit Error Rate (BER) measurements indicated a 3-4dB penalty was incurred at 1.244Gbits/s.

7.6 References

[1] JD Burton, PJ Fiddyment, MJ Robertson, P Scully, "Monolithic InGAAsP-InP Laser Amplifier Gate Switch Matrix" IEEE Journal of Quantum Electronics 1993, Vol. 29 No. 6, pp2023-2026.

[2] A.W. Nelson, P.C. Spurdens, *et al* "The Role of MOVPE in the manufacture of high performance InP Based Optoelectronic devices", J. Crystal Growth, Vol. 93, 1988, pp792-802.

[3]. S.M. Ojha, G.H.B. Thompson, C.G. Cureton,C.B. Rogers, S.J. Clements, M. Asghari, I.H. White, "Demonstration Of Low-Loss Integrated InGaAsP/InP Demultiplexer Device With Low Polarization Sensitivity" Electronics Letters, 1993, Vol.29, No.9, pp.805-807

[4]F.A. Jenkins, H.E. White, "Fundementals of Optics - Fourth Edition", McGraw-Hill 1981, pp 360.

[5] J.B.D Soole, K. Poguntke, A. Schere, M.P. Leblanc, *et al* "Multiple stripe array grating in a cavity (MAGIC) laser, a new semiconductor laser for WDM applications", Electronics Letters, Vol. 28, pp1805-1807.

[6] M. Zirngibl, C.H. Joyner, L.W. Stulz, U. Koren, *et al* "Digitally Tunable Laser Based on th Integration of a Waveguide Grating Multiplexer and an Optical Amplifier", IEE PTL, Vol. 6, No. 4, April 1994, pp517-520.

[7] C.H. Joyner, M. Zirngibl, J.P. Meester, "A Multifrequency Waveguide Grating Laser by Selective Area Epitaxy", IEEE PTL, Vol. 6, No. 11, November 1994, pp 1277-1279.

[8] C.H. Joyner, M. Zirngibl, J.C. Centanni, "An 8-Channel Digitally Tunable Transmitter with Electroabsorption Modulated Output by Selective Area Epitaxy", IEEE PTL, Vol. 7, No. 9, September 1995, pp1013-1015.

[9] M. Zirngibl, C.H. Joyner, C.R. Doerr, L.W. Stultz, H.M. Presby, "An 18-Channel Multifrequency Laser", IEEE PTL, Vol. 8, No. 7, July 1996, pp870-874.

[10] A.A.M. Staring, L.H. Spiekman, J.J. Binsma, E.J. Jansen *et al* "A Compact Nine-Channel Multiwavelength Laser", IEEE PTL, Vol. 8, No. 9, September 1996, pp 1139-1141.

[11] R. Monard, C.R. Doerr, C. H. Joyner, M. Zirngibl, L.H. Stulz, "Direct Modulation of a Multifrequency Laser up to 16x622Mbits/s", IEEE PTL, Vol. 9, No. 6, June 1997, pp815-817.

[12] M. Owen, J.D. Bainbridge, M.F.C. Stephens, *et al* "Highly Flexible all-Optical Wavelength Conversion at 2.488Gbits/s using a multi-output wavelength Laser", CLEO1998, paper CThZ6.

[13] E. Hecht, "Hecht Optics - Second Edition", Addison Wiley Publishing Co., pp 372.

[14] R.W.H. Engelmann, C. Shieh, C. Shu, "Multi-Quantum Well Lasers: Chapter 3, Threshold Considersations", Academic Press Inc. pp 166-167.

[15] Private Communication with Dr. K.R. Poguntke, BT Research Laboratories Martlesham Heath.

[16] R. Zengerle, O. Leminger, "Phase-Shifted Bragg-Grating Filters with improved Transmission Characteristics", JLT Vol. 13, No. 12, December 1995, pp 2354-2358.

[17] International Telecomunications Union, Standardisation sector, Study Group IS, Constribution 4S, ITU-TS SG14-45E, July 1993.

[18] G. Morthier, P. Vankwikelberge, "Handbook of Distributed Feedback Laser Diodes", Artech House, Inc. 1997.

[19] G.P. Agrawal, N.P. Dutta, "Semiconductor Lasers - Second Edition", Van Nostrand Reinhold, Chapter 5

Monolithic Integration of Optical Space Switches

Chapter 8

8.1 Conclusions and Future Work

The previous five chapters of work have discussed three different methods for achieving optical space switching. This chapter briefly summarises the results and conclusions of the work contained within this thesis. A discussion of future work will be given which shows that the crosspoint switch proposed in chapters 4,5 and 6 is still under development. The methods being used to fabricate the final 4x4 active/passive prototype design will be briefly discussed. Methods for achieving 4x4 optical switching using the MGC laser are also proposed.

8.2 Summary

8.2.1 Introduction and Motivation

Chapter 1 has given a brief introduction into the evolution of the modern optical communications systems. Both Optical Time Division multiplexing (OTDM) and Wavelength Division Multiplexing (WDM) have been introduced as methods of more effectively utilising the bandwidth of optical fibre. However, to date, they have only been employed in terms of the point to point network, whereby information is transferred between two distinct points. It was shown that the future of optical communications lies in a more transparent scheme, where optics is used to route information across the entire network. Several key components were required in these optical routing networks, such as ADD/DROP demultiplexers and optical network nodes. It was shown that the optical space switch lies at the core of these components and is therefore required for future networking schemes. Passive Wavelength Routing was also highlighted as a method of achieving space switching in WDM network schemes. Therefore an introduction to various of methods of wavelength conversion was given which focused on the work presented in chapter 7.

Chapter 2 was concerned with the many methods of achieving monolithic integration of crosspoint switches. It was shown that InP is currently the material system most suited to optical crosspoint development at 1.55μm, owing to potentially lossless device performance. It was highlighted that the problem associated with the integration of InP crosspoints with large device orders was the exponential increase of waveguide crossings. Waveguide S-bends were shown to be incompatible with waveguide crossings and therefore not suited to high order crosspoint development. Multi-level architectures were also shown to offer no great advantage in device size and therefore not ideal candidates for monolithic integration on InP (only modular). A summary of the published optical space switches was given, which suggested that total internal reflection was a method of achieving compact switch design. This lead to the proposal of two new crosspoint architectures. The first introduced the concept of two dimensional integrated optics which eliminated the need for waveguide crossings and was discussed further in chapter 3. The second proposed device used conventional waveguides to shuffle each input to each output. A combination of Total Internal Reflection, the use of the electroabsorption modulator and strong and weak guiding was shown to result in the most compact device possible. This work was the main focus of this thesis which was presented in chapters 4, 5 and 6.

8.2.2 Two Dimensionally Integrated Crosspoint Architecture

Chapter 3 discussed the role of Two Dimensional Integrated Optics (2DIO) in the monolithic integration of optical space switches. 2DIO offered lossless optical crossings which is extremely attractive for high order crosspoint development. A novel 2DIO crosspoint architecture was proposed which combined input and output waveguides with parabolic mirrors, spatial filters and broad area amplifier gate switches. A 2DIO modal propagation model was developed in order to optimise the device for both loss and crosstalk (appendix B). Analysis of the broad area amplifier gate switches was carried out with a combination of rate equation analysis and beam propagation (appendix A). Results showed that a lossless 4x4 2DIO broadcast switch could be monolithically integrated onto an InP substrate less than $2x2mm^2$ in area. If realised the device would be the smallest broadcast 4x4 crosspoint fabricated to date.

8.2.3 Conventional Waveguide Crosspoint Architecture

Chapter 4 was concerned with the theoretical optimisation of a conventional *NxN* crosspoint switch architecture proposed in chapter 2. The complete theoretical optimisation of the device was given which began with an investigation of the single mode nature of a ridge waveguide on a BT passive wafer design. After calculations on the waveguide crossing loss and waveguide coupling, this allowed the optimised shallow etched waveguide for the device to be finalised. The modal cut-off of the deep etched waveguides allowed the design of tapered mode converters which were required to achieve low loss coupling between the regions of strong and weak guiding. A modal propagation model was developed for the analysis of the multimode interference coupler (appendix B) which permitted fabrication tolerant MMI design. Finally, after determining the minimum radius of curvature for the S-bends a prediction of the device size was made. This calculation showed that the 4x4 device could be fabricated on an InP substrate approximately $1x2.5mm^2$ in area. This architecture is approximately half as small as the 2DIO architecture presented in Chapter 3 and therefore offered a significant advantage over the 2DIO approach.

Chapter 5 was concerned with the practical realisation of the architecture theoretically optimised in chapter 4. The problems associated with mask alignment between deep and shallow etched regions was highlighted with both the TIR mirror and tapered mode converter. It was shown how alignment tolerances could be relaxed by a combination of mask design and the self alignment process. Several test structures were then proposed which were to be used to justify the theoretical calculations made in chapter 4. A discussion of the fabrication process was given, highlighting the problems behind vertical InP etching. Finally analysis of the

fabricated test structures on a Scanning Electron Microscope (SEM) gave an indication of the etching quality and tolerances achieved.

Chapter 6 was concerned with the measurement and assessment of the test structures presented in chapter 5. This began with near field measurements of straight waveguides to confirm single mode operation, as theoretically predicted in chapter 4. The losses of all the crosspoint components were given, which included waveguide crossings, TIR mirrors, tapered mode converters, MMI couplers, and S-bend waveguides. All components agreed, within experimental error, to the theoretical calculations made in chapter 4. These measurements allowed a prediction on the loss performance of the 4x4 passive crosspoint test structure, which suggested an excess device loss of 7.2±0.5dB. Subsequent calculations on the tapered mode converters and S-bend waveguides indicated a further reduction in the proposed architecture size. This resulted in a final prediction on the full active/passive 4x4 prototype of 1x2mm^2, which was comparable to the same wafer area required to fabricate 8 DFB lasers. This represents an order of magnitude improvement on the smallest InP broadcast crosspoint switch fabricated to date [1].

8.2.4 The MGC Laser and Wavelength Routing

Finally, chapter 7 introduced the Multi-Grating Cavity (MGC) laser fabricated by BT Research Laboratories Martlesham Heath. A brief discussion of the device fabrication and method of operation was given, before comparing the device with the other types of monolithic multi-wavelength laser so far reported. Initial device characterisation showed CW operation on four wavelength channels spaced by 3.7nm (453GHz) about 1557nm. The device threshold was approximately 140mA per stripe. Wavelength conversion was then demonstrated for the first time in a multi-wavelength laser at 2.488Gbits/s. Three novel modes of operation were discussed which achieved multi-wavelength conversion, WDM multiplexing and most importantly 1x4 space switching. The wavelength selectivity of the grating allowed space switching without the need for post filtering, and thus demonstrated wavelength routing in a single monolithically integrated device.

8.3 Suggestions for Future Work

8.3.1 A 4x4 Wavelength Routing Space Switch

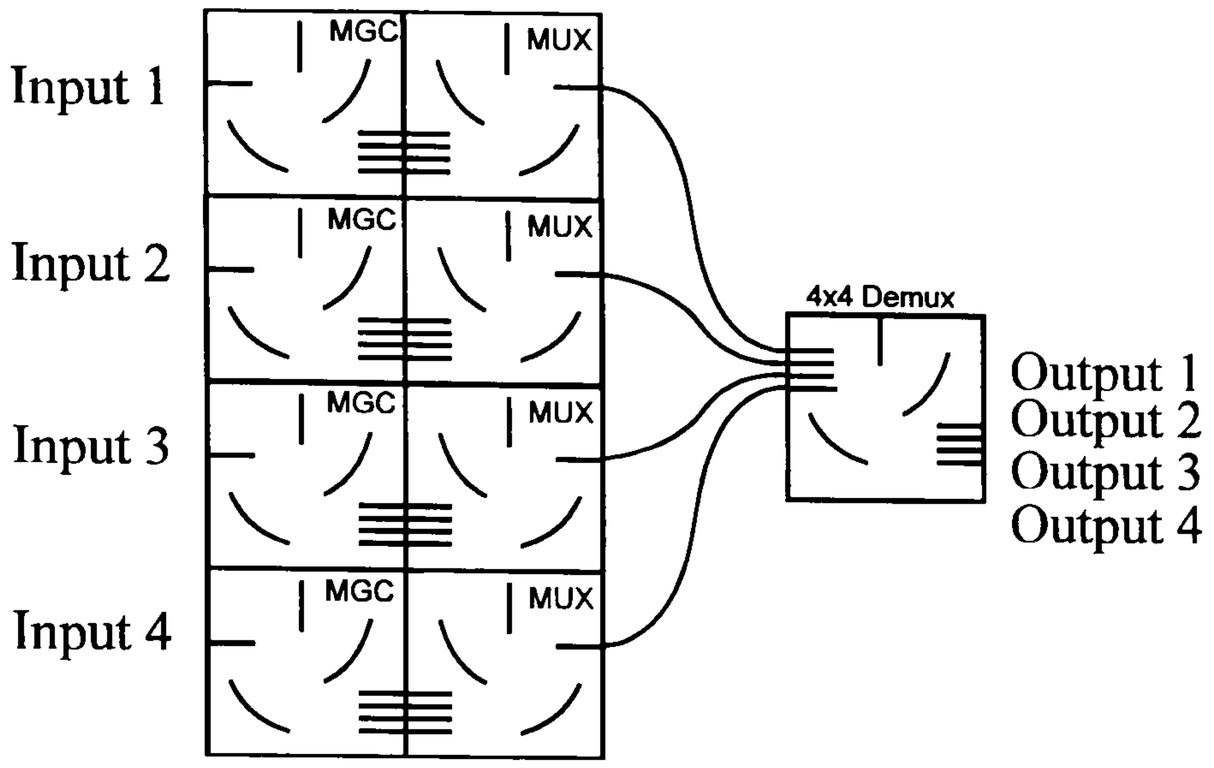

Figure 8.1 Schematic diagram of the MGC laser used in a 4x4 passive wavelength router

Chapter 7 has demonstrated wavelength conversion for the first time at 2.488Gbits/s in a multi-wavelength laser. Subsequent experiments showed that 1x4 space switching could be achieved in a single integrated device, with no post filtering, by using the concept of wavelength routing. Although this result is impressive, a fully functional WDM network node would require a number of optical input fibres rather than just one as demonstrated here. Extended 4x4 operation could be demonstrated using the MGC by the use of a 4x4 passive grating multiplexer and an array of four lasers as drawn schematically in figure 8.1. Each MGC is able to convert onto any of its lasing wavelengths before being multiplexed to a single optical fibre and routed to each output (via the 4x4 passive router). The need for the multiplexers after each MGC may be removed by the use of 2x2 couplers and a fibre shuffle as shown in figure 8.2. However it should be noted that in order to achieve a 4x4 routing capability in either design, the number of components required is not trivial. Indeed it is still a matter for debate whether wavelength routing is viable alternative to the conventional crosspoint switch discussed in chapters 4,5 and 6.

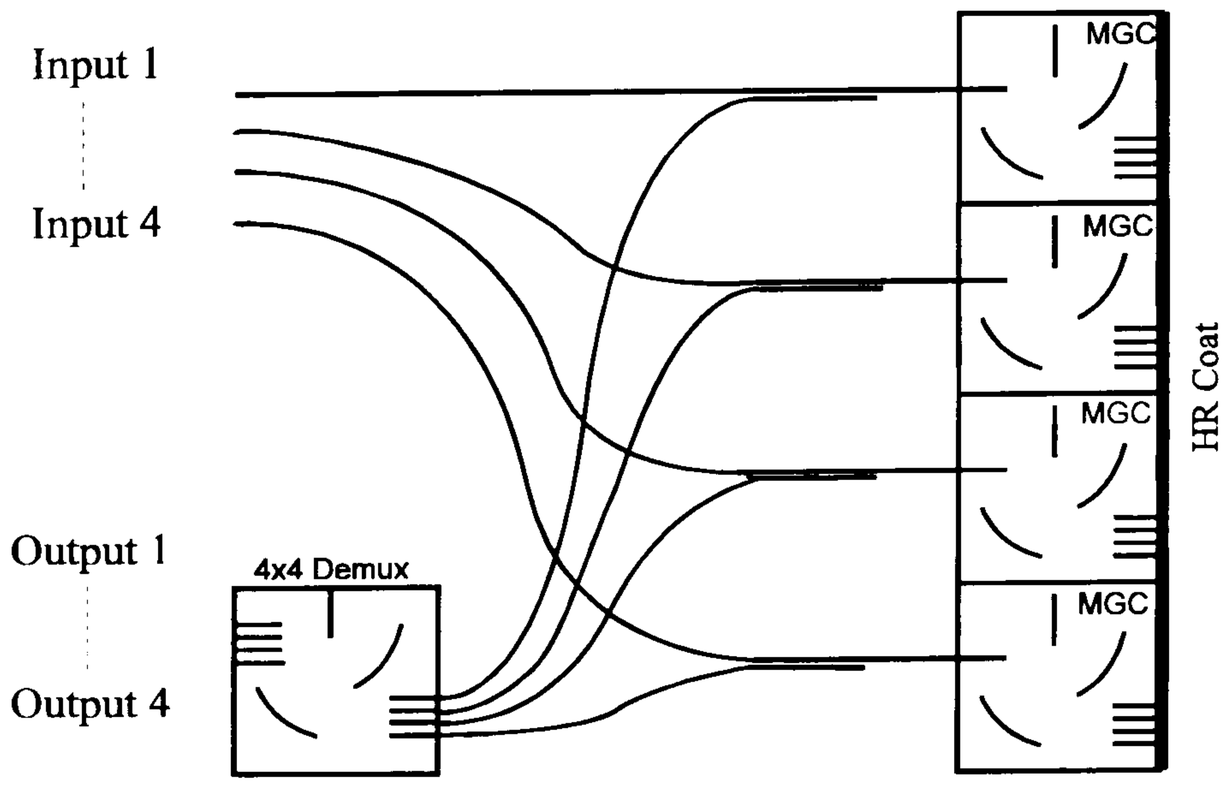

Figure 8.2 Alternative method for achieving a 4x4 wavelength routing space switch.

8.3.2 An ITU Grid Aligning WDM transmitter

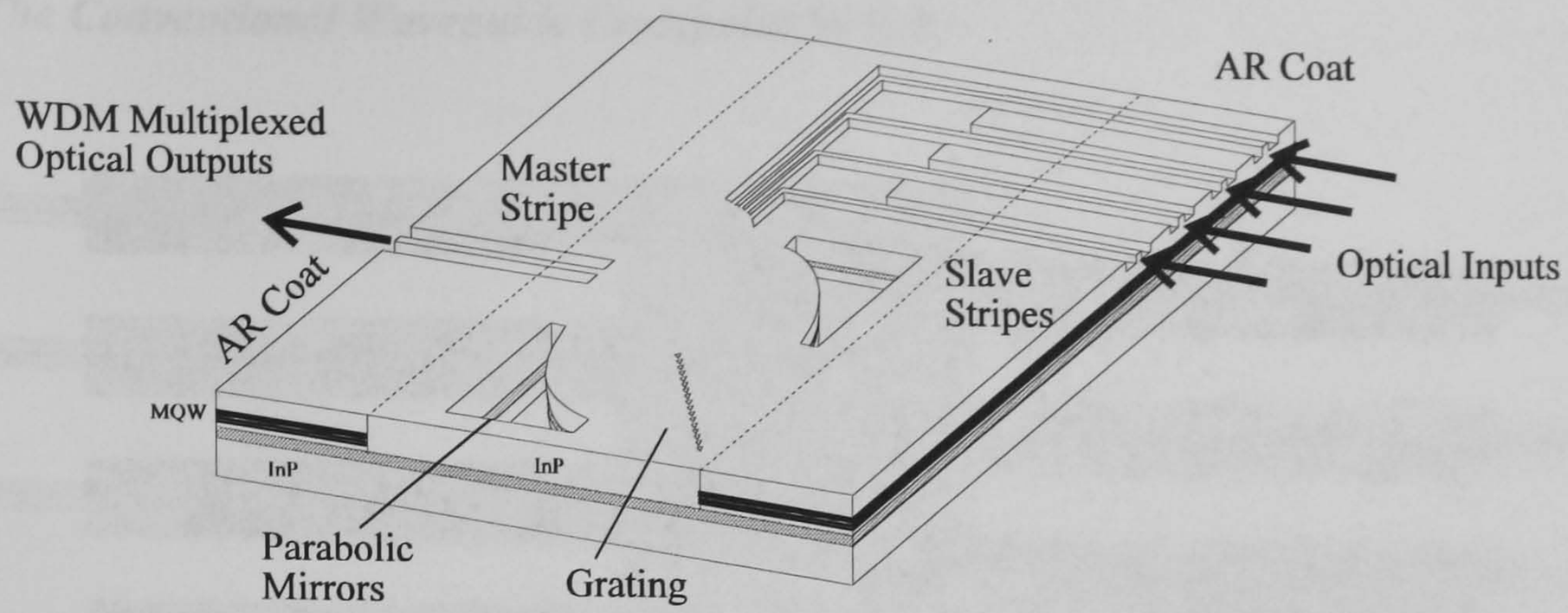

Figure 8.3 Schematic diagram of the MGC laser as a WDM multiplexer

It was also suggested in chapter 7 that WDM multiplexing could be achieved by injecting the input signal into the slave side of the device. Thus any input optical signal could be automatically aligned to the ITU grid whilst being multiplexed to a single output fibre as shown schematically in figure 8.3. However, it was shown that this could not be achieved simultaneously on all channels owing to inter-channel crosstalk. This extremely useful function could be achieved in the MGC by using the device as two amplifiers sandwiching a passive grating section rather than operating the device as a laser. This can be achieved by AR (Anti reflection) coating both the slave and master facets. Wavelength conversion may then be induced in each slave stripe by gain saturation as shown in figure 8.4. It may be observed that another MGC laser is required in order to provide the CW probe signal which multiplexed to the final output. Provided that the combined optical power in the master facet of the AR coated device is far below the input saturation power, then inter-channel crosstalk may be eliminated and a fully functional ITU grid aligning WDM transmitter is realised.

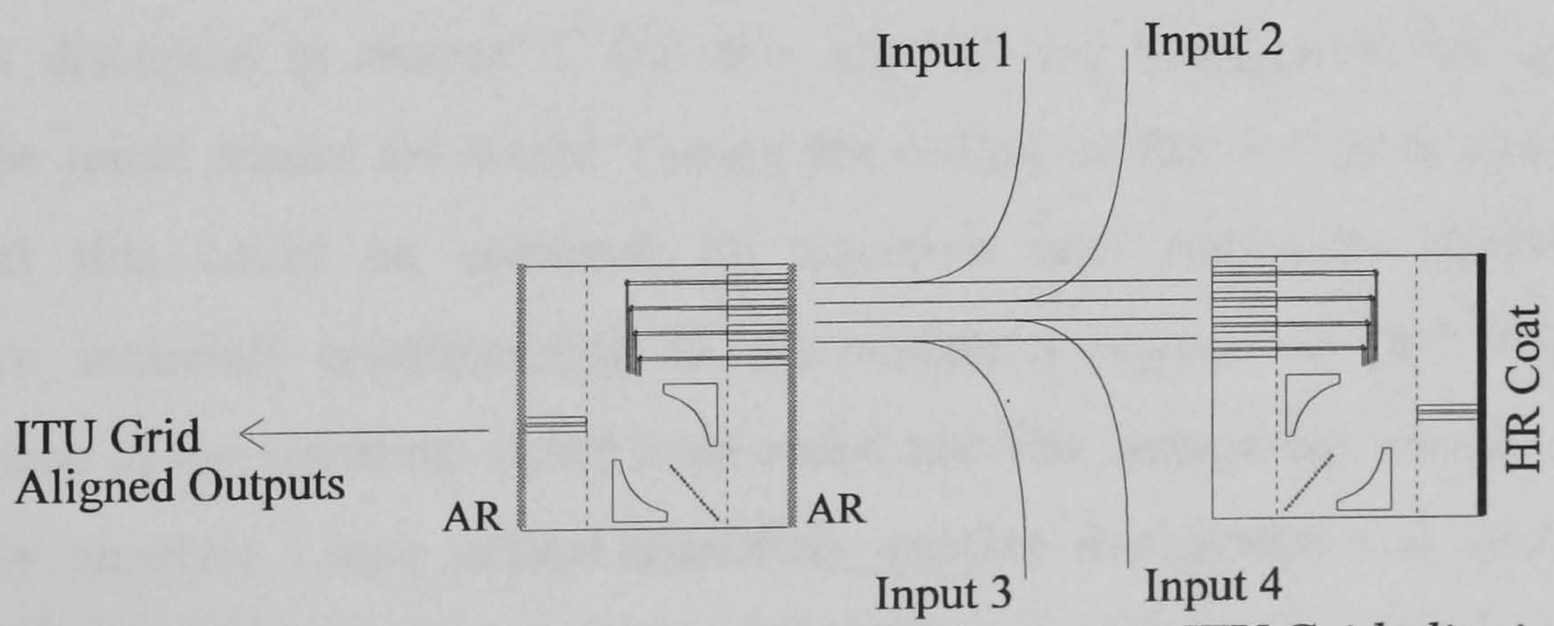

Figure 8.4 Schematic diagram of an AR coated MGC laser as a ITU Grid aligning WDM transmitter

8.4 Overall Conclusions

8.4.1 The Conventional Waveguide Crosspoint Switch

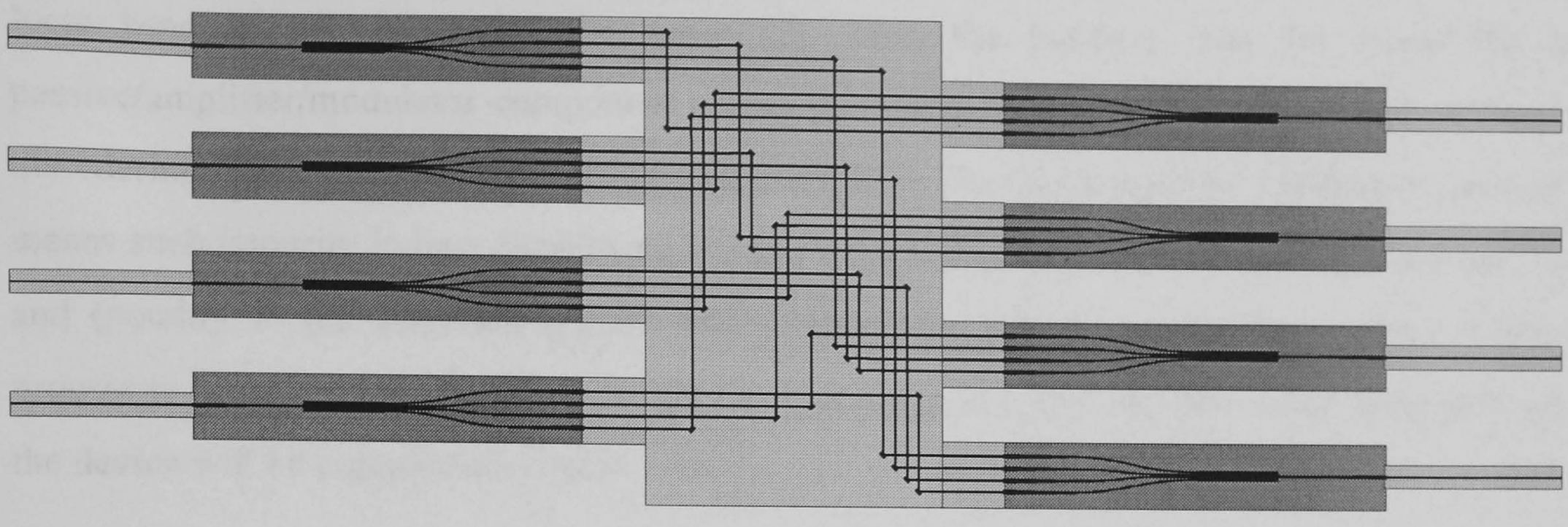

Figure 8.5 Mask Design of the proposed 4x4 InP Crosspoint Switch

Finally, the main focus of this thesis has been the design and realisation of the crosspoint switch drawn in figure 8.5. The complete fabrication and assessment of the active/passive device has not been possible owing to time limitations. However, owing to significant benefits offered by the device, its fabrication still continues under an EPSRC funded grant jointly awarded to Bristol University, Glasgow University, BT Research Laboratories and British Aerospace. The grant aims to fabricate 2x2, 4x4 and 8x8 InP crosspoint switches using the architecture discussed in this thesis. When fabricated the 4x4 device will be an order of magnitude smaller in wafer area than the smallest InP crosspoint realised to date [1].

Chapters 5 and 6 have shown the viability of the device from the fabrication and assessment of several test structures, although a more rigorous analysis may be required in order to assess the effects of growth variations between and/or across an InP wafer. The final factor in the realisation of the device lies in the method for achieving the electroabsorption modulators, passive waveguides and optical amplifiers on different regions of the wafer. It has already been discussed in chapter 2 that this requires the bandgap of the semiconductor material to be tuned across the wafer. During the design of the device in chapter 4 it was assumed that this could be achieved by selective area regrowth, whereby different semiconductor materials corresponding to active/passive regions are epitaxial grown on different regions of the substrate. It has been stated that this method has already been used to monolithically integrate 1.5μm optical amplifiers, passive waveguides and electroabsorption modulators. However the process is extremely labour intensive, thus simpler methods are currently being investigated in order to achieve spatial variations in bandgap across the wafer.

One such method which has been proposed by Glasgow University (amongst others) relies on the variation of the effective bandgap of an MQW wafer as a function of well width (as discussed in chapter 2). Different regions of the wafer may be masked and undergo a

process termed 'disordering'. In the InGaAsP/InGaAs material system, this causes a local diffusion of Phosphor in the barriers into the wells, so smoothing out the discrete potential step formed by the quantum well. This in turn changes the effective width of the well and lowers the local bandgap wavelength of the wafer [2]. Thus the bandgap may be tuned for a passive/amplifier/modulator component across the wafer by controlling the amount of local disordering. This has been achieved to date (mainly in the GaAs material system) by several means such impurity induce disordering [3], ion implantation [4], impurity free disordering [5] and (notably in InP material system) laser intermixing [6]. A detailed description of this process is far beyond the scope of this thesis, however it is hoped that the entire fabrication of the device will be completed by early 1999.

8.5 References

[1] W. van Berlo, M. Janson, L. Lundgren *et al*, "Monolithically Insensitive Monolthic 4x4 InGaAsP-InP Laser Amplifier Gate Switch Matrix", IEEE PTL, Vol. 9, No. 11, November 1995, pp1291-1293.

[2] A. McKee, C.J. McLean, G. Lullo, A.C. Bryce, R.M. De La Rue, J.H. Marsh, C.C. Button, "Monolithic Integration in InGaAs-InGaAsP multiple-Quantum-Well Structures Using Laser Intermiximg" IEEE JQE, Vol. 33, No. 1, January 1997, pp45-55.

[3] S.A. Schwarz, P. Mei, *et al*, "InGaAs/InP Superlattice Mixing Induced by An or Si Diffusion", Appl. Phys. Lett, Vol. 53, 1988, pp1051-1053.

[4] B. Tell, J. Shah, P.M. Thomas, *et al*, "Phosphorus ion Implantation Induced Intermixing of InGaAs/InP Qunatum well Structures", Appl. Phys Lett, Vol. 54 1989, pp1570-1572.

[5] T. Miyazawa, H. Iwamura, M. Naganuma, "Integrated External-Cavity InGaAs/InP Lasers using Dielectric Cap Disordering", IEEE PTL, Vol. 3, 1991, pp421-424.

[6] C.J. McLean, J.H. Marsh, R.M. Del La Rue, A.C. Bryce, B. Garrett, R.W. Grew, "Layer Selective Disordering by Photo-Absorption induced thermal diffusion in InGaAs/InP Based MQW Strucutres", Elec. Lett, Vol. 28, 1992, pp1117-1119.

Appendix A : Rate Equation Analysis of a Broad Area Amplifier

By using a truncation filter and optimising the amplifier taper angle, the propagating mode through a broad area amplifier length can be forced to a zero order gaussian mode, as discussed in Chapter 3. The effects of hole burning which alter the transverse refractive index distribution are calculated from a multi-section rate equation model, in order to approximately calculate the phase of the emitted wavefront.

The rate equation analysis separates the amplifier cavity into a mesh of lumped regions, however carrier diffusion effects between each section are ignored. The model is purely travelling wave i.e. zero facet reflectivity, and assumes that only monomode radiation is present. The carrier density rate equation for each section is therefore described by [a1]

$$\frac{dn(x,z)}{dt} = \frac{i_a}{eV} - \frac{n}{\tau_s} - g_m \frac{P}{E} - \beta\, g_m S_{sp} \frac{c}{\mu} \tag{A1}$$

where $n(x,z)$ is the carrier concentration in each section, i_a is the current in the active region, g_m is the material gain (in each section), e is the electronic charge, V is the volume of the cavity, t_s is the carrier recombination lifetime (in each section), E is the photon energy density, S_{sp} is the average photon density in each section due to spontaneous emission, β is the spontaneous coupling coefficient and c is the speed of light where μ is the refractive index of the cavity. P is the optical power in each section.

The gain spectrum is assumed to be parabolic with a peak wavelength λ_p, thus the material gain is represented by [a2]

$$g_m = a_0(n - n_0) - a_1(\lambda - \lambda_p)^2 \tag{A2}$$

where a_o, a_1 are material gain constants, n_o is the transparency carrier density and λ is the photon wavelength in free space at the input.

The gain per unit length of each section is then described by the equation [a3]

$$g = \Gamma g_m - \alpha \tag{A3}$$

where Γ is the confinement factor and α takes into account scattering losses.

Calculation of the carrier recombination lifetime takes into account non-radiative, bimolecular and Auger recombination using the expression [a4]

$$\tau_s = \frac{1}{A + Bn + Cn^2} \tag{A4}$$

where A, B and C are the constants relating to each process respectively.

The spontaneous emission photon density is averaged over the gain spectrum, and assuming bimolecular recombination is given for each section by [a3]

$$S_{sp} = \frac{Bn^2 \mu_0}{gc}\left[\frac{(e^{gz} - 1)}{gz} - 2\right] \tag{A5}$$

where, μ is the refractive index and c is the speed of light in a vacuum.

The power in each section, P, is determined from the MPM calculation, P_{MPM},(x,z), determined from the equation

$$P = P_{BPM}(x,z)e^{gz} \tag{A6}$$

Each section is solved dynamically, and the approximate refractive index distribution $\mu(x,z)$ across the amplifier cavity can be calculated from the equation [a5]

$$\frac{d\mu}{dn} = -\frac{\alpha_h \lambda}{4\pi} a_0 \tag{A7}$$

where α_h is the line broadening factor and λ is the operating wavelength.

The phase front variation due to the gain region may then be calculated from the equation

$$\phi(x) = \frac{2\pi}{\lambda}\int_0^l \frac{\mu(x,z)}{\mu_0} dz \tag{A8}$$

Parameters Used

Constant	Description	Value
A	Non-radiative Recombination Constant	$10^8 s^{-1}$
B	Bimolecular Recombination Constant	$8x10^{-11} cm^3 s^{-1}$
C	Auger Recombination Constant	$4x10^{-29} cm^6 s^{-1}$
β	Spontaneous Coupling Coefficient	$1x10^{-4}$
d	Active waveguide thickness	0.4μm
W	Active waveguide width	20μm
L	Active waveguide length	500μm
a_0	Material Gain Constant	$3.5x10^{-16} cm^2$
a_1	Material Gain Constant	$0.12 cm^{-1} nm^{-2}$
λ_p	Peak Gain Wavelength	1.550μm
Γ	Confinement Factor	0.53
α	Scattering Losses	$20 cm^{-1}$
μ_0	Effective Refractive index of active waveguide	3.197
α_h	Linewidth Enhancement Factor	6

Table A1 Typical Parameters used in the Rate Equation Analysis

Table A1 lists the parameters used in the multi-section rate equation analysis of the broad area amplifier switches. These are typical values which may be found in the literature and discussed further in [a5]. The rate equation A1 may then be solved iteratively in each section to determine the phase front variation as given by equation A8.

References

[a1] H. Kawaguchi, "Absorptive and Dispersive Bistability in Semiconductor Injection Lasers", Opt. Quantum Electron., 1987, No. 19, pp S1-S36.

[a2] J. Wang, H. Olesen, K. Stubkjaer, "Recombination Gain and Bandwidth Characteristics of 1.3μm Semiconductor Amplifiers", JLT, No. 5 1987, pp184-189.

[a3] M.J. Adams, J.V. Collins, I.D. Henning, "Analysis of Semiconductor Laser Optical Amplifiers", IEE Proceedings, Vol. 132, No. 1, February 1985, pp 58-63.

[a4] G.P. Agrawal, N.P. Dutta, "Semiconductor Lasers - Second Edition", Van Nostrand Reinhold.

[a5] J.A. Constable, I.H. White, A.N Coles, D.G. Cunningham, "Harmonic and Phase Distortion of Analogue AM Signals in Bulk Near Travelling-Wave Semiconductor Amplifiers", IEE Proc.-J, Vol. 139, No. 6, December 1992, pp 389-398.

Appendix B : Modal Propagation Theory

The beam propagation models discussed in chapters 3 and 4 are derived from first principles. The analysis begins with the solution of the wave equation for a slab waveguide. This yields solutions for both a 1D dielectric waveguide in the vertical plane and the 2D slab waveguide in the horizontal. These equations form the basis for the models used to analyse both the 2DIO crosspoint architecture and the Multi-Mode Interference couplers used in the waveguide crosspoint switch.

Solution of the 3D Wave Equation

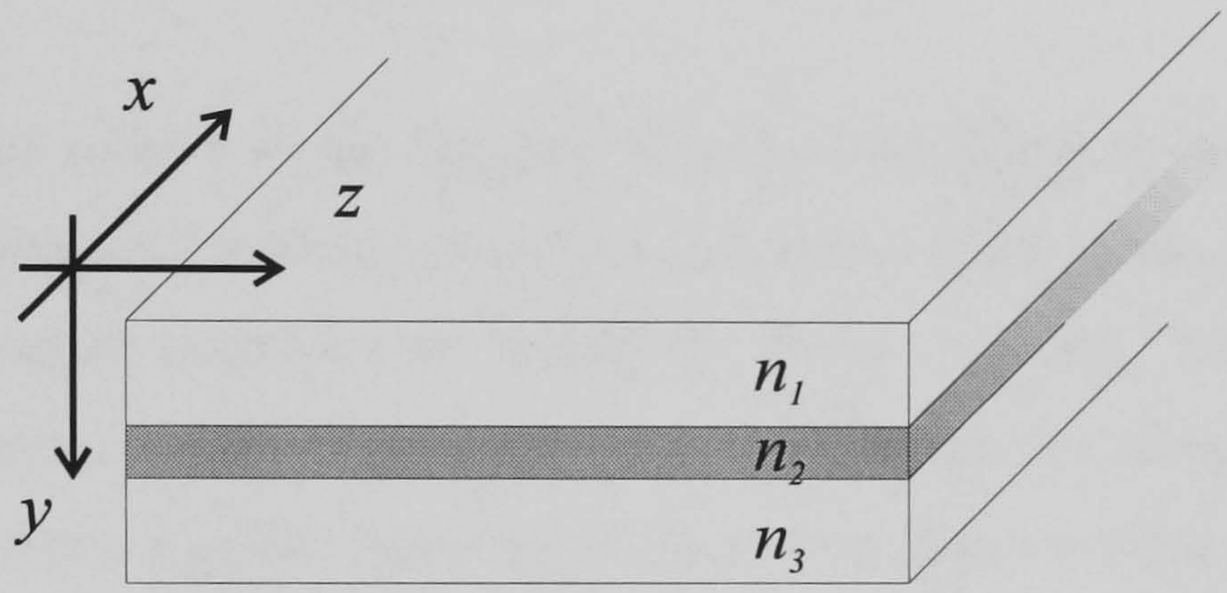

Figure B1 Dielectric slab waveguide.

Light propagating in a slab waveguide as drawn schematically in figure B1 obeys the wave equation which is given by

$$\nabla^2 \vec{E}(x,y,z,t) - \frac{n^2}{c^2}\frac{\partial^2}{\partial\, t^2}\vec{E}(x,y,z,t) = 0 \qquad \text{(B1)}$$

where *c/n* is the speed of light in the slab and *E* is the vector electric (or magnetic) field component of the EM wave.

If the slab is assumed to be homogeneous and extends to infinity in all directions the electric field can be assumed to be of the form

$$\vec{E}(x,y,z,t) = \vec{E}_s(y,t)\vec{E}_p(x,z,t)e^{i(wt-\beta z)} \qquad \text{(B2)}$$

where E_S represents the electric field through a section of the slab and E_p represents the electric field in the slab plane, β is the wave vector and ω is the angular frequency of the EM radiation. Substitution of this solution into the wave-equation B1 yields

$$\vec{E}_s \frac{\partial^2 \vec{E}_p}{\partial x^2} + \vec{E}_s \frac{\partial^2 \vec{E}_p}{\partial z^2} + \vec{E}_p \frac{\partial^2 \vec{E}_s}{\partial y^2} + (k^2 n^2 - \beta^2)\vec{E}_s \vec{E}_p = 0 \tag{B3}$$

which may be solved by initially assuming that the field gradient is much larger in the vertical plane, i.e.

$$\frac{\partial^2 \vec{E}_s}{\partial y^2} >> \frac{\partial^2 \vec{E}_p}{\partial x^2} + \frac{\partial^2 \vec{E}_p}{\partial z^2} \tag{B4}$$

This reduces equation B3 to the one dimensional wave equation given by

$$\frac{\partial^2 \vec{E}_s}{\partial y^2} + (k^2 n^2 - \beta^2)\vec{E}_s = 0 \tag{B5}$$

which can be solved subject to the dielectric boundary conditions (n_1, n_2, n_3 in figure B1) imposed by the guiding and cladding layers. This calculation is not discussed here, since it may found in many standard textbooks on waveguide theory [b1, b2]. The solution yields a complete orthonormal basis set of functions, ψ_n, which propagate along the z axis with an effective refractive index $n_{eff}=\beta/k$. These functions may be shown to from the solutions for the TE and TM guided modes of the slab waveguide.

Substitution of the guided optical mode E_s and effective propagation constant β calculated from equation B5, back into the wave-equation B3 yields the two dimensional wave equation which describes the propagation of the EM waves in the slab plane, given by

$$\frac{\partial^2 \vec{E}_p}{\partial x^2} + \frac{\partial^2 \vec{E}_p}{\partial z^2} + (k^2 n^2 - \beta^2)\frac{\partial^2 \vec{E}_p}{\partial t^2} = 0 \tag{B6}$$

Therefore after calculating E_s and β the slab mode may then be ignored. The solution of this equation forms the basis of the MPM analysis presented in chapter 3 and is discussed further in the next section

Solution of the 2D Wave Equation

Assuming that the radiation in the slab consists of a paraxial beam and the electric and magnetic component can be represented by a scalar field distribution, the solution of equation B6 is an eigen-value problem which yields an infinite number of eigen-functions (a complete orthonormal basis set) which describe EM modes propagating along the z axis. These modes are described by the Hermite-Gaussian set of functions given by the equation [b3]

$$E_p(x,z,t) = E_0\psi_n(x,z,t) \text{ and}$$

$$\psi_n(x,z,t) = A_n H_n\left\{\frac{\sqrt{2}x}{w(z)}\right\} e^{-\left[i\phi_n + z^2\left\{\left(\frac{1}{w(z)}\right)^2 + \frac{i\beta}{2R(z)}\right\}\right]} \tag{B7}$$

where n is the mode order, E_0 is the electric field at $z=0$, β is the wave vector and ω is the angular frequency of the EM radiation. $\phi_n(z)$, $w(z)$ and $R(z)$ are functions describing the phase change along the axis of propagation, the beam divergence and radius of curvature of the phase front respectively and are described by the equations

$$\phi_n(z) = (n + ½)\tan^{-1}\left(\frac{2z}{kw_0^2}\right) \tag{B8}$$

$$w(z)^2 = w_0^2\left[1 + \left(\frac{2z}{kw_0^2}\right)^2\right] \tag{B9}$$

$$R(z) = z\left[1 + \left(\frac{kw_0^2}{2z}\right)^2\right] \tag{B10}$$

where w_o represents the beam radius at $z=0$. A_n is a normalisation constant to ensure conservation of energy from the origin of propagation and is described by the equation

$$A_n = \frac{1}{\int_{-\infty}^{+\infty}\psi_n\psi_n^* dx} = \left(2^n n! w(z)\sqrt{\frac{\pi}{2}}\right)^{-\frac{1}{2}} \tag{B11}$$

$H_n\{f(x)\}$ is the n^{th} order Hermite polynomial of $f(x)$ which may be calculated from the recursion relation [b4],

$$H_{n+1}\{f(x)\} = 2f(x)H_n\{f(x)\} - 2nH_{n-1}\{f(x) \tag{B12}$$

Given that $H_0\{f(x)\}=1$ and $H_1\{f(x)\}=2f(x)$, any n^{th} order Hermite-Gaussian may be deduced.

Modal Propagation Model

The 2DIO modal propagation model discussed in chapter 3 may be justified by the following equations. Firstly, owing to the linearity of the two dimensional wave-equation B6, its complete solution is given by the infinite sum of all the Hermite-Gaussian modes weighted by a constant C_n [b5], hence

$$E_p(x,z,t) = E_0 \sum_{n=0}^{\infty} C_n \psi_n(x,z,t) \tag{B13}$$

Given the electric field in one x-plane $E_p(x,z'=Const)$ the gaussian coefficients C_n may be calculated from equation B13 by observing the orthonormality of ψ_n.

$$C_n \delta_{nm} = \int_{-\infty}^{\infty} E(z' = Const)\psi_m dx \tag{B14}$$

where δ_{nm} is the Kronecker delta function. Thus the component or proportion of the n^{th} order gaussian in the field $E(z'=Const)$ i.e. C_n may be calculated. The resulting propagation of the field $z'=Const+z$ may then be constructed from equation B12 since the propagation in the z direction of each individual gaussian order is known from equation B6.

Modal analysis of the MMI couplers is very similar, however requires the solution of the 2D wave-equation B6, subject to the boundary conditions imposed by horizontal waveguiding. This calculation has already been briefly discussed as it also forms the solution of the 1D wave-equation B5. After calculating the guided mode solutions in the horizontal MMI waveguide, the field propagation may be determined by following the same analysis as given above. This is achieved by substitution of the 2DIO gaussian solution, ψ_n, with the MMI guided mode solutions in equations B13 and B14.

References

[b1] D.L. Lee "Electromagnetic principles of Integrated Optics", John-Wiley & Sons 1986.

[b2] Deitricht Marcuse "Light Transmission Optics Second Edition" Van Nostrand Reinhold Company

[b3] J.C.G. Lesurf, "Millimeter-wave Optics, Devices and Systems", Adam Hilger 1990, pp34-42.

[b4] M.L. Boas, "Mathematical Methods in the Physical Sciences - Second Edition", John Wiley 1983, pp 531.

[b5] M.L. Boas, "Mathematical Methods in the Physical Sciences - Second Edition", John Wiley 1983, Chapter 8.